A Model Stitching Architecture for Continuous Full Flight-Envelope Simulation of Fixed-Wing Aircraft and Rotorcraft from Discrete-Point Linear Models

Eric L. Tobias and Mark B. Tischler
Aviation Development Directorate
Aviation and Missile Research, Development, and Engineering Center

April 2016

DESTRUCTION NOTICE

DISCLAIMER

TRADE NAMES

REPORT DOCUMENTATION PAGE

Public reporting burden for this collection of information is estimated to average 1 hour per response, including the time for reviewing instructions, searching existing data sources, gathering and maintaining the data needed, and completing and reviewing this collection of information. Send comments regarding this burden estimate or any other aspect of this collection of information, including suggestions for reducing this burden to Washington Headquarters Services, Directorate for Information Operations and Reports, 1215 Jefferson Davis Highway, Suite 1204, Arlington, VA 22202-4302, and to the Office of Management and Budget, Paperwork Reduction Project (0704-0188), Washington, DC 20503

1. AGENCY USE ONLY	2. REPORT DATE April 2016	3. REPORT TYPE AND DATES COVERED Final

4. TITLE AND SUBTITLE

A Model Stitching Architecture for Continuous Full Flight-Envelope Simulation of Fixed-Wing Aircraft and Rotorcraft from Discrete-Point Linear Models

5. FUNDING NUMBERS

6. AUTHOR(S)

Eric L. Tobias and Mark B. Tischler

7. PERFORMING ORGANIZATION NAME(S) AND ADDRESS(ES)

Commander, U.S. Army Research, Development, and
   Engineering Command
ATTN: RDMR-ADF
Redstone Arsenal, AL 35898-5000

8. PERFORMING ORGANIZATION REPORT NUMBER

SR-RDMR-AF-16-01

9. SPONSORING / MONITORING AGENCY NAME(S) AND ADDRESS(ES)

10. SPONSORING / MONITORING AGENCY REPORT NUMBER

11. SUPPLEMENTARY NOTES

12a. DISTRIBUTION / AVAILABILITY STATEMENT

Approved for public release; distribution is unlimited.

12b. DISTRIBUTION CODE

A

13. ABSTRACT (Maximum 200 Words)

A comprehensive model stitching simulation architecture has been developed, which allows continuous, full flight-envelope simulation based on a collection of discrete-point linear models and trim data. The model stitching simulation architecture is applicable to any aircraft configuration readily modeled by state equations and for which test data can be obtained. Individual linear models and trim data for specific flight conditions are incorporated with nonlinear elements to produce a continuous, quasi-nonlinear simulation model. Extrapolation methods within the model stitching architecture permit accurate simulation of off-nominal aircraft loading configurations, including variations in weight, inertia, and center of gravity, and variations in altitude, which together minimize the required number of point models for full-envelope simulation. The model stitching simulation architecture is applied herein to a model of a CJ1 business jet and to a model of a UH-60 utility helicopter. For both the fixed-wing and the rotorcraft application, configuring the stitched simulation models with 8 discrete-point linear models (4 point models each at two altitudes) plus additional trim data was found to allow accurate simulation over the full airspeed and altitude envelope. Flight-test implications for the development of stitched models from flight-identified point models are presented for fixed-wing and rotorcraft applications.

14. SUBJECT TERMS

Model Stitching, Stitched Simulation Model, Quasi-Nonlinear, Piloted Simulation, Flight-Test Implications, System Identification, Off-Nominal Loading Extrapolation, Stability and Control Derivatives

15. NUMBER OF PAGES

219

16. PRICE CODE

17. SECURITY CLASSIFICATION OF REPORT UNCLASSIFIED	18. SECURITY CLASSIFICATION OF THIS PAGE UNCLASSIFIED	19. SECURITY CLASSIFICATION OF ABSTRACT UNCLASSIFIED	20. LIMITATION OF ABSTRACT SAR

A Model Stitching Architecture for Continuous Full Flight-Envelope Simulation of Fixed-Wing Aircraft and Rotorcraft from Discrete-Point Linear Models

Eric L. Tobias

San Jose State University

U.S. Army Aviation Development Directorate (AMRDEC)

Moffett Field, CA

Mark B. Tischler

U.S. Army Aviation Development Directorate (AMRDEC)

Moffett Field, CA

April 2016

Abstract

A comprehensive model stitching simulation architecture has been developed, which allows continuous, full flight-envelope simulation based on a collection of discrete-point linear models and trim data. The model stitching simulation architecture is applicable to any aircraft configuration readily modeled by state equations and for which test data can be obtained. Individual linear models and associated trim data for specific flight conditions are tabulated and incorporated with nonlinear elements to produce a continuous, quasi-nonlinear simulation model. Extrapolation methods within the model stitching architecture permit accurate simulation of off-nominal aircraft loading configurations, including variations in weight, inertia, and center of gravity, and variations in altitude, which together minimize the required number of point models for full-envelope simulation. The model stitching simulation architecture is applied herein to a model of a CJ1 business jet and to a model of a UH-60 utility helicopter. For both the fixed-wing and the rotorcraft application, configuring the stitched simulation models with 8 discrete-point linear models (4 point models each at two altitudes) plus additional trim data, and employing the appropriate altitude extrapolation technique for each case, was found to allow accurate simulation over the full airspeed and altitude envelope. The dynamic responses of the resulting stitched simulation models are verified with the original point models used in the simulation model development, as well as off-nominal points to demonstrate the accuracy of the extrapolation methods. Flight-test implications for the development of stitched models from flight-identified point models are presented for fixed-wing and rotorcraft applications.

Contents

List of Figures

List of Tables

Nomenclature

$\boldsymbol{A}, \boldsymbol{B}, \boldsymbol{C}, \boldsymbol{D}$	state-space matrix representation of dynamic system model
b	wing span
$\bar{c}$	wing mean aerodynamic chord
$\boldsymbol{F}$	external force vector
g	acceleration due to gravity
$\boldsymbol{I}$	inertia tensor
I_{xx}, I_{yy}, I_{zz}	moments of inertia (roll, pitch, yaw)
I_{xz}	product of inertia
L, M, N	moments about the aircraft CG (roll, pitch, yaw)
$\boldsymbol{M}$	external moment vector
$\boldsymbol{\mathcal{M}}$	mass matrix comprised of aircraft mass and inertia tensor
m	aircraft mass
n_{c}	number of controls
n_{H}	number of higher-order states
P, Q, R	fuselage total angular rates (roll, pitch, yaw)
$\bar{q}$	dynamic pressure $\left(\bar{q} = \frac{1}{2}\rho V_{\mathrm{tot}}^2\right)$
S	wing planform area
s	Laplace variable
$\boldsymbol{U}$	total vector of controls
$\boldsymbol{u}$	perturbation vector of controls
U, V, W	body-axis total airspeeds (longitudinal, lateral, vertical)
u, v, w	body-axis perturbation airspeeds (longitudinal, lateral, vertical)
V_{tot}	total airspeed
$\boldsymbol{V}$	velocity vector, body-fixed axis system
$\boldsymbol{X}$	total vector of states
$\boldsymbol{x}$	perturbation vector of states
X, Y, Z	external forces on the aircraft CG (longitudinal, lateral, vertical)
$\boldsymbol{Y}$	total vector of outputs
$\boldsymbol{y}$	perturbation vector of outputs
α	angle of attack
β	angle of sideslip
Δ	perturbation
$\delta_{\mathrm{a}}, \delta_{\mathrm{e}}, \delta_{\mathrm{r}}, \delta_{\mathrm{t}}$	total control inputs, fixed-wing aircraft (aileron, elevator, rudder, thrust)
$\delta_{\mathrm{lat}}, \delta_{\mathrm{lon}}, \delta_{\mathrm{col}}, \delta_{\mathrm{ped}}$	total control inputs, rotorcraft (lateral cyclic, longitudinal cyclic, collective, pedals)
ζ	damping ratio
Φ, Θ, Ψ	fuselage total attitudes (roll, pitch, yaw)
ϕ, θ, ψ	fuselage perturbation attitudes (roll, pitch, yaw)

ρ	atmospheric air density
τ	time constant
$\boldsymbol{\omega}$	angular velocity vector, body-fixed axis system
ω_n	natural frequency

Subscripts

b	body-axes coordinate system
f	filtered (low-pass)
s	stability-axes coordinate system
sim	simulation value
0	trim value

Acronyms

AAA	Advanced Aircraft Analysis software (DARcorporation)
CG	center of gravity
DOF	degree(s) of freedom
KTAS	knots true airspeed
MAC	mean aerodynamic chord

Glossary

anchor point An anchor point is a specific flight condition for which a linear model or trim data have been included in the stitched model. Additionally, a linear model for a particular included flight condition is referred to as an *anchor point model*, and trim data for a particular included flight condition are collectively referred to as an *anchor trim point*.

baselining In this process, the extrapolation methods for off-nominal values of weight, inertia, and CG are employed to accurately retrim flight-test trim data and relinearize identification point models to a common loading configuration. These *baselined* anchor points are then used to construct the final stitched model.

model stitching Model stitching refers to the technique of combining together individual linear models and trim data for discrete flight conditions to produce a continuous, full-envelope, quasi-nonlinear flight-dynamics simulation model.

off-nominal An off-nominal configuration is an aircraft loading configuration with values of aircraft mass, inertia, and/or center of gravity (CG) location that differ from the identified/baseline values.

relinearize To obtain a state-space representation (and the corresponding stability and control derivatives) for an off-nominal simulation loading configuration or alternate flight condition by linearizing the stitched simulation model.

retrim To determine a trim solution for an off-nominal simulation loading configuration or alternate flight condition using a numerical trimming procedure.

stitched model A stitched simulation model, or stitched model, is the continuous, full flight-envelope simulation model produced by the model stitching technique.

stitching in ... When model stitching is applied to a particular airspeed component, such as x-body airspeed U, this is termed "stitching in U." When stitching in an airspeed component, the stability derivatives associated with that airspeed (e.g., X_u, M_u) are nulled, yet preserved implicitly by the variation in trim aircraft states and controls.

Acknowledgments

1 Introduction

Linear state-space perturbation models, which represent the dynamic response of an aircraft for a discrete reference flight condition and configuration, are accurate within some limited range of the reference condition. These discrete-point linear models, as derived from system identification from flight testing or a non-realtime model, for example, may be produced at suitable airspeed and altitude increments to construct a collection of discrete models to describe the aircraft dynamics at specific points over the desired flight envelope. These discrete models are suitable for point design of control systems and point handling qualities analyses; however, continuous, full-envelope simulation is desirable for full-mission piloted simulation and flight control evaluations within hardware-in-the-loop simulation.

Model stitching refers to the technique of combining or "stitching" together individual linear models and trim data for discrete flight conditions to produce a continuous, full flight-envelope simulation model [1]. In this technique, the stability and control derivatives and trim data for each discrete point model are stored in lookup tables as a function of key parameters such as airspeed and altitude. The look-up of trim and derivatives is combined with nonlinear equations of motion and nonlinear gravitational force equations to produce a continuous, quasi-nonlinear, *stitched* simulation model.

The theoretical concept of the model stitching technique has been applied to develop a *model stitching simulation architecture*, which incorporates extrapolation methods for the simulation of off-nominal aircraft loading configurations, including variations in weight, inertia, and center of gravity. These extrapolation methods allow for continuous simulation of aircraft loading changes due to fuel burn-off or jettisoning of external stores, for example. Also incorporated into the model stitching architecture are additional modeling components, including turbulence and a standard atmosphere model, as well as accommodations for user-specified modeling components, such as engine models and landing gear. The model stitching simulation architecture is applicable to any flight vehicle for which point-wise linear models and trim data can be obtained, and is demonstrated herein with models of a light business jet and a utility helicopter.

The objectives of the current effort are to:

- Thoroughly present the implementation details of the model stitching technique as developed into the model stitching simulation architecture.
- Expand on concepts and implementation details of off-nominal extrapolation methods to minimize the number of required flight-test or physics-based point models.
- Discuss additional concepts including the use of high-order models, stitching in multiple dimensions, and data processing.
- Apply the model stitching simulation architecture to produce a state-of-the-art fixed-wing aircraft stitched model representative of the Cessna Citation CJ1, and also a high-order rotorcraft stitched model representative of the UH-60 Black Hawk, and verify the models against known off-nominal simulation points.
- Provide guidance on flight-test implications for the development of stitched models applicable to fixed-wing aircraft and rotorcraft.

Chapter 2 covers the details of the model stitching simulation architecture, including theoretical concepts and key implementation elements. Extrapolation methods for the simulation of off-nominal loading configurations are presented. Also presented is an air density-ratio scaling method for the simulation of alternate altitudes, applicable to fixed-wing aircraft. Additional concepts are discussed, including the use of high-order linear models in the model stitching architecture, stitching in multiple dimensions, and data formatting and processing techniques.

Chapter 3 presents the application of the model stitching architecture to produce a state-of-the-art fixed-wing aircraft stitched simulation model representative of the Cessna Citation CJ1 (Figure 1.1a). The formulation of state-space point models and the inclusion of additional modeling features are discussed. A full verification of the stitched model is presented, including comparisons of trim and stability and control derivatives for ranges of off-nominal loading configurations and alternate altitudes. Two dynamic check cases

(a) Cessna Citation CJ1 (Model 525)   (b) UH-60 Black Hawk

Figure 1.1: Aircraft model applications presented herein.

are provided, including frequency and time-history response comparisons. Flight-test implications for the development of fixed-wing aircraft stitched models from flight-identified point models are presented.

Chapter 4 presents the model stitching architecture as applied to the development of a high-order rotorcraft stitched simulation model of the UH-60 Black Hawk helicopter (Figure 1.1b). The formulation of high-order state-space linear point models is covered. Discussion and verification of hover/low-speed trim data for the accurate simulation of low-speed forward, rearward, sideward, and quartering flight, as well as the simulation of hovering flight in the presence of winds, are provided. A detailed verification of the stitched model is presented, including comparisons of trim and stability and control derivatives for ranges of off-nominal loading configurations and alternate altitudes. Two dynamic check cases are presented, including frequency and time-history response comparisons. Flight-test implications for the development of rotorcraft stitched models from flight-identified point models are presented.

Chapter 5 provides general conclusions of the current effort, as well as specific conclusions determined from the Cessna Citation CJ1 stitched model and the UH-60 Black Hawk stitched model. Stability and control derivative definitions and conversions used in the development of the bare-airframe models for the CJ1 stitched model are provided in Appendix A. Supplemental verification figures for the CJ1 and UH-60 stitched models are provided in Appendix B and Appendix C, respectively.

2 Model Stitching Simulation Architecture

The term *model stitching* refers to the technique of combining or "stitching" together a collection of linear state-space models for discrete flight conditions, with corresponding trim data, into one continuous, full-envelope flight-dynamics simulation model. In this technique, the stability and control derivatives and trim data for each discrete point model are stored in lookup tables as a function of key parameters such as airspeed, altitude, or aircraft configuration. This modeling technique is in the class of quasi-linear-parameter-varying (qLPV) models [2]. The resulting *stitched model* is time-varying and quasi-nonlinear in that the linear stability and control derivatives and trim data are scheduled, but nonlinear equations of motion and nonlinear gravitational force equations are implemented. Essentially, the stitched model is a nonlinear flight-dynamics simulation model with linear, time-varying aerodynamics.

A comprehensive *model stitching simulation architecture* has been developed that is applicable to any flight vehicle readily modeled by state equations and for which test data can be obtained, and allows flight-identified models to be used directly. Simulation of off-nominal aircraft loading configurations, including variations in weight, inertia, and center of gravity (CG) location, is accomplished by extrapolation methods within the model stitching architecture. This capability also allows for real-time simulation of aircraft loading changes due to fuel burn-off or jettisoning of external stores, for example.

Closed-loop control system analysis and full flight-envelope piloted simulation of bare-airframe dynamics are key applications for a stitched model. Because of the continuous nature of the stitched model, a full mission consisting of takeoff, climb, cruise, and flight maneuvers, for example, can be executed in an uninterrupted, real-time fashion. The incorporation of airframe-specific modeling elements such as landing gear, flaps, and spoilers, and atmospheric elements such as turbulence and steady wind into the stitched model adds fidelity and realism to the simulation environment.

Some background and previous work are mentioned in Section 2.1. Basic theory and concepts of the model stitching technique, following closely those presented in Tischler [1], are covered in Section 2.2. Implementation of the theory into the model stitching simulation architecture is presented in Section 2.3, which includes a detailed, step-by-step walkthrough of the simulation architecture key elements. Additional elements of the simulation architecture, including atmospheric disturbances, are discussed in Section 2.4. Discussion of extrapolation methods for simulating off-nominal loading configurations without additional data is presented in Section 2.5, and altitude extrapolation methods are presented in Section 2.6. Formalities of implementing high-order models in the model stitching architecture are provided in Section 2.7. An explanation of the ability to store, and subsequently look-up, trim data as a function of multiple variables is provided in Section 2.8. Guidelines for the formatting and processing of data for use in the model stitching architecture are covered in Section 2.9.

2.1 Background and Previous Work

The model stitching technique was first proposed by Aiken [3] and Tischler [4]. Aiken documents a model of a helicopter for use in piloted simulation in which the nonlinear gravitational and inertial terms of the six-degree-of-freedom equations of motion are utilized, and the aerodynamic forces and moments are expressed as first-order terms of a Taylor series expansion about a reference flight condition as a function of longitudinal airspeed; this describes the basic technique of model stitching in x-body airspeed. Tischler outlines the model stitching approach as applicable to a piloted V/STOL simulation, and covers key theoretical model stitching concepts including the implicit representation of speed perturbation derivatives, the balancing of gravity forces by the trim aerodynamic forces, the inclusion of nonlinear equations of motion, and data requirements for accurate simulation throughout the flight envelope.

Zivan and Tischler [5] built on this early work and produced a stitched model of the Bell 206 helicopter from a series of individual, flight-identified point models. Seven state-space point models, covering a flight envelope of hover through high-speed forward flight and two altitudes, were generated using frequency-domain system identification in CIFER® [1]. The stitched model was implemented in a simple, fixed-base simulator

and evaluated by several pilots, all qualified in the Bell 206. The evaluation procedure was based on the pilots rating the similarity between the model and the actual aircraft using a specialized rating scale. Evaluation maneuvers included large and small amplitude doublets/steps, coordinated turns, and climbs/descents to cover most of the helicopter's flight envelope. Overall pilot opinion was that the simulation was a good representation of the aircraft for all evaluated tasks.

Tischler elaborates on the theoretical approach of the model stitching technique in Ref. [1] for applications to fixed-wing and rotary-wing aircraft. When the trim data are included in the stitched model as a function of x-body axis airspeed component U, the interpolation is in turn performed as a function of U, and is referred to as "stitching in U." This is the most common approach for fixed-wing aircraft, and for rotorcraft in high-speed forward flight. A more accurate rotorcraft model for hover, low-speed, and quartering flight is obtained from "stitching in U and V," in which all trim data are tabulated as a two-dimensional lookup table and subsequently interpolated in x-body axis airspeed U and y-body axis airspeed V. In this case the stability and control derivatives are still stored as a function of forward airspeed U only. Tischler [1] also presents thorough analyses of the typical variations of fixed-wing aircraft and rotorcraft trim and dynamics over their respective flight envelopes. Required flight conditions and suggestions for spacing of flight-test points are discussed to aide in the planning of flight testing for the development of stitched models.

In their development of a stitched simulation model of a tiltrotor, Lawrence et al. [6] employed the stitching technique in x-body airspeed U as well as in engine nacelle angle to develop a real-time simulation of a large civil tiltrotor at hover through low speed (up to 60 kn). This model is based on 13-state regressive-flap models (9 rigid-body states plus first-order longitudinal- and lateral-flapping states for the left and right rotors) as reduced from high-order matrices numerically extracted from the CAMRAD II comprehensive analysis. This model has been used in several piloted studies of hover/low-speed handling-qualities requirements for large civil tiltrotor configurations.

Two notable applications in support of rotorcraft flight control development and fielding are the unmanned BURRO/K-MAX helicopter [7] and the unmanned MQ-8B Fire Scout helicopter [8]. For the BURRO/K-MAX, four identified state-space models (two at low altitude and two at high altitude) were shown to effectively cover the desired flight envelope. Evaluations of a full-envelope mission stitched simulation validated that a broad spacing of identified point models was satisfactory. For the Fire Scout program, a stitched simulation model based on extensive system identification flight testing was used for flight control development, hardware-in-the-loop testing, and failure assessment.

Greiser and Seher-Weiss [9] developed a stitched model of DLR's ACT/FHS, which is a highly-modified EC135, from five flight-identified high-order linear models and trim data. The identified linear models included higher-order rotor flapping, dynamic inflow, and regressive lead-lag effects, which were retained in the stitched model. The stitched model was verified against linear operating point models and flight-test data, showing good agreement.

Recently, Spires and Horn [10] utilized the model stitching technique to combine 24-state linear models of the UH-60 into a full flight envelope flight dynamics model for evaluation of two model-following control design approaches. Frequency- and time-domain analyses of command model fidelity and cross-coupling reduction performance of the controllers compared to the bare-airframe stitched model are presented at a flight condition near hover (10 kn) and at forward flight (120 kn). Additionally, disturbance rejection performance was evaluated at the same flight conditions.

2.2 Model Stitching Basic Concepts

The key requirement for model stitching is a series of state-space models and associated trim data of the states and controls for several point flight conditions, or "anchor" points, covering a range of airspeed and perhaps altitude and aircraft configuration. The point models and trim data may be identified from flight testing or derived from a more complex, non-realtime model, for example.

The model stitching simulation architecture must accommodate both fixed-wing aircraft and rotorcraft (in hover and forward flight). *Body axes* are exclusively used in rotorcraft stability and control analyses and simulation. For fixed-wing aircraft, however, stability and control derivatives are commonly formulated in *stability axes*, which is a body-fixed system aligned with the trim velocity vector (i.e., rotated through the trim angle of attack α_0). Stability and control derivatives given in stability axes are easily transformed into

body axes using classical transformation equations, as demonstrated for the fixed-wing aircraft stitched model application in Section 3.2.2. Therefore, to develop a comprehensive model stitching simulation architecture that can accommodate *both fixed-wing aircraft and rotorcraft* the body-axes reference system was chosen.

Although model stitching may be performed as a function of multiple simultaneous interpolation dimensions (see Section 2.8) this overview of basic concepts will demonstrate model stitching in forward x-body airspeed only (i.e., "stitching in U"). For the model stitching architecture, the tables of stability and control derivatives and trim data are obtained from simulation models or extracted from flight tests using system identification methods [1]. The data may be provided as a function of total trim airspeed:

$$V_{\text{tot}} = \sqrt{U^2 + V^2 + W^2} \tag{2.1}$$

A good approximation is [11]

$$V_{\text{tot}} \cong U \tag{2.2}$$

so the x-body airspeed U and the total airspeed V_{tot} can be used interchangeably. This is convenient for "stitching in U" wherein the stability and control derivatives and trim data need to be interpolated for a given instantaneous x-body airspeed U.

Following Ref. [1], given a linear model of a specific aircraft configuration, the generalized state-space representation is utilized to give the appropriate perturbation dynamic response about a *reference flight condition* (i.e., anchor point) with trim x-body airspeed U_0:

$$\dot{\boldsymbol{x}} = \boldsymbol{A}|_{U_0} \boldsymbol{x} + \boldsymbol{B}|_{U_0} \boldsymbol{u} \tag{2.3}$$

$$\boldsymbol{y} = \boldsymbol{C}|_{U_0} \boldsymbol{x} + \boldsymbol{D}|_{U_0} \boldsymbol{u} \tag{2.4}$$

which is expressed in terms of the stability and control derivatives for the reference flight condition (i.e., the $\boldsymbol{A}$, $\boldsymbol{B}$, $\boldsymbol{C}$, and $\boldsymbol{D}$ matrices from the state-space model in body axes for trim x-body airspeed U_0), the perturbation state vector $\boldsymbol{x}$, and the perturbation control vector $\boldsymbol{u}$.

The state-space representation is then rewritten in terms of the vector of total values of states $\boldsymbol{X}$, vector of total values of controls $\boldsymbol{U}$, and vector of total values of outputs $\boldsymbol{Y}$ rather than perturbation values, and at the *instantaneous* x-body airspeed U instead of reference trim x-body airspeed U_0. Vectors of trim states $\boldsymbol{X}_0$ and trim controls $\boldsymbol{U}_0$ are included forming a continuous, full flight-envelope simulation model by expressing the state-space equations as

$$\dot{\boldsymbol{X}} = \boldsymbol{A}|_U \left(\boldsymbol{X} - \boldsymbol{X}_0|_U \right) + \boldsymbol{B}|_U \left(\boldsymbol{U} - \boldsymbol{U}_0|_U \right) \tag{2.5}$$

$$\boldsymbol{Y} = \boldsymbol{C}|_U \left(\boldsymbol{X} - \boldsymbol{X}_0|_U \right) + \boldsymbol{D}|_U \left(\boldsymbol{U} - \boldsymbol{U}_0|_U \right) + \boldsymbol{Y}_0|_U \tag{2.6}$$

For "stitching in U," all trim data and stability and control derivative values are tabulated and subsequently interpolated as a function of *instantaneous* x-body airspeed U, as denoted by $|_U$. That is,

$$\left(V_0|_U, \ W_0|_U, \ \Phi_0|_U, \ \Theta_0|_U, \ \delta_{\text{lat}_0}|_U, \ \delta_{\text{lon}_0}|_U, \ \delta_{\text{col}_0}|_U, \ \delta_{\text{ped}_0}|_U \right) = f(U) \tag{2.7}$$

$$\left(\boldsymbol{A}|_U, \ \boldsymbol{B}|_U, \ \boldsymbol{C}|_U, \ \boldsymbol{D}|_U \right) = f(U) \tag{2.8}$$

For a helicopter in pure sideward flight (e.g., x-body airspeed $U = 0$ and y-body airspeed $V = 20$ ft/sec), the stability and control derivative values associated with hover ($U = 0$) would be looked-up, since the relevant point model is based on hovering flight. The perturbation forces and moments are then based on the instantaneous deviation of the states and controls from trim hovering flight [Eq. (2.7)] and the stability and control derivatives for the hover condition [Eq. (2.8)].

As expected from Equations (2.5) and (2.6), at reference speed of $U = U_0$, the continuous simulation will trim ($\dot{\boldsymbol{X}} = 0$) with model states, controls, and outputs at the anchor point values:

$$\boldsymbol{X} = \boldsymbol{X}_0|_U \tag{2.9}$$

$$\boldsymbol{U} = \boldsymbol{U}_0|_U \tag{2.10}$$

$$\boldsymbol{Y} = \boldsymbol{Y}_0|_U \tag{2.11}$$

which is crucial for good fidelity in piloted simulation.

5

As u is included as a state, a subtle yet important detail becomes evident from Eq. (2.5). All stability derivatives for forward speed perturbation u (i.e., X_u, Z_u, M_u, etc.) are nulled-out (multiplied by 0) because the instantaneous x-body airspeed U (the query for the lookup table) and the returned table value of x-body airspeed are always identical (i.e., $U_0|_U = U$ and therefore $U - U_0|_U = 0$). As a result, the explicit u-speed derivatives can be omitted from the model. However, the effect of these nulled-out derivatives is preserved and is contained *implicitly* in the speed variation of the trim states and controls, so the dynamic response of the anchor point model is maintained.

To demonstrate the implicit preservation of the u-speed derivatives, consider the fixed-wing aircraft three-DOF longitudinal equation of motion for the x-body axis:

$$\dot{U} = -QW + \bar{X} \tag{2.12}$$

where $\bar{X}$, the total specific x-force, is defined as the total x-force divided by the aircraft mass, and is the sum of the specific gravity x-force and the specific aerodynamic x-force:

$$\bar{X} \equiv X/m = \bar{X}_{\text{grav}} + \bar{X}_{\text{aero}} \tag{2.13}$$

The specific gravity x-force and the specific aerodynamic x-force can be written as Taylor series expansions for small perturbation motion about the reference trim airspeed U_0. The specific gravity x-force expands to

$$\bar{X}_{\text{grav}} = \bar{X}_{\text{grav}_0} - (g \cos \Theta_0)(\Theta - \Theta_0) \tag{2.14}$$

where $\bar{X}_{\text{grav}_0} = -g \sin \Theta_0$. The specific aerodynamic x-force expands to

$$\begin{aligned}
\bar{X}_{\text{aero}} = \bar{X}_{\text{aero}_0} + X_u|_{U_0}(U - U_0) + X_w|_{U_0}(W - W_0) + X_q|_{U_0}(Q - Q_0) \\
+ X_{\delta_e}|_{U_0}(\delta_e - \delta_{e_0}) + X_{\delta_t}|_{U_0}(\delta_t - \delta_{t_0})
\end{aligned} \tag{2.15}$$

in which δ_e is elevator deflection and δ_t is engine thrust.

At the rectilinear trim condition, the trim aerodynamic x-force balances the trim gravity x-force:

$$\bar{X}_{\text{aero}_0} = -\bar{X}_{\text{grav}_0} = g \sin \Theta_0 \tag{2.16}$$

and Eq. (2.15) becomes

$$\begin{aligned}
\bar{X}_{\text{aero}} = g \sin \Theta_0 + X_u|_{U_0}(U - U_0) + X_w|_{U_0}(W - W_0) + X_q|_{U_0}Q \\
+ X_{\delta_e}|_{U_0}(\delta_e - \delta_{e_0}) + X_{\delta_t}|_{U_0}(\delta_t - \delta_{t_0})
\end{aligned} \tag{2.17}$$

Continuous full flight-envelope simulation is achieved as in Eqs. (2.5) and (2.6) by rewriting the Taylor series expansion of Eq. (2.17) about the instantaneous x-body airspeed U:

$$\begin{aligned}
\bar{X}_{\text{aero}} = g \sin \Theta_0|_U + X_w|_U(W - W_0|_U) + X_q|_U Q \\
+ X_{\delta_e}|_U(\delta_e - \delta_{e_0}|_U) + X_{\delta_t}|_U(\delta_t - \delta_{t_0}|_U)
\end{aligned} \tag{2.18}$$

noting that $U - U_0|_U = 0$ at all times, thus the term $X_u|_U(U - U_0|_U)$ is omitted. The stability and control derivatives and trim data are then interpolated for the instantaneous x-body airspeed U.

Finally, the effective, *implicit representation* of the speed-damping derivative X_u is found by taking the partial derivative of Eq. (2.18) to independent perturbations in u:

$$\begin{aligned}
X_u \equiv \frac{\partial \bar{X}_{\text{aero}}}{\partial u} = g \cos \Theta_0|_U \left(\frac{\partial \Theta_0|_U}{\partial u} \right) - X_w|_U \left(\frac{\partial W_0|_U}{\partial u} \right) \\
- X_{\delta_e}|_U \left(\frac{\partial \delta_{e_0}|_U}{\partial u} \right) - X_{\delta_t}|_U \left(\frac{\partial \delta_{t_0}|_U}{\partial u} \right)
\end{aligned} \tag{2.19}$$

Equation (2.19), as introduced in Ref. [1], demonstrates that although the explicit X_u term is nulled by the Taylor series expansion in Eq. (2.18) its effect is *preserved implicitly* in the variation of the trim states and

controls with x-body airspeed U. Analogous derivations are performed to find the implicit representations of Z_u (this demonstration assumes wings-level trim flight) and M_u:

$$Z_u \equiv \frac{\partial \bar{Z}_{\text{aero}}}{\partial u} = g \sin \Theta_0|_U \left(\frac{\partial \Theta_0|_U}{\partial u} \right) - Z_w|_U \left(\frac{\partial W_0|_U}{\partial u} \right)$$
$$- Z_{\delta_{\text{e}}}|_U \left(\frac{\partial \delta_{\text{e}_0}|_U}{\partial u} \right) - Z_{\delta_{\text{t}}}|_U \left(\frac{\partial \delta_{\text{t}_0}|_U}{\partial u} \right) \tag{2.20}$$

$$M_u \equiv \frac{\partial \bar{M}_{\text{aero}}}{\partial u} = -M_w|_U \left(\frac{\partial W_0|_U}{\partial u} \right) - M_{\delta_{\text{e}}}|_U \left(\frac{\partial \delta_{\text{e}_0}|_U}{\partial u} \right) - M_{\delta_{\text{t}}}|_U \left(\frac{\partial \delta_{\text{t}_0}|_U}{\partial u} \right) \tag{2.21}$$

This concept of implicit speed derivatives is fundamental to the model stitching technique, and will be referenced throughout this document.

Figure 2.1 shows an example comparison of the values of the implicit expressions for X_u, Z_u, and M_u with the actual explicit derivative values from the CJ1 fixed-wing aircraft linear point models (see Chapter 3) over a range of airspeeds at a constant altitude. As can be seen, the effective, implicit representations of the u-speed derivatives are very accurate, with small differences due to higher-order terms and linear gradients taken between the discrete points. This validates the model stitching equations of Eqs. (2.19)–(2.21).
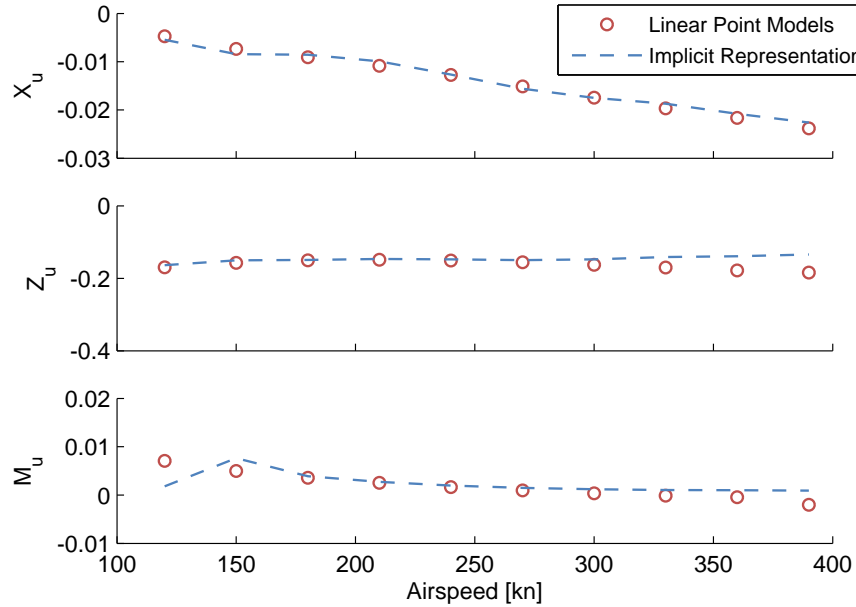
Figure 2.1: Implicit vs. explicit values of u-speed derivatives, CJ1 stitched model.

2.3 Key Simulation Elements

Section 2.2 provided the basic theoretical concepts of the model stitching technique. As an application, the model stitching equations are implemented as individual components in block-diagram form in MATLAB® Simulink® [12]. As a collection, the model stitching simulation elements, along with off-nominal extrapolation methods and additional features, form the *model stitching simulation architecture*.

This section provides a walkthrough of the top-level model stitching simulation architecture. Figure 2.2 shows a top-level schematic of the model stitching architecture, illustrating all of the key simulation elements. Each element is discussed individually over Sections 2.3.1–2.3.9, and is diagrammatically depicted in relation to the top-level schematic. Table 2.1 provides a legend of nomenclature used in the model stitching architecture schematics and references key equations. For the purpose of demonstration, a typical 6-DOF representation, with stitching in x-body airspeed U only, will be assumed throughout this walkthrough.

7
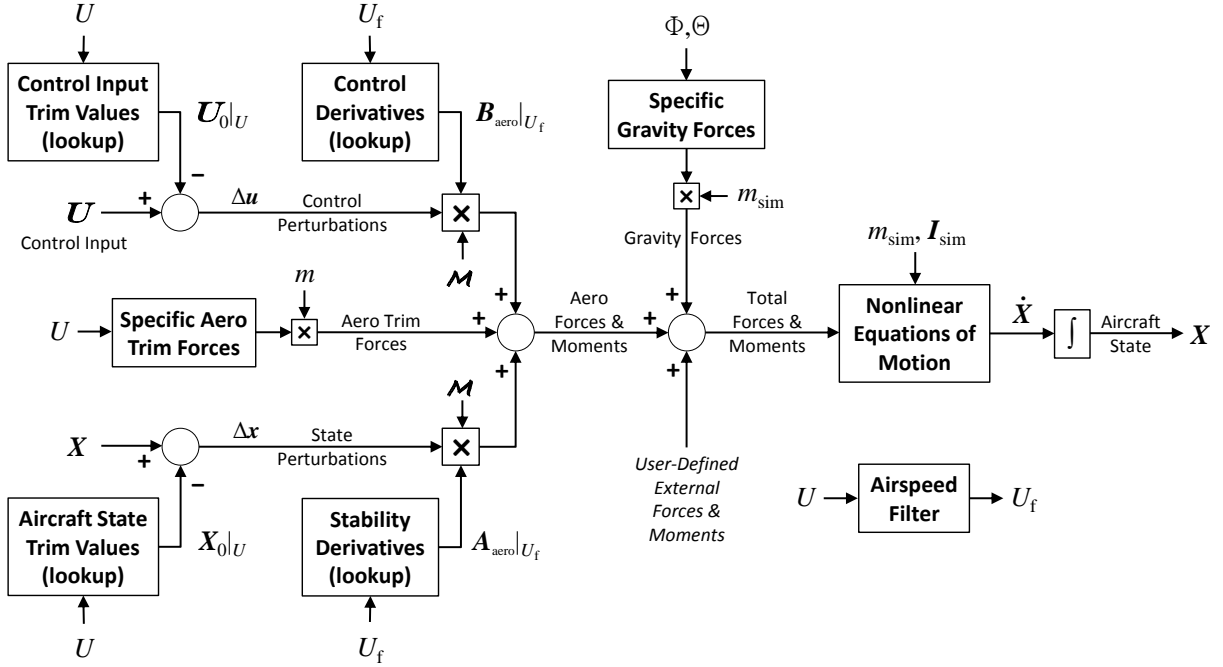
Figure 2.2: Model stitching simulation architecture – top level schematic.

Table 2.1: Model stitching simulation architecture – schematic nomenclature

Symbol	Description	Equation
$\boldsymbol{A}_{\mathrm{aero}}$	matrix of aerodynamic dimensional stability derivatives	(2.32)
$\boldsymbol{B}_{\mathrm{aero}}$	matrix of aerodynamic dimensional control derivatives	(2.33)
$\boldsymbol{I}_{\mathrm{sim}}$	inertia tensor (simulation values)	(2.56)
$\boldsymbol{\mathcal{M}}$	dimensional mass matrix (comprised of m and $\boldsymbol{I}$)	(2.34)
m	aircraft mass	see (2.34, 2.39)
m_{sim}	aircraft mass (simulation value)	see (2.45, 2.50)
U	x-body airspeed	see (2.66)
U_{f}	x-body airspeed (filtered)	(2.67)
$\boldsymbol{U}$	vector of control values	see (2.23, 2.25)
$\boldsymbol{U}_0$	vector of trim control values	see (2.23, 2.25)
$\dot{\boldsymbol{X}}$	vector of state-dot values	(2.65)
$\boldsymbol{X}$	vector of state values	(2.66)
$\boldsymbol{X}_0$	vector of trim state values	see (2.22, 2.24)
$\Delta\boldsymbol{u}$	vector of control perturbations	(2.23, 2.25)
$\Delta\boldsymbol{x}$	vector of state perturbations	(2.22, 2.24)
Φ, Θ	aircraft attitude (roll angle, pitch angle)	see (2.66)
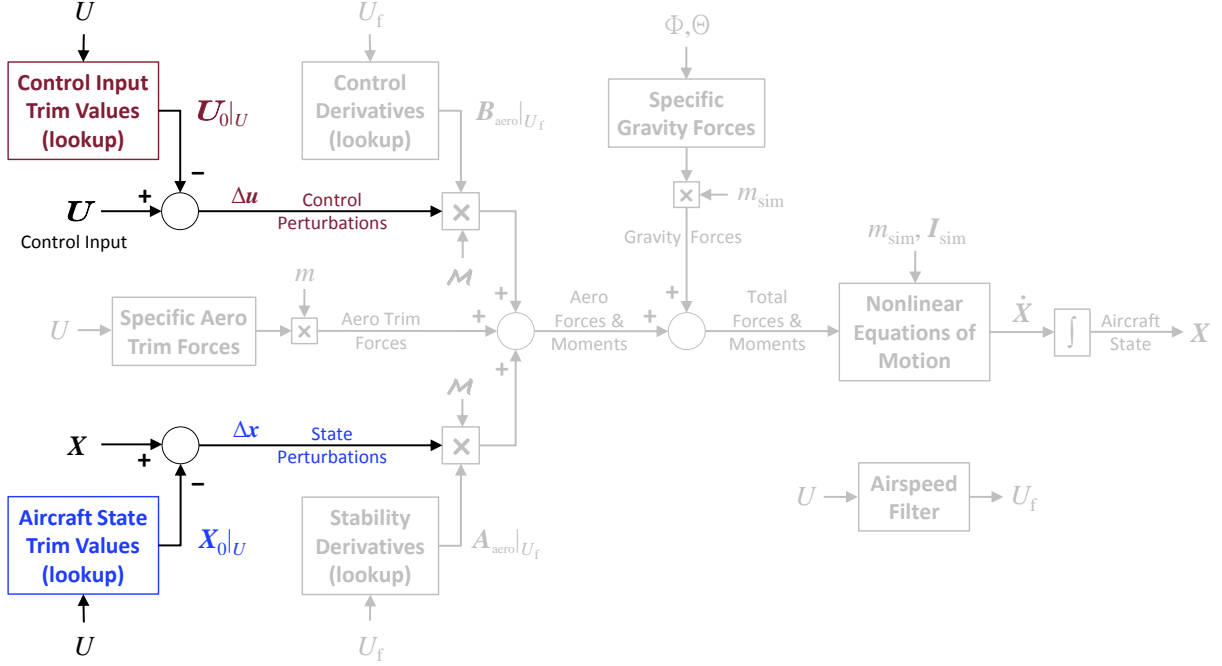
Figure 2.3: Model stitching simulation architecture – state and control perturbations.

2.3.1 State and Control Perturbations

The first simulation element involves calculating state and control perturbations based on the difference between the current values of states and controls and the trim values of states and controls at the current airspeed. Given the current x-body airspeed U, table look-ups are performed to find the vectors of trim aircraft states $\boldsymbol{X}_0$ and trim controls $\boldsymbol{U}_0$. With the current aircraft state vector $\boldsymbol{X}$ and current control vector $\boldsymbol{U}$, the state perturbation vector $\Delta\boldsymbol{x}$ and control perturbation vector $\Delta\boldsymbol{u}$ are found using the following definitions:

$$\Delta\boldsymbol{x} \equiv \boldsymbol{X} - \boldsymbol{X}_0|_U \tag{2.22}$$

$$\Delta\boldsymbol{u} \equiv \boldsymbol{U} - \boldsymbol{U}_0|_U \tag{2.23}$$

This arithmetic is shown schematically in Figure 2.3.

The state and control perturbation vectors of Eqs. (2.22) and (2.23) ultimately are used in the calculation of aerodynamic perturbation forces and moments (see Section 2.3.2). Therefore, these vectors are comprised of only those states and controls that directly contribute to the aerodynamic forces and moments. For this 6-DOF demonstration, the state perturbation vector and the control perturbation vector are as follows:

$$\Delta\boldsymbol{x} = \begin{bmatrix} U \\ V \\ W \\ P \\ Q \\ R \end{bmatrix} - \begin{bmatrix} U_0 \\ V_0 \\ W_0 \\ P_0 \\ Q_0 \\ R_0 \end{bmatrix}\Bigg|_U \tag{2.24}$$

$$\Delta\boldsymbol{u} = \begin{bmatrix} \delta_{\mathrm{a}} \\ \delta_{\mathrm{e}} \\ \delta_{\mathrm{r}} \\ \delta_{\mathrm{t}} \end{bmatrix} - \begin{bmatrix} \delta_{\mathrm{a}_0} \\ \delta_{\mathrm{e}_0} \\ \delta_{\mathrm{r}_0} \\ \delta_{\mathrm{t}_0} \end{bmatrix}\Bigg|_U \tag{2.25}$$

Note that in this example the state perturbation vector contains only the fuselage velocity and angular rate states (6 states total); it does not include Euler angle states since the aerodynamic forces and moments do

9

not depend explicitly on the Euler angles. Kinematics are introduced, however, in the nonlinear equations of motion, as discussed in Section 2.3.7. The 6-state vector of Eq. (2.24) will henceforth be designated as $\boldsymbol{X}_6$:

$$\boldsymbol{X}_6 \equiv \begin{bmatrix} U \\ V \\ W \\ P \\ Q \\ R \end{bmatrix} \tag{2.26}$$

2.3.2 Aerodynamic Perturbation Forces and Moments

Next, aerodynamic perturbation forces and moments are calculated based on the state and control perturbation vectors [Eqs. (2.22) and (2.23)] found in the previous section. This process involves looking-up the dimensional stability and control derivatives at the current airspeed. Special matrices containing only the aerodynamic dimensional stability and control derivatives are first presented and discussed.

For a typical 6-DOF fixed-wing aircraft model, with 9 rigid-body states and 4 controls, the conventional state-space representation in body axes is given as follows [11]:

$$\dot{\boldsymbol{x}} = \boldsymbol{A}\boldsymbol{x} + \boldsymbol{B}\boldsymbol{u} \tag{2.27}$$

$$\boldsymbol{x} = \begin{bmatrix} u & v & w & p & q & r & \phi & \theta & \psi \end{bmatrix}_9^{\mathrm{T}} \tag{2.28}$$

$$\boldsymbol{u} = \begin{bmatrix} \delta_{\mathrm{a}} & \delta_{\mathrm{e}} & \delta_{\mathrm{r}} & \delta_{\mathrm{t}} \end{bmatrix}_4^{\mathrm{T}} \tag{2.29}$$

$$\boldsymbol{A} = \begin{bmatrix}
X_u & X_v & X_w & X_p & X_q - W_0 & X_r + V_0 & 0 & -g\cos\Theta_0 & 0 \\
Y_u & Y_v & Y_w & Y_p + W_0 & Y_q & Y_r - U_0 & g\cos\Phi_0\cos\Theta_0 & -g\sin\Phi_0\sin\Theta_0 & 0 \\
Z_u & Z_v & Z_w & Z_p - V_0 & Z_q + U_0 & Z_r & -g\sin\Phi_0\cos\Theta_0 & -g\cos\Phi_0\sin\Theta_0 & 0 \\
L'_u & L'_v & L'_w & L'_p & L'_q & L'_r & 0 & 0 & 0 \\
M_u & M_v & M_w & M_p & M_q & M_r & 0 & 0 & 0 \\
N'_u & N'_v & N'_w & N'_p & N'_q & N'_r & 0 & 0 & 0 \\
0 & 0 & 0 & 1 & \sin\Phi_0\tan\Theta_0 & \cos\Phi_0\tan\Theta_0 & 0 & 0 & 0 \\
0 & 0 & 0 & 0 & \cos\Phi_0 & -\sin\Phi_0 & 0 & 0 & 0 \\
0 & 0 & 0 & 0 & \sin\Phi_0\sec\Theta_0 & \cos\Phi_0\sec\Theta_0 & 0 & 0 & 0
\end{bmatrix}_{9\times 9} \tag{2.30}$$

$$\boldsymbol{B} = \begin{bmatrix}
X_{\delta_{\mathrm{a}}} & X_{\delta_{\mathrm{e}}} & X_{\delta_{\mathrm{r}}} & X_{\delta_{\mathrm{t}}} \\
Y_{\delta_{\mathrm{a}}} & Y_{\delta_{\mathrm{e}}} & Y_{\delta_{\mathrm{r}}} & Y_{\delta_{\mathrm{t}}} \\
Z_{\delta_{\mathrm{a}}} & Z_{\delta_{\mathrm{e}}} & Z_{\delta_{\mathrm{r}}} & Z_{\delta_{\mathrm{t}}} \\
L'_{\delta_{\mathrm{a}}} & L'_{\delta_{\mathrm{e}}} & L'_{\delta_{\mathrm{r}}} & L'_{\delta_{\mathrm{t}}} \\
M_{\delta_{\mathrm{a}}} & M_{\delta_{\mathrm{e}}} & M_{\delta_{\mathrm{r}}} & M_{\delta_{\mathrm{t}}} \\
N'_{\delta_{\mathrm{a}}} & N'_{\delta_{\mathrm{e}}} & N'_{\delta_{\mathrm{r}}} & N'_{\delta_{\mathrm{t}}} \\
0 & 0 & 0 & 0 \\
0 & 0 & 0 & 0 \\
0 & 0 & 0 & 0
\end{bmatrix}_{9\times 4} \tag{2.31}$$

where primed derivatives ($'$) are defined in Section A.1.3. Note that the $\boldsymbol{A}$ matrix includes gravity terms (e.g., $-g\cos\Theta_0$), Coriolis terms (e.g., $-W_0$), and kinematic terms (e.g., $\sin\Phi_0\tan\Theta_0$).

For use in the model stitching architecture, we introduce variations of the $\boldsymbol{A}$ and $\boldsymbol{B}$ matrices that contain only the *aerodynamic* dimensional stability and control derivatives; they do not contain gravity, Coriolis, or kinematic terms, and do not include Euler angle states $\begin{bmatrix} \phi & \theta & \psi \end{bmatrix}$. Gravity is later incorporated using a nonlinear representation of the gravitational forces, as discussed in Section 2.3.5, and Coriolis and kinematics are incorporated within the nonlinear equations of motion, as discussed in Section 2.3.7. These special

matrices containing only the aerodynamic dimensional stability and control derivatives, denoted $\boldsymbol{A}_\text{aero}$ and $\boldsymbol{B}_\text{aero}$, are given as

$$\boldsymbol{A}_\text{aero} = \begin{bmatrix} X_u & X_v & X_w & X_p & X_q & X_r \\ Y_u & Y_v & Y_w & Y_p & Y_q & Y_r \\ Z_u & Z_v & Z_w & Z_p & Z_q & Z_r \\ L'_u & L'_v & L'_w & L'_p & L'_q & L'_r \\ M_u & M_v & M_w & M_p & M_q & M_r \\ N'_u & N'_v & N'_w & N'_p & N'_q & N'_r \end{bmatrix}_{6 \times 6} \tag{2.32}$$

$$\boldsymbol{B}_\text{aero} = \begin{bmatrix} X_{\delta_\text{a}} & X_{\delta_\text{e}} & X_{\delta_\text{r}} & X_{\delta_\text{t}} \\ Y_{\delta_\text{a}} & Y_{\delta_\text{e}} & Y_{\delta_\text{r}} & Y_{\delta_\text{t}} \\ Z_{\delta_\text{a}} & Z_{\delta_\text{e}} & Z_{\delta_\text{r}} & Z_{\delta_\text{t}} \\ L'_{\delta_\text{a}} & L'_{\delta_\text{e}} & L'_{\delta_\text{r}} & L'_{\delta_\text{t}} \\ M_{\delta_\text{a}} & M_{\delta_\text{e}} & M_{\delta_\text{r}} & M_{\delta_\text{t}} \\ N'_{\delta_\text{a}} & N'_{\delta_\text{e}} & N'_{\delta_\text{r}} & N'_{\delta_\text{t}} \end{bmatrix}_{6 \times 4} \tag{2.33}$$

For the current 6-DOF demonstration, these matrices have dimensions of 6×6 and 6×4, respectively. See Section 2.7 for details on implementing high-order models.

Table look-ups are performed on the $\boldsymbol{A}_\text{aero}$ and $\boldsymbol{B}_\text{aero}$ matrices to find the dimensional stability and control derivatives at the current, filtered x-body airspeed U_f [see Eq. (2.67)]. A low-pass filtered airspeed U_f is used for look-up of derivatives only, and is implemented to ensure that the derivative values remain constant for short-term motion, thereby retaining accurate dynamic responses at the discrete anchor points. The airspeed filter will be discussed in more detail in Section 2.3.9.

Next we introduce a dimensional mass matrix $\boldsymbol{\mathcal{M}}$ comprised of the aircraft mass m (identified/baseline value) and inertia tensor $\boldsymbol{I}$ (identified/baseline body-axes values):

$$\boldsymbol{\mathcal{M}} = \begin{bmatrix} m & & & & & \\ & m & & & & \\ & & m & & & \\ & & & I_{xx} & & -I_{xz} \\ & & & & I_{yy} & \\ & & & -I_{xz} & & I_{zz} \end{bmatrix}_{6 \times 6} \tag{2.34}$$

Multiplying the mass matrix $\boldsymbol{\mathcal{M}}$ into the matrix of aerodynamic stability derivatives $\boldsymbol{A}_\text{aero}$ and the state perturbation vector $\Delta \boldsymbol{x}$ yields a vector of aerodynamic dimensional perturbation forces and moments. Likewise, multiplying the mass matrix into the matrix of aerodynamic control derivatives $\boldsymbol{B}_\text{aero}$ and the control perturbation vector $\Delta \boldsymbol{u}$ produces a vector of dimensional perturbation control forces and moments. The sum of both vectors yields the complete aerodynamic dimensional perturbation forces and moments:

$$\begin{bmatrix} \Delta \boldsymbol{F}_\text{aero} \\ \Delta \boldsymbol{M}_\text{aero} \end{bmatrix}_{6 \times 1} = \boldsymbol{\mathcal{M}} \boldsymbol{A}_\text{aero}|_{U_\text{f}} \Delta \boldsymbol{x} + \boldsymbol{\mathcal{M}} \boldsymbol{B}_\text{aero}|_{U_\text{f}} \Delta \boldsymbol{u} \tag{2.35}$$

where the perturbation force vector consists of indices 1–3 and the perturbation moment vector consists of indices 4–6. This expression is shown schematically in Figure 2.4.

2.3.3 Aerodynamic Trim Forces

This simulation element determines the dimensional aerodynamic trim forces based on the trim aircraft attitude at the current airspeed. A lookup is first performed to find the trim Euler angles at the current x-body airspeed U. Subsequently, the *specific* aerodynamic trim forces are obtained as follows [11]:

$$\bar{X}_{\text{aero}_0} = g \sin \Theta_0|_U \tag{2.36}$$

$$\bar{Y}_{\text{aero}_0} = -g \cos \Theta_0|_U \sin \Phi_0|_U \tag{2.37}$$

$$\bar{Z}_{\text{aero}_0} = -g \cos \Theta_0|_U \cos \Phi_0|_U \tag{2.38}$$
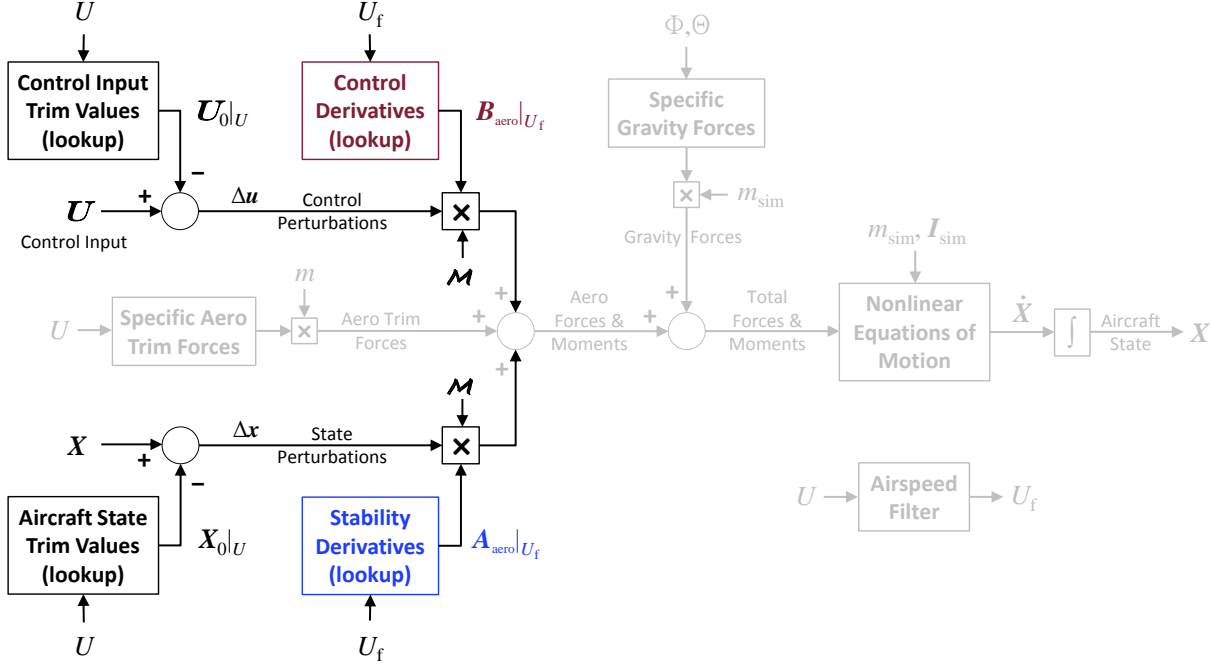
Figure 2.4: Model stitching simulation architecture – aero perturbation forces and moments.

The specific aerodynamic trim forces are then multiplied by the identified/baseline aircraft mass m to obtain the dimensional aerodynamic trim forces:

$$\boldsymbol{F}_{\mathrm{aero}_0} = \begin{bmatrix} X_{\mathrm{aero}_0} \\ Y_{\mathrm{aero}_0} \\ Z_{\mathrm{aero}_0} \end{bmatrix} = \begin{bmatrix} \bar{X}_{\mathrm{aero}_0} \\ \bar{Y}_{\mathrm{aero}_0} \\ \bar{Z}_{\mathrm{aero}_0} \end{bmatrix} m \tag{2.39}$$

This process of obtaining the dimensional aerodynamic trim forces is shown schematically in Figure 2.5.

2.3.4   Total Aerodynamic Forces and Moments

Calculating the total dimensional aerodynamic forces and moments combines the components covered thus far. The aerodynamic dimensional perturbation forces and moments [Eq. (2.35)] are summed with the dimensional aerodynamic trim forces [Eq. (2.39)] to yield the total aerodynamic forces and moments. This summation is expressed by

$$\boldsymbol{F}_{\mathrm{aero}} = \Delta \boldsymbol{F}_{\mathrm{aero}} + \boldsymbol{F}_{\mathrm{aero}_0} \tag{2.40}$$

$$\boldsymbol{M}_{\mathrm{aero}} = \Delta \boldsymbol{M}_{\mathrm{aero}} \tag{2.41}$$

and is shown graphically in Figure 2.6.

2.3.5   Nonlinear Gravitational Forces

As previously mentioned, the model stitching architecture incorporates nonlinear kinematics, thus small angle approximations are not made. Consequently, the *specific* gravity forces acting at the aircraft CG are nonlinear with respect to the aircraft Euler angles, and are computed as follows [11]:

$$\bar{X}_{\mathrm{grav}} = -g \sin \Theta \tag{2.42}$$

$$\bar{Y}_{\mathrm{grav}} = g \cos \Theta \sin \Phi \tag{2.43}$$

$$\bar{Z}_{\mathrm{grav}} = g \cos \Theta \cos \Phi \tag{2.44}$$
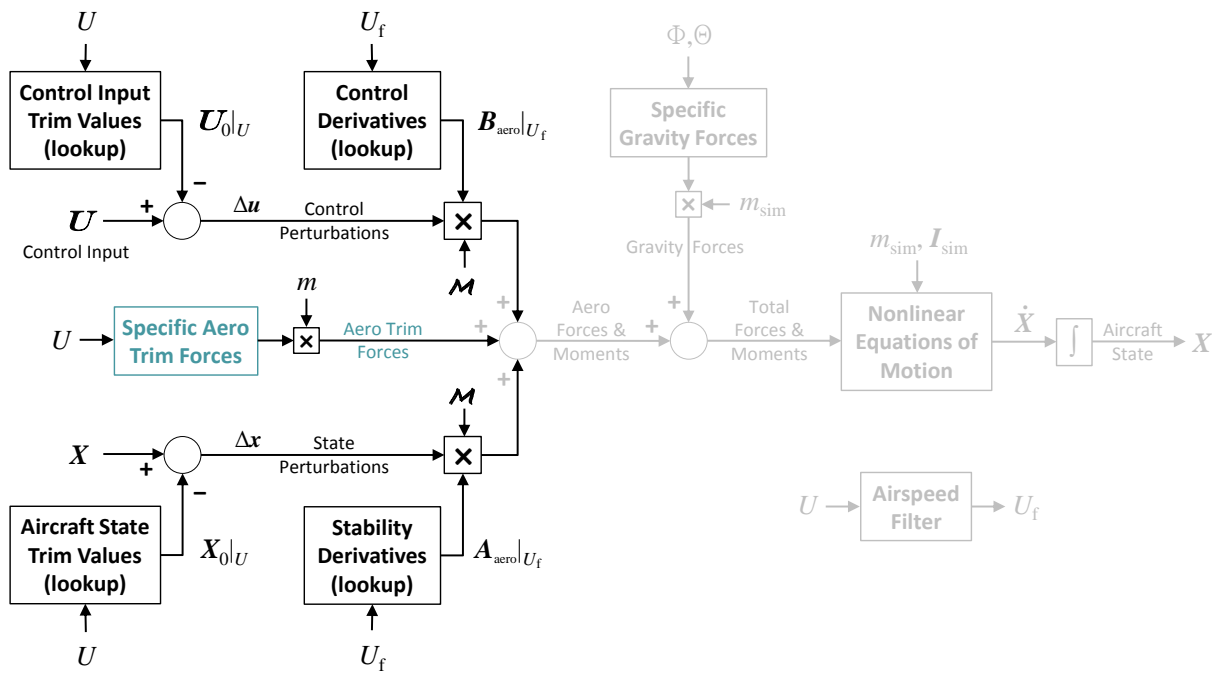
Figure 2.5: Model stitching simulation architecture – aero trim forces.
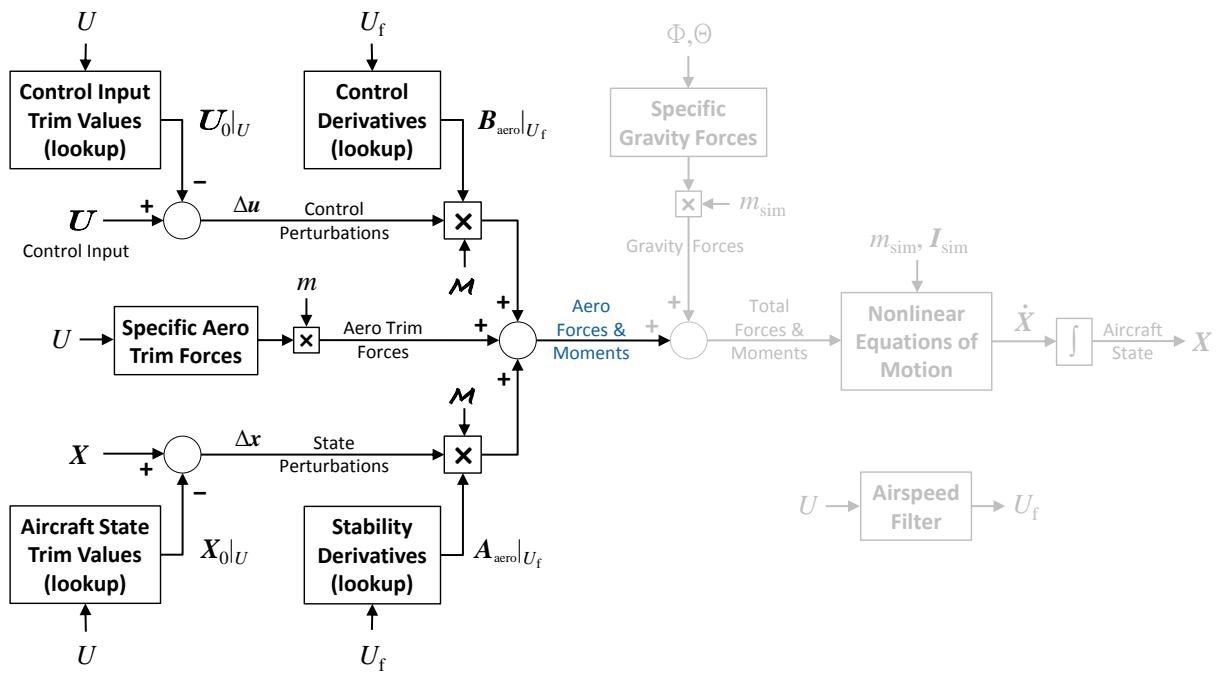
Figure 2.6: Model stitching simulation architecture – total aero forces and moments.
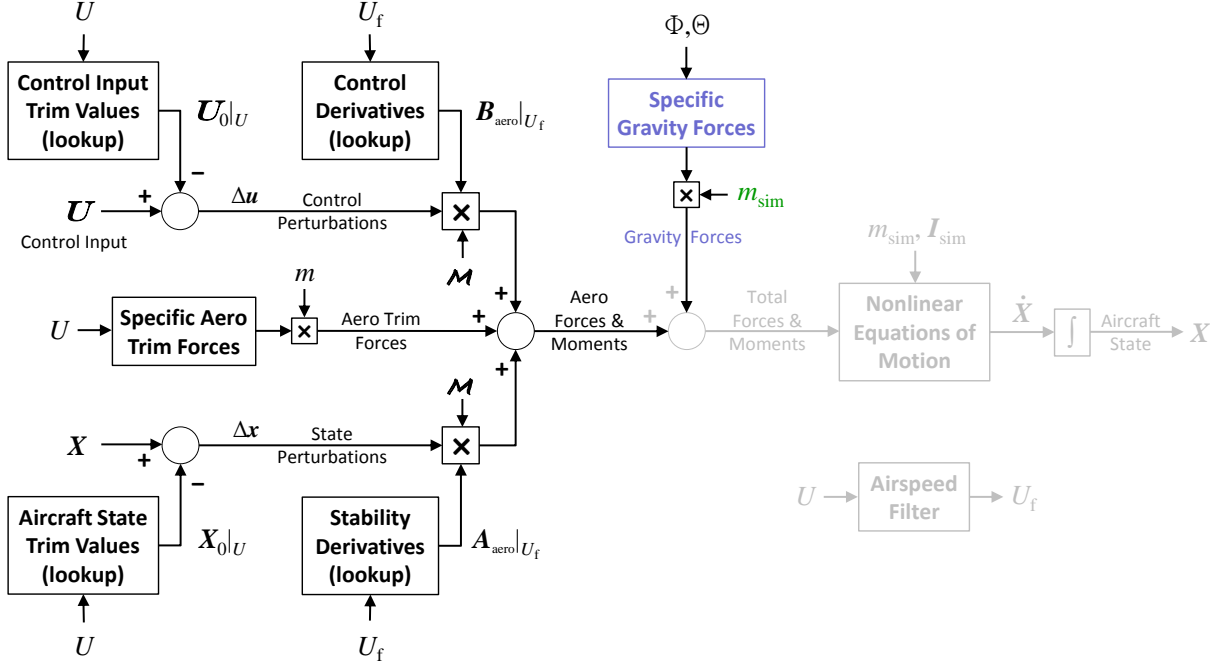
Figure 2.7: Model stitching simulation architecture – nonlinear gravitational forces.

It is important to emphasize that no look-up of trim data is performed for the gravitational force computation, but rather the current, instantaneous values of the aircraft Euler angles are used in the computation. At trim, note that the specific aerodynamic trim forces [Eqs. (2.36)–(2.38)] must balance these specific gravity forces. The specific gravity forces are multiplied by the current *simulation value* of aircraft mass to obtain the dimensional gravity forces:

$$\boldsymbol{F}_{\text{grav}} = \begin{bmatrix} X_{\text{grav}} \\ Y_{\text{grav}} \\ Z_{\text{grav}} \end{bmatrix} = \begin{bmatrix} \bar{X}_{\text{grav}} \\ \bar{Y}_{\text{grav}} \\ \bar{Z}_{\text{grav}} \end{bmatrix} m_{\text{sim}} \tag{2.45}$$

The current simulation value of aircraft mass m_{sim}, which is not necessarily the same mass value associated with the baseline/identified anchor point models, is utilized here to simulate off-nominal aircraft weight; see Section 2.5.1 for a discussion on off-nominal weight extrapolation. Note that the aircraft's center of gravity is assumed to be coincident with its center of mass, so the gravity forces produce no external moment about that point. The dimensional gravity force calculation is shown diagrammatically in Figure 2.7.

2.3.6 Total Forces and Moments

The aerodynamic forces and moments [Eqs. (2.40) and (2.41)] are summed with the gravity forces [Eq. (2.45)] to yield the total external, dimensional forces and moments acting at the CG. This summation is shown schematically in Figure 2.8 and is expressed by

$$\boldsymbol{F} = \boldsymbol{F}_{\text{aero}} + \boldsymbol{F}_{\text{grav}} \tag{2.46}$$

$$\boldsymbol{M} = \boldsymbol{M}_{\text{aero}} \tag{2.47}$$

Note again that the gravity force produces no external moment about the CG, so the total external moment is due to the total aerodynamic moment alone. The total forces and moments may be augmented, however, with user-specified external forces and moments for the simulation of additional modeling components (e.g., landing gear, etc.); see Section 2.4.2 for a discussion of user-specified external forces and moments.
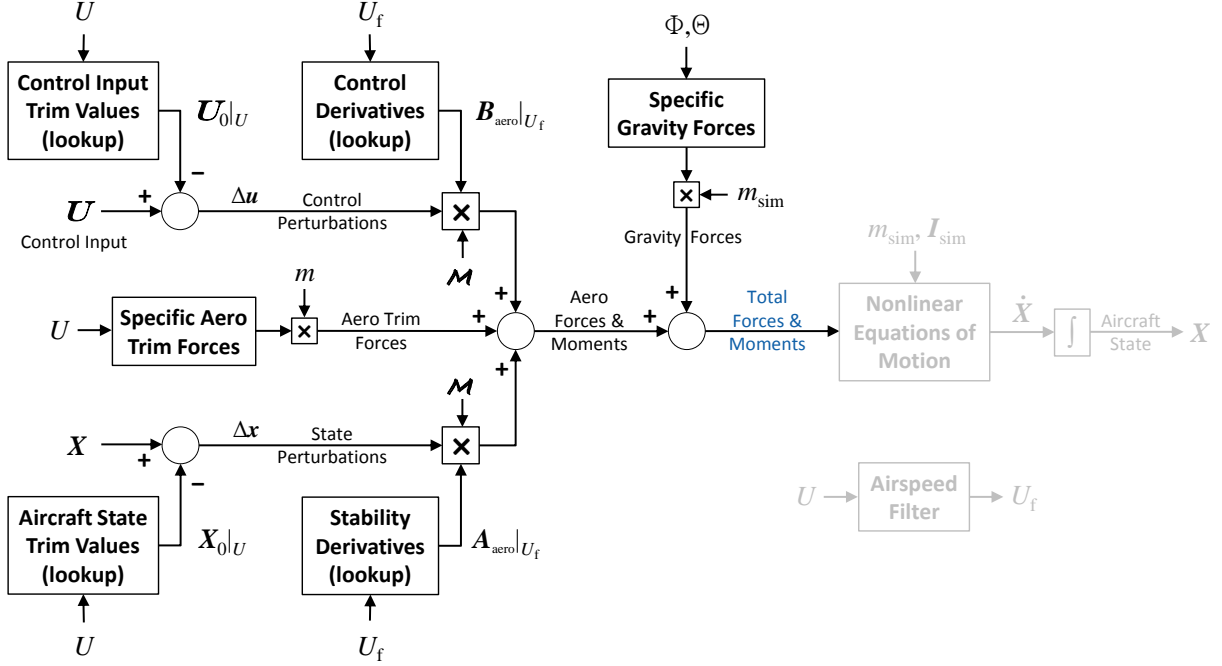
Figure 2.8: Model stitching simulation architecture – total forces and moments.

2.3.7 Nonlinear Equations of Motion

Another nonlinear component incorporated in the model stitching simulation architecture, aside from the previously discussed nonlinear representation of gravitational forces, is the nonlinear representation of Newton's equations of motion in the body-fixed (Eulerian) frame. Given the total forces and moments about the aircraft CG, along with the current aircraft state and simulation values of mass and inertia, the 6-DOF body-axes nonlinear equations of motion are implemented to obtain the fuselage accelerations and Euler-angle rates. The equations of motion contain the nonlinear Euler equations, which include the cross-coupling inertial and Coriolis terms in full nonlinear form.

The nonlinear equations of motion block is shown in the schematic in Figure 2.9. Note that the *simulation value* of aircraft mass m_{sim} and the inertia tensor containing the *simulation values* of inertia $\boldsymbol{I}_{\mathrm{sim}}$ are employed to accommodate the simulation of off-nominal aircraft loading configurations. See Section 2.5.1 for a discussion on off-nominal weight and inertia extrapolation within the model stitching architecture.

The following derivation of the force, moment, and kinematic equations is presented in a concise form. See Ref. [11], for example, for a more complete development.

Force Equations

The relationship between the total external force resolved at the vehicle's CG and the vehicle's acceleration is given by Newton's Second Law, defined in the inertial frame of reference:

$$m_{\mathrm{sim}} \frac{\mathrm{d}^I \boldsymbol{V}}{\mathrm{d}t} = \boldsymbol{F} \tag{2.48}$$

in which m_{sim} is the current simulation value of aircraft mass and $\boldsymbol{F}$ is the total dimensional force vector, as given in Eq. (2.46). The flight dynamics are expressed in the body-fixed (Eulerian) frame as

$$m_{\mathrm{sim}} \frac{\mathrm{d}^B \boldsymbol{V}}{\mathrm{d}t} + m_{\mathrm{sim}} \left(\boldsymbol{\omega} \times \boldsymbol{V} \right) = \boldsymbol{F} \tag{2.49}$$

15
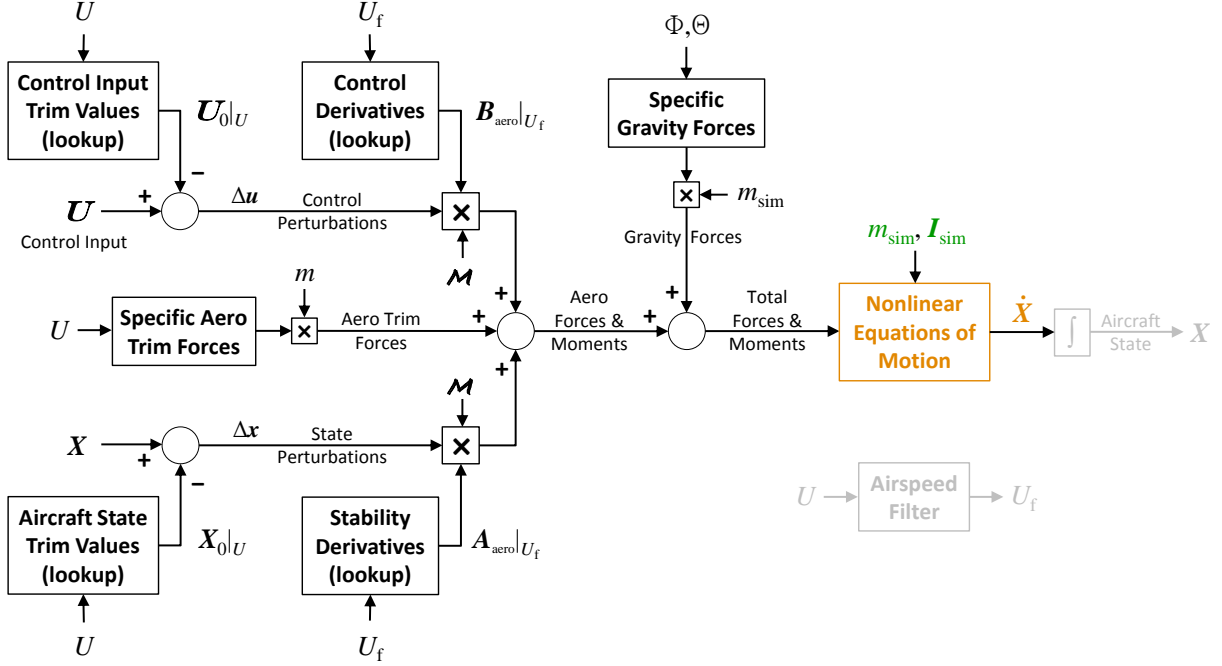
Figure 2.9: Model stitching simulation architecture – nonlinear equations of motion.

where $\boldsymbol{\omega}$ and $\boldsymbol{V}$ are the body-fixed angular and translational velocity vectors, respectively. Rearranging, the body-axis acceleration is then given as

$$\frac{\mathrm{d}^B \boldsymbol{V}}{\mathrm{d}t} = -(\boldsymbol{\omega} \times \boldsymbol{V}) + \frac{\boldsymbol{F}}{m_{\mathrm{sim}}} \tag{2.50}$$

Expanding out each component, the body-axes accelerations are given by

$$\dot{U} = RV - QW + X/m_{\mathrm{sim}} \tag{2.51}$$

$$\dot{V} = PW - RU + Y/m_{\mathrm{sim}} \tag{2.52}$$

$$\dot{W} = QU - PV + Z/m_{\mathrm{sim}} \tag{2.53}$$

where X, Y, and Z are the total dimensional x-, y-, and z-forces, respectively.

Moment Equations

The relationship between the total external moment about the vehicle's CG and the vehicle's angular acceleration is also given by Newton's Second Law, defined again in the inertial frame of reference:

$$\boldsymbol{I}_{\mathrm{sim}} \frac{\mathrm{d}^I \boldsymbol{\omega}}{\mathrm{d}t} = \boldsymbol{M} \tag{2.54}$$

in which $\boldsymbol{M}$ is the vector of total external moments, as given in Eq. (2.47). This relationship is expressed in the body-fixed (Eulerian) frame as

$$\boldsymbol{I}_{\mathrm{sim}} \frac{\mathrm{d}^B \boldsymbol{\omega}}{\mathrm{d}t} + (\boldsymbol{\omega} \times \boldsymbol{I}_{\mathrm{sim}} \boldsymbol{\omega}) = \boldsymbol{M} \tag{2.55}$$

where $\boldsymbol{I}_{\mathrm{sim}}$ is the inertia tensor, which is comprised of the current *simulation values* of aircraft body-axes inertias. The inertia tensor and inverse inertia tensor are given by

$$\boldsymbol{I}_{\mathrm{sim}} = \begin{bmatrix} I_{xx} & 0 & -I_{xz} \\ 0 & I_{yy} & 0 \\ -I_{xz} & 0 & I_{zz} \end{bmatrix} \tag{2.56}$$

16

$$\boldsymbol{I}_{\text{sim}}^{-1} = \frac{1}{\Gamma} \begin{bmatrix} I_{zz} & 0 & I_{xz} \\ 0 & \Gamma/I_{yy} & 0 \\ I_{xz} & 0 & I_{xx} \end{bmatrix} \tag{2.57}$$

where $\Gamma = I_{xx}I_{zz} - I_{xz}^2$ [13]. The body-axis angular acceleration is then obtained from Eq. (2.55):

$$\frac{\mathrm{d}^B \boldsymbol{\omega}}{\mathrm{d}t} = \boldsymbol{I}_{\text{sim}}^{-1} \left[-(\boldsymbol{\omega} \times \boldsymbol{I}_{\text{sim}}\boldsymbol{\omega}) + \boldsymbol{M} \right] \tag{2.58}$$

Expanding out each component in Eq. (2.58), the body-axes angular accelerations are given by [13]

$$\dot{P} = \frac{I_{xz}\left(I_{xx} - I_{yy} + I_{zz}\right)PQ - \left(I_{zz}^2 - I_{yy}I_{zz} + I_{xz}^2\right)QR + I_{zz}L + I_{xz}N}{I_{xx}I_{zz} - I_{xz}^2} \tag{2.59}$$

$$\dot{Q} = \frac{\left(I_{zz} - I_{xx}\right)PR - I_{xz}\left(P^2 - R^2\right) + M}{I_{yy}} \tag{2.60}$$

$$\dot{R} = \frac{\left(I_{xx}^2 - I_{xx}I_{yy} + I_{xz}^2\right)PQ - I_{xz}\left(I_{xx} - I_{yy} + I_{zz}\right)QR + I_{xz}L + I_{xx}N}{I_{xx}I_{zz} - I_{xz}^2} \tag{2.61}$$

Kinematic Equations

The nonlinear kinematic relationship between the body-axes angular rates and the Euler-angle rates is given by the following [11]:

$$\dot{\Phi} = P + Q\sin\Phi\tan\Theta + R\cos\Phi\tan\Theta \tag{2.62}$$

$$\dot{\Theta} = Q\cos\Phi - R\sin\Phi \tag{2.63}$$

$$\dot{\Psi} = Q\sin\Phi\sec\Theta + R\cos\Phi\sec\Theta \tag{2.64}$$

Total body-axes accelerations [Eqs. (2.51)–(2.53)], body-axes angular accelerations [Eqs. (2.59)–(2.61)], and Euler-angle rates [Eqs. (2.62)–(2.64)] are then collated to form the 6-DOF total state-dot vector:

$$\dot{\boldsymbol{X}} = \begin{bmatrix} \dot{U} \\ \dot{V} \\ \dot{W} \\ \dot{P} \\ \dot{Q} \\ \dot{R} \\ \dot{\Phi} \\ \dot{\Theta} \\ \dot{\Psi} \end{bmatrix} \tag{2.65}$$

which is the output of the nonlinear equations of motion simulation element (Figure 2.9).

2.3.8 Time Integration

The 6-DOF state-dot vector $\dot{\boldsymbol{X}}$ [Eq. (2.65)], comprised of the total body-axes accelerations, body-axes angular accelerations, and Euler-angle rates, is integrated forward in time to obtain the current 6-DOF aircraft state vector $\boldsymbol{X}$, given by

$$\boldsymbol{X} = \begin{bmatrix} U \\ V \\ W \\ P \\ Q \\ R \\ \Phi \\ \Theta \\ \Psi \end{bmatrix} \tag{2.66}$$

This integration is represented in the schematic as depicted in Figure 2.10.
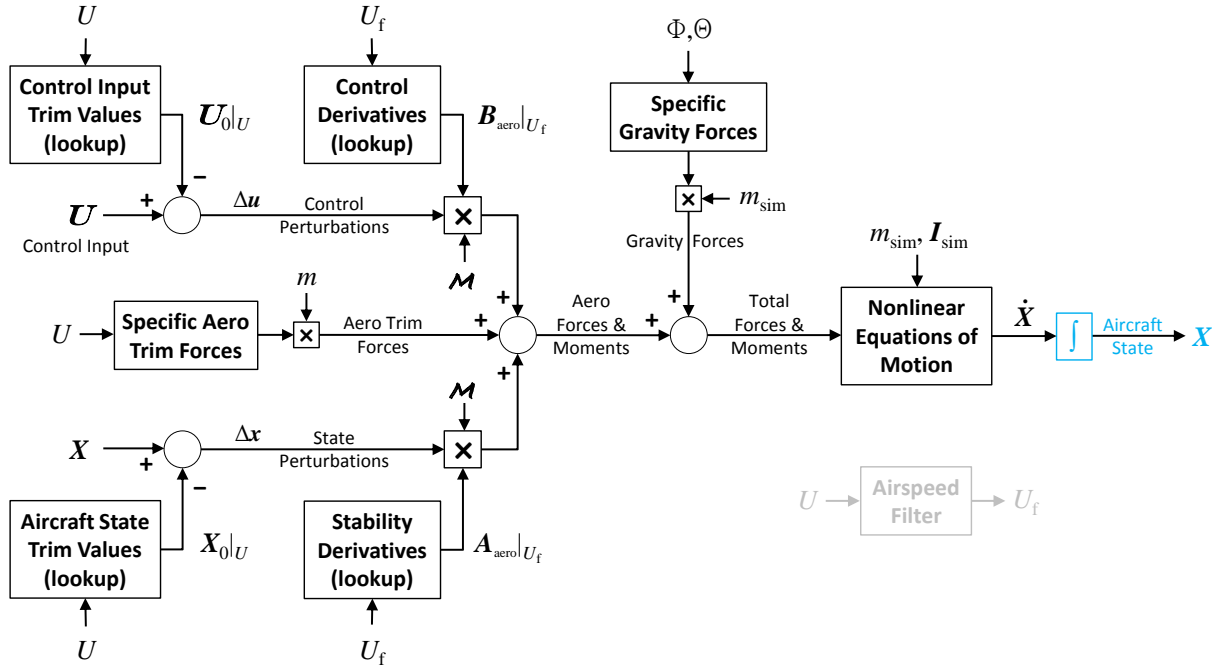
Figure 2.10: Model stitching simulation architecture – time integration.

2.3.9 Airspeed Filter

The final key element of the model stitching simulation architecture is the airspeed filter. A low-pass filtered airspeed is used for look-up of the stability and control derivatives only (i.e., *not* the trim data), as mentioned in Section 2.3.2. Applying the filter ensures that the derivative values remain constant for short-term motion, thereby retaining accurate dynamic responses at the discrete anchor points.

The total x-body airspeed U is filtered using a first-order low-pass filter to produce the filtered total x-body airspeed U_{f}:

$$U_{\mathrm{f}} = \frac{\omega_{\mathrm{f}}}{s + \omega_{\mathrm{f}}} U \tag{2.67}$$

The airspeed filter and output filtered x-body airspeed U_{f} are shown schematically in Figure 2.11. A break frequency of $\omega_{\mathrm{f}} = 0.2$ rad/sec has been found to be satisfactory, in that it corresponds to the lower end of the frequency range of applicability for most identified models and yet is still fast enough to allow accurate simulation of moderately-aggressive acceleration/deceleration [1]. A higher break frequency may be appropriate for applications involving small aircraft, in which the flight envelope can be flown through rapidly.
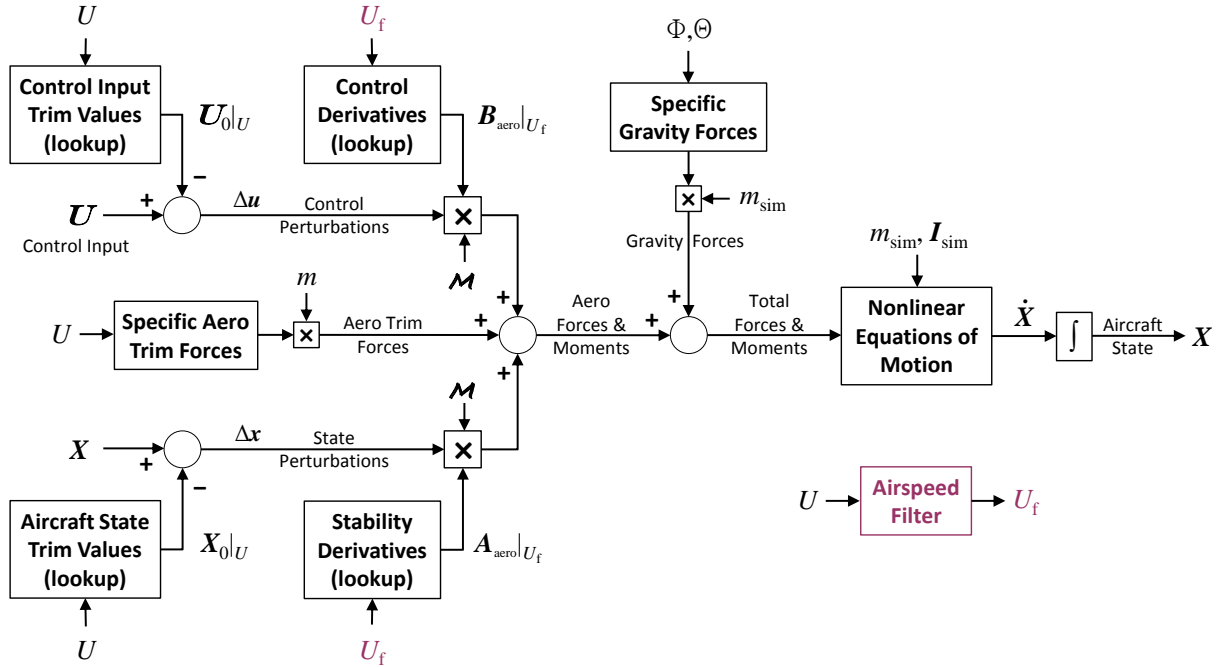
Figure 2.11: Model stitching simulation architecture – airspeed filter.

2.4 Additional Simulation Elements

Key simulation elements of the model stitching architecture were presented in Section 2.3. Additional simulation elements, which are generic in nature and are applicable to both fixed-wing aircraft and rotorcraft, are incorporated into the model stitching architecture. These additional elements include:

- atmospheric disturbances
- user-specified external forces and moments
- standard atmosphere model
- simple landing gear model

These elements are discussed individually over the succeeding subsections.

2.4.1 Atmospheric Disturbances

The ability to simulate atmospheric disturbances, including steady wind and turbulence, is included in the model stitching architecture. Each disturbance type—steady wind, turbulence, and user-specified disturbances—is covered in this section.

The steady wind formulation is applicable to any flight vehicle, but it is important to note that the type of turbulence model used is dictated by the aircraft type for which the stitched model is configured. The Dryden wind turbulence model [14] is used for fixed-wing aircraft applications, whereas a Control Equivalent Turbulence Input (CETI) [15] model is used for rotorcraft applications.

Steady Wind

Steady wind, with defined magnitude and direction, can be simulated in the stitched model. The wind velocity, given in the horizontal ground reference system, must first be determined in the body-axes coordinate system.

Given the local wind magnitude V_{wind} and wind direction in azimuth degrees from North, ψ_{wind}, the wind vector in the horizontal ground reference system is constructed:

$$[\boldsymbol{V}_{\text{wind}}]_{\text{h}} = \begin{bmatrix} V_{\text{wind}} \cos \psi_{\text{wind}} \\ V_{\text{wind}} \sin \psi_{\text{wind}} \\ 0 \end{bmatrix} \tag{2.68}$$

which is defined using north-east-down (NED) coordinates. Note that there is no "down" component; the wind is assumed to always flow parallel to the local horizontal.

Given the orientation of the aircraft, the direction cosine matrix [11] from horizontal ground reference coordinates to body-axes coordinates is given by

$$\boldsymbol{C}_{\text{b/h}} = \begin{bmatrix} \cos\theta\cos\psi & \cos\theta\sin\psi & -\sin\theta \\ -\cos\phi\sin\psi + \sin\phi\sin\theta\cos\psi & \cos\phi\cos\psi + \sin\phi\sin\theta\sin\psi & \sin\phi\cos\theta \\ \sin\phi\sin\psi + \cos\phi\sin\theta\cos\psi & -\sin\phi\cos\psi + \cos\phi\sin\theta\sin\psi & \cos\phi\cos\theta \end{bmatrix} \tag{2.69}$$

which is the complete ψ-θ-ϕ (3-2-1) Euler rotation matrix.

Finally, the wind vector expressed in body-axes coordinates can be found:

$$[\boldsymbol{V}_{\text{wind}}]_{\text{b}} = \boldsymbol{C}_{\text{b/h}} [\boldsymbol{V}_{\text{wind}}]_{\text{h}} \tag{2.70}$$

Henceforth, mention of the wind velocity vector refers to the body-axes version, and is simply written $\boldsymbol{V}_{\text{wind}}$.

Turbulence

The choice of atmospheric turbulence model is dictated by the aircraft configuration being modeled; a Dryden wind turbulence model is used for fixed-wing aircraft and a Control Equivalent Turbulence Input (CETI) model is used for rotorcraft. This distinction is important in that the Dryden model is not applicable for hovering/low-speed rotorcraft, and should not be used for this application.

A Dryden turbulence model [14] is implemented for use in fixed-wing aircraft applications and can also be used for rotorcraft in forward flight conditions. The Dryden model includes low- and high-altitude components with altitude blending, and is configurable for specified turbulence characteristics and aircraft properties. The output of the Dryden model includes body-axes u, v, and w disturbances and p, q, and r disturbances, which are collated to form vectors $\boldsymbol{V}_{\text{Dryden}}$ and $\boldsymbol{\omega}_{\text{Dryden}}$, respectively.

A Control Equivalent Turbulence Input (CETI) [15] model is used for rotorcraft applications, particularly in hover/low-speed conditions. The CETI model uses white-noise driven transfer functions to provide control inputs that mimic flight-identified control disturbances for various levels of turbulence.

User-Specified Disturbance

The simulation architecture accommodates user-specified disturbance inputs, which are to be defined in body-axes coordinates to form vector $\boldsymbol{V}_{\text{user disturb}}$. The user-specified disturbances are useful for playing-in discrete and one-minus-cosine gust inputs, but can be any generic input.

Total Disturbance

Summing all individual atmospheric disturbance vectors yields the total atmospheric disturbance vector in body axes:

$$\boldsymbol{V}_{\text{total disturb}} = \boldsymbol{V}_{\text{wind}} + \boldsymbol{V}_{\text{Dryden}} + \boldsymbol{V}_{\text{user disturb}} \tag{2.71}$$

which is the sum of the steady wind contribution, the Dryden turbulence model output (fixed-wing applications only), and any user-defined disturbance input. Angular rate disturbances are from the Dryden turbulence model and any user-defined angular-rate disturbance, thus:

$$\boldsymbol{\omega}_{\text{total disturb}} = \boldsymbol{\omega}_{\text{Dryden}} + \boldsymbol{\omega}_{\text{user disturb}} \tag{2.72}$$

Relative Velocities and Angular Rates

Given the total atmospheric disturbance velocity vector and the total atmospheric disturbance angular rate vector, the relative velocity vector and relative angular rate vector are

$$\boldsymbol{V}_{\mathrm{rel}} = \boldsymbol{V} - \boldsymbol{V}_{\mathrm{total\ disturb}} \tag{2.73}$$

$$\boldsymbol{\omega}_{\mathrm{rel}} = \boldsymbol{\omega} - \boldsymbol{\omega}_{\mathrm{total\ disturb}} \tag{2.74}$$

which can be written in component form as

$$\begin{bmatrix} U \\ V \\ W \end{bmatrix}_{\mathrm{rel}} = \begin{bmatrix} U \\ V \\ W \end{bmatrix} - \begin{bmatrix} U \\ V \\ W \end{bmatrix}_{\mathrm{total\ disturb}} \tag{2.75}$$

$$\begin{bmatrix} P \\ Q \\ R \end{bmatrix}_{\mathrm{rel}} = \begin{bmatrix} P \\ Q \\ R \end{bmatrix} - \begin{bmatrix} P \\ Q \\ R \end{bmatrix}_{\mathrm{total\ disturb}} \tag{2.76}$$

The relative velocities and relative angular rates are concatenated to form the relative 6-state vector:

$$\boldsymbol{X}_{6_{\mathrm{rel}}} = \begin{bmatrix} U \\ V \\ W \\ P \\ Q \\ R \end{bmatrix}_{\mathrm{rel}} \tag{2.77}$$

This vector is analogous to that of Eq. (2.26). The full state vector containing these relative velocities and relative angular rates is referred to as the relative state vector, $\boldsymbol{X}_{\mathrm{rel}}$.

Ultimately, the relative velocities and relative angular rates explicitly affect the calculation of aerodynamic forces and moments only, specifically in the following three simulation elements:

1) state and control perturbation vectors, analogous to Eqs. (2.22) and (2.23)

$$\Delta\boldsymbol{x} = \boldsymbol{X}_{\mathrm{rel}} - \boldsymbol{X}_0|_{U_{\mathrm{rel}}} \tag{2.78}$$

$$\Delta\boldsymbol{u} = \boldsymbol{U} - \boldsymbol{U}_0|_{U_{\mathrm{rel}}} \tag{2.79}$$

2) aerodynamic dimensional perturbation forces and moments, analogous to Eq. (2.35)

$$\begin{bmatrix} \Delta\boldsymbol{F}_{\mathrm{aero}} \\ \Delta\boldsymbol{M}_{\mathrm{aero}} \end{bmatrix}_{6\times 1} = \boldsymbol{\mathcal{M}}\boldsymbol{A}_{\mathrm{aero}}|_{(U_{\mathrm{rel}})_{\mathrm{f}}}\Delta\boldsymbol{x} + \boldsymbol{\mathcal{M}}\boldsymbol{B}_{\mathrm{aero}}|_{(U_{\mathrm{rel}})_{\mathrm{f}}}\Delta\boldsymbol{u} \tag{2.80}$$

and 3) specific aerodynamic trim forces, analogous to Eqs. (2.36)–(2.38)

$$\bar{X}_{\mathrm{aero}_0} = g\sin\Theta_0|_{U_{\mathrm{rel}}} \tag{2.81}$$

$$\bar{Y}_{\mathrm{aero}_0} = -g\cos\Theta_0|_{U_{\mathrm{rel}}}\sin\Phi_0|_{U_{\mathrm{rel}}} \tag{2.82}$$

$$\bar{Z}_{\mathrm{aero}_0} = -g\cos\Theta_0|_{U_{\mathrm{rel}}}\cos\Phi_0|_{U_{\mathrm{rel}}} \tag{2.83}$$

The relative state vector $\boldsymbol{X}_{\mathrm{rel}}$, relative x-body airspeed U_{rel}, and filtered relative x-body airspeed $(U_{\mathrm{rel}})_{\mathrm{f}}$ are indicated in Figure 2.12.

It is important to emphasize that these relative state values are used for the calculation of the aerodynamic forces and moments only. The *inertial states* of Eq. (2.66) are used in the calculation of the gravity forces [Eqs. (2.42)–(2.44)] and in the equations of motion [Eqs. (2.51)–(2.53) and (2.59)–(2.64)].
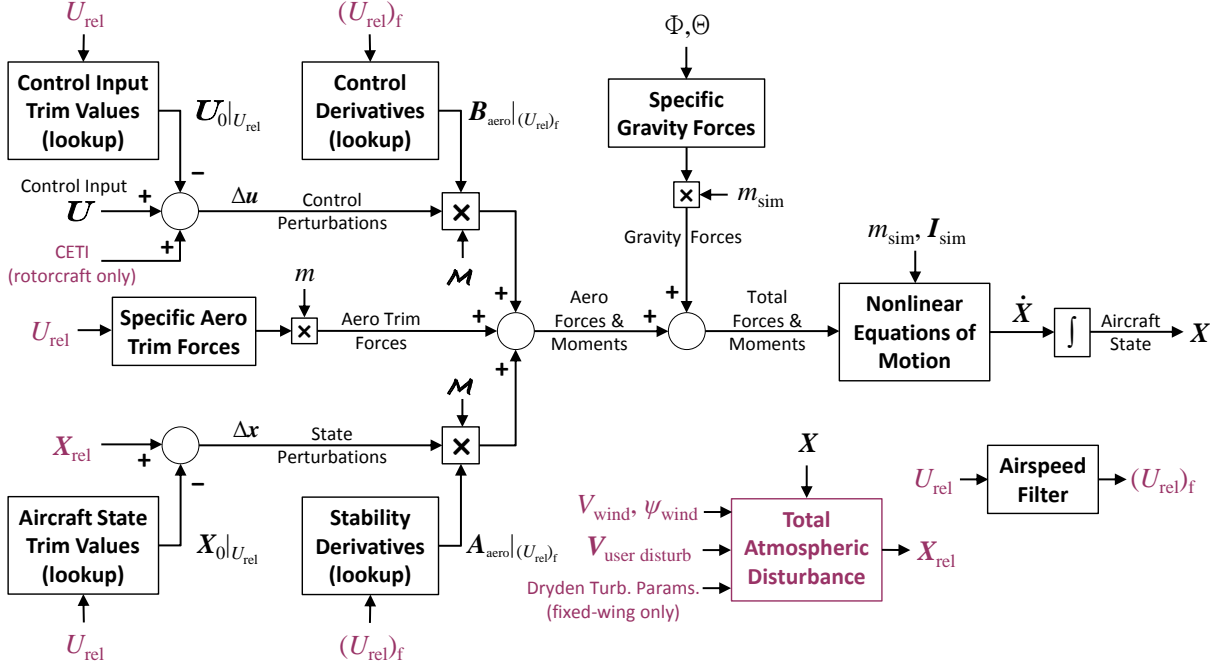
Figure 2.12: Model stitching simulation architecture – atmospheric disturbances.

2.4.2 User-Specified External Forces and Moments

The model stitching simulation architecture has an accommodation to input user-specified external forces and moments directly at the CG, which are summed with the stitched model's calculated total forces and moments (see schematic shown in Figure 2.2). This accommodation allows a convenient means of including model features that are not expressly contained within the stability and control derivatives. Examples include:

- unmodeled drag from spoilers, deployed landing gear, external stores, etc.
- landing gear contact with the ground
- asymmetrical thrust due to inoperative engine(s)

With user-specified external forces and moments, the equations for the calculation of total forces and moments [Eqs. (2.46) and (2.47)] become

$$\boldsymbol{F} = \boldsymbol{F}_{\mathrm{aero}} + \boldsymbol{F}_{\mathrm{grav}} + \boldsymbol{F}_{\mathrm{user}} \tag{2.84}$$

$$\boldsymbol{M} = \boldsymbol{M}_{\mathrm{aero}} + \boldsymbol{M}_{\mathrm{user}} \tag{2.85}$$

Application of user-specified external forces and moments is demonstrated herein in the CJ1 fixed-wing aircraft example stitched model of Chapter 3.

2.4.3 Standard Atmosphere Model

A model of the standard atmosphere is integrated into the model stitching architecture. Its primary function is to output air density for a given altitude, which is used to calculate the air density ratio ρ_{sim}/ρ for fixed-wing aircraft altitude extrapolation (see Section 2.6). A secondary function is to output speed of sound for a given altitude for the calculation of Mach number (e.g., for table look-up based on Mach).

2.4.4 Simple Landing Gear

An elementary landing gear model is incorporated into the simulation architecture, which utilizes a spring force proportional to strut displacement and body rate damping to arrest vertical motion and zero-out

attitude at some height offset above ground level. This basic capability allows landing simulation for fixed-wing aircraft and hovering rotorcraft. Additionally, saturation logic is included to reasonably mimic separate main- and nose-gear contact for fixed-wing aircraft, which allows for basic rotation for takeoff. This simple model enables reasonable assessment of landing and touch-and-go traffic pattern flying.

2.5   Extrapolation to Off-Nominal Loading Configurations

A powerful feature of the model stitching architecture is the ability to accurately simulate off-nominal aircraft loading configurations in real time, without the need for additional data. Simulation of off-nominal loading configurations, i.e., loading configurations with values of aircraft mass, inertia, and/or center of gravity (CG) location that differ from the identified/baseline values, is accomplished using extrapolation methods within the model stitching architecture. Although mass, CG, and inertia are physically related, these parameters can be adjusted independently. This extrapolation capability can be used to simply simulate an alternate gross weight, as well as continuous, real-time simulation of fuel burn-off and changes in inertia/CG location due to jettisoning of external stores, for example.

These extrapolation capabilities allow a stitched model to be constructed using only a small number of point models, and dramatically reduce the required number of flight-test points for identified models. Further discussions of flight-test implications are provided for fixed-wing aircraft and rotorcraft applications in Sections 3.9 and 4.9, respectively.

This section covers the extrapolation methods used for each off-nominal loading configuration parameter. Specifically, weight and inertia are discussed in Section 2.5.1, and CG location is covered in Section 2.5.2. Verification of these extrapolation methods are presented as applied to the CJ1 fixed-wing aircraft example case in Section 3.6, and to the UH-60 Black Hawk helicopter example case in Section 4.6.

2.5.1   Weight and Inertia

For simulation of off-nominal weight and inertia, the mass used in the calculation of the nonlinear gravitational forces (Section 2.3.5) and the mass and inertia tensor used in the nonlinear equations of motion (Section 2.3.7) are replaced with those values of the current simulation loading configuration. The simulation mass and inertia tensor, denoted by m_{sim} and I_{sim}, are incorporated as shown in Figure 2.13, and are seen incorporated in the top-level architecture schematics shown previously in Figures 2.7 and 2.9.
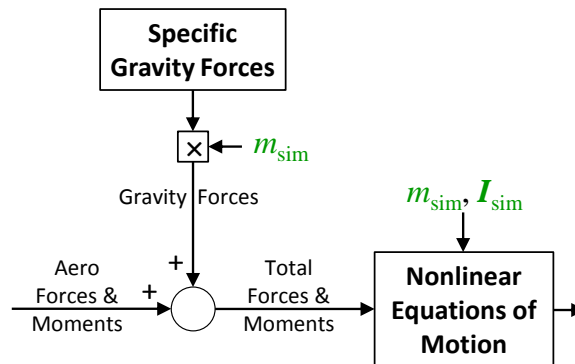
Figure 2.13: Simulation values of mass and inertia.

Reiterating Eq. (2.45), the dimensional gravitational force vector is found using the current *simulation value* of mass:

$$\boldsymbol{F}_{\text{grav}} = \begin{bmatrix} \bar{X}_{\text{grav}} \\ \bar{Y}_{\text{grav}} \\ \bar{Z}_{\text{grav}} \end{bmatrix} m_{\text{sim}} \tag{2.86}$$

Likewise, reiterating Eqs. (2.50) and (2.58), the current *simulation values* of mass and inertia are used in the force and moment equations, respectively, in the nonlinear equations of motion:

$$\frac{\mathrm{d}^B \boldsymbol{V}}{\mathrm{d}t} = -(\boldsymbol{\omega} \times \boldsymbol{V}) + \frac{\boldsymbol{F}}{m_{\mathrm{sim}}} \tag{2.87}$$

$$\frac{\mathrm{d}^B \boldsymbol{\omega}}{\mathrm{d}t} = \boldsymbol{I}_{\mathrm{sim}}^{-1} \left[-(\boldsymbol{\omega} \times \boldsymbol{I}_{\mathrm{sim}} \boldsymbol{\omega}) + \boldsymbol{M} \right] \tag{2.88}$$

When an alternate weight is implemented, the simulation will no longer be in trim at the flight-test (baseline) lookup-table values of the trim state vector $\boldsymbol{X}_0|_U$ and trim control vector $\boldsymbol{U}_0|_U$ (Section 2.3.1). Therefore, the stitched simulation model is *retrimmed*, in which trim is determined using a numerical trimming procedure (i.e., the MATLAB® function `findop` [12]) to achieve a steady-state condition for the current simulation loading configuration. Furthermore, the stitched model may be *relinearized* (using the MATLAB function `linearize` [12]) to obtain a new state-space representation and the corresponding stability and control derivatives of the current simulation loading configuration. In contrast to changes in weight, changes in values of inertia will not affect trim, but rather only the dynamics (and associated stability and control derivatives) will be affected.

Verification results of the off-nominal weight and inertia extrapolation methods are provided in Sections 3.6.1 and 3.6.2, respectively, as applied to the fixed-wing case. Sections 4.6.1 and 4.6.2 provide verification results of the off-nominal weight and inertia extrapolation methods, respectively, as applied to the rotorcraft case.

2.5.2 Center of Gravity

Off-nominal center of gravity (CG) locations may be simulated in the stitched model given an offset vector $\boldsymbol{r}_{S/O}$, which is a vector defining the desired simulation CG location "S" with respect to the original (identified) CG location "O". The components of $\boldsymbol{r}_{S/O}$ are the x-, y-, and z-offset distances, in feet, from the original CG to the simulated CG, following the conventional body-axes designation and sign convention as shown in Figure 2.14.
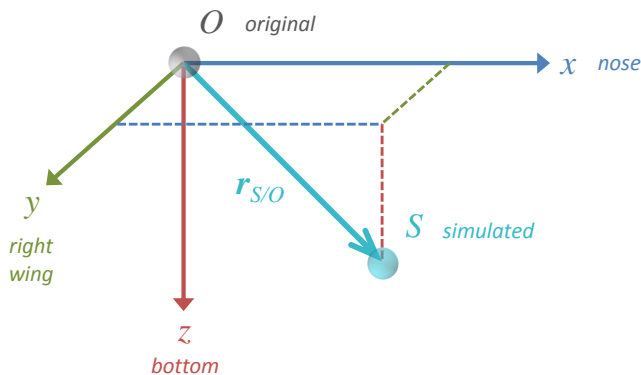
Figure 2.14: Simulated CG location axis convention.

For example, to configure a simulated CG that is 6 inches forward and 2 inches below the original CG location, the offset vector $\boldsymbol{r}_{S/O}$, which, again, defines the simulated CG with respect to the original CG, would be $\boldsymbol{r}_{S/O} = \begin{bmatrix} 0.5 & 0 & 0.167 \end{bmatrix}$, ensuring the units are in feet. To simulate a CG that is purely aft 4 inches, the offset vector would be entered as $\boldsymbol{r}_{S/O} = \begin{bmatrix} -0.333 & 0 & 0 \end{bmatrix}$.

Outlined below is the process for obtaining the resultant external aerodynamic moment for an off-nominal CG location. First, the velocity vector is determined at the location of the original CG, and used in the lookup of trim and derivatives. Then, the calculated aerodynamic moment is transferred to the simulated CG location. The transferred moment is ultimately passed to the nonlinear equations of motion, affecting trim and the dynamic response of the stitched model.

24

Determine Velocity at Original CG Location

Because the trim data and the stability and control derivatives stored in the lookup tables were obtained at the original CG and at a specific trim condition, the current simulation body-axes velocity components and angular rates must be determined at the location of the original CG before performing the lookup. The body-axes angular rates will be identical between the original and off-nominal configurations, but the velocity at the original location is found as follows:

$$\boldsymbol{V}_O = \boldsymbol{V}_S + \left(\boldsymbol{\omega} \times \boldsymbol{r}_{O/S}\right) \tag{2.89}$$

where $\boldsymbol{r}_{O/S} = -\boldsymbol{r}_{S/O}$. Expanding (2.89) in component form and writing out the velocity transfer for each axis component yields the following:

$$\begin{bmatrix} U \\ V \\ W \end{bmatrix}_O = \begin{bmatrix} U \\ V \\ W \end{bmatrix}_S + \left(\begin{bmatrix} P \\ Q \\ R \end{bmatrix} \times \begin{bmatrix} x_{O/S} \\ y_{O/S} \\ z_{O/S} \end{bmatrix} \right) \tag{2.90}$$

$$U_O = U_S + Q z_{O/S} - R y_{O/S} \tag{2.91}$$
$$V_O = V_S - P z_{O/S} + R x_{O/S} \tag{2.92}$$
$$W_O = W_S + P y_{O/S} - Q x_{O/S} \tag{2.93}$$

For demonstration, a schematic depicting the z-body airspeed W transfer from simulated to original CG is shown in Figure 2.15 for a pure x-axis offset. Note that in this case the value of $x_{O/S}$ is negative (simulated CG is forward), so $W_0 > W_S$.
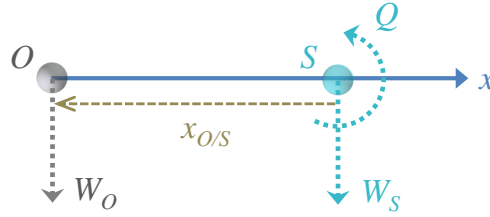
Figure 2.15: Simulated CG location – velocity transfer.

The transferred velocity is then used in the table look-ups to obtain the values of trim and stability and control derivatives. Subsequently, perturbations are calculated, and the total aerodynamic forces and moments are output.

Transfer Moments

The output forces and moments are those of the configuration with the original CG location, and must be transferred to that of the current simulated CG. The forces simply transfer and are identical between original and simulated configurations, but the moment vector of the configuration with the simulated CG is found as follows:

$$\boldsymbol{M}_S = \boldsymbol{M}_O + \left(\boldsymbol{r}_{O/S} \times \boldsymbol{F}\right) \tag{2.94}$$

again in which $\boldsymbol{r}_{O/S} = -\boldsymbol{r}_{S/O}$. This yields the appropriate aerodynamic moments at the current simulation configuration. Showing (2.94) in component form and writing out the moment transfer for each axis yields:

$$\begin{bmatrix} L \\ M \\ N \end{bmatrix}_S = \begin{bmatrix} L \\ M \\ N \end{bmatrix}_O + \left(\begin{bmatrix} x_{O/S} \\ y_{O/S} \\ z_{O/S} \end{bmatrix} \times \begin{bmatrix} F_x \\ F_y \\ F_z \end{bmatrix} \right) \tag{2.95}$$

$$L_S = L_O + F_z y_{O/S} - F_y z_{O/S} \tag{2.96}$$
$$M_S = M_O - F_z x_{O/S} + F_x z_{O/S} \tag{2.97}$$
$$N_S = N_O + F_y x_{O/S} - F_x y_{O/S} \tag{2.98}$$

25

Continuing the demonstration, a schematic depicting the pitching moment M transfer from original to simulated CG is shown in Figure 2.16 for a pure x-axis offset. Note that in this case the value of $x_{O/S}$ is negative (simulated CG is forward), so $M_S > M_0$.
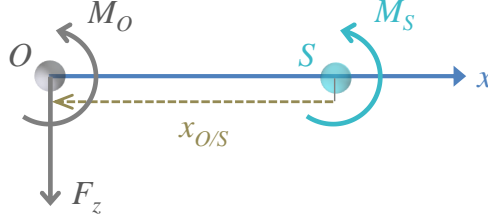
Figure 2.16: Simulated CG location – moment transfer.

When the simulation is retrimmed and relinearized for an off-nominal CG location, the significant effect on static stability derivative M_w (analogous to M_α) is captured. Verification of this effect and other results of the off-nominal CG extrapolation method are provided herein. See Section 3.6.3 for results of off-nominal CG extrapolation as applied to the fixed-wing case, and Section 4.6.3 for those of the rotorcraft case.

2.6 Altitude Extrapolation

Extrapolation to alternate altitudes for fixed-wing aircraft applications is accomplished within the model stitching architecture by employing air density scaling. The aerodynamic perturbation forces and moments (Section 2.3.2) and the aerodynamic trim forces (Section 2.3.3) are scaled by the air density ratio ρ_{sim}/ρ, which is the ratio of air density at the simulation altitude to that at the altitude at which the models were identified/configured. This method ignores secondary effects associated with Mach variations, and nonlinear effects, such as engine performance. Mach effects can be included, however, by storing the nondimensional stability and control derivatives as a function of Mach number, and regenerating the dimensional derivatives.

The scaled aerodynamic perturbation forces and moments, analogous to Eq. (2.35), are found as

$$\begin{bmatrix} \Delta \boldsymbol{F}_{\mathrm{aero}} \\ \Delta \boldsymbol{M}_{\mathrm{aero}} \end{bmatrix}_{6\times 1} = \left(\boldsymbol{A}_{\mathrm{aero}}|_{U_{\mathrm{f}}} \Delta \boldsymbol{x} + \boldsymbol{B}_{\mathrm{aero}}|_{U_{\mathrm{f}}} \Delta \boldsymbol{u} \right) \boldsymbol{\mathcal{M}} \left[\rho_{\mathrm{sim}}/\rho \right]_{6\times 1} \tag{2.99}$$

where $[\rho_{\mathrm{sim}}/\rho]_{6\times 1}$ is a column vector of the air density ratio value, for appropriate dimensions. Similarly, the scaled aerodynamic trim forces, analogous to Eq. (2.39), are found as

$$\boldsymbol{F}_{\mathrm{aero}_0} = \begin{bmatrix} \bar{X}_{\mathrm{aero}_0} \\ \bar{Y}_{\mathrm{aero}_0} \\ \bar{Z}_{\mathrm{aero}_0} \end{bmatrix} m \left(\rho_{\mathrm{sim}}/\rho \right) \tag{2.100}$$

The extent to which the air density scaling may be satisfactorily applied is dependent on the aircraft application. In the case of the CJ1 stitched model, it was determined that air density-ratio scaling may be accurately applied within approximately ±10,000 ft of an anchor altitude, therefore trim data and point models were included at two altitudes to accurately cover the entire altitude envelope (see Section 3.6.4). Furthermore, certain derivatives do not scale directly with altitude, and therefore must be taken into consideration. For example, control derivatives of non-aerodynamic control surfaces, such as the dimensional thrust derivative $X_{\delta_{\mathrm{t}}}$, do not scale directly with air density, and therefore must be omitted from the density-ratio scaling of Eq. (2.99). See Section 3.6.4 for verification results of the simulation of alternate altitudes in the CJ1 stitched model using air density scaling.

For rotorcraft applications, most dimensional derivatives do not scale uniformly with air density, so air density-ratio scaling is not used. Instead, trim data and identified models are needed for two altitudes to capture key trends, and linear interpolation of the trim data and dimensional stability and control derivatives is employed to accurately simulate alternate altitudes. See Section 4.6.4 for verification results of the simulation of alternate altitudes in the UH-60 stitched model using linear interpolation.

26

2.7 Implementing High-Order Models

Up to this point we have concentrated on a 6-DOF representation of the bare-airframe dynamics. However, the model stitching architecture is capable of accurately simulating high-order dynamic models. Applicable high-order models may be, but are not limited to, those which represent quasi-steady fixed-wing aircraft dynamics augmented with higher-order structural states, or those of a multi-body rotorcraft simulation. An example of the former is the hybrid flexible model structure described in Ref. [1], in which aeroelastic dynamics from a flexible structure are combined with the dynamics of the rigid body. An example of the latter is the fully-coupled, multi-body model of the UH-60 Black Hawk helicopter presented in Chapter 4.

Regardless of the form of the high-order model, the higher-order states are considered to be those beyond the fuselage and Euler angle states. These higher-order states may include rotor states, downwash/fuselage-interaction states, engine states, or structural flexibility states, for example. Given a high-order state-space model with n_{H} higher-order states $\begin{bmatrix} x_1 & \dots & x_{n_{\mathrm{H}}} \end{bmatrix}$ and n_{c} controls $\begin{bmatrix} u_1 & \dots & u_{n_{\mathrm{c}}} \end{bmatrix}$, the full-state $\boldsymbol{A}$ and $\boldsymbol{B}$ matrices are automatically partitioned into sub-matrices as indicated in the following:

$$
\begin{bmatrix} \dot{u} \\ \dot{v} \\ \dot{w} \\ \dot{p} \\ \dot{q} \\ \dot{r} \\ \hline \dot{x}_1 \\ \vdots \\ \dot{x}_{n_{\mathrm{H}}} \end{bmatrix} = \left[\begin{array}{c|c} \boldsymbol{A}_{66} & \boldsymbol{A}_{6\mathrm{H}} \\ \hline \boldsymbol{A}_{\mathrm{H}6} & \boldsymbol{A}_{\mathrm{HH}} \end{array} \right] \begin{bmatrix} u \\ v \\ w \\ p \\ q \\ r \\ \hline x_1 \\ \vdots \\ x_{n_{\mathrm{H}}} \end{bmatrix} + \left[\begin{array}{c} \boldsymbol{B}_{6\mathrm{C}} \\ \hline \boldsymbol{B}_{\mathrm{HC}} \end{array} \right] \begin{bmatrix} u_1 \\ \vdots \\ u_{n_{\mathrm{c}}} \end{bmatrix} \tag{2.101}
$$

Descriptions of the individual sub-matrices are provided in Table 2.2.

Table 2.2: High-order models – matrix partitioning

Matrix	Description	# rows	# cols
$\boldsymbol{A}_{66}$	rigid-body/fuselage stability derivatives	6	6
$\boldsymbol{A}_{6\mathrm{H}}$	higher-order to rigid-body/fuselage stability derivatives	6	n_{H}
$\boldsymbol{A}_{\mathrm{H}6}$	rigid-body/fuselage to higher-order stability derivatives	n_{H}	6
$\boldsymbol{A}_{\mathrm{HH}}$	higher-order stability derivatives	n_{H}	n_{H}
$\boldsymbol{B}_{6\mathrm{C}}$	rigid-body/fuselage control derivatives	6	n_{c}
$\boldsymbol{B}_{\mathrm{HC}}$	higher-order control derivatives	n_{H}	n_{c}

Analogous to Eqs. (2.22) and (2.23), the 6-DOF state perturbation vector, higher-order state perturbation vector, and control perturbation vector are now determined by

$$
\Delta \boldsymbol{x}_6 \equiv \boldsymbol{X}_6 - [\boldsymbol{X}_6]_0 |_U \tag{2.102}
$$

$$
\Delta \boldsymbol{x}_{\mathrm{H}} \equiv \boldsymbol{X}_{\mathrm{H}} - [\boldsymbol{X}_{\mathrm{H}}]_0 |_U \tag{2.103}
$$

$$
\Delta \boldsymbol{u} \equiv \boldsymbol{U} - \boldsymbol{U}_0 |_U \tag{2.104}
$$

where $\boldsymbol{X}_6$ is the vector of rigid-body/fuselage states [Eq. (2.26)], $\boldsymbol{X}_{\mathrm{H}}$ is the vector of higher-order states, and $\boldsymbol{U}$ is the vector of controls. This implementation is robust in that it will accurately calculate the aerodynamic dimensional perturbation forces and moments for either a multi-body or augmented quasi-steady high-order model. Likewise, analogous to the aerodynamic perturbation forces and moments for the 6-DOF representation given by Eq. (2.35), the complete aerodynamic dimensional perturbation forces and moments for the high-order system are found as

$$
\begin{bmatrix} \Delta \boldsymbol{F}_{\mathrm{aero}} \\ \Delta \boldsymbol{M}_{\mathrm{aero}} \end{bmatrix}_{6 \times 1} = \boldsymbol{\mathcal{M}} \boldsymbol{A}_{\mathrm{aero}} |_{U_{\mathrm{f}}} \Delta \boldsymbol{x} + \boldsymbol{\mathcal{M}} \boldsymbol{B}_{\mathrm{aero}} |_{U_{\mathrm{f}}} \Delta \boldsymbol{u}
$$

$$
= \boldsymbol{\mathcal{M}} \left(\boldsymbol{A}_{66} |_{U_{\mathrm{f}}} \Delta \boldsymbol{x}_6 + \boldsymbol{A}_{6\mathrm{H}} |_{U_{\mathrm{f}}} \Delta \boldsymbol{x}_{\mathrm{H}} + \boldsymbol{B}_{6\mathrm{C}} |_{U_{\mathrm{f}}} \Delta \boldsymbol{u} \right) \tag{2.105}
$$

The higher-order state-dot vector is finally given by

$$\begin{bmatrix} \dot{x_1} \\ \vdots \\ \dot{x_{n_\mathrm{H}}} \end{bmatrix} = \boldsymbol{A}_{\mathrm{H6}}|_{U_\mathrm{f}}\Delta\boldsymbol{x}_6 + \boldsymbol{A}_{\mathrm{HH}}|_{U_\mathrm{f}}\Delta\boldsymbol{x}_\mathrm{H} + \boldsymbol{B}_{\mathrm{HC}}|_{U_\mathrm{f}}\Delta\boldsymbol{u} \tag{2.106}$$

and is time integrated simultaneously with the fuselage state-dot vector [Eq. (2.65)] to obtain the current vector of higher-order states.

2.8 Stitching in Multiple Dimensions

Model stitching can be applied in more than one dimension simultaneously. For instance, a more accurate rotorcraft model for hover, low-speed, and quartering flight is obtained from "stitching in U and V," as demonstrated for the UH-60 stitched model in Chapter 4. In this implementation, all *trim data* are tabulated as a two-dimensional lookup table and subsequently interpolated in both x-body airspeed U and y-body airspeed V, as denoted by $|_{U,V}$. All *stability and control derivatives*, however, continue to be tabulated and interpolated *solely as a function of x-body airspeed U* as before (Section 2.2). That is,

$$\left(V_0|_{U,V},\ W_0|_{U,V},\ \Phi_0|_{U,V},\ \Theta_0|_{U,V},\ \delta_{\mathrm{lat}_0}|_{U,V},\ \delta_{\mathrm{lon}_0}|_{U,V},\ \delta_{\mathrm{col}_0}|_{U,V},\ \delta_{\mathrm{ped}_0}|_{U,V}\right) = f(U,V) \tag{2.107}$$

$$\left(\boldsymbol{A}|_U,\ \boldsymbol{B}|_U,\ \boldsymbol{C}|_U,\ \boldsymbol{D}|_U\right) = f(U) \tag{2.108}$$

Stitching in both U and V is advantageous for rotorcraft applications to enable continuous, high-fidelity simulation at and around hover, including sideward, rearward, and quartering flight, as well as the simulation of hovering flight in the presence of winds.

The state and control perturbations are then based on the deviation of instantaneous values of the states and controls from the two-dimensional lookup-table values of the trim states and controls:

$$\Delta\boldsymbol{x} = \boldsymbol{X} - \boldsymbol{X}_0|_{U,V} \tag{2.109}$$

$$\Delta\boldsymbol{u} = \boldsymbol{U} - \boldsymbol{U}_0|_{U,V} \tag{2.110}$$

analogous to Eqs. (2.22) and (2.23). Likewise, analogous to Eqs. (2.36)–(2.38), the specific aerodynamic trim forces are obtained by looking-up the trim Euler angles as a function of U and V:

$$\bar{X}_{\mathrm{aero}_0} = g\sin\Theta_0|_{U,V} \tag{2.111}$$

$$\bar{Y}_{\mathrm{aero}_0} = -g\cos\Theta_0|_{U,V}\sin\Phi_0|_{U,V} \tag{2.112}$$

$$\bar{Z}_{\mathrm{aero}_0} = -g\cos\Theta_0|_{U,V}\cos\Phi_0|_{U,V} \tag{2.113}$$

It is important to note that stitching in a particular body-axis airspeed results in the implicit representation of the corresponding speed derivatives (see Section 2.2); e.g., stitching in y-body axis airspeed V results in the implicit representation of the v-speed derivatives, such as Y_v and L_v, as based on the gradients of the trim states and controls, which is analogous to the implicit representation of the u-speed derivatives when stitching in x-body axis airspeed U. See Section 4.3 for a discussion of "stitching in U and V" as applied to the UH-60 stitched model example, including verification of the implicit u- and v-speed derivatives.

2.9 Data Formatting and Processing

This section covers guidelines and formatting requirements for data used in the stitched model. The model stitching simulation architecture utilizes an N-D linear interpolation scheme, which allows real-time data interpolation/extrapolation over multiple axes (e.g., airspeed, altitude, loading configuration, etc.). This N-D linear interpolation scheme is formulated in MATLAB® and utilizes the MATLAB function `bitget` [12] to perform bit-wise (i.e., binary) interpolation of tabulated data over each axis. The interpolation scheme is formulated in this manner to run in real time as an embedded MATLAB function block within Simulink®. As such, a standardized data storage format is necessary.

2.9.1 Full Rectangular Grid

The model stitching simulation architecture requires data to be formatted as a full rectangular grid, which is a grid constructed from defined axis values for each interpolation dimension. The axes values do not need to be evenly spaced (i.e., the grid may be non-uniform), but values must be consistent if multiple interpolation dimensions are to be used. Because the grid must be full (a value must be specified for each element), data processing, including spline fitting and data manipulation, may be required to align data to the grid.

To demonstrate the characteristics of the full rectangular grid, the following two examples will be covered: 1) several airspeeds, one altitude (1-D), and 2) several airspeeds, two altitudes (2-D). See Section 3.3 for an additional demonstration of this process as applied to the CJ1 fixed-wing aircraft stitched model.

Single-Altitude Example

To illustrate the definition of axis values for a single altitude, Figure 2.17 shows example points at which flight-test trim data were collected over a range of airspeed. For "stitching in U," the data are stored in the grid as a function of x-body airspeed U. Note that the data are not at evenly-spaced airspeed values; this is not a requirement and is typical of real-life flight-test collection of trim data.
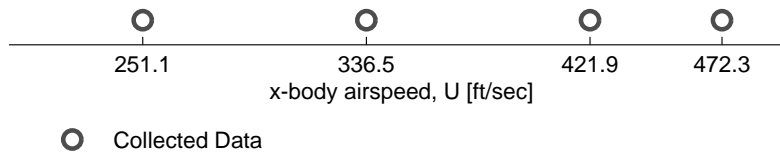
Figure 2.17: Example collected data points – single altitude.

The x-axis values are simply:

$$x = \begin{bmatrix} 251.1 & 336.5 & 421.9 & 472.3 \end{bmatrix} \text{ ft/sec} \tag{2.114}$$

Two-Altitude Example

Elaborating on the single-altitude example, suppose flight-test trim data were collected at two altitudes. In this example case, the data points presented in the single-altitude example are assigned to an altitude of 5000 ft, and suppose there were three additional points collected at a second altitude of 15,000 ft. These data points are shown in Figure 2.18. The three higher-altitude points were collected at unique airspeeds that do not correspond to those of the lower altitude. The data are required to be stored in a single rectangular grid, however, so the data must be *aligned* (i.e., interpolated/extrapolated) to a grid.

Figure 2.18: Example collected data points – two altitudes.

When defining a grid, the following should be taken into consideration: 1) the grid points should coincide closely with those of the collected data, and 2) the grid should cover the entire airspeed/altitude envelope of applicability for simulation. With this in mind, we will choose the x-axis values to be those of the 5000-ft data plus the high-speed point of the 15,000-ft data (506.6 ft/sec), and the y-axis values are simply the two altitudes. Thus the example rectangular grid is defined by

$$x = \begin{bmatrix} 251.1 & 336.5 & 421.9 & 472.3 & 506.6 \end{bmatrix} \text{ ft/sec} \tag{2.115}$$

$$y = \begin{bmatrix} 5000 & 15000 \end{bmatrix} \text{ ft} \tag{2.116}$$

It is therefore necessary to manipulate the data as follows: 1) the 5000-ft data must be extrapolated to create a high-speed point at 506.6 ft/sec; 2) likewise, the 15,000-ft data must be extrapolated to create a low-speed point at 251.1 ft/sec; and 3) the mid-speed points of the 15,000-ft data must be interpolated to align to the grid. This process is shown graphically in Figure 2.19.
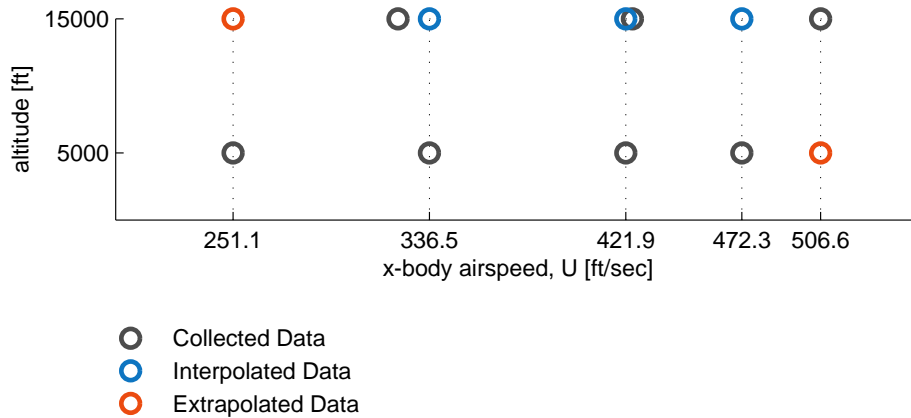
Figure 2.19: Example interpolated/extrapolated data points.

The end result is data points which are aligned to the full rectangular grid (i.e., grid data) defined by Eqs. (2.115) and (2.116). This is shown graphically in Figure 2.20. Two-dimensional linear interpolation of all grid data is then performed in real time during simulation of the stitched model.
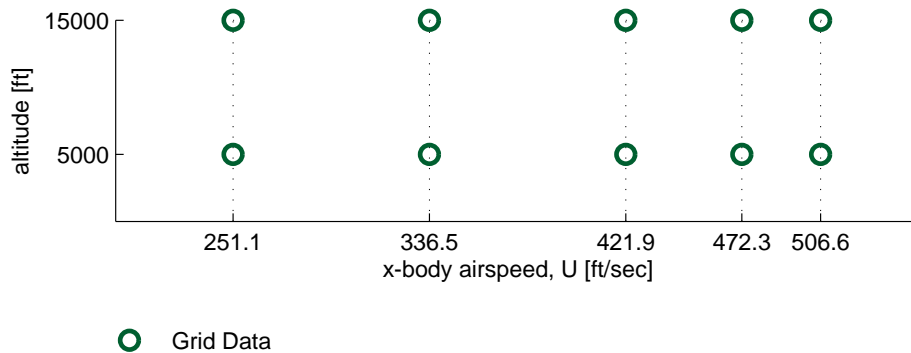
Figure 2.20: Example data points aligned to full rectangular grid.

2.9.2 Spline Fitting

Although linear interpolation is performed on the data at a binary level, piecewise cubic spline interpolation may be used in data processing to interpolate the collected data to a finely-spaced full rectangular grid. Spline fitting enables the efficient capture of subtle inflections in the data, and permits satisfactory extrapolation

beyond the range of collected data. This process of fitting data with splines is applied to the fixed-wing aircraft stitched model of Chapter 3 to populate a full flight-envelope airspeed/altitude grid (see Section 3.3), and is applied to the rotorcraft stitched model of Chapter 4 to generate a fine two-dimensional x- and y-body airspeed grid for "stitching in U and V" in the hover/low-speed regime (see Section 4.5). Specific interpolation schemes, such as shape-preserving piecewise cubic spline interpolation (e.g., MATLAB function `interp1` with method 'pchip' [12]), may be used based on the characteristics of the data to be fit.

2.10   Chapter Summary

This chapter presented the theory and concepts of the model stitching technique and its implementation into a comprehensive model stitching simulation architecture. A detailed walkthrough of the model stitching architecture key simulation elements was provided. Additional elements, such as atmospheric disturbances and user-specified external forces and moments, were discussed. A thorough discussion on extrapolation methods for the simulation of off-nominal aircraft loading configurations, including variations in weight, inertia, and CG location, was presented. A method for extrapolating fixed-wing aircraft stitched models to alternate altitudes using air density-ratio scaling was discussed. Formalities of using high-order linear models and stitching in multiple dimensions were provided. Requirements and guidelines for the formatting and processing of data for use in the model stitching architecture were covered.

3 Fixed-Wing Aircraft Stitched Model: Cessna CJ1

A state-of-the-art stitched simulation model of a light business jet, representative of the Cessna Citation CJ1 (Model 525), was developed using the model stitching simulation architecture, as presented in Section 2.3, and discrete-point linear models derived from DARcorporation's Advanced Aircraft Analysis [16] (AAA) software. AAA was configured using the Cessna 525 model included with the software to generate nondimensional stability and control derivatives in stability axes, along with corresponding trim data, for a collection of discrete flight conditions. Post-processing was performed on the AAA data to convert the output nondimensional derivatives into dimensional, body-axes derivatives for the formulation of state-space point models. Additional modeling features, including flap effects and a simple engine model, were integrated into the CJ1 stitched model for added fidelity in full-mission piloted simulation.

Verification results of the off-nominal extrapolation methods covered in Section 2.5 are presented comparing outputs of the stitched model to values from point models for off-nominal loading configurations. The fixed-wing aircraft altitude extrapolation method discussed in Section 2.6 is verified for a range of altitudes. Two check cases are provided to verify overall simulation fidelity at two discrete flight conditions and configurations. Check case results include comparisons of frequency responses, mode natural frequency and damping, and time-history responses. Lessons learned and implications are considered to provide guidance on future flight testing for the development of stitched models involving fixed-wing aircraft.

3.1 Aircraft Model Description

The fixed-wing aircraft results herein were generated using AAA configured for a light business jet representative of the Cessna Citation CJ1 (Model 525), shown in Figure 3.1. The general characteristics and performance are as follows:

- Crew: 1–2
- Capacity: 6–7 passengers
- Length: 42 ft 7 in
- Wingspan: 46 ft 11 in
- Empty weight: 6,765 lb
- Max. takeoff weight: 10,700 lb
- Powerplant: 2 × Williams FJ44 turbofan, 1,900 lb thrust each
- Max. cruise speed: 389 kn
- Stall speed: 83 kn
- Range: 1,300 nm
- Service ceiling: 41,000 ft
- Rate of climb: 3,290 ft/min

3.2 State-Space Point Models

3.2.1 Overview of AAA Software

Advanced Aircraft Analysis (AAA) [16] is an aircraft design and stability/control analysis software tool produced by DARcorporation. AAA employs design methodology from classical textbooks, digital DATCOM, and wind tunnel test data to calculate the aerodynamics of the configured aircraft model at user-specified flight conditions. AAA was configured using the Cessna 525 model included with the software to obtain the results presented herein.

The AAA CJ1 model is accurate over most of the relevant flight envelope, but does not include certain nonlinearities, such as stall, departure, and aerobatic dynamics. These edge-of-the-envelope conditions are

Figure 3.1: Cessna Citation CJ1 (Model 525).

considered for this application to be outside the flight envelope of interest for this study. Additionally, the AAA model does not include structural flexibility effects.

3.2.2 State Space Formulation

The model stitching simulation architecture discussed in Chapter 2 is designed to accommodate both fixed-wing aircraft and rotorcraft, and requires the state-space point models to be formulated using dimensional stability and control derivatives in *body axes* (see Section 2.2). AAA generates nondimensional derivatives in stability axes, so transformations were necessary. Using methods and equations covered in Stevens and Lewis [13] and McRuer et al. [11], the nondimensional, stability-axes stability and control derivatives from AAA were transformed into dimensional, body-axes stability and control derivatives. A simple schematic is provided in Figure 3.2 which shows the transformation from AAA output to formulated state-space matrices. See Appendix A for details on the calculation of dimensional derivatives and the transformation from stability axes to body axes. See also Section A.2.2 for the dimensional thrust control derivative equations.
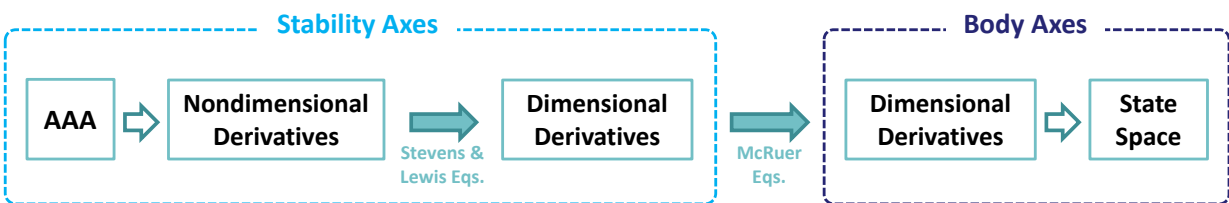
Figure 3.2: Transformation of stability and control derivatives from stability axes to body axes.

The complete 6-DOF state space formulation for the AAA CJ1 point models is given in body axes as [11]:

$$
\begin{bmatrix}
1 & 0 & -X_{\dot{w}} & 0 & 0 & 0 & 0 & 0 \\
0 & 1 & 0 & 0 & 0 & 0 & 0 & 0 \\
0 & 0 & 1-Z_{\dot{w}} & 0 & 0 & 0 & 0 & 0 \\
0 & 0 & 0 & 1 & 0 & 0 & 0 & 0 \\
0 & 0 & -M_{\dot{w}} & 0 & 1 & 0 & 0 & 0 \\
0 & 0 & 0 & 0 & 0 & 1 & 0 & 0 \\
0 & 0 & 0 & 0 & 0 & 0 & 1 & 0 \\
0 & 0 & 0 & 0 & 0 & 0 & 0 & 1
\end{bmatrix}
\begin{bmatrix}
\dot{u} \\ \dot{v} \\ \dot{w} \\ \dot{p} \\ \dot{q} \\ \dot{r} \\ \dot{\phi} \\ \dot{\theta}
\end{bmatrix}
=
$$

$$
\begin{bmatrix}
X_u & 0 & X_w & 0 & X_q - W_0 & V_0 & 0 & -g\cos\Theta_0 \\
0 & Y_v & 0 & Y_p + W_0 & 0 & Y_r - U_0 & g\cos\Theta_0 & 0 \\
Z_u & 0 & Z_w & -V_0 & Z_q + U_0 & 0 & 0 & -g\sin\Theta_0 \\
0 & L'_v & 0 & L'_p & 0 & L'_r & 0 & 0 \\
M_u & 0 & M_w & 0 & M_q & 0 & 0 & 0 \\
0 & N'_v & 0 & N'_p & 0 & N'_r & 0 & 0 \\
0 & 0 & 0 & 1 & 0 & \tan\Theta_0 & 0 & 0 \\
0 & 0 & 0 & 0 & 1 & 0 & 0 & 0
\end{bmatrix}
\begin{bmatrix}
u \\ v \\ w \\ p \\ q \\ r \\ \phi \\ \theta
\end{bmatrix}
\quad (3.1)
$$

$$
+
\begin{bmatrix}
0 & X_{\delta_e} & 0 & X_{\delta_t} \\
Y_{\delta_a} & 0 & Y_{\delta_r} & 0 \\
0 & Z_{\delta_e} & 0 & Z_{\delta_t} \\
L'_{\delta_a} & 0 & L'_{\delta_r} & 0 \\
0 & M_{\delta_e} & 0 & M_{\delta_t} \\
N'_{\delta_a} & 0 & N'_{\delta_r} & 0 \\
0 & 0 & 0 & 0 \\
0 & 0 & 0 & 0
\end{bmatrix}
\begin{bmatrix}
\delta_a \\ \delta_e \\ \delta_r \\ \delta_t
\end{bmatrix}
$$

which assumes wings-level trim flight. Primed derivatives ($'$), as defined following Ref. [11] and given in Section A.1.3, account for the influence of the cross-product of inertia I_{xz}. In the remainder of the text, the primed notation is implied but is generally dropped for convenience.

$\boldsymbol{A}_{\text{aero}}$ and $\boldsymbol{B}_{\text{aero}}$ matrices are employed in the model stitching architecture that contain only the aerodynamic dimensional stability and control derivatives, as discussed in Section 2.3.2. Eq. (3.1) is first rewritten in conventional $\dot{\boldsymbol{x}} = \boldsymbol{A}\boldsymbol{x} + \boldsymbol{B}\boldsymbol{u}$ form, and the gravity terms (e.g., $g\cos\Theta_0$), Coriolis terms (e.g., $-W_0$), and Euler angle states (ϕ and θ) are removed giving

$$
\boldsymbol{A}_{\text{aero}} =
\begin{bmatrix}
X_u + \frac{Z_u X_{\dot{w}}}{1-Z_{\dot{w}}} & 0 & X_w + \frac{Z_w X_{\dot{w}}}{1-Z_{\dot{w}}} & 0 & X_q + \frac{Z_q X_{\dot{w}}}{1-Z_{\dot{w}}} & 0 \\
0 & Y_v & 0 & Y_p & 0 & Y_r \\
\frac{Z_u}{1-Z_{\dot{w}}} & 0 & \frac{Z_w}{1-Z_{\dot{w}}} & 0 & \frac{Z_q}{1-Z_{\dot{w}}} & 0 \\
0 & L'_v & 0 & L'_p & 0 & L'_r \\
M_u + \frac{Z_u M_{\dot{w}}}{1-Z_{\dot{w}}} & 0 & M_w + \frac{Z_w M_{\dot{w}}}{1-Z_{\dot{w}}} & 0 & M_q + \frac{Z_q M_{\dot{w}}}{1-Z_{\dot{w}}} & 0 \\
0 & N'_v & 0 & N'_p & 0 & N'_r
\end{bmatrix}
\quad (3.2)
$$

$$
\boldsymbol{B}_{\text{aero}} =
\begin{bmatrix}
0 & X_{\delta_e} + \frac{Z_{\delta_e} X_{\dot{w}}}{1-Z_{\dot{w}}} & 0 & X_{\delta_t} + \frac{Z_{\delta_t} X_{\dot{w}}}{1-Z_{\dot{w}}} \\
Y_{\delta_a} & 0 & Y_{\delta_r} & 0 \\
0 & \frac{Z_{\delta_e}}{1-Z_{\dot{w}}} & 0 & \frac{Z_{\delta_t}}{1-Z_{\dot{w}}} \\
L'_{\delta_a} & 0 & L'_{\delta_r} & 0 \\
0 & M_{\delta_e} + \frac{Z_{\delta_e} M_{\dot{w}}}{1-Z_{\dot{w}}} & 0 & M_{\delta_t} + \frac{Z_{\delta_t} M_{\dot{w}}}{1-Z_{\dot{w}}} \\
N'_{\delta_a} & 0 & N'_{\delta_r} & 0
\end{bmatrix}
\quad (3.3)
$$

3.3 Flight Condition Anchor Points

As mentioned in the discussion of model stitching basic concepts in Section 2.2, the key requirement for a full flight-envelope stitched simulation model is a collection of state-space models and trim data of the states and controls for several discrete flight conditions, or "anchor" points, covering a range of airspeed and perhaps altitude. The required quantity and spacing of anchor trim points and anchor point models for a high-fidelity stitched model is largely dictated by vehicle type, applicable flight envelope, and intended simulation purpose. For piloted simulation of a light business jet class of aircraft, as presented herein, which has a broad airspeed/altitude flight envelope, the dynamics must be accurately represented throughout. Of course one could generate a large collection of models to finely cover the entire flight envelope, but this approach is not only impractical for the collection of flight-identified models, in which frequency sweeps must be performed at each flight condition, but is unnecessary considering data processing techniques and the inclusion of extrapolation methods within the model stitching architecture.

Data processing techniques (Section 2.9) include fitting the data with splines to interpolate/extrapolate data with airspeed to allow fewer anchor trim points and point models, and ultimately to construct a full rectangular grid of data points with uniformly-spaced values of x-body airspeed U (for "stitching in U"), per requirements of the model stitching architecture. Air density scaling (Section 2.6) may then be employed in the model stitching architecture to extrapolate data from a particular altitude to a broader range of altitudes. Additionally, incorporated into the model stitching simulation architecture are extrapolation methods for the simulation of off-nominal aircraft loading configurations, including variations in weight, inertia, and center of gravity, without the need for additional data. These extrapolation techniques allow models of a single baseline (nominal) configuration to be used to simulate a wide range of flight conditions and loading configurations throughout.

The CJ1 stitched simulation model presented herein was developed using the above processing techniques, keeping flight-test implications in mind. A demonstration of the complete process is presented below, with example data in Figure 3.3 referenced throughout.

A series of AAA data was first generated covering a range of true airspeed at two altitudes: 10,000 ft and 30,000 ft. The state-space formulation procedure described in Section 3.2.2 was then employed to produce four body-axis dimensional state-space anchor point models at each altitude, indicated by the solid circle markers shown in Figure 3.3(a). Additionally, trim data alone were taken from the remaining AAA data points to incorporate finely-spaced anchor trim points at about every 30 knots (50 ft/sec), as indicated by the empty square markers in Figure 3.3(a). Note that trim data are included with each anchor point model, as well. A depiction of a representative flight envelope for the CJ1 is included with the anchor points to show the broad spacing of anchor point models and more finely-spaced anchor trim points covering the airspeed envelope. Values of the corresponding trim thrust in pounds, δ_t, and directional static-stability derivative N_v (analogous to N_β) are shown in Figure 3.3(d) and (g), respectively.

Next, the trim data and stability and control derivatives from the anchor points are fit with cubic splines and interpolated to fine, evenly-spaced values of airspeed U in 10-ft/sec increments. The resulting full rectangular grid defined by airspeed $U = \begin{bmatrix} 130:10:700 \end{bmatrix}$ ft/sec and altitude $= \begin{bmatrix} 10000 & 30000 \end{bmatrix}$ ft is shown in Figure 3.3(b). Note that some points lie outside the operational flight envelope, but it is a requirement of the model stitching architecture to have the full grid defined. As such, there are data defined for all points in the grid, even if those points would ordinarily not be flown. The spline-fit, interpolated data for thrust and N_v are shown in Figure 3.3(e) and (h), respectively.

Finally, using the grid of data defined in Figure 3.3(b), which consists of the full range of airspeed at two altitudes, the air density-ratio scaling (ρ_{sim}/ρ) method described in Section 2.6 is employed to extrapolate the data to other altitudes, and the stitched model is retrimmed and relinearized. Following the guidance of the flight-test implications of Section 3.9, the identified 10,000-ft data are extrapolated to sea level and 20,000 ft, and the identified 30,000-ft data are extrapolated to 40,000 ft, covering the entire altitude envelope in 10,000-ft increments, as depicted in Figure 3.3(c). The retrimmed values of thrust and relinearized values of N_v are shown in Figure 3.3(f) and (i), respectively. The model stitching architecture was then configured with this full rectangular grid of data and stored in two-dimensional lookup tables to represent the bare-airframe dynamics of the CJ1 stitched simulation model as a function of x-body airspeed U and altitude.
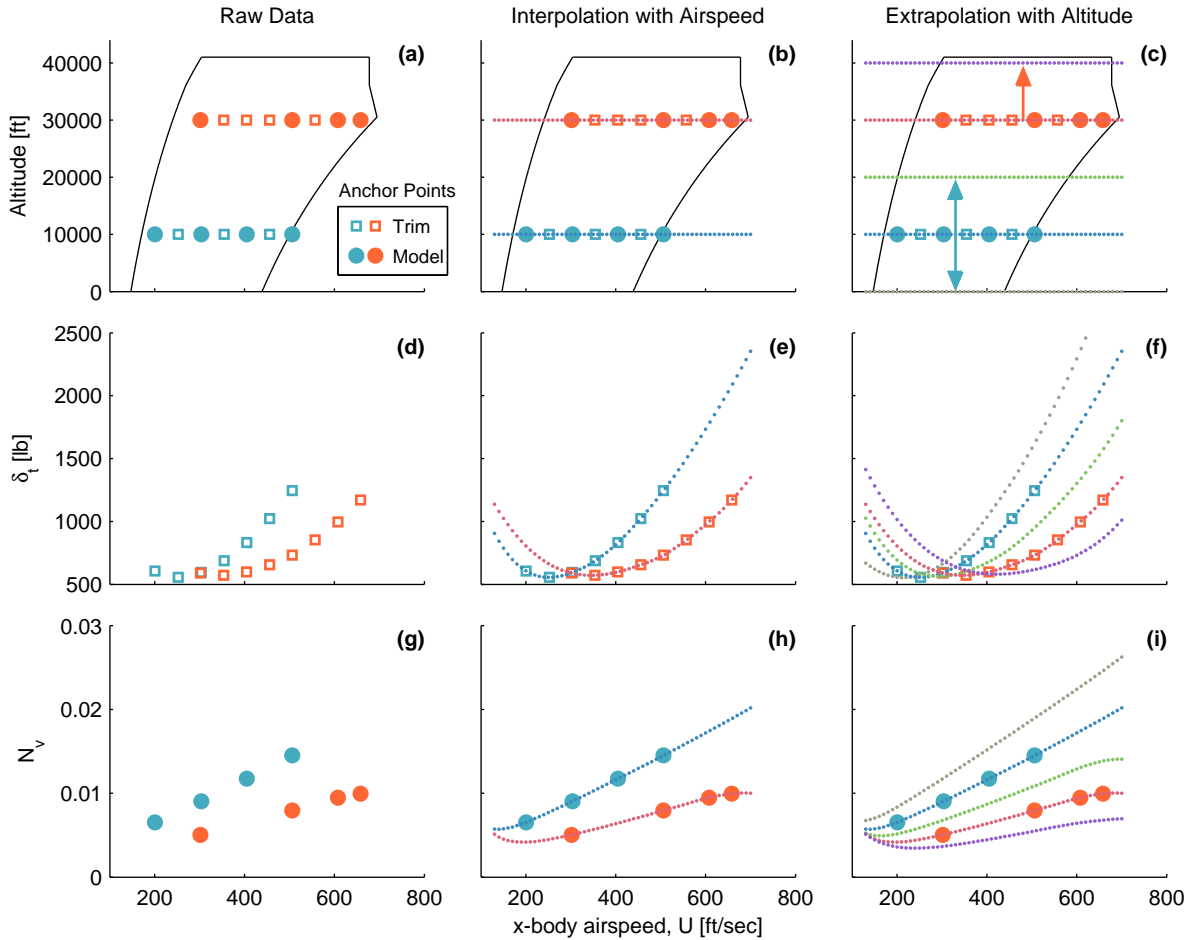
Figure 3.3: Spline-fit data and air density-ratio extrapolation to cover entire flight envelope.

3.4 Additional Features

Additional features specific to a light business jet class of aircraft were incorporated into the CJ1 stitched model. Flap effects, simple engine model with the capability to control thrust output from each aircraft engine separately, and drag from deployed landing gear and spoilers are discussed.

3.4.1 Flap Effects

The aerodynamic effects of flaps on trim and bare-airframe dynamics have been integrated into the CJ1 stitched model. Scaling and corrections of the values of trim attitude, trim controls, and some secondary stability and control derivatives as a function of flap deflection and airspeed were analyzed from AAA truth models configured with two different flap settings. These correction effects were then applied to the baseline point models and stored as an additional interpolation dimension in the lookup tables of derivatives and trim. This additional interpolation dimension allows for continuous simulation of various flap settings throughout the flight envelope for piloted evaluations.

For the flight conditions analyzed using the AAA CJ1 model, flap deflection considerably affects trim pitch attitude, elevator deflection, and thrust, but has only a minor effect on the stability and control derivatives [1]. As a result, an adequate simulation of first-order effects for deployed flaps is achieved by using changes in trim only and retaining the flaps-up stability and control derivatives. Verification of this approach in the CJ1 stitched model for flap deflections of 15 and 35 degrees is provided in Section 3.8.

3.4.2 Simple Engine Model

A simple engine model has been incorporated into the CJ1 stitched model, which takes input in throttle position and converts it to engine thrust in pounds, δ_t. Throttle position (with a range of 0–1) is first scaled by the maximum available engine thrust to convert to commanded thrust, $\delta_{t_{cmd}}$. Maximum and idle thrust values are looked-up as functions of altitude and Mach. Finally, the engine response dynamics are modeled by a second-order transfer function with a natural frequency of 3 rad/sec and a damping ratio of 1:

$$\frac{\delta_t}{\delta_{t_{cmd}}} = \frac{\omega_n^2}{s^2 + 2\zeta\omega_n s + \omega_n^2} = \frac{9}{s^2 + 6s + 9} \tag{3.4}$$

Included in the engine model is the ability to control the thrust output of each of the two engines separately. Rather than formulating the state-space models with two thrust control derivative (one for each engine), a simple moment arm component is introduced in conjunction with total thrust output and is summed with the total moment calculation (see Section 2.4.2). For piloted simulation, this feature allows the pilot to realistically employ each throttle. Asymmetrical thrust could be utilized to simulate a one-engine-out condition, for example.

3.4.3 Component Drag

Unlike the drag effects due to flaps which are implicitly included (i.e., in X_u) by scheduling trim attitude and controls with flap deflection, the drag effects due to the deployment of landing gear and spoilers are incorporated in the stitched model through an external force. Each drag component is modeled as an equivalent flat-plate drag area and scaled by dynamic pressure and deployment amount (with a continuous range of 0–1) to obtain dimensional drag force in pounds. Total drag of all components is summed and input as an external force vector into the nonlinear equations of motion (see Section 2.4.2).

3.5 Nondimensional Derivatives

The argument can be made that nondimensional stability and control derivatives are relatively constant and remain essentially unchanged over the flight envelope, thus utilizing nondimensional derivatives as opposed to their dimensional counterparts may reduce the required number of point models necessary to formulate a stitched model. Although some nondimensional derivatives are indeed relatively constant as a function of Mach over the flight envelope, there are some key nondimensional derivatives that are significantly affected by Mach affects. Additionally, some nondimensional derivatives do not collapse with Mach, but rather are a function of additional variables including angle of attack and density altitude.

The following demonstration will show that the same number of point models are required if nondimensional derivatives are employed. Figure 3.4 shows values of example nondimensional derivatives from the AAA CJ1 model for the full flight-envelope range of airspeed and altitude plotted versus Mach; y-axes are scaled to approximately ±40% of the mean derivative value. Indeed some nondimensional derivatives do collapse nicely, showing a smooth trend as a function of Mach alone. However, even relatively-constant derivatives such as C_{l_p} and $C_{y_{\delta_r}}$ do not collapse to a single value but vary somewhat over the flight envelope; C_{l_p} and $C_{y_{\delta_r}}$ vary by approximately 15% and 25%, respectively, over the flight envelope.

As mentioned, there are key nondimensional derivatives that are significantly affected by Mach effects. C_{m_α} is shown to be nearly constant up to Mach 0.6, at which point the values change by a modest 10%. The values of $C_{D_{\delta_e}}$, however, begin diverging at Mach 0.5 and result in a 20% change by Mach 0.68.

An extreme result of Mach effect is seen in the "tuck" derivative C_{m_u}, in which the values around Mach 0.6 rapidly change sign and also increase in magnitude by approximately 45–65%, depending on altitude. This sudden change in sign must be captured for accurate simulation through the high-subsonic regime. Additionally, the values of the lateral-directional derivative C_{n_β} are not solely a function of Mach, but also depend on angle of attack and density altitude.

These effects necessitate the inclusion of various point models throughout the flight envelope. Recommended guidelines for the selection of flight-test points are summarized in Section 3.9, which are applicable to both dimensional and nondimensional derivatives.
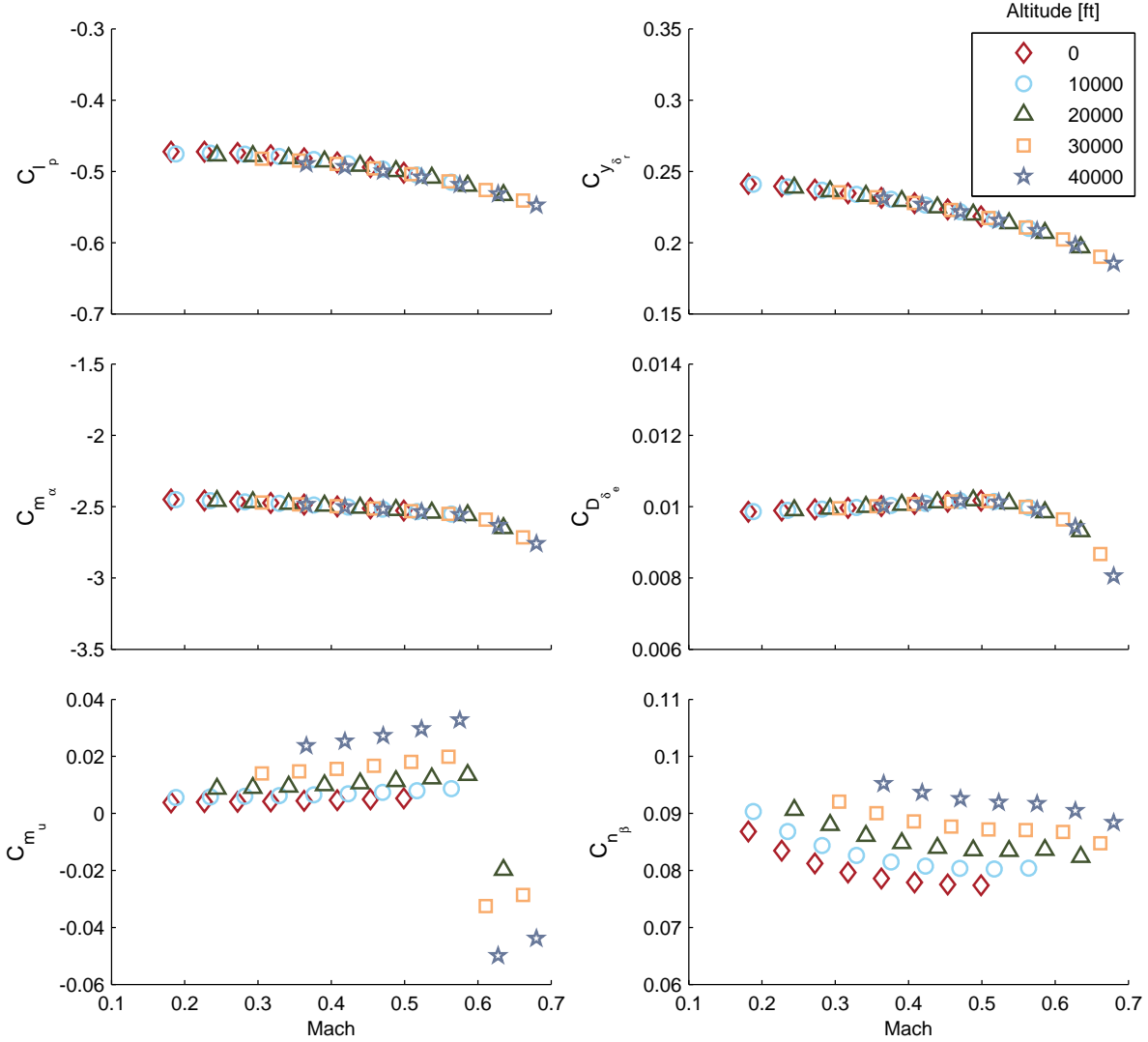
Figure 3.4: Nondimensional derivative values vs. Mach over flight envelope, AAA CJ1 model.

3.6 Verification of Extrapolation Methods

The model stitching architecture incorporates extrapolation methods which allow simulation of off-nominal aircraft loading configurations, as discussed in Section 2.5. In order to verify the extrapolation methods used to simulate off-nominal loading configurations in the CJ1 stitched model, a collection of AAA truth models were generated covering ranges of airspeed, gross weight, inertia, and fuselage-station and waterline CG locations. Additionally, the altitude extrapolation method presented in Section 2.6 is employed and the results are compared to a collection of AAA truth models covering the full flight-envelope altitude range.

A baseline (nominal) configuration of 8500 lb, mid CG was chosen for the AAA anchor point models and anchor trim points used in the stitched model for all results presented in this section. The stitched model, configured only with these baseline anchor points, was then retrimmed (using the MATLAB function `findop` [12]) and relinearized (using the MATLAB function `linearize` [12]) at each off-nominal verification point, with the results verified against the database of AAA truth models.

The results presented in this section verify the accommodation in the model stitching architecture for off-nominal weight and inertia (Section 2.5.1), CG location (Section 2.5.2), and altitude (Section 2.6) as applied to the CJ1 fixed-wing aircraft example. Additional verification results are provided in Appendix B.

3.6.1 Weight

Variations in the simulation value of gross weight were investigated in the CJ1 stitched model. Note that weight was varied independently, with values of inertia held constant.

Figure 3.5 shows results of simulating off-nominal values of weight in the CJ1 stitched mode. The stitched model, configured only with anchor point models and trim data of the nominal 8500-lb configuration (solid symbols), was retrimmed and relinearized for various simulation values of gross weight over a range of airspeed (dashed lines) and compared with values from the AAA truth models (solid lines). Overall, there is excellent agreement between the stitched model and the truth data.

An increase in trim angle of attack is needed with an increase in gross weight, as expected, due to greater lift required to balance the weight. This effect is seen more strongly in the lower-airspeed regime, where a greater change in angle of attack is required to generate the required lift due to lower dynamic pressure. The stitched model tracks the changes in trim angle of attack nearly perfectly, as compared to the truth data. Similarly, the required trim thrust in pounds δ_t increases with an increase in gross weight, but effectively only in the low- to mid-speed regime. The stitched model accurately extrapolates the trim thrust required for the range of off-nominal weights, with some disparity in the simulated 6000- and 9750-lb configurations at the low-speed end of the flight envelope. Pertinent stability derivatives Z_q and Y_v (analogous to Y_β) agree perfectly with values from the AAA truth data.

These results verify the capability to extrapolate to off-nominal values of weight using only point models and trim data of a nominal weight. See Section B.1 for additional off-nominal weight verification results.
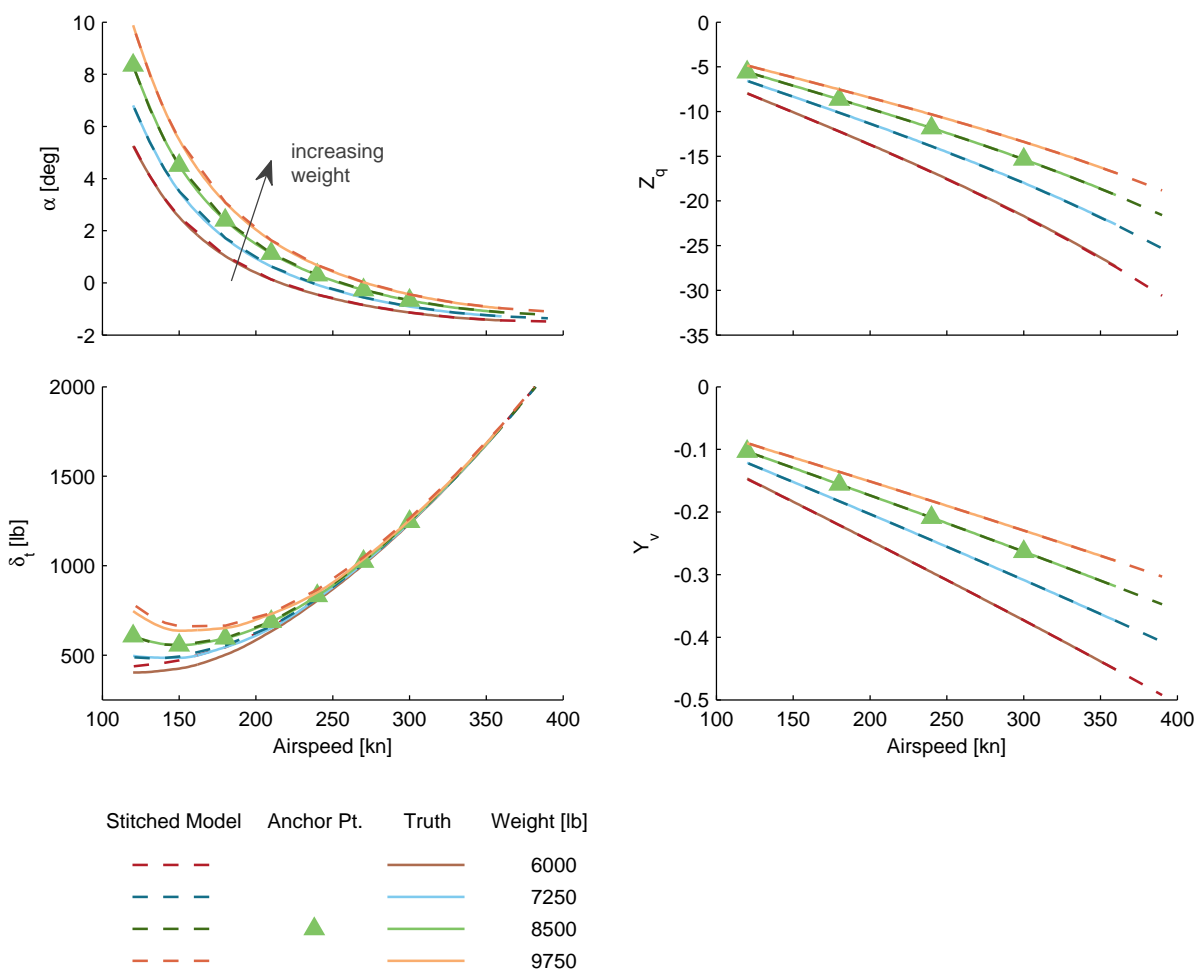
Figure 3.5: Verification of off-nominal weight extrapolation.

3.6.2 Inertia

Variations in the simulation values of the moments of inertia I_{xx}, I_{yy}, and I_{zz} were investigated individually within the CJ1 stitched model. The results are discussed over the succeeding subsections, with an example figure for the roll inertia results only; see Section B.2 for the complete set of off-nominal inertia verification figures. Note that inertia was varied independently of weight for the results presented herein.

Roll Inertia

Results of simulating off-nominal values of roll inertia I_{xx} are shown in Figure 3.6. The stitched model, configured with only anchor point models and trim data of the nominal configuration (solid symbols), was retrimmed and relinearized for various simulation values of roll inertia over a range of airspeed (dashed lines) and compared with values from the AAA truth models (solid lines). There is virtually perfect agreement between the stitched model and the truth data.

Trim angle of attack is unaffected by the change in inertia, as expected, and is in agreement with the truth data. Roll inertia affects the lateral/directional stability and control *moment* derivatives only, most notably L_v, L_p, L_r, L_{δ_a}, L_{δ_r}, N_p, and N_{δ_a}. The values of these key lateral/directional moment derivatives are inversely proportional to values of I_{xx}, as tracked well by the stitched model. In the case of L_{δ_a}, for example, an increase in roll inertia yields a smaller external roll moment for a given aileron input. Lateral stability and control *force* derivatives, such as Y_v, are unaffected by changes in roll inertia. Additionally, trim controls and longitudinal stability and control derivatives are unaffected by changes in roll inertia, as predicted by the stitched model. See Section B.2.1 for additional off-nominal roll inertia verification results.
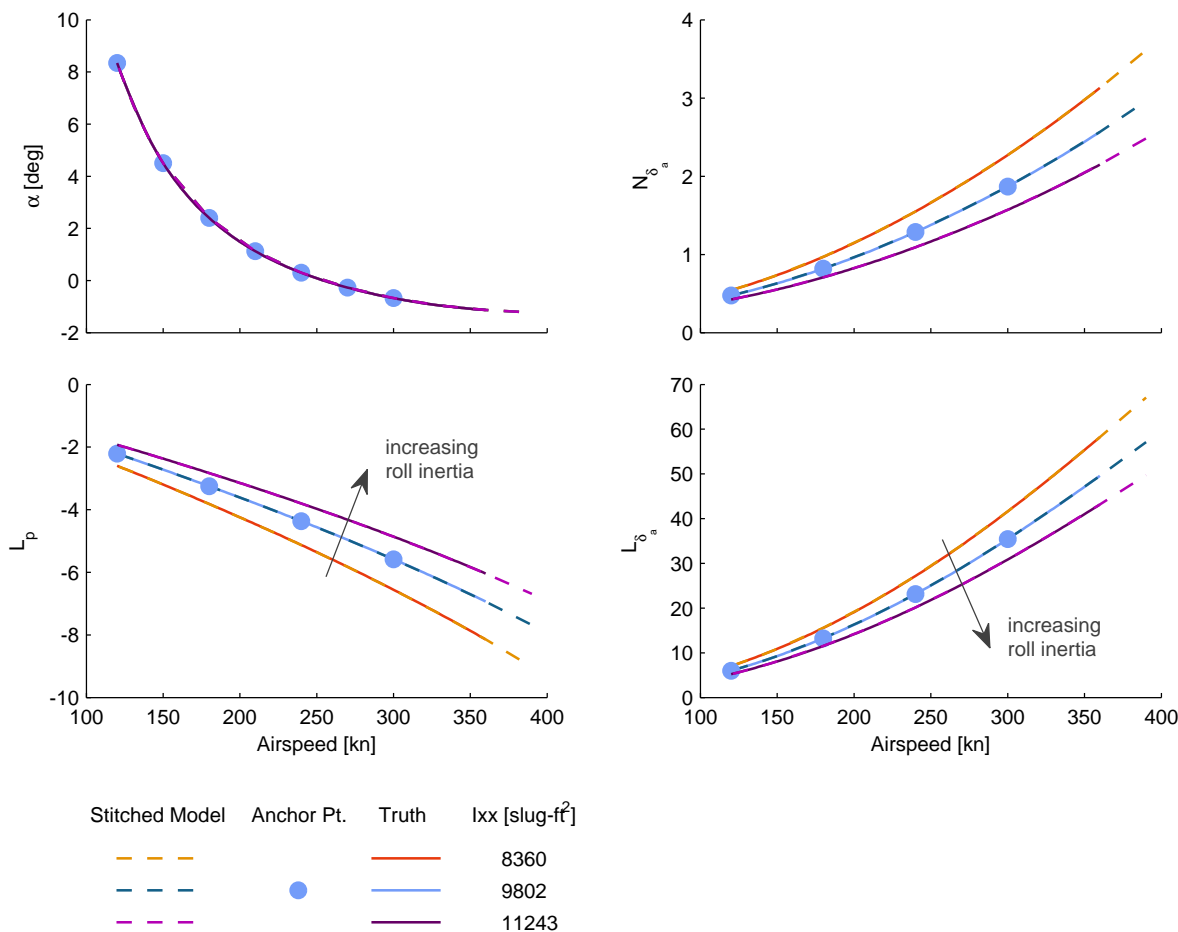
Figure 3.6: Verification of off-nominal inertia extrapolation, roll inertia I_{xx}.

Pitch Inertia

See Section B.2.2 for the off-nominal pitch inertia verification results. In contrast to changes in roll inertia, a change in pitch inertia I_{yy} affects only the *longitudinal* moment derivatives, specifically M_u, M_w, M_q, M_{δ_e}, and M_{δ_t}. The values of the primary pitching moment derivatives are inversely proportional to values of I_{yy}, as captured by the stitched model. With key control derivative M_{δ_e}, for example, an increase in pitch inertia yields a smaller external pitch moment for a given elevator input. An equivalent relation is seen in the values of the pitch damping derivative M_q. Trim attitude and controls and all lateral/directional stability and control derivatives are unaffected by changes in pitch inertia, as expected.

Yaw Inertia

See Section B.2.3 for the off-nominal yaw inertia verification results. A change in yaw inertia I_{zz} has a significant effect only on the lateral/directional moment derivatives, specifically N_v, N_p, N_r, N_{δ_a}, N_{δ_r}, L_r, and L_{δ_r}. The values of these lateral/directional moment derivatives are inversely proportional to values of I_{zz}, as captured well by the stitched model. Trim attitude and controls, and longitudinal stability and control derivatives are unaffected by changes in yaw inertia.

3.6.3   Center of Gravity

Off-nominal simulation values of center of gravity (CG) location were investigated in the CJ1 stitched model. Changes in fuselage-station CG location (x-body axis, positive *aft*) and waterline CG location (z-body axis, positive *up*) were investigated. The results are discussed in the succeeding subsections, with an example figure for the fuselage-station CG results only; see Section B.3 for the complete set of off-nominal CG verification figures.

Station CG

Figure 3.7 shows results of simulating off-nominal values of fuselage-station CG location (x-body axis, positive *aft*) in the CJ1 stitched model. The stitched model, configured only with anchor point models and trim data of the nominal mid-CG (244.3 in, or 22.5% MAC) configuration (solid symbols), was retrimmed and relinearized for simulation values of a forward (240.1 in, or 16.5% MAC) and aft (248.4 in, or 28.5% MAC) fuselage-station CG over a range of airspeed (dashed lines) and compared with values from the AAA truth data (solid lines). Overall the stitched model agrees nearly perfectly with the truth data.

Trim elevator deflection moves downward (positive direction) as the CG moves aft (higher value of station CG) due to decreased download required on the tail, while trim angle of attack remains virtually unchanged as gross weight is held constant. In addition, key stability derivative M_w, which is analogous to M_α, decreases in magnitude, thus indicating decreased static margin, as expected for the aft CG shift. A similar trend is seen in the directional static-stability derivative N_v, which is analogous to N_β.

This verifies the capability to extrapolate to off-nominal values of CG using only point models of a nominal CG. See Section B.3.1 for additional off-nominal fuselage-station CG verification results.

Waterline CG

See Section B.3.2 for the off-nominal waterline CG verification figures. Variations in waterline CG (z-body axis, positive *up*) over the investigated range yield little change in trim attitude and controls; this includes trim elevator, which contrasts the fuselage-station results. Changes in waterline CG location are most evident in the roll dynamics, particularly the L_v, L_r, and L_{δ_r} derivatives. The longitudinal stability and control derivatives are essentially unaffected by vertical CG location, with the exception of M_{δ_t}; the pitching moment due to a change in thrust is affected by the vertical offset distance between the CG and the engines. With an increase in value of waterline CG (up), the vertical offset between the CG and engines decreases, thus M_{δ_t} decreases, as confirmed by the data.
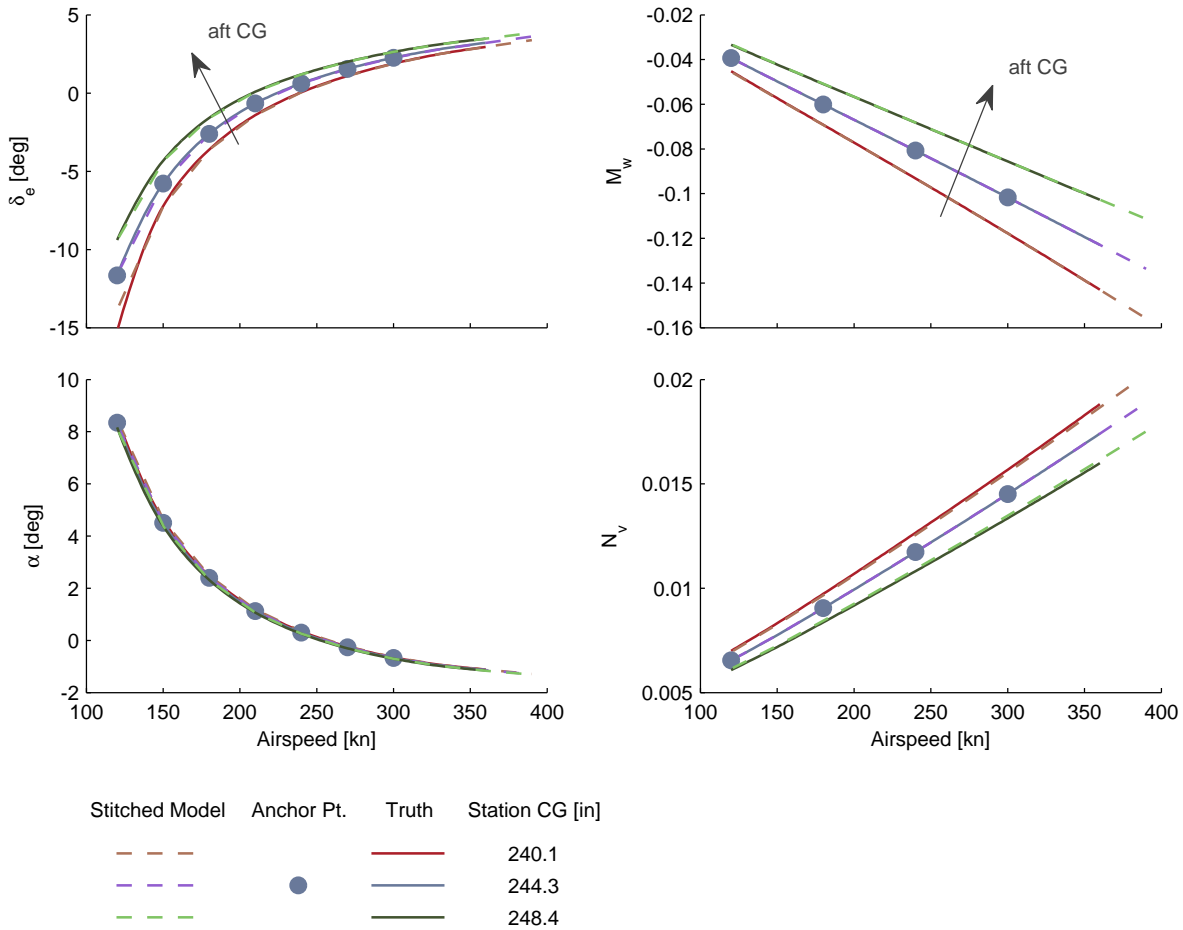
Figure 3.7: Verification of off-nominal CG extrapolation, fuselage station.

3.6.4 Altitude

Simulation of alternate altitudes in the stitched model involves scaling the dimensional stability and control derivatives and specific aerodynamic trim forces by the air density ratio ρ_{sim}/ρ, which is the ratio of air density at the simulation altitude to that at the baseline altitude, and retrimming/relinearizing the stitched model (see Section 2.6). Considering flight-test implications, the strategy implemented in this case of the CJ1 model was to perform the extrapolation based on two sets of anchor point models and trim data; one set of data configured at 10,000 ft, and the second set configured at 30,000 ft. The air density-ratio extrapolation was then performed on each set of data and the results were combined. Specifically, the 10,000-ft data are extrapolated to sea level and 20,000 ft, and the 30,000-ft data are extrapolated to 40,000 ft, covering the entire altitude envelope in 10,000-ft increments. See the discussion of flight-test implications in Section 3.9 for more details on this strategy. An alternate technique would be to linearly interpolate between the known anchor point data to cover the entire altitude range; however, the following demonstration will show the advantage of air density-ratio scaling for the CJ1 model.

Figure 3.8 compares results of the two abovementioned techniques (air density-ratio scaling and linear interpolation) applied to data of two 240-knot point models, one at 10,000 ft and the other at 30,000 ft, to cover the full range of altitude. Several additional 240-kn point models were generated for a range of altitudes, which serve as truth data, and the values of example parameters are plotted versus altitude (square symbols). The data at the two anchor altitudes of 10,000 ft and 30,000 ft (circle symbols) are shown connected with solid lines and extended over the full altitude range, indicating linear interpolation. Conversely, the data at the two anchor altitudes were also retrimmed and relinearized over the full range of altitude using the air

density-ratio scaling technique, as shown by the blue dashed lines for the 10,000-ft data, and by the orange dashed lines for the 30,000-ft data.
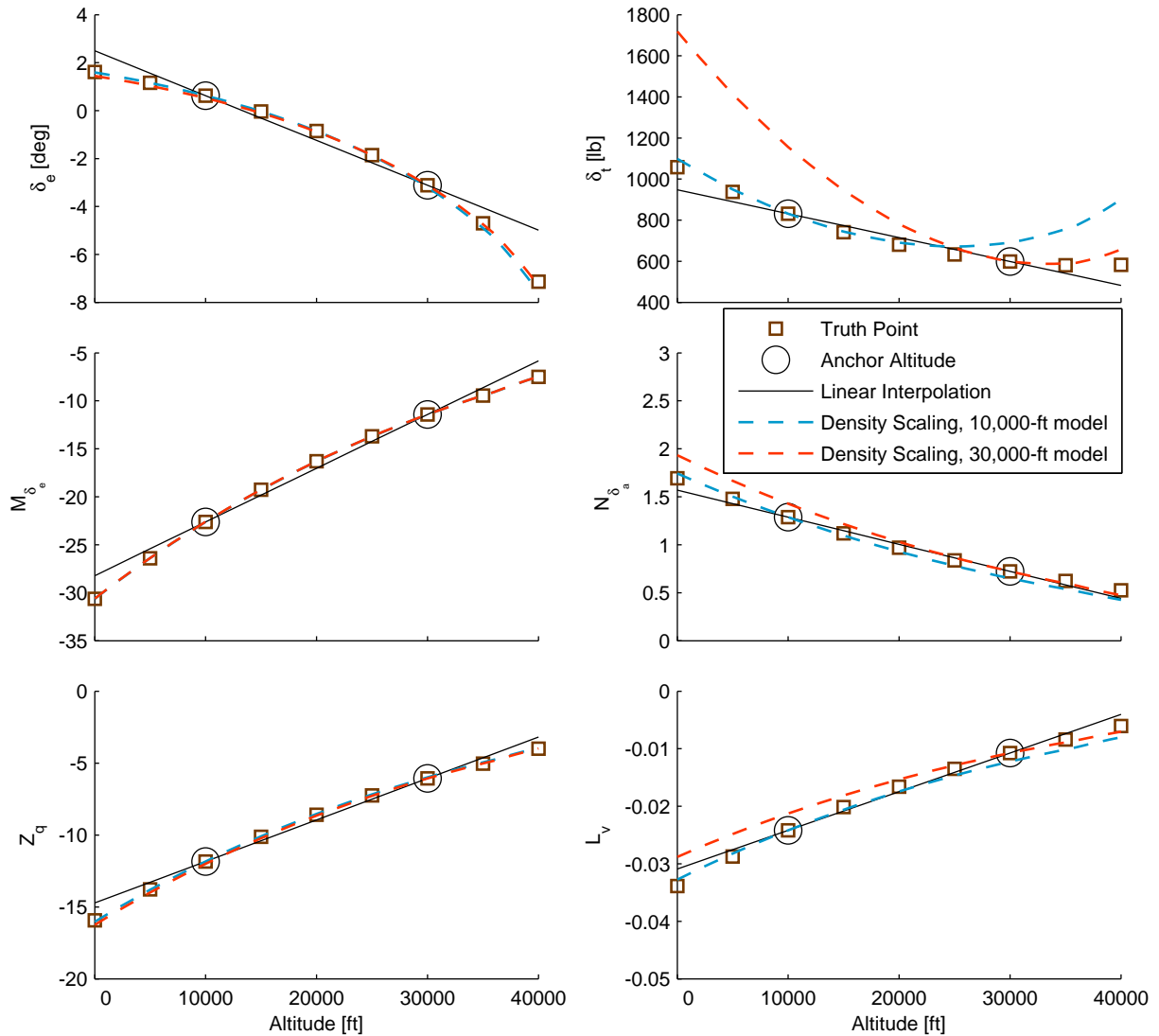
Figure 3.8: Altitude density-ratio scaling vs. linear interpolation, 240-kn point models.

For trim elevator deflection δ_e, control derivative M_{δ_e}, and stability derivative Z_q, the results generated by the density-ratio scaling technique nearly perfectly match the values of the truth points over the entire altitude range. The linear variation resulting from interpolation, however, only somewhat coincides with the truth values for these parameters, with the largest disparities seen at the limits of the altitude range. Furthermore, nearly identical results are seen between the scaled 10,000-ft and 30,000-ft data, suggesting that the density-ratio scaling technique could be applied to point models and trim data from a single altitude to generate accurate data over the full altitude range.

Examining trim thrust δ_t, control derivative N_{δ_a}, and stability derivative L_v, however, there are differences between the 10,000-ft and 30,000-ft density-scaled data. The 10,000-ft scaled data very closely match the truth data from sea level through 20,000 ft, and begin to diverge through the higher altitudes. On the other hand, the 30,000-ft scaled data very closely match the truth data between 30,000 and 40,000 ft, with large disparities seen at the lower altitudes. This result suggests that the extent to which air density-ratio

scaling may be accurately applied to the CJ1 stitched model is within approximately ±10,000 ft of an anchor altitude.

Unlike with δ_e, M_{δ_e}, and Z_q, in which the density-ratio scaling technique may be applied to data from a single altitude to generate accurate data over the full altitude range, trim thrust, N_{δ_a}, and L_v exhibit more complex variations with changes in altitude. To accurately cover the full range of altitude for these parameters, the density-scaled results from the two altitude sets are combined. Specifically, the scaled 10,000-ft data are used from sea level through 20,000 ft, and the scaled 30,000-ft data are used from 30,000 ft to 40,000 ft, accurately representing the data over the entire altitude range in 10,000-ft increments. These data in 10,000-ft altitude increments can subsequently be used to populate the lookup tables in the stitched model, which was the strategy used in the CJ1 stitched model, as discussed in Section 3.3.

Figure 3.9 shows results of a range of simulation flight altitudes in the CJ1 stitched model. The stitched model, configured only with point models and trim data from the two anchor altitudes of 10,000 and 30,000 ft (solid symbols), was retrimmed and relinearized over the full altitude/airspeed flight envelope (dashed lines) using the density-ratio scaling technique and compared with values from the AAA truth models (solid lines). Trim elevator deflection and trim thrust track very well with the AAA truth data. The implicit u-speed derivatives are well preserved over the full flight envelope.

These results verify the accuracy of the air density-ratio scaling technique applied to point models and trim data at two altitudes for fixed-wing aircraft applications. See Section B.4 for the complete set of off-nominal altitude verification results.
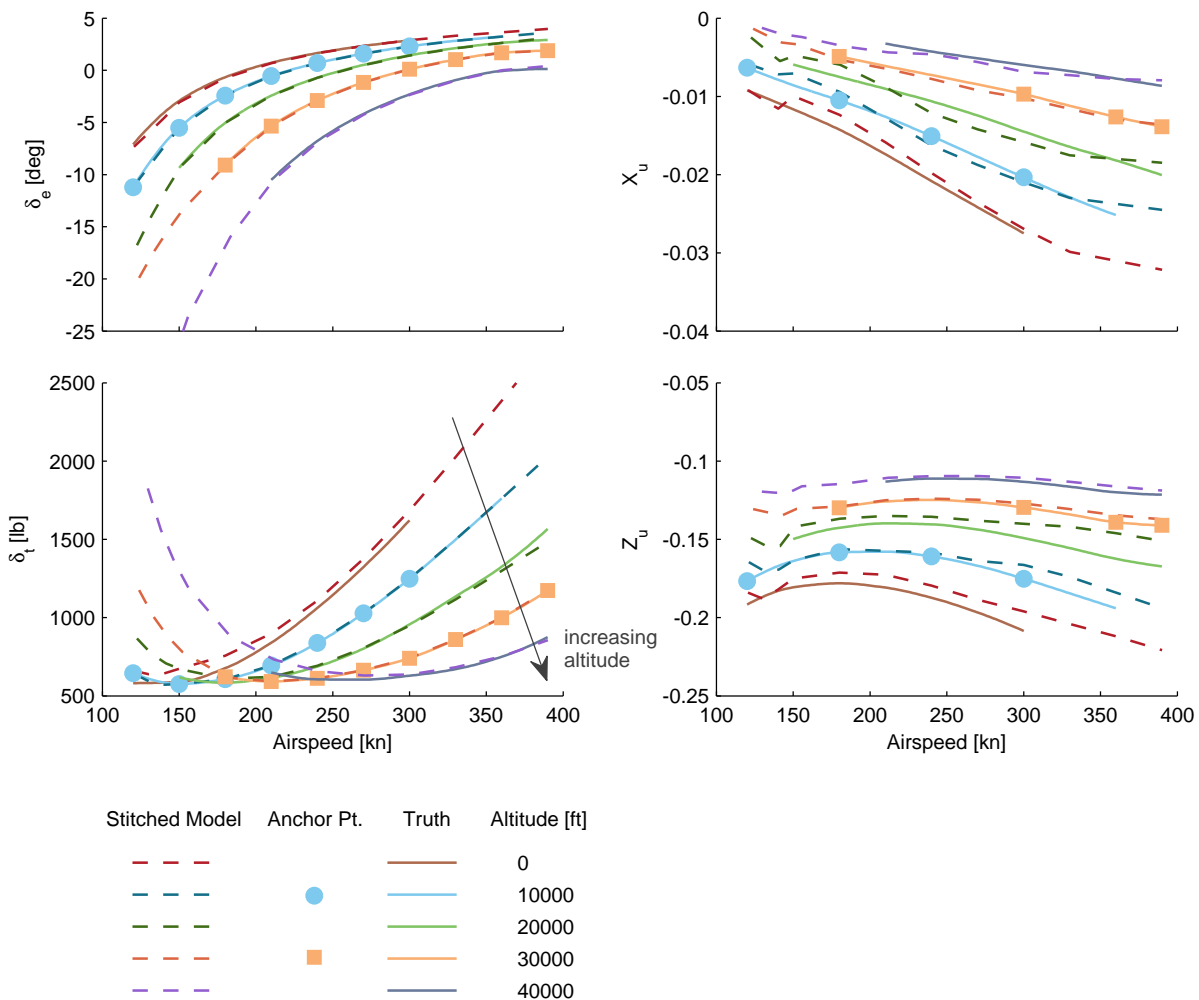
Figure 3.9: Verification of altitude extrapolation.

45

3.7 Dynamic Response Check Cases

Two check cases are presented in this section to verify the dynamic response of the CJ1 stitched model at a particular off-nominal flight condition and configuration as compared to the corresponding truth linear point model from AAA. The stitched model, configured only with anchor points as outlined in Section 3.3, was retrimmed and relinearized at each check case condition. Primary longitudinal and lateral/directional frequency responses, dimensional stability and control derivative values, modes, and time-history verification plots are presented and discussed for each check case.

3.7.1 Case 1: Mach 0.3, 5000 ft, Nominal Loading Configuration

This section presents the primary dynamic responses for check case 1: Mach 0.3 (195 KTAS), 5000 ft altitude, and nominal weight and CG configuration. This flight condition is one that is at an altitude and airspeed that differ from the anchor point models. As such, the stitched model has interpolated between anchor points in airspeed and extrapolated in altitude using air density-ratio scaling (see Section 3.6.4). A summary of the simulation loading configuration values compared to those of the nominal configuration, and the simulation flight condition values compared to the nearest anchor point values are provided in Table 3.1. A summary of the mode natural frequency and damping results is provided in Table 3.2, and a summary of the values of dimensional stability and control derivatives is provided in Table 3.3.

Table 3.1: Simulation loading configuration and flight condition – Case 1

	Parameter	Simulation Value	Nominal/Anchor Value(s)	Off-Nominal
Loading Configuration	Weight [lb]	8500	8500	
	CG [in]	244.3	244.3	
Flight Condition	Airspeed [kn]	195	180, 210	✓
	Altitude [ft]	5000	10000	✓

Figures 3.10–3.13 show the primary longitudinal frequency responses for check case 1. There is near-perfect agreement between the stitched model and the truth AAA point model. The Short Period mode is perfectly captured by the stitched model, and the Phugoid mode is very closely represented (a close match in natural frequency but a damping of $\zeta = 0.049$ as compared to $\zeta = 0.052$ for the point model, as shown in Table 3.2). The Phugoid mode can be approximated as $2\,(\zeta\omega_n)_{\mathrm{P}} = -X_u$ from Ref. [11], indicating that Phugoid natural frequency and damping are proportional to the value of X_u. With essentially equal values of Phugoid natural frequency between the stitched model and the truth point model, this slight disparity of approximately 6% in Phugoid damping can be attributed to the 6% disparity in values of X_u between the implicit representation of the stitched model compared to that of the point model, as shown in Table 3.3.
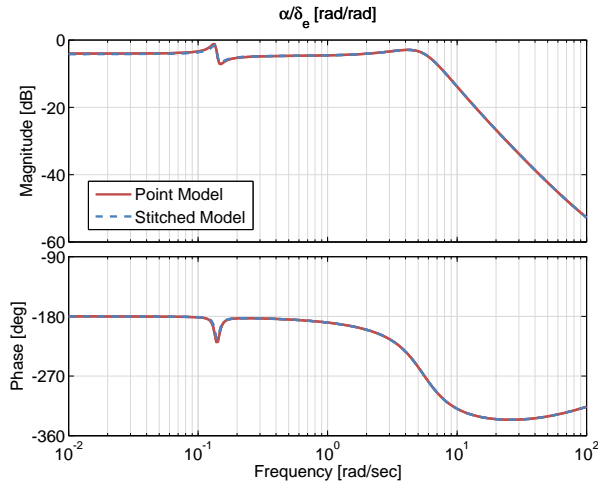
Figure 3.10: Case 1: angle of attack response to elevator input comparison.
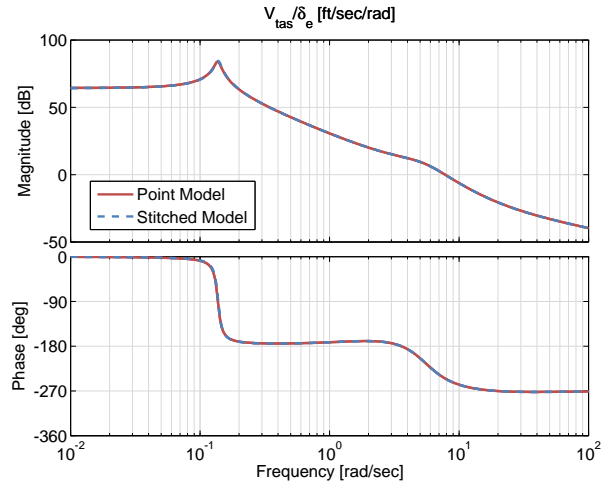
Figure 3.11: Case 1: true airspeed response to elevator input comparison.
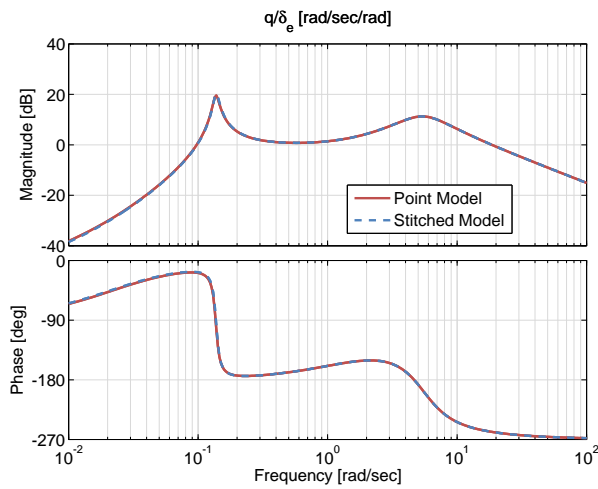
Figure 3.12: Case 1: pitch rate response to elevator input comparison.
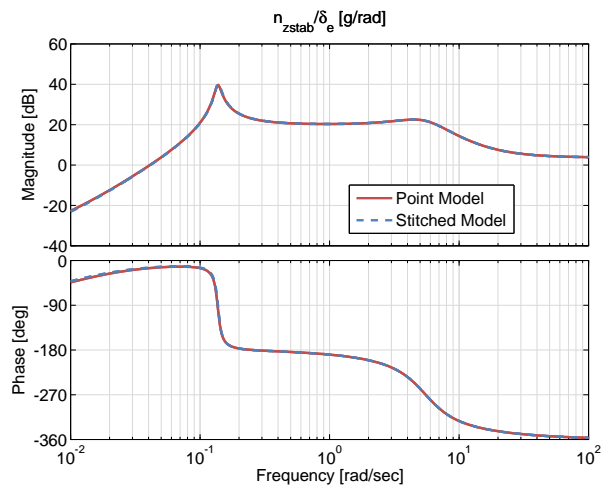
Figure 3.13: Case 1: normal acceleration response to elevator input comparison.

Figures 3.14–3.17 show the primary lateral/directional frequency response comparisons for check case 1. There is near-perfect agreement in dynamic responses between the stitched model and the truth AAA point model, as confirmed by the near-perfect agreement of all lateral/directional modes and derivatives.
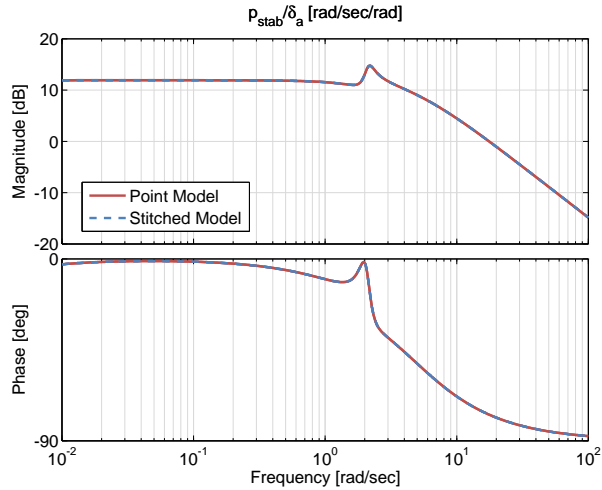
Figure 3.14: Case 1: roll rate response to aileron input comparison.
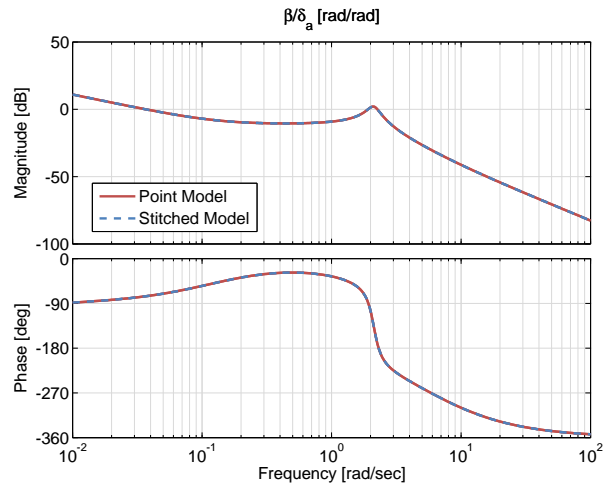
Figure 3.15: Case 1: sideslip response to aileron input comparison.
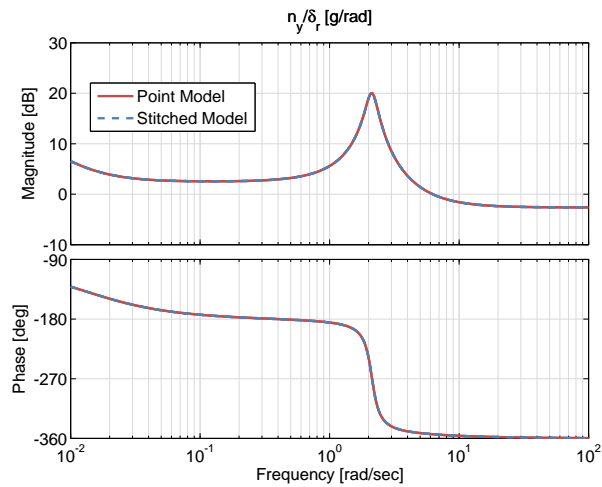
Figure 3.16: Case 1: lateral acceleration response to rudder input comparison.
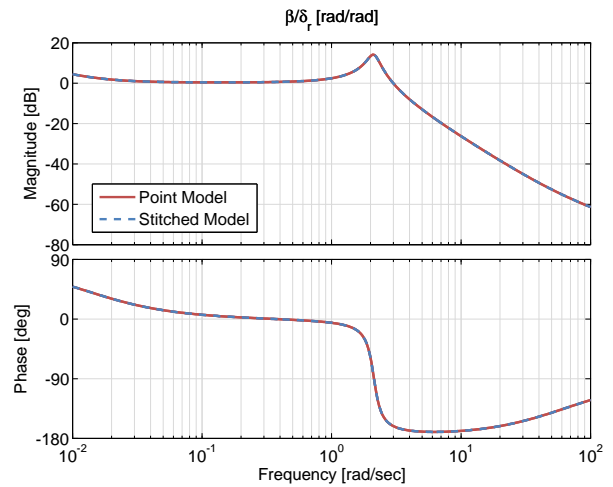
Figure 3.17: Case 1: sideslip response to rudder input comparison.

Summaries of the natural modes and dimensional stability and control derivative values for this check case are provided in Tables 3.2 and 3.3, respectively. Overall, there is near-perfect agreement in natural frequency and damping of the modes. The only noteworthy discrepancy is that the Phugoid mode in the stitched simulation model is slightly less damped ($\zeta = 0.049$ as compared to $\zeta = 0.052$ of the truth point model), as already mentioned.

Figures 3.18–3.20 show the short- and long-term time-history response comparisons for three separate control input doublets. Figure 3.18 shows the total airspeed V_{tot} and angle of attack response comparisons for a 5-deg elevator doublet. Angle of attack is nearly perfectly simulated by the stitched model, and excellent agreement is seen in the airspeed response. Figure 3.19 shows the response comparisons of roll rate and sideslip angle for a 5-deg aileron doublet, and Figure 3.20 shows the lateral acceleration and sideslip angle response comparisons for a 5-deg rudder doublet, with near-perfect agreement for all lateral/directional responses.

Table 3.2: Modes – Case 1

Mode	Parameter	Stitched Model	Point Model
Phugoid	ω_n [rad/sec]	0.1379	0.1371
	ζ	0.0487	0.0515
Short Period	ω_n [rad/sec]	5.4745	5.4745
	ζ	0.4597	0.4598
Spiral	$1/\tau$ [rad/sec]	-0.0004	-0.0004
Dutch Roll	ω_n [rad/sec]	2.1190	2.1189
	ζ	0.1019	0.1019
Roll Subsidence	$1/\tau$ [rad/sec]	4.2035	4.2034

Table 3.3: Stability and Control Derivatives, Body Axes – Case 1

Derivative	Stitched Model	Point Model
X_u	-0.0125	-0.0132
Z_u	-0.1652	-0.1663
M_u	0.0028	0.0027
X_w	0.0801	0.0800
Z_w	-1.8684	-1.8684
M_w	-0.0756	-0.0756
X_q	0.2169	0.2166
Z_q	-10.9679	-10.9676
M_q	-3.1661	-3.1670
Y_v	-0.1971	-0.1971
L_v	-0.0217	-0.0216
N_v	0.0111	0.0111
Y_p	-0.8436	-0.8436
L_p	-4.0914	-4.0913
N_p	-0.4193	-0.4193
Y_r	2.2137	2.2137
L_r	0.6004	0.6005
N_r	-0.3463	-0.3463
X_{δ_e}	-0.0267	-0.0276
Z_{δ_e}	-49.3874	-49.4219
M_{δ_e}	-17.5990	-17.5971
X_{δ_t}	0.0038	0.0038
Z_{δ_t}	-0.0002	-0.0002
M_{δ_t}	-0.0001	-0.0001
L_{δ_a}	18.0682	18.0666
N_{δ_a}	1.0515	1.0513
Y_{δ_r}	23.7677	23.7655
L_{δ_r}	1.7534	1.7530
N_{δ_r}	-4.5688	-4.5684
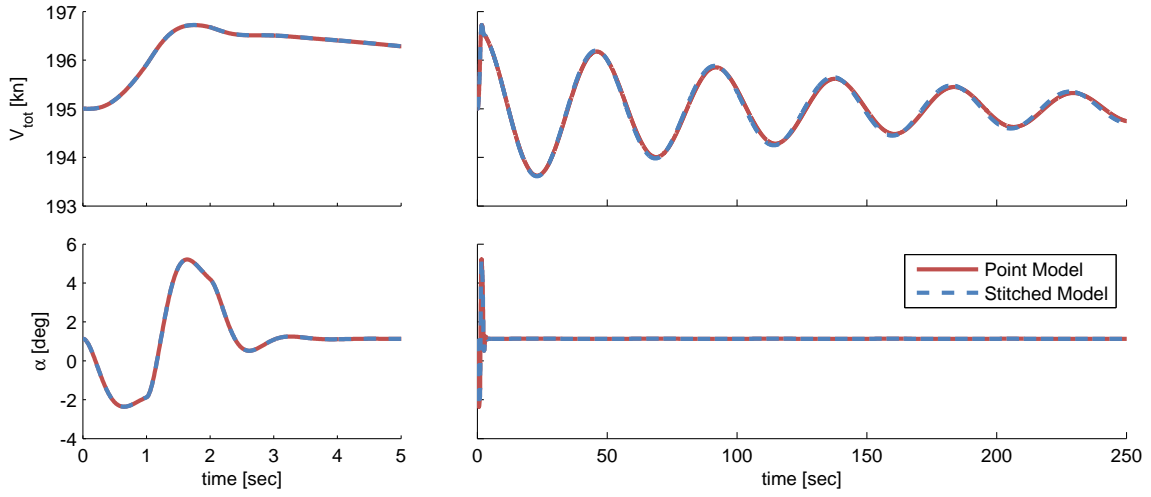
Figure 3.18: Case 1: short- and long-term time history responses, elevator doublet.
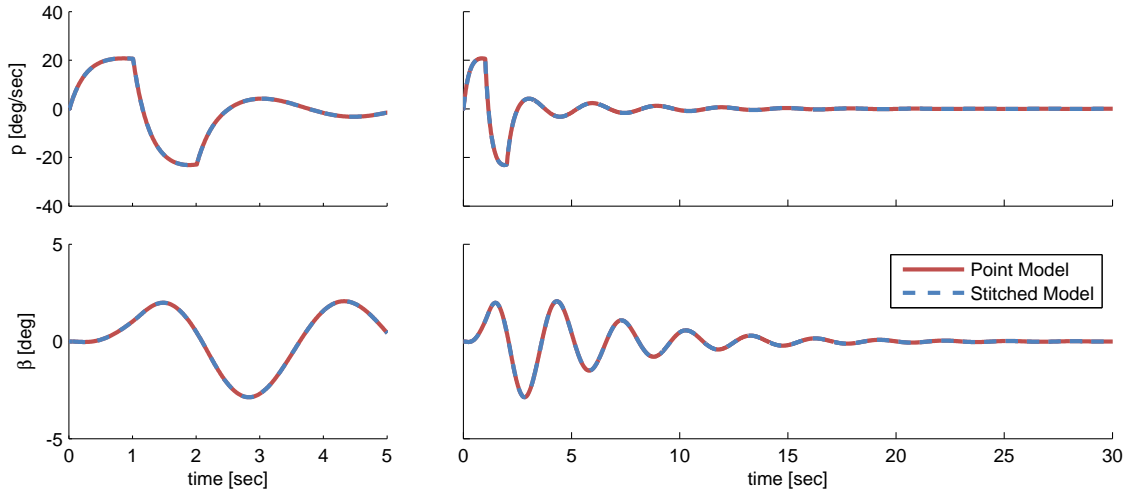
Figure 3.19: Case 1: short- and long-term time history responses, aileron doublet.
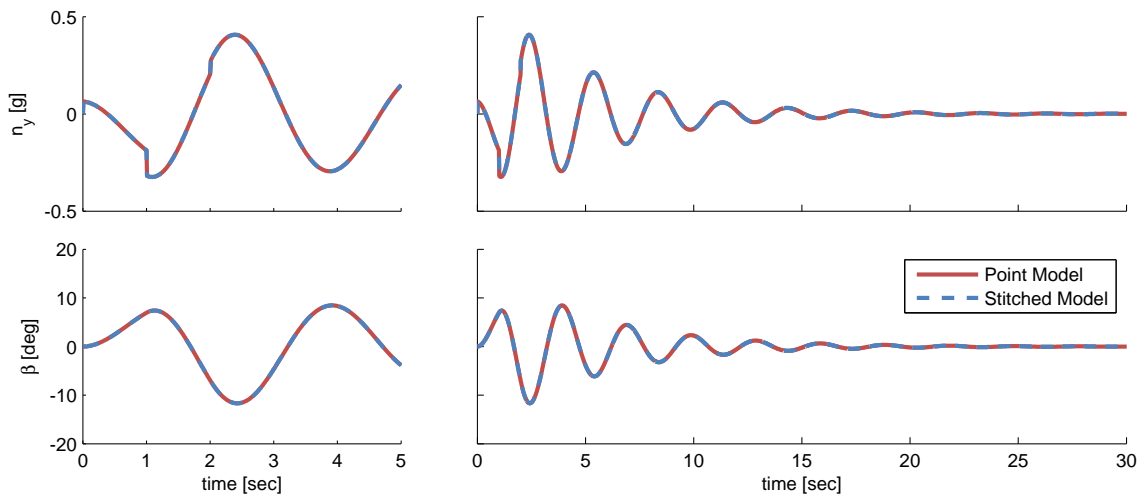
Figure 3.20: Case 1: short- and long-term time history responses, rudder doublet.

50

3.7.2   Case 2: Mach 0.6, FL350, Heavy Weight, Aft CG

This section presents the primary dynamic responses for check case 2: Mach 0.6 (346 KTAS), Flight Level 350 (35,000 ft altitude), heavy weight, aft CG. This check case demonstrates the simulation of a flight condition and loading configuration to which the stitched model has extrapolated in altitude, weight, and CG, and is interpolated in airspeed. A summary of the simulation loading configuration values compared to those of the nominal configuration, and the simulation flight condition values compared to the nearest anchor point values are provided in Table 3.4. A summary of the mode natural frequency and damping results for the stitched model versus AAA truth point model is presented in Table 3.5, and a summary of the values of dimensional stability and control derivatives is provided in Table 3.6.

Table 3.4: Simulation loading configuration and flight condition – Case 2

	Parameter	Simulation Value	Nominal/Anchor Value(s)	Off-Nominal
Loading Configuration	Weight [lb]	9750	8500	✓
	CG [in]	248.4	244.3	✓
Flight Condition	Airspeed [kn]	346	330, 360	✓
	Altitude [ft]	35000	30000	✓

Overall, the stitched model extrapolates to this flight condition and loading configuration very well. The only notable disparity is seen in the Phugoid mode, where the stitched model predicts a natural frequency of $\omega_n = 0.076$ versus $\omega_n = 0.093$ for the truth point model, and a damping of $\zeta = 0.071$ as compared to $\zeta = 0.046$ for the truth point model, as shown in Table 3.5. The discrepancy in Phugoid frequency and damping is a result of the mismatch in the values of the speed damping derivatives X_u and Z_u between the point model and the implicit representation from the stitched model at this flight condition, as shown in Table 3.6.

Figures 3.21–3.24 show the longitudinal frequency responses for check case 2. There is near-perfect agreement in the Short Period mode, but the disparity in the Phugoid frequency and damping is evident in the low-frequency portion of the responses. The mid- to high-frequency discrepancy seen in the true airspeed responses of Figure 3.22 is attributed to the mismatch in values of X_w at this flight condition, as tabulated in Table 3.6.
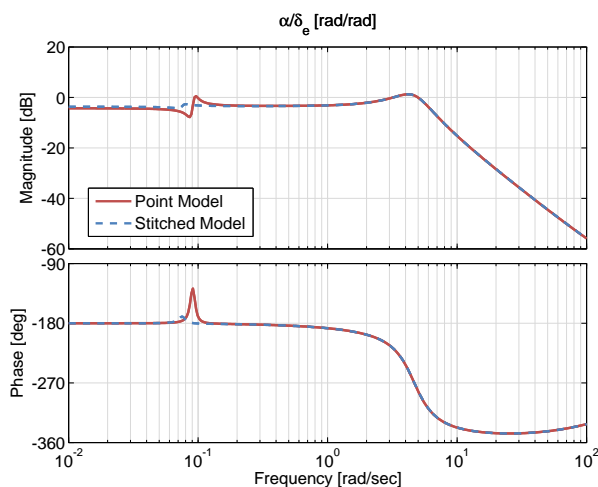
Figure 3.21: Case 2: angle of attack response to elevator input comparison.
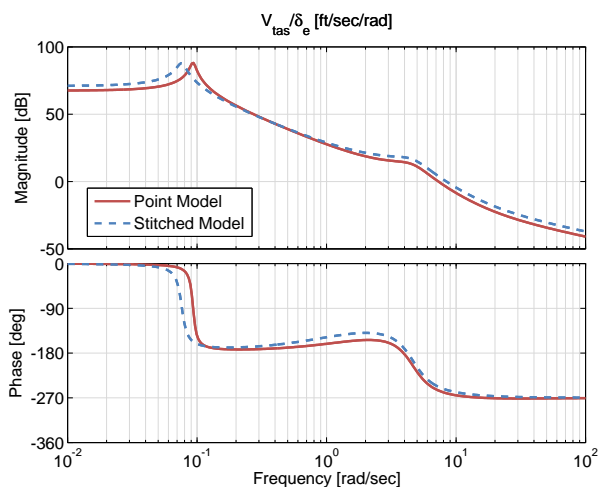
Figure 3.22: Case 2: true airspeed response to elevator input comparison.
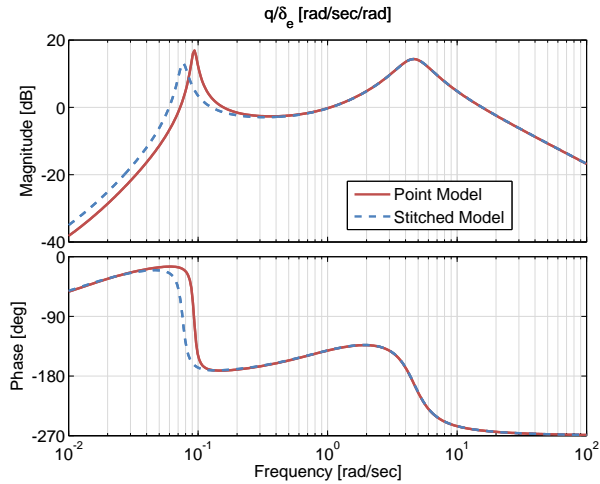
Figure 3.23: Case 2: pitch rate response to elevator input comparison.
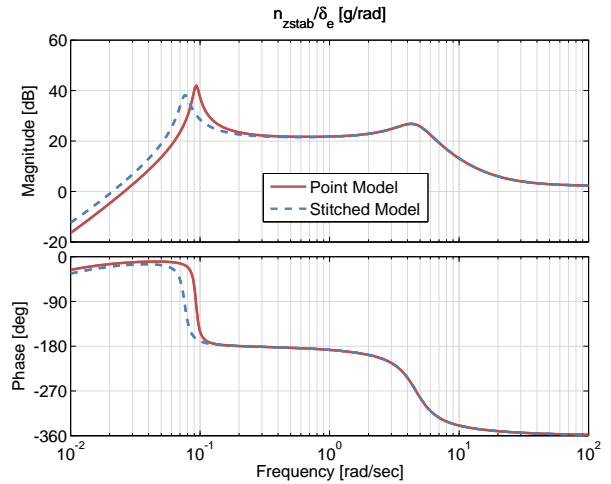
Figure 3.24: Case 2: normal acceleration response to elevator input comparison.

Figures 3.25–3.28 show the lateral/directional frequency responses for check case 2. There is excellent agreement overall between the stitched model and the point model. The stitched model represents the Dutch Roll mode very well (a close match in natural frequency and a damping within approximately 7%), and captures the Roll Subsidence inverse time constant within 1%.
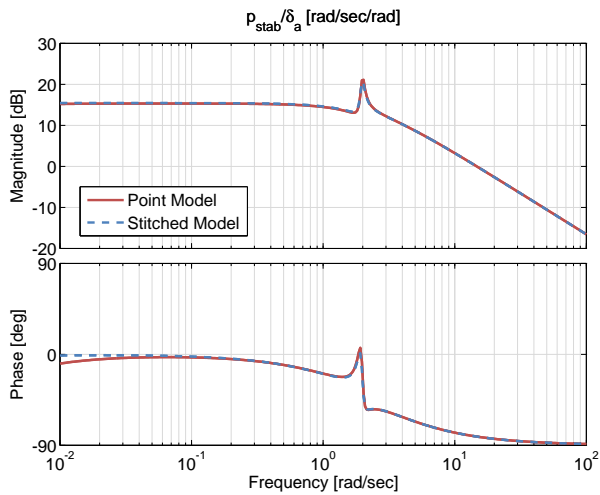
Figure 3.25: Case 2: roll rate response to aileron input comparison.
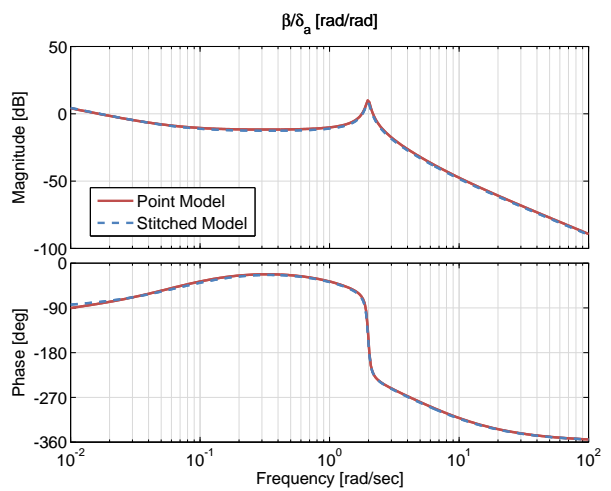
Figure 3.26: Case 2: sideslip response to aileron input comparison.
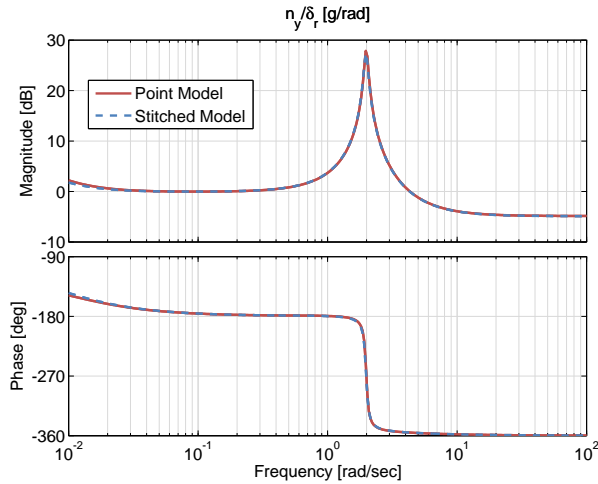
Figure 3.27: Case 2: lateral acceleration response to rudder input comparison.
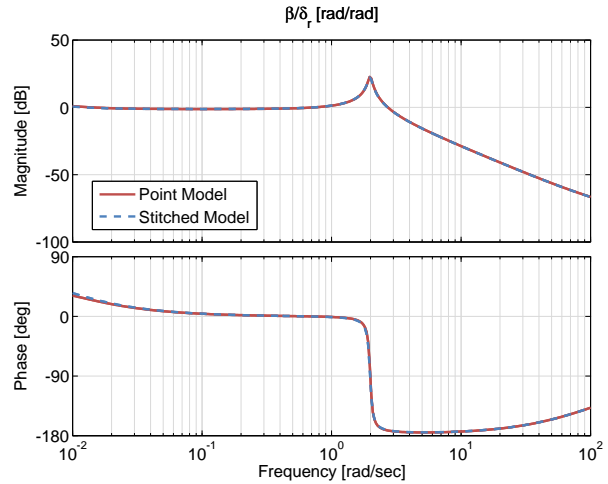
Figure 3.28: Case 2: sideslip response to rudder input comparison.

The modes for this high-speed cruise check case are summarized in Table 3.5. Overall, there is very good agreement in natural frequency and damping of all modes. The Phugoid mode is simulated to be at a lower frequency ($\omega_n = 0.076$ rad/sec versus $\omega_n = 0.093$ of the truth point model) and more damped ($\zeta = 0.071$ as compared to $\zeta = 0.046$ of the truth point model). There is excellent agreement in Short Period, Dutch Roll, and Roll Subsidence modes.

Figures 3.29–3.31 show the short- and long-term time-history response comparisons for three separate control doublets. Figure 3.29 shows the airspeed and angle of attack response comparisons for a 5-deg elevator doublet. Angle of attack is nearly perfectly simulated by the stitched model. The airspeed response is captured relatively well, with the discrepancies in Phugoid frequency and damping as seen in Table 3.5 evident in the long-term response comparison. Nevertheless, the differences amount to three cycles in airspeed oscillation observed in 4 minutes as opposed to three and a half cycles seen from the AAA truth point model over the same time period. This difference in Phugoid frequency is likely unnoticeable to a pilot in simulation. Figure 3.30 shows the response comparisons of roll rate and sideslip angle for a 5-deg aileron doublet. Roll rate is represented very well by the stitched model, and sideslip angle is in excellent agreement. Figure 3.31 shows the lateral acceleration and sideslip-angle response comparisons for a 5-deg rudder doublet. There is excellent agreement in the short- and long-term responses.

Table 3.5: Modes – Case 2

Mode	Parameter	Stitched Model	Point Model
Phugoid	ω_n [rad/sec]	0.0761	0.0930
	ζ	0.0712	0.0460
Short Period	ω_n [rad/sec]	4.6459	4.6369
	ζ	0.3050	0.3046
Spiral	$1/\tau$ [rad/sec]	−0.0002	−0.0016
Dutch Roll	ω_n [rad/sec]	1.9811	1.9882
	ζ	0.0333	0.0309
Roll Subsidence	$1/\tau$ [rad/sec]	2.3862	2.4021

Table 3.6: Stability and Control Derivatives, Body Axes – Case 2

Derivative	Stitched Model	Point Model
X_u	−0.0095	−0.0068
Z_u	−0.0792	−0.1182
M_u	0.0011	0.0017
X_w	0.0310	0.0489
Z_w	−1.0497	−1.0548
M_w	−0.0341	−0.0340
X_q	0.0484	0.1226
Z_q	−5.9440	−5.9278
M_q	−1.7856	−1.7720
Y_v	−0.1014	−0.1016
L_v	−0.0127	−0.0123
N_v	0.0058	0.0058
Y_p	−0.4663	−0.4663
L_p	−2.2417	−2.2505
N_p	−0.1758	−0.1968
Y_r	1.1122	1.1226
L_r	0.3351	0.3874
N_r	−0.1750	−0.1712
X_{δ_e}	−0.4872	−0.0201
Z_{δ_e}	−41.4377	−41.3179
M_{δ_e}	−14.4982	−14.4494
X_{δ_t}	0.0030	0.0030
Z_{δ_t}	−0.0002	−0.0002
M_{δ_t}	−0.0001	−0.0001
L_{δ_a}	14.8535	14.8654
N_{δ_a}	0.6203	0.6410
Y_{δ_r}	18.3189	18.3758
L_{δ_r}	1.4757	1.4802
N_{δ_r}	−3.4624	−3.4732
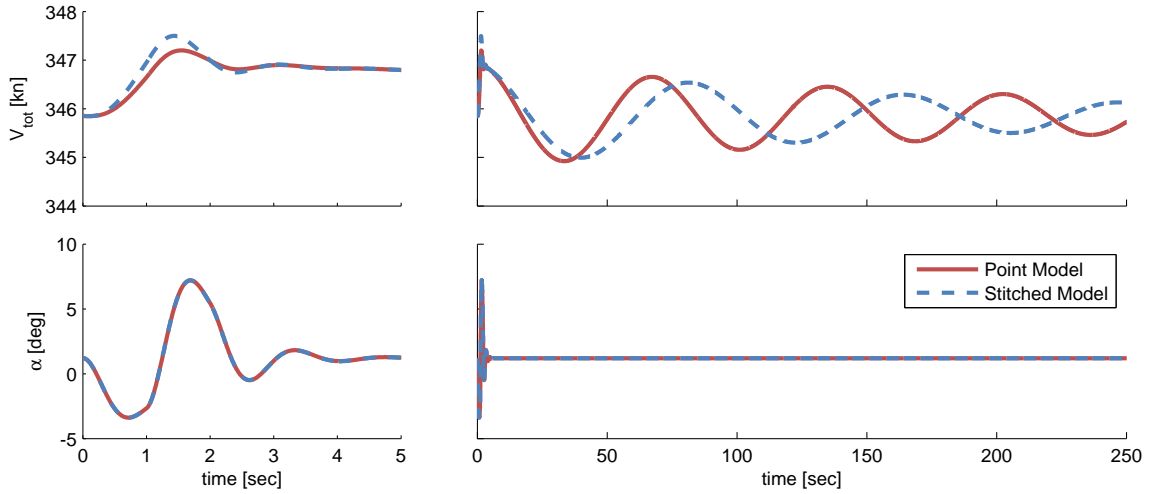
Figure 3.29: Case 2: short- and long-term time history responses, elevator doublet.
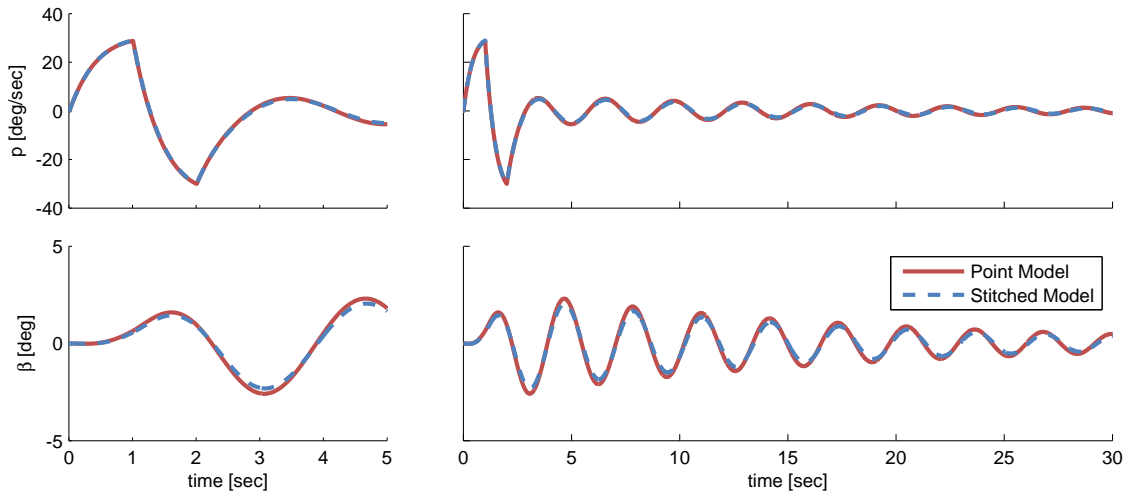
Figure 3.30: Case 2: short- and long-term time history responses, aileron doublet.
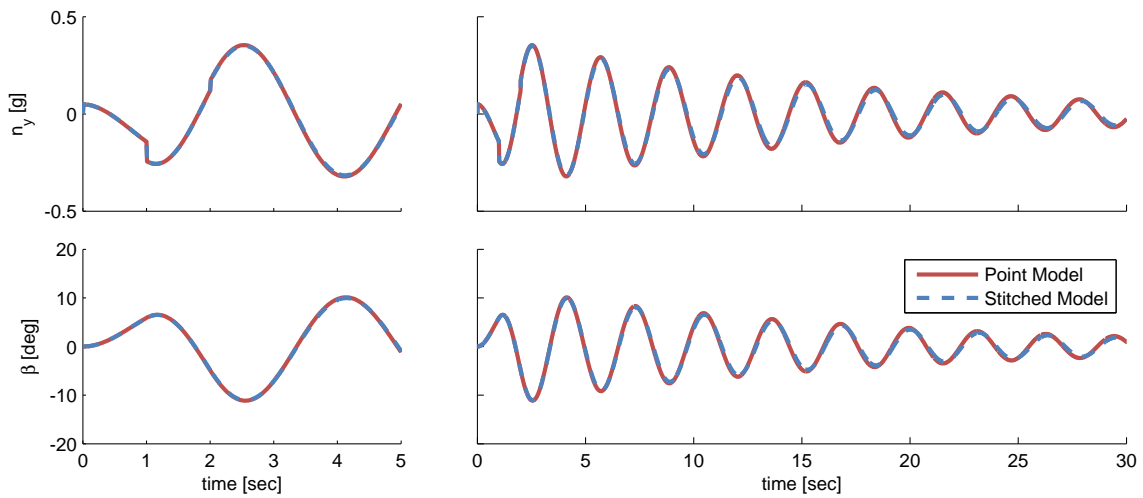
Figure 3.31: Case 2: short- and long-term time history responses, rudder doublet.

3.8 Simulation of Alternate Configurations – Flap Setting

Flap effects were incorporated into the CJ1 stitched model for the piloted simulation fidelity assessment presented in Ref. [17]. For the piloted simulation, the effects of flaps on both trim and derivatives, as determined from AAA, were applied to the baseline point models as a function of flap deflection and airspeed, and stored as an additional interpolation dimension in the lookup tables. This technique provided continuous look-up of trim and derivatives with deflection of flaps and changes in airspeed for a high-fidelity simulated approach to landing. Pilot reaction indicated that *trim behavior*, and the corresponding migration of the controls, however, were the most important effects upon deployment of flaps [17].

Analyses of the variations in trim and derivative values from AAA as a function of flap deflection indicate significant changes in trim angle of attack, elevator, and thrust for deployed flaps at a given airspeed. Although some stability and control derivatives also vary with flap deflection, the largest and most significant variations are seen in trim angle of attack and controls. As such, the initial flap implementation was simplified to changes in trim only; the explicit stability and control derivatives remain those of the nominal flaps-up configuration. This approach ensures that trim is correct and allows for efficient flight testing.

Considering the implications of collecting flight-test data for the development of a stitched model, the following will demonstrate the modeling of flap deflection as a change in trim only. Figure 3.32 shows results of the CJ1 stitched model for simulated flap deflections of 15 and 35 deg. The stitched model, configured with trim data and derivatives of the baseline (i.e., flaps-up) configuration, and with trim data only for the two flap deflection configurations (solid symbols), was retrimmed and relinearized over a range of airspeed (dashed lines) and compared to values from AAA truth models (solid lines).
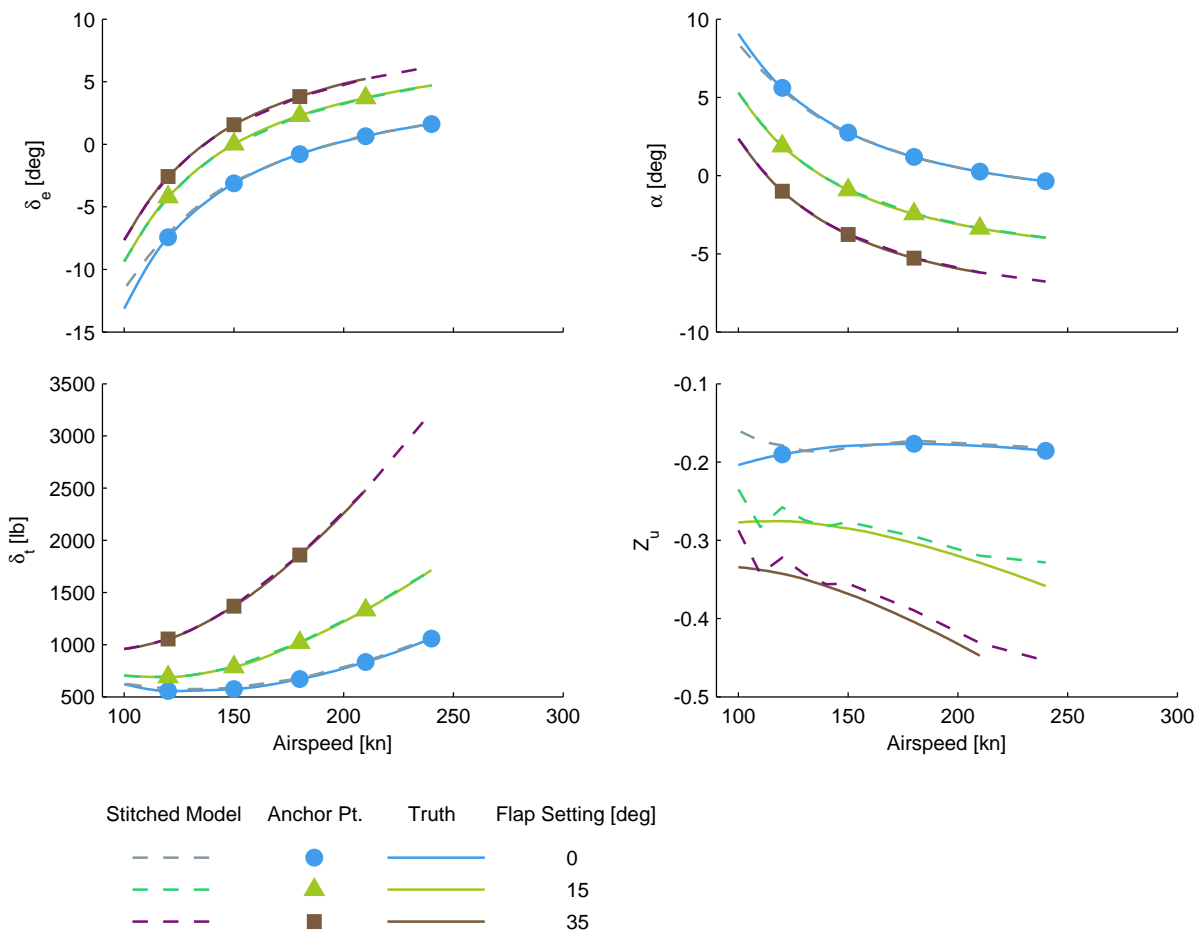
Figure 3.32: Alternate configuration verification, flap deflection.

For a given airspeed, an increase in flap deflection results in an increase in lift and drag, thus less angle of attack is needed and a greater total thrust is required to maintain trim. The angle of attack and thrust results from the stitched model track precisely at the anchor trim points, as expected, and overall match nearly perfectly with values from the off-nominal AAA truth data over a wide range of airspeed.

The values of the implicit speed derivative Z_u for all flap settings agree very well with the truth data. This confirms the implicit preservation of Z_u in the stitched model by the trim data. Referring to the complete set of flap verification figures in Section B.5, some disparities are seen in the values of the implicit speed derivative X_u for the flaps-down configurations. Note that the values of derivatives X_w and X_{δ_e} affect the values of implicit X_u in the stitched model [see Eq. (2.19)]. From the AAA truth data these derivatives are indeed functions of flap deflection, but are not represented by the trim-only flap implementation in the stitched model. Overall, the modeling of flap deflection as a change in trim only yields good agreement between the CJ1 stitched model and the AAA data.

3.9 Flight-Test Implications for Fixed-Wing Aircraft[1]

A key application of the model stitching architecture is the development of full flight-envelope stitched simulation models from flight-identified point models using system identification methods [1] and associated flight-test trim data. The extrapolation methods employed in the model stitching architecture permit continuous, full flight-envelope simulation of a full range of aircraft loading configurations using only a small number of point models and trim points. This requirement for a small number of flight-test points directly reduces the associated flight-test time, cost, and data analysis effort.

This section covers the overall considerations for planning and conducting a flight test involving fixed-wing aircraft for the development of stitched simulation models. Analyses of the sample CJ1 fixed-wing data trends discussed herein and lessons learned are applied to provide guidance on the spacing and quantity of trim data and point models to be obtained in flight testing. A method is presented for repurposing longitudinal static stability data, which accurately capture speed derivatives for use in the identified point models, to be combined with the collected trim data in the stitched model. Data processing techniques are presented, including a technique to account for the natural variance in aircraft weight, CG, and inertia between test points due to fuel burn-off. A summary of the overall flight-test recommendations for fixed-wing aircraft is provided in Table 3.7.

3.9.1 Flight-Test Data Collection

Trim Data

The collection of trim test data is accomplished by trimming the aircraft at the desired flight condition and recording data for a duration of approximately 3–5 seconds. Post-flight processing of the data is done to determine the trim (average) values of the controls, thrust/power setting, aircraft attitude, and any additional states for the particular flight-test point. It is important to know the loading configuration at each test point, whether it be from accurate onboard estimations of weight and CG or measurements of the fuel load at each point for use with a fuel-burn data sheet post-flight. The trim points are then collectively *baselined* to a nominal loading during data processing, as discussed in Section 3.9.2.

Trim data as a function of airspeed should be obtained via the "trim shot" method, in which power setting is used to vary airspeed while a level flight path angle is maintained with elevator. It is important to capture critical inflections in trim curves (e.g., bottom of the power curve, Mach effects, etc.) for accurate simulation over the full airspeed envelope. Collecting trim data at a speed increment of approximately 30–50 knots over the entire airspeed range should ensure capture of the key trim trends. Prior knowledge of the aircraft response behavior over specific airspeed ranges may allow trim to be collected at coarser speed increments (e.g., every 50 knots) between regions of inflection, necessitating a finer increment for the critical regions only.

---

[1]This section was coauthored with Tom Berger, Aviation Development Directorate (AMRDEC), Moffett Field, CA.

Identification Point Models

A frequency-domain-based approach of system identification is suggested, which involves performing piloted or automated frequency sweeps in the primary axes and processing the flight-test data in CIFER® [1] to extract state-space models at each flight-test condition. See Ref. [1] for detailed discussions on the collection of flight-test data, including instrumentation requirements, pilot input methods, and record duration guidelines. The process of identifying point models is more time consuming than the collection of trim data and involves both flight testing and identification analysis efforts, so careful consideration of the required identification points is critical. As with the collection of trim data, it is important to note the loading configuration at the start of each frequency sweep run, as this information is used during the baselining process.

The analyses of CJ1 stability and control derivative trends over ranges of airspeed (Section 3.6) show that 4 identified point models are typically sufficient to accurately represent the dynamic response of the fixed-wing aircraft over the entire airspeed range for a particular altitude. This guidance is applicable to both dimensional and nondimensional derivatives (see Section 3.5). The 4 identification points may be roughly evenly spaced over the entire airspeed range. It is suggested to more-closely space the high-speed identification points (Mach ≥ 0.5) to accurately capture variations in stability and control derivatives due to Mach effects.

Longitudinal Static Stability Data

When performing system identification it is common for speed derivatives X_u and M_u to be insensitive due to lack of frequency response data at frequencies low enough to accurately capture the Phugoid mode. Therefore longitudinal static stability data are collected, which can be used to explicitly calculate these speed derivatives [1]. There are various methods for obtaining longitudinal static stability data, but herein the "throttle-fixed" method is suggested. In this method, power setting is held constant while the elevator is used to vary airspeed by varying flight path angle (i.e., rate of climb or descent). This is also referred to as the "stabilized point" method [18]. It is recommended that longitudinal static stability data be collected at each point for which a model is identified. Collecting the static stability data over a range of approximately -30 to $+30$ knots relative to each point model flight condition, at an increment of approximately 10 knots, is suggested to accurately capture the X_u and M_u speed derivatives.

While the primary purpose of the longitudinal static stability data is for accurate identification of the speed derivatives in the point models, these data do provide an additional, and more finely spaced, source of trim data around the identification flight conditions. However, these collected data must be processed (i.e., retrimmed) to a level flight path angle using the model stitching architecture to be combined with the collected trim data, as discussed in Section 3.9.2.

Verification Doublets

Performing piloted doublets at each point for which a model is identified is useful for time-domain verification of the identified point models and the final stitched model at the anchor point flight conditions. Two doublets, one each for a positive and negative input, in each of the primary axes at each identified point model flight condition are required for verification.

3.9.2 Data Processing

Baselining

Typically during flight testing there will be a natural variance in aircraft weight between test points due to fuel burn-off. This change in weight will also affect the inertia values, and will likely affect the CG location. Furthermore, fuel transfers during flight (e.g., from external tanks to wing) may also directly affect inertia and CG. As a result, the precise loading configuration will likely vary among the anchor points. To remove the effects of loading configuration on trim and dynamics, the anchor trim data and identified point models may be *baselined* to a nominal, or baseline, loading configuration using the model stitching simulation architecture. In this process, the integrated extrapolation methods (Section 2.5) are employed to accurately retrim the anchor trim points and relinearize the anchor point models to a common loading configuration. These *baselined* anchor points are then used to construct the final stitched model.

When extrapolating for *simultaneous changes* in inertia and CG it is important to have good estimated values of the actual baseline aircraft loading configuration inertia values at each ID point for the most accurate extrapolation in loading configuration. Inertia estimates may be determined from conceptual design sizing equations [19], or derived from identification data collected a two different CG locations, as proposed in Ref. [1].

Longitudinal static stability data collected using the throttle-fixed method, in which rate of climb or descent is varied, must also be baselined (i.e., retrimmed) to a level flight path angle using the model stitching architecture to employ the data as additional trim points. This is accomplished by ensuring the climb or descent is represented by the difference in pitch attitude and angle of attack in the collected flight-test data, then simply retrimming each data point to zero flight path angle. Retrimming to a level flight path angle necessitates a different trim thrust value, so thrust control derivatives must be identified or explicitly modeled (see Section A.2.2).

Interpolation

Upon completion of the *baselining* processing step, the full collection of data is then further processed for direct use in the model stitching architecture. These processing steps include the fitting of splines to the data and interpolating the data to a fine grid. Trim data must be formatted as a full rectangular grid, which is a grid constructed from defined axis values for each interpolation dimension, per requirements of the model stitching architecture interpolation scheme (see Section 2.9.1). Typically, the grid will be defined for a set range of x-body airspeed U in one dimension and a set range of altitude in the second dimension, covering the entire flight envelope. Employing shape-preserving piecewise cubic splines, for example, as discussed in Section 2.9.2, allow the collected data to be interpolated to the defined grid while retaining critical inflections in the data.

3.9.3 Aircraft Configurations

The extrapolation methods integrated into the model stitching architecture were shown to very accurately simulate loading configurations with off-nominal values of weight, inertia, and CG (see Section 3.6). Therefore, collecting trim data and identification models is necessary using only a nominal (baseline) aircraft loading configuration.

Analyses of the variations in trim and derivative values from AAA as a function of flap deflection indicate significant changes in trim angle of attack, elevator deflection, and thrust for deployed flaps at a given airspeed. Although some stability and control derivatives also vary somewhat with flap deflection, the largest and most significant variations are seen in trim angle of attack and controls. Herein, the flap deflection implementation was simplified to changes in trim only. Trim data were included for flap settings of 15 and 35 deg, while the stability and control derivatives remain at the nominal (flaps-up) configuration (see Section 3.8). This approach ensures that flaps-down trim is correct, which is important for piloted simulation [17], and allows for efficient flight testing. Cost permitting, it may be advantageous, however, to directly identify the dynamics of a single flaps-down approach configuration using system identification flight testing.

3.9.4 Altitude

Altitude extrapolation for fixed-wing aircraft is accomplished within the model stitching architecture by scaling the dimensional stability and control derivatives and specific aerodynamic trim forces by the air density ratio (ρ_{sim}/ρ) and retrimming/relinearizing the stitched model, as discussed in Section 2.6. This extrapolation method has been shown to be very accurate over $\pm 10,000$ ft in altitude change for the CJ1 light business jet modeled herein (see Section 3.6.4), and reasonable results were found for greater altitude changes. Based on this applicable range for altitude extrapolation, point linear models and trim data were generated herein at altitudes of 10,000 ft and 30,000 ft; the 10,000-ft data were extrapolated to sea level (0 ft) and 20,000 ft, and the 30,000-ft data were extrapolated to 40,000 ft, which is approximately the operational service ceiling of the CJ1. With data at only two altitudes, the entire altitude envelope was effectively and accurately covered in 10,000-ft increments by the extrapolation method, as presented and verified in Section 3.6.4.

Based on the sample CJ1 results, flight testing at two altitudes is recommended to allow the extrapolation method to accurately cover the entire altitude envelope. Therefore, the flight-test data collection process outlined in Section 3.9.1 should be performed at two altitudes. If flight testing at more than one altitude is cost prohibitive, data collected at a single altitude may be extrapolated to cover the entire flight envelope; however, certain trim and derivative trends may not be precisely represented. Alternatively, trim data alone may be collected at various altitudes to ensure the capture of key thrust, attitude, and elevator deflection trends, whereas just the stability and control derivatives from a single altitude may be extrapolated.

3.9.5 Summary of Recommendations

The overall flight-test recommendations for the development of a fixed-wing aircraft stitched simulation model are summarized in Table 3.7. These recommendations are based on the analyses of the sample CJ1 stitched model presented herein, and are appropriate for typical business jet and transport aircraft applications. The table provides recommended airspeed increments, quantity of points, and example profile at which to identify point models and collect trim data. Additionally, recommended altitudes at which to perform the data collection are provided.

Table 3.7: Summary of flight-test recommendations for development of fixed-wing aircraft stitched models

Interpolation Dimension	Parameter	ID Point Models	Trim Data
Airspeed	Increment [kn]	80–100[a]	30–50[b,c]
	# of airspeeds	4–6	8–12
	Example profile	[approach[d] 180 270 330 360]	[approach[e] 120 150 180 210 240 270 300 330 360 390]
Altitude	Increment [ft]	20,000	20,000
	# of altitudes	1–2[f]	1–2[f]
	Example profile	[10,000 30,000]	[10,000 30,000]

[a] Finer increment at high speed (Mach $\geq$ 0.5) to capture nondimensional derivative variation due to Mach effects
[b] May need finer increment around critical inflections (e.g., bottom of the power curve)
[c] Can include baselined longitudinal static stability data as fine-increment trim data around identification points
[d] Single airspeed; flap effects may be modeled as a change in trim only
[e] Trim data should be collected for two flap settings over a range of representative airspeeds
[f] Data collection at two altitudes recommended for accurate altitude extrapolation

3.10 Chapter Summary

This chapter presented a state-of-the-art stitched model representative of a Cessna Citation CJ1 developed using linear point models and trim data derived from the Advanced Aircraft Analysis (AAA) software. AAA was configured with the CJ1 model included with the software to generate nondimensional stability and control derivatives for point flight conditions. Post-processing was performed on the AAA data to convert the nondimensional derivatives into dimensional, body-axes derivatives for the formulation of state-space point models. Additional features, including flap effects and a simple engine model, were integrated into the CJ1 stitched model for added realism in piloted simulation.

Verification results of off-nominal extrapolation methods were presented comparing outputs of the stitched model to values from AAA truth data for off-nominal loading configurations and alternate altitudes. Two dynamic response check cases were provided to verify overall simulation fidelity at two discrete flight conditions. Lessons learned and implications were considered to provide guidance on future flight testing for the development of stitched models involving fixed-wing aircraft.

4 Rotorcraft Stitched Model: UH-60 Black Hawk

Application of the model stitching simulation architecture for a rotorcraft is demonstrated in this chapter with a high-order model of the UH-60 Black Hawk helicopter. Rotorcraft present unique modeling challenges due to their inherent instability, rotor complexity, and large changes in trim and linear stability and control derivatives over the flight envelope. It is essential to capture key trends and have sufficient modeling detail for accurate, full flight-envelope piloted simulation.

In addition to demonstrating the use of high-order models in the model stitching simulation architecture, this application also demonstrates the storing and subsequent look-up of data in multiple dimensions, i.e., *stitching* in x-body airspeed U *and* y-body airspeed V, to achieve a more accurate simulation around hover. Stitching in y-body airspeed V results in the implicit representation of the v-speed derivatives (e.g., Y_v, L_v, and N_v), analogous to the implicit representation of the u-speed derivatives when stitching in x-body airspeed U. "Stitching in U and V" is implemented for increased accuracy in hover/low-speed conditions, and "stitching in U" only is employed for forward-flight conditions.

Verification results of the off-nominal extrapolation methods covered in Section 2.5 are presented comparing outputs of the stitched model to values from truth point models for off-nominal configurations and conditions. Two dynamic response check cases are provided to verify overall simulation fidelity at two discrete flight conditions and loading configurations. Check case results include comparisons of frequency responses, mode natural frequency and damping, stability and control derivative values, and time-history responses. Lessons learned and implications are considered to provide guidance on future flight testing for the development of stitched models from system identification results of rotorcraft.

4.1 Aircraft Model Description

The rotorcraft results herein were generated from high-order simulation models representative of the UH-60A Black Hawk helicopter. The Black Hawk, pictured in Figure 4.1, is a four-bladed, twin-engine, medium-lift utility helicopter manufactured by Sikorsky Aircraft Corporation. The general characteristics and performance of the UH-60 are as follows:

- Crew: 2 pilots with 2 crew chiefs
- Capacity: 2,640 lb of internal cargo, including 11 troops, or 8,000 lb external load
- Rotor diameter: 53 ft 8 in
- Length: 64 ft 10 in
- Empty weight: 10,624 lb
- Loaded weight: 22,000 lb
- Powerplant: 2 × General Electric T700-GE-701C turboshaft, 1,890 hp each
- Max. cruise speed: 159 kn
- Combat radius: 368 mi
- Service ceiling: 19,000 ft
- Rate of climb: 1,315 ft/min

4.2 State-Space Point Models

4.2.1 Overview of FORECAST Software

The FORECAST [20] mathematical model simulation program was employed to generate state-space models of the UH-60. FORECAST implements a set of nonlinear first-order ordinary differential equations from the Gen Hel [21] blade-element type nonlinear simulation model, and solves for the coupled rotor/fuselage dynamics to produce a trim solution. The blade motion is for rigid flapping and lead/lag at a hinge; flexible

Figure 4.1: UH-60 Black Hawk.

blades are not modeled. Numerical perturbations are used to extract high-order linearized models in state-space form. The linear models are formulated to include the higher-order dynamics of the aircraft (including rotor flapping and lead/lag motion, inflow, downwash interaction with the fuselage, engine dynamics, and primary servo dynamics) coupled with the six degrees of freedom of the fuselage.

Although FORECAST is capable of producing high-order linear models with over 50 states, somewhat reduced 26-state models were used herein as an example of highly-accurate yet reasonable high-order models. The models used for the results presented herein do not include primary servo (i.e., actuator) dynamics, engine dynamics, or fuselage/downwash interactions.

4.2.2 State Space Formulation

Twenty-six-state FORECAST models were chosen for the analyses presented herein. These flight-validated, high-order models offer excellent fidelity while employing a reasonable number of states. The 26 states include the 8 fuselage states, plus 18 rotor states: 6 main rotor flapping states, 6 main rotor lead/lag states, 4 inflow states (3 main rotor dynamic inflow states and 1 tail rotor inflow state), and 2 main rotor rotational speed states. The full 26-state state vector is given as

$$
\boldsymbol{x} = \begin{bmatrix} u & v & w & p & q & r & \phi & \theta & \dot{\beta}_0 & \dot{\beta}_{1c} & \dot{\beta}_{1s} & \beta_0 & \beta_{1c} & \beta_{1s} \\ \dot{\zeta}_0 & \dot{\zeta}_{1c} & \dot{\zeta}_{1s} & \zeta_0 & \zeta_{1c} & \zeta_{1s} & \lambda_0 & \lambda_{1c} & \lambda_{1s} & \lambda_t & \psi_R & \Omega \end{bmatrix}^{\mathrm{T}}_{26}
\tag{4.1}
$$

Two subsets of the full state vector, one containing the first 6 fuselage states, and the other containing the 18 higher-order rotor states, are referred to as the following:

$$
\boldsymbol{x}_6 = \begin{bmatrix} u & v & w & p & q & r \end{bmatrix}^{\mathrm{T}}_6
\tag{4.2}
$$

$$
\boldsymbol{x}_{\mathrm{H}} = \begin{bmatrix} \dot{\beta}_0 & \dot{\beta}_{1c} & \dot{\beta}_{1s} & \beta_0 & \beta_{1c} & \beta_{1s} & \dot{\zeta}_0 & \dot{\zeta}_{1c} & \dot{\zeta}_{1s} & \zeta_0 & \zeta_{1c} & \zeta_{1s} & \lambda_0 & \lambda_{1c} & \lambda_{1s} & \lambda_t & \psi_R & \Omega \end{bmatrix}^{\mathrm{T}}_{18}
\tag{4.3}
$$

The full high-order state-space representation in $\dot{\boldsymbol{x}} = \boldsymbol{A}\boldsymbol{x} + \boldsymbol{B}\boldsymbol{u}$ form is as follows:

$$
\begin{bmatrix}
\dot{u} \\ \dot{v} \\ \dot{w} \\ \dot{p} \\ \dot{q} \\ \dot{r} \\ \dot{\phi} \\ \dot{\theta} \\ \ddot{\beta}_0 \\ \vdots \\ \dot{\Omega}
\end{bmatrix}
=
\begin{bmatrix}
X_u & X_v & X_w & X_p & X_q - W_0 & X_r + V_0 & 0 & -gc\Theta_0 & X_{\dot{\beta}_0} & \dots & X_\Omega \\
Y_u & Y_v & Y_w & Y_p + W_0 & Y_q & Y_r - U_0 & gc\Phi_0 c\Theta_0 & -gs\Phi_0 s\Theta_0 & Y_{\dot{\beta}_0} & \dots & Y_\Omega \\
Z_u & Z_v & Z_w & Z_p - V_0 & Z_q + U_0 & Z_r & -gs\Phi_0 c\Theta_0 & -gc\Phi_0 s\Theta_0 & Z_{\dot{\beta}_0} & \dots & Z_\Omega \\
L'_u & L'_v & L'_w & L'_p & L'_q & L'_r & 0 & 0 & L'_{\dot{\beta}_0} & \dots & L'_\Omega \\
M_u & M_v & M_w & M_p & M_q & M_r & 0 & 0 & M_{\dot{\beta}_0} & \dots & M_\Omega \\
N'_u & N'_v & N'_w & N'_p & N'_q & N'_r & 0 & 0 & N'_{\dot{\beta}_0} & \dots & N'_\Omega \\
0 & 0 & 0 & 1 & s\Phi_0 t\Theta_0 & c\Phi_0 t\Theta_0 & 0 & 0 & 0 & \dots & 0 \\
0 & 0 & 0 & 0 & c\Phi_0 & -s\Phi_0 & 0 & 0 & 0 & \dots & 0 \\
\frac{\partial \ddot{\beta}_0}{\partial u} & \frac{\partial \ddot{\beta}_0}{\partial v} & \frac{\partial \ddot{\beta}_0}{\partial w} & \frac{\partial \ddot{\beta}_0}{\partial p} & \frac{\partial \ddot{\beta}_0}{\partial q} & \frac{\partial \ddot{\beta}_0}{\partial r} & 0 & 0 & \frac{\partial \ddot{\beta}_0}{\partial \dot{\beta}_0} & \dots & \frac{\partial \ddot{\beta}_0}{\partial \Omega} \\
\vdots & \vdots & \vdots & \vdots & \vdots & \vdots & \vdots & \vdots & \vdots & \ddots & \vdots \\
\frac{\partial \dot{\Omega}}{\partial u} & \frac{\partial \dot{\Omega}}{\partial v} & \frac{\partial \dot{\Omega}}{\partial w} & \frac{\partial \dot{\Omega}}{\partial p} & \frac{\partial \dot{\Omega}}{\partial q} & \frac{\partial \dot{\Omega}}{\partial r} & 0 & 0 & \frac{\partial \dot{\Omega}}{\partial \dot{\beta}_0} & \dots & \frac{\partial \dot{\Omega}}{\partial \Omega}
\end{bmatrix}
\begin{bmatrix}
u \\ v \\ w \\ p \\ q \\ r \\ \phi \\ \theta \\ \dot{\beta}_0 \\ \vdots \\ \Omega
\end{bmatrix}
$$

$$
+
\begin{bmatrix}
X_{\delta_\text{lat}} & X_{\delta_\text{lon}} & X_{\delta_\text{col}} & X_{\delta_\text{ped}} \\
Y_{\delta_\text{lat}} & Y_{\delta_\text{lon}} & Y_{\delta_\text{col}} & Y_{\delta_\text{ped}} \\
Z_{\delta_\text{lat}} & Z_{\delta_\text{lon}} & Z_{\delta_\text{col}} & Z_{\delta_\text{ped}} \\
L'_{\delta_\text{lat}} & L'_{\delta_\text{lon}} & L'_{\delta_\text{col}} & L'_{\delta_\text{ped}} \\
M_{\delta_\text{lat}} & M_{\delta_\text{lon}} & M_{\delta_\text{col}} & M_{\delta_\text{ped}} \\
N'_{\delta_\text{lat}} & N'_{\delta_\text{lon}} & N'_{\delta_\text{col}} & N'_{\delta_\text{ped}} \\
0 & 0 & 0 & 0 \\
0 & 0 & 0 & 0 \\
\frac{\partial \ddot{\beta}_0}{\partial \delta_\text{lat}} & \frac{\partial \ddot{\beta}_0}{\partial \delta_\text{lon}} & \frac{\partial \ddot{\beta}_0}{\partial \delta_\text{col}} & \frac{\partial \ddot{\beta}_0}{\partial \delta_\text{ped}} \\
\vdots & \vdots & \vdots & \vdots \\
\frac{\partial \dot{\Omega}}{\partial \delta_\text{lat}} & \frac{\partial \dot{\Omega}}{\partial \delta_\text{lon}} & \frac{\partial \dot{\Omega}}{\partial \delta_\text{col}} & \frac{\partial \dot{\Omega}}{\partial \delta_\text{ped}}
\end{bmatrix}
\begin{bmatrix}
\delta_\text{lat} \\ \delta_\text{lon} \\ \delta_\text{col} \\ \delta_\text{ped}
\end{bmatrix}
\tag{4.4}
$$

where sin, cos, and tan have been abbreviated as s, c, and t, respectively. Primed derivatives ($'$), as defined following Ref. [11] and given in Section A.1.3, account for the influence of the cross-product of inertia I_{xz}. In the remainder of the text, the primed notation is implied but is generally dropped for convenience.

Stability and control derivatives of the higher-order state equations above are represented in their generic form, but specific nomenclature may be assigned to pertinent derivatives. For example, in the last row we can recognize that the $\dot{\Omega}$ derivatives are associated with the main rotor toque state equation, e.g., $\frac{\partial \dot{\Omega}}{\partial \Omega} = \frac{\partial R}{\partial \Omega} = R_\Omega$, as used in the state-space model structure for engine response identification in Ref. [1].

The linear $\boldsymbol{A}$ and $\boldsymbol{B}$ matrices of Eq. (4.4) are partitioned into submatrices for use in the model stitching simulation architecture following Eq. (2.101). The resultant $\boldsymbol{A}_{66}$, $\boldsymbol{A}_{6\text{H}}$, $\boldsymbol{A}_{\text{H}6}$, $\boldsymbol{A}_{\text{HH}}$, $\boldsymbol{B}_{6\text{C}}$, and $\boldsymbol{B}_{\text{HC}}$ matrices are given as

$$
\boldsymbol{A}_{66} =
\begin{bmatrix}
X_u & X_v & X_w & X_p & X_q & X_r \\
Y_u & Y_v & Y_w & Y_p & Y_q & Y_r \\
Z_u & Z_v & Z_w & Z_p & Z_q & Z_r \\
L'_u & L'_v & L'_w & L'_p & L'_q & L'_r \\
M_u & M_v & M_w & M_p & M_q & M_r \\
N'_u & N'_v & N'_w & N'_p & N'_q & N'_r
\end{bmatrix}_{6\times6}
\tag{4.5}
$$

$$
\boldsymbol{A}_{6\text{H}} =
\begin{bmatrix}
X_{\dot{\beta}_0} & \dots & X_\Omega \\
Y_{\dot{\beta}_0} & \dots & Y_\Omega \\
Z_{\dot{\beta}_0} & \dots & Z_\Omega \\
L'_{\dot{\beta}_0} & \dots & L'_\Omega \\
M_{\dot{\beta}_0} & \dots & M_\Omega \\
N'_{\dot{\beta}_0} & \dots & N'_\Omega
\end{bmatrix}_{6\times18}
\tag{4.6}
$$

$$\boldsymbol{A}_{\text{H6}} = \begin{bmatrix} \frac{\partial \ddot{\beta}_0}{\partial u} & \frac{\partial \ddot{\beta}_0}{\partial v} & \frac{\partial \ddot{\beta}_0}{\partial w} & \frac{\partial \ddot{\beta}_0}{\partial p} & \frac{\partial \ddot{\beta}_0}{\partial q} & \frac{\partial \ddot{\beta}_0}{\partial r} \\ \vdots & \vdots & \vdots & \vdots & \vdots & \vdots \\ \frac{\partial \dot{\Omega}}{\partial u} & \frac{\partial \dot{\Omega}}{\partial v} & \frac{\partial \dot{\Omega}}{\partial w} & \frac{\partial \dot{\Omega}}{\partial p} & \frac{\partial \dot{\Omega}}{\partial q} & \frac{\partial \dot{\Omega}}{\partial r} \end{bmatrix}_{18 \times 6} \tag{4.7}$$

$$\boldsymbol{A}_{\text{HH}} = \begin{bmatrix} \frac{\partial \ddot{\beta}_0}{\partial \dot{\beta}_0} & \cdots & \frac{\partial \ddot{\beta}_0}{\partial \Omega} \\ \vdots & \ddots & \vdots \\ \frac{\partial \dot{\Omega}}{\partial \dot{\beta}_0} & \cdots & \frac{\partial \dot{\Omega}}{\partial \Omega} \end{bmatrix}_{18 \times 18} \tag{4.8}$$

$$\boldsymbol{B}_{\text{6C}} = \begin{bmatrix} X_{\delta_{\text{lat}}} & X_{\delta_{\text{lon}}} & X_{\delta_{\text{col}}} & X_{\delta_{\text{ped}}} \\ Y_{\delta_{\text{lat}}} & Y_{\delta_{\text{lon}}} & Y_{\delta_{\text{col}}} & Y_{\delta_{\text{ped}}} \\ Z_{\delta_{\text{lat}}} & Z_{\delta_{\text{lon}}} & Z_{\delta_{\text{col}}} & Z_{\delta_{\text{ped}}} \\ L'_{\delta_{\text{lat}}} & L'_{\delta_{\text{lon}}} & L'_{\delta_{\text{col}}} & L'_{\delta_{\text{ped}}} \\ M_{\delta_{\text{lat}}} & M_{\delta_{\text{lon}}} & M_{\delta_{\text{col}}} & M_{\delta_{\text{ped}}} \\ N'_{\delta_{\text{lat}}} & N'_{\delta_{\text{lon}}} & N'_{\delta_{\text{col}}} & N'_{\delta_{\text{ped}}} \end{bmatrix}_{6 \times 4} \tag{4.9}$$

$$\boldsymbol{B}_{\text{HC}} = \begin{bmatrix} \frac{\partial \ddot{\beta}_0}{\partial \delta_{\text{lat}}} & \frac{\partial \ddot{\beta}_0}{\partial \delta_{\text{lon}}} & \frac{\partial \ddot{\beta}_0}{\partial \delta_{\text{col}}} & \frac{\partial \ddot{\beta}_0}{\partial \delta_{\text{ped}}} \\ \vdots & \vdots & \vdots & \vdots \\ \frac{\partial \dot{\Omega}}{\partial \delta_{\text{lat}}} & \frac{\partial \dot{\Omega}}{\partial \delta_{\text{lon}}} & \frac{\partial \dot{\Omega}}{\partial \delta_{\text{col}}} & \frac{\partial \dot{\Omega}}{\partial \delta_{\text{ped}}} \end{bmatrix}_{18 \times 4} \tag{4.10}$$

It is important to note that in this case the stability derivatives of $\boldsymbol{A}_{66}$ shown in Eq. (4.5) are *not* the 6-DOF stability derivatives, rather they are the fuselage-only contributions to the combined multi-body model.

In order to allow meaningful comparisons of stability and control derivative values between those of the linearized high-order stitched model and those from FORECAST, *quasi-steady* 6-DOF representations were generated by performing model reductions (i.e., state elimination and order reduction using the MATLAB® function `modred` [12]) on the full 26-state models. Henceforth, unless otherwise noted, reference to or comparison of stability and control derivative values will be those of the quasi-steady 6-DOF representation.

4.3   Hover/Low-Speed Trim Data

Fine-increment trim points around hover are necessary to accurately capture the migration of controls and helicopter attitude for the simulation of low-speed forward, rearward, sideward, and quartering flight, as well as the simulation of hovering flight in the presence of winds. These low-speed trim data are included in the stitched model as a function of both x-body airspeed U *and* y-body airspeed V; therefore, we employ in this application "stitching in U and V" in the hover/low-speed regime. As a result, the v-speed derivatives (e.g., Y_v, L_v, and N_v), like the u-speed derivatives, are represented implicitly (see Section 2.8). The spacing and corresponding gradients between the trim data affect the accuracy of the implicit speed derivatives, which in turn affect the dynamic response of the stitched model.

Scenarios were investigated to determine recommended spacing and strategies for the collection of trim points around hover and the low-speed regime. Sections 4.3.1–4.3.3 present separately the analyses of trim data for forward/rearward, sideward, and quartering flight. Section 4.3.3 presents also the simulation results of hovering flight in the presence of steady winds. In total, the overall recommended trim data points are used for the UH-60 stitched model anchor points, as presented in Section 4.5, and are summarized in the flight-test implications for the development of rotorcraft stitched models in Section 4.9.

4.3.1   Forward/Rearward Flight Trim Data

The effect of the spacing of low-speed forward and rearward trim data points on the accuracy of the implicit u-speed derivatives and the dynamic response at hover is presented. Trim data points as a function of only x-body airspeed U at increments of 3, 5, and 10 knots, covering a range of airspeed from -20 kn (rearward) to 20 kn forward airspeed, were investigated in the stitched model. These data points are shown graphically in Figure 4.2. Also included and shown graphically in Figure 4.2 are stability and control derivative values
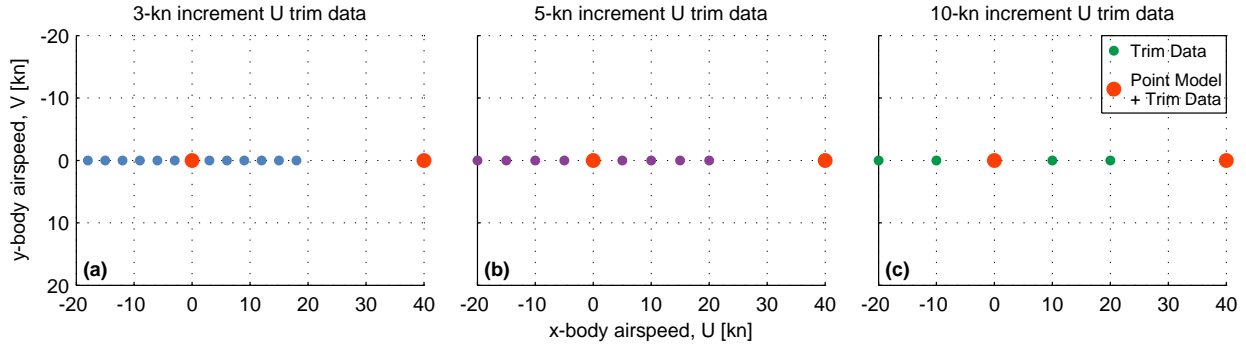
Figure 4.2: Forward/rearward flight trim data points at 3-, 5-, and 10-kn x-body airspeed U increments, and point models at hover and 40 kn.

(i.e., point models) only at two points in this low-speed regime: hover and 40 kn, as is typical for rotorcraft identification [1]. The data were fit with shape-preserving piecewise cubic splines (i.e., MATLAB function `interp1` with method 'pchip' [12]) to interpolate the data to fine 1-kn increment sets over the airspeed range of the data. The stitched model, configured with the three different trim data sets of varying x-body airspeed increment, was then retrimmed and linearized over the −20 to 20 knot airspeed range.

Figure 4.3 shows trim values of the controls, attitude, and longitudinal rotor flapping angle β_{1c} from the stitched model configured for each of the three trim data sets as compared to truth values from FORECAST. Circle, square, and triangle symbols indicate the original data points of the 3-, 5-, and 10-kn sets, respectively, used as anchor points for the spline fits.
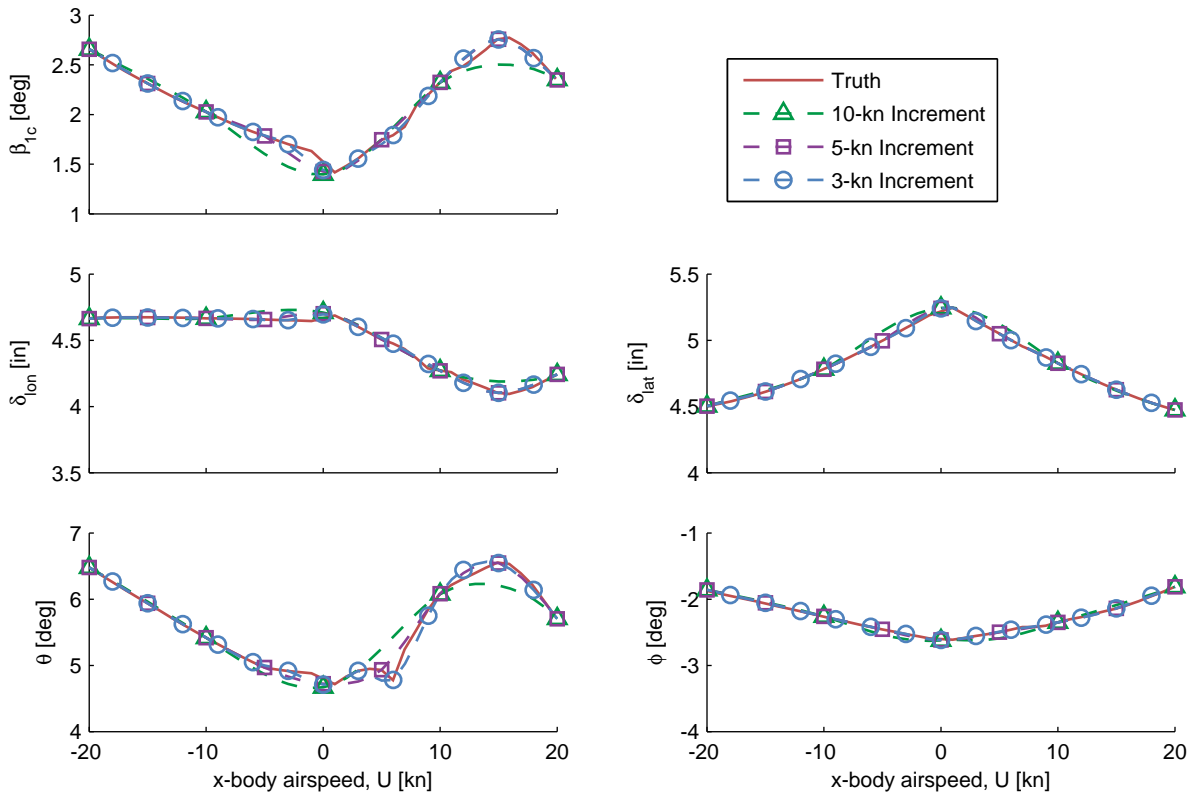
Figure 4.3: Spline-fit forward/rearward flight trim values with various spacing.

The truth trim data are captured very well with the 3- and 5-kn spacing over the investigated rearward/forward airspeed range. The 10-kn spacing roughly captures the data, but misses subtle inflections in the trends of pitch attitude θ, longitudinal cyclic stick δ_{lon}, and longitudinal rotor flapping angle.

The implicit u-speed derivative values, due to the x-body airspeed U trim data of various spacing, are shown in Figure 4.4 and compared to FORECAST truth data over the same airspeed range of -20 to 20 knots. Overall there is excellent agreement of the quasi-steady, implicit u-speed derivative values with the truth data, with the fine 3-kn-increment data most-closely matching the truth data over the airspeed range, and the 5-kn-increment data also matching well. The 10-kn-increment data once again does not capture subtle inflections in the derivative values. In addition to the closeness of match of the derivative values over the airspeed range, the derivative values at the hover point ($U = 0$) are also affected by the spacing of the data, due to the gradients between the data to either side of the hover point. As such, the fine 3-kn-increment data most-closely match the truth values, and the match slightly degrades as the data become coarser.
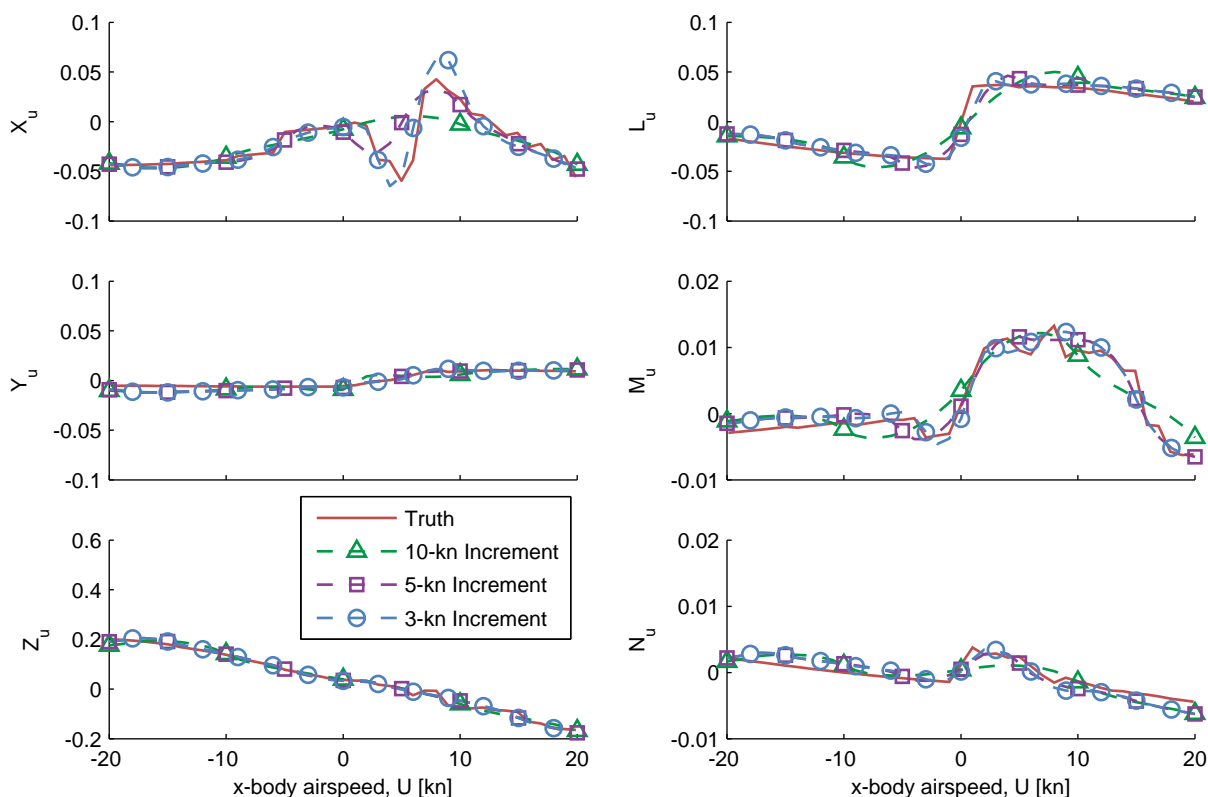
Figure 4.4: Implicit u-speed derivative values due to forward/rearward flight trim data of various spacing.

To illustrate the effect of the implicit u-speed derivative values at the hover point on the dynamic response of the stitched model, primary on-axis frequency response comparisons between the high-order stitched model and the FORECAST truth point model are presented in Figures 4.5 and 4.6. The values of the u-speed derivatives affect the low-frequency coupled Pitch and Roll Phugoid modes, as seen most notably in the low-frequency portions of the magnitude responses. With coarser spacing of the forward/rearward x-body airspeed trim data around hover, the frequency response match below approximately 0.6 rad/sec degrades.

To quantify the effect of the implicit u-speed derivative values on the dynamic response at hover, the natural frequencies and damping ratios of the Pitch and Roll Phugoid modes are tabulated in Table 4.1, in which values of the linearized stitched model for the various trim data increments are compared to values from the truth FORECAST hover point model. There is good agreement in natural frequencies between the linearized stitched model and the truth point model; however, the Phugoid damping ratios are most affected by the spacing of the trim data. The accuracy of the Pitch and Roll Phugoid damping ratio values from the stitched model degrades with increasing data coarseness; Pitch Phugoid damping values are within 14%,
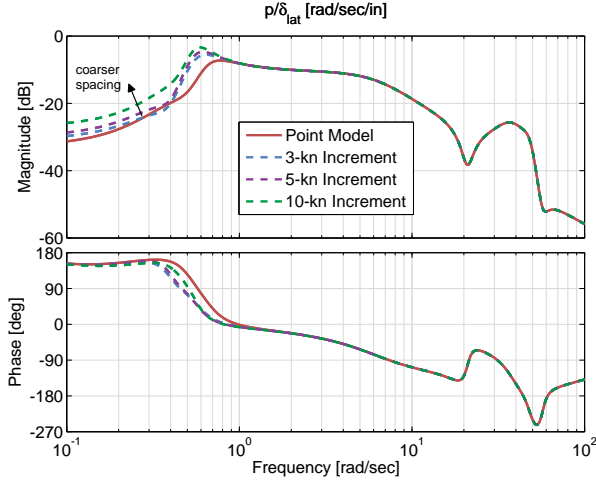
Figure 4.5: Roll rate response to lateral cyclic input comparison for forward/rearward trim data of various spacing, hover.
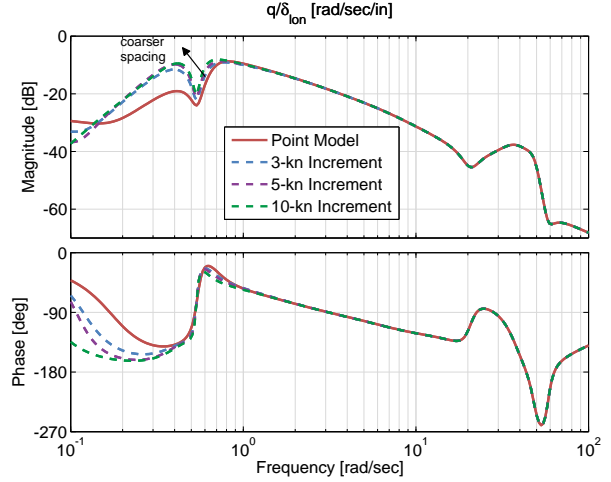
Figure 4.6: Pitch rate response to longitudinal cyclic input comparison for forward/rearward trim data of various spacing, hover.

Table 4.1: Hover Phugoid modes for forward/rearward trim data of varying x-body airspeed U increment

| Mode | Parameter | Stitched Model | | | Point Model |
		10-kn inc.	5-kn inc.	3-kn inc.	
Pitch Phugoid	ω_n [rad/sec]	0.4437	0.4229	0.4291	0.5207
	ζ	-0.3591	-0.3748	-0.4196	-0.4840
Roll Phugoid	ω_n [rad/sec]	0.5556	0.5602	0.5716	0.6524
	ζ	0.1755	0.2138	0.2388	0.2543

23%, and 26% for the 3-, 5-, and 10-kn-increment data, respectively, and Roll Phugoid damping values are within 7%, 16%, and 31% for the 3-, 5-, and 10-kn-increment data, respectively.

Overall, the 3- and 5-kn-increment x-body airspeed U trim data yield satisfactory results, and are recommended for the collection of forward/rearward trim data in the hover/low-speed regime. A 5-kn increment set of forward/rearward trim data is used in the UH-60 stitched model (see Section 4.5).

4.3.2 Sideward Flight Trim Data

Analyses of the spacing of low-speed forward/rearward trim data points on the accuracy of the implicit u-speed derivatives for stitching in U were presented in the previous section. In this section, the effect of the spacing of low-speed sideward flight trim data points on the accuracy of the implicit v-speed derivatives for stitching in V and the dynamic response at hover are presented. Three pure-sideward flight trim data sets of various spacing (3-, 5-, and 7-kn y-body airspeed V increments) were generated in FORECAST covering -15 to 15 knots y-body airspeed V. These data points are shown graphically in Figure 4.7. Stability and control derivative values (i.e., point models) are again included only at hover and 40 kn forward airspeed in this low-speed regime. The data were fit with shape-preserving piecewise cubic splines to interpolate the data to fine 1-kn increment sets over the full -15 to 15 knot sideward flight range. The stitched model, configured with the three different sideward flight trim data sets, was then retrimmed and linearized for pure sideward flight between -15 and 15 knots y-body airspeed V.

Figure 4.8 shows trim values of the controls, bank angle, and lateral rotor flapping angle β_{1s} from the stitched model configured for each of the three sideward trim data sets as compared to truth values from FORECAST over the sideward airspeed range. Circle, square, and triangle symbols indicate the original data points of the 3-, 5-, and 7-kn sets, respectively, used as anchor points for the spline fits. The truth data
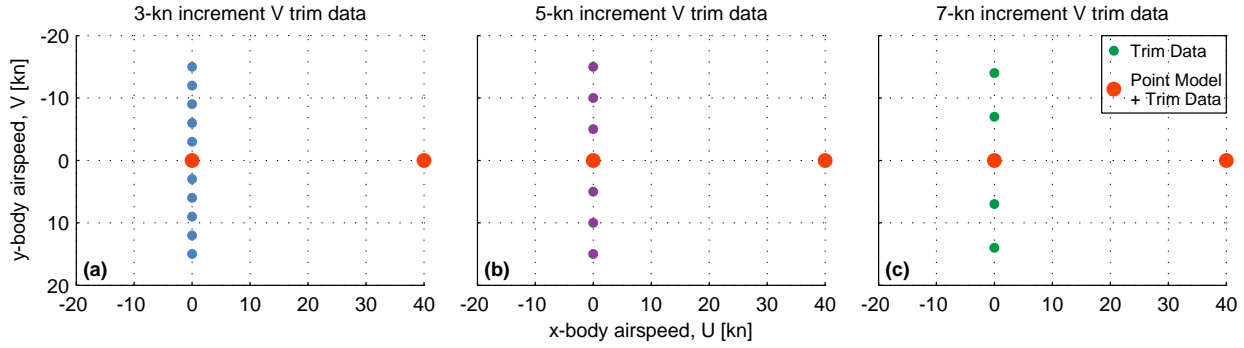
Figure 4.7: Sideward flight trim data points at 3-, 5-, and 7-kn y-body airspeed V increments, and point models at hover and 40 kn.

are captured very well with the 3- and 5-kn spacing over the displayed sideward airspeed range. The 7-kn spacing also captures the trends well, but slightly misses subtle inflections near the extremities of the data, and the fitted spline does not precisely capture the collective δ_{col} data near hover.

Also shown in Figure 4.8 are data labeled "stitching in U only," which are the results of trimming the stitched model without any y-body airspeed V trim data at all; anchor data points are those shown previously in Figure 4.2(b). The stitched model is capable of trimming to the sideward flight points, but without known sideward trim data the stitched model must rely on the values of the stability and control derivatives at the hover point to determine a trim solution. As such, the stitched model predicts a linear trend over the sideward airspeed range, missing much of the truth data. This supports the need to capture sideward flight trim data trends around hover and employ stitching in U and V for accurate hover/low-speed simulation.
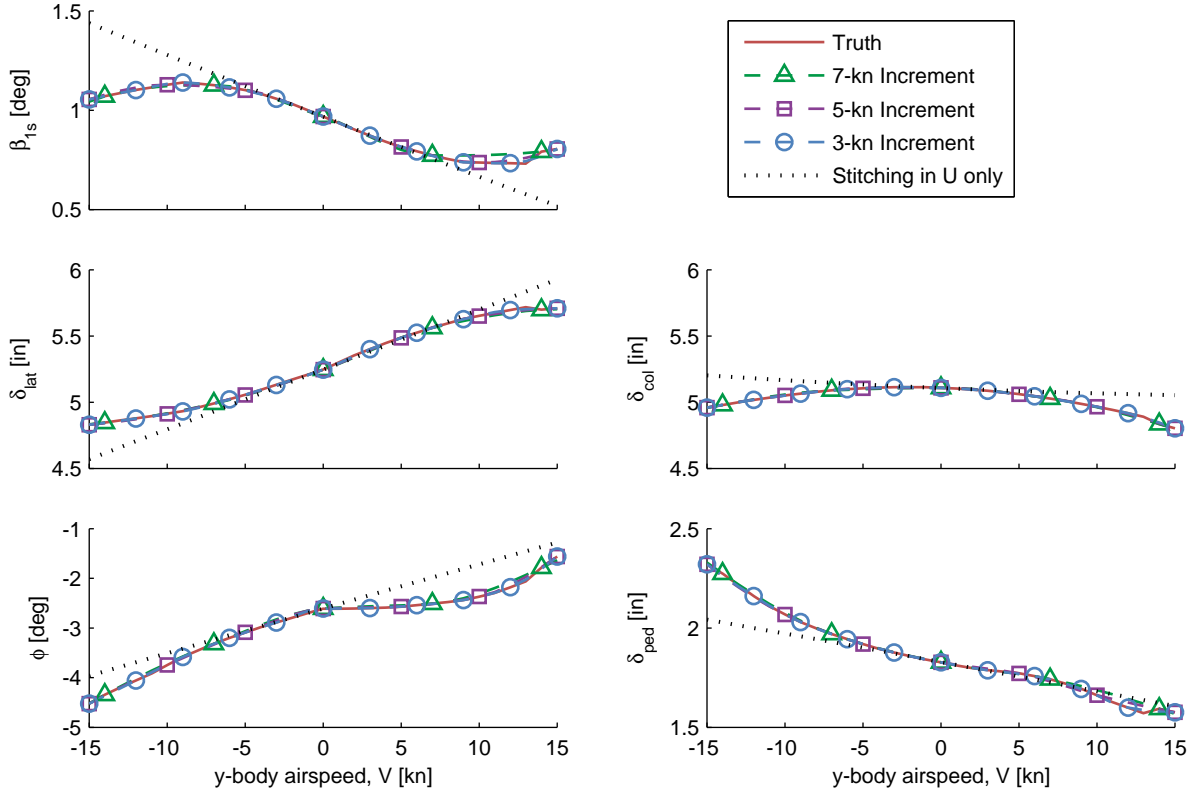
Figure 4.8: Spline-fit sideward flight trim values with various spacing.

68

The implicit v-speed derivative values, due to the sideward flight trim data of various spacing, are presented in Figure 4.9 and compared to FORECAST truth data over the same sideward airspeed V range of -15 to 15 knots. Overall there is very good agreement between the quasi-steady, implicit v-speed derivative values and the truth data, with the fine 3-kn-increment data most-closely matching the truth data over the sideward airspeed range, and the 5-kn-increment data also matching well. The 7-kn-increment results are degraded, especially in the key stability derivatives Y_v and L_v. In addition to the closeness of match of the derivative values over the airspeed range, the derivative values at the hover point $(V = 0)$ are also affected by the spacing of the data, due to the gradients between the data to either side of the hover point; this is most clearly seen in the hover point values of L_v. As such, the fine 3-kn-increment data most-closely match the truth values, and the match slightly degrades as the data become coarser.

Again, data labeled "stitching in U only" are the results of trimming/linearizing the stitched model over the sideward airspeed range without any y-body airspeed V trim data; forward airspeed U is the only interpolation dimension. Because the value of U remains at the hover value $(U = 0)$, the looked-up values of the v-speed derivatives are, in turn, constantly those of the hover point model over the entire sideward airspeed range, as seen in the straight dotted lines. These results further support the need for sideward flight trim data and employing stitching in U and V around hover to accurately preserve the dynamic response in sideward flight.
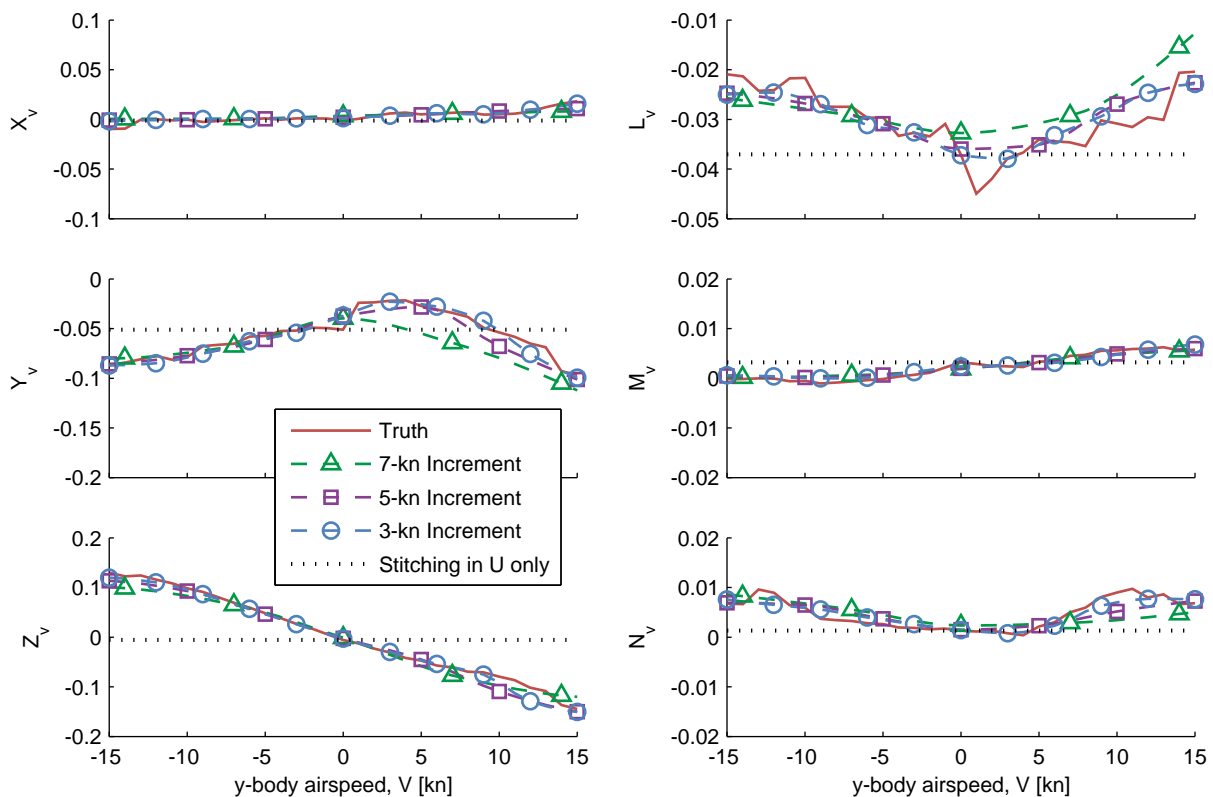
Figure 4.9: Implicit v-speed derivative values due to sideward flight trim data of various spacing.

To illustrate the effect of the implicit v-speed derivative values at the hover point on the dynamic response of the stitched model, primary on-axis frequency response comparisons between the high-order stitched model and the FORECAST truth point model are presented in Figures 4.10 and 4.11. The values of the v-speed derivatives affect the low-frequency coupled Pitch and Roll Phugoid modes, as seen most notably in the low-frequency portions of the magnitude responses. With increasing (coarser) spacing of the sideward trim data, the frequency response match slightly degrades below approximately 0.6 rad/sec.

To quantify the effect of the implicit v-speed derivative values on the dynamic response at hover, the natural frequency and damping ratio of the Pitch and Roll Phugoid modes are tabulated in Table 4.2, in which
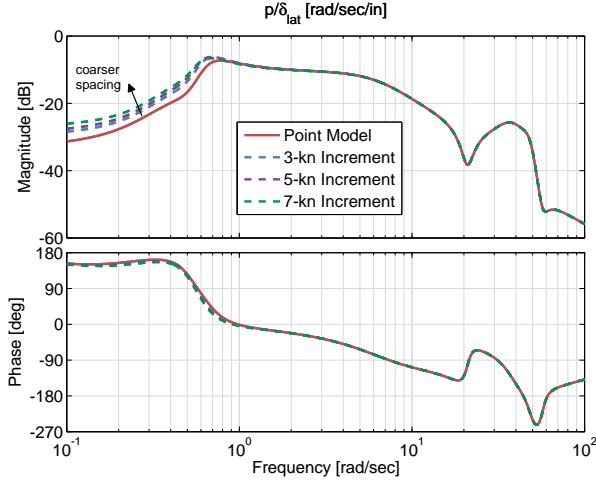
Figure 4.10: Roll rate response to lateral cyclic input comparison for sideward trim data of various spacing, hover.
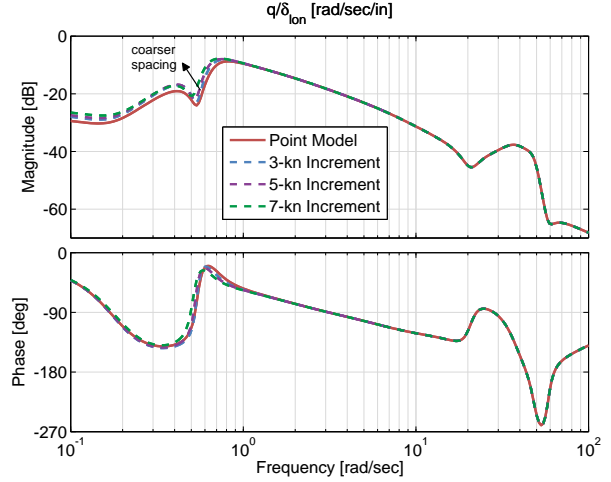
Figure 4.11: Pitch rate response to longitudinal cyclic input comparison for sideward trim data of various spacing, hover.

Table 4.2: Hover Phugoid modes for sideward trim data of varying y-body airspeed V increment

Mode	Parameter	Stitched Model			Point Model
		7-kn inc.	5-kn inc.	3-kn inc.	
Pitch Phugoid	ω_n [rad/sec]	0.4985	0.5043	0.5097	0.5207
	ζ	−0.4317	−0.4345	−0.4444	−0.4840
Roll Phugoid	ω_n [rad/sec]	0.5948	0.6093	0.6223	0.6524
	ζ	0.2011	0.2191	0.2226	0.2543

values of the linearized stitched model for the various sideward flight trim data increments are compared to those from the truth FORECAST hover point model. There is very good agreement in natural frequency and damping between the linearized stitched model with the 3-kn-spaced data and the truth point model; natural frequency and damping are within 3% and 9%, respectively, of the values from the point model for the Pitch Phugoid mode, and within 5% and 13% for the Roll Phugoid mode. There is also good agreement between the stitched model with the 5-kn-spaced data and the truth point model; natural frequency is within 4% and damping is within 11% for the Pitch Phugoid mode, and within 7% and 14% for the Roll Phugoid mode. The agreement between the stitched model with the 7-kn-spaced data and the truth point model is acceptable, yet the greatest disparities are seen overall; frequency and damping values within 5% and 11%, respectively, for the Pitch Phugoid mode, and values within 9% and 21% for the Roll Phugoid mode.

Based on these results, the 3- and 5-kn-increment y-body airspeed V trim data yield the most satisfactory accuracy, and are therefore recommended for the collection of sideward trim data in the hover/low-speed regime. A 5-kn increment set of sideward trim data is used in the UH-60 stitched model (see Section 4.5).

4.3.3 Quartering Flight Trim Data

Trim data of low-speed quartering flight (i.e., high-sideslip, diagonal flight toward some reference heading) are necessary not only for the simulation of such flight, but also for the simulation of hovering flight in the presence of quartering winds. Quartering flight at 45 degrees over a range of airspeed was investigated in the stitched model to verify the accuracy of the implicit v-speed derivatives. Additionally, scenarios of data with varying radial spacing were investigated to determine recommended radial increments and strategies for the collection of low-speed quartering trim points around hover.

Constant Flight Direction, Varying Airspeed

Quartering flight (i.e., 45-deg) trim data points at 5-kn airspeed V_{tot} increments were generated in FORE-CAST covering 0 to 20 knots total airspeed. These data points are shown graphically in Figure 4.12(a). Additionally, forward/sideward-only data points (i.e., no quartering data), shown in Figure 4.12(b), were also generated for comparison. Stability and control derivative values from point models are again included only at hover and 40 kn forward airspeed in both data sets in this low-speed regime. The data were fit with shape-preserving piecewise cubic splines to interpolate the data to a fine 1-kn increment over the 0 to 20 knot V_{tot} quartering flight range. The stitched model, configured with each of the two data sets, was then retrimmed and linearized for 45-deg quartering flight between hover and 20 knots total airspeed.
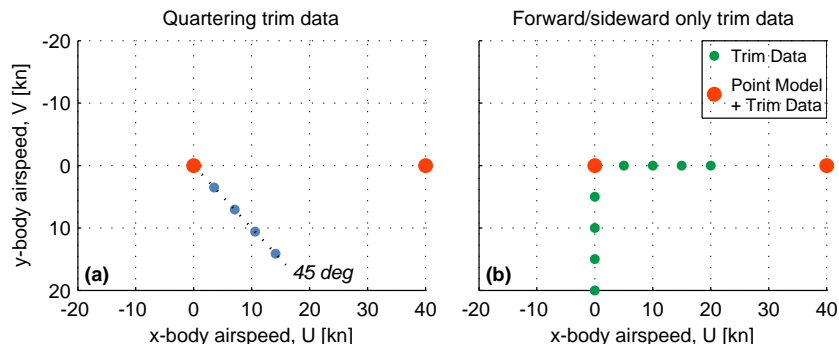
Figure 4.12: Quartering and pure forward/sideward flight trim data points at 5-kn airspeed V_{tot} increments, and point models at hover and 40 kn.

Figure 4.13 shows trim values of the controls, bank angle, and longitudinal rotor flapping angle β_{1c} from the stitched model, configured separately with quartering trim data and with forward/sideward only trim data, as compared to truth values from FORECAST over the 45-deg quartering airspeed range. The circle symbols indicate the original quartering flight trim data points used as anchor points for the spline fits. The truth data are captured very well by the stitched model configured with quartering data over the displayed quartering airspeed range, with the major trends represented. The results of the stitched model configured with forward/sideward-only trim data show good agreement near hover, but subtle inflections in the truth data are not captured, and the agreement degrades at the higher quartering airspeeds. For higher accuracy, especially for applications involving shipboard operations in which quartering flight is common, quartering data should be collected.

Data labeled "stitching in U only" are the results of trimming the stitched model without any quartering or sideward trim data; anchor data points are instead a function of x-body airspeed U only, and are those shown previously in Figure 4.2(b). The stitched model is capable of trimming to the quartering flight airspeed points without known sideward or quartering trim data, but the stitched model must rely on the values of the stability and control derivatives as a function of U only to determine a trim solution. As such, the stitched model predicts a trend that is roughly consistent with the truth data over the quartering airspeed range, but does not capture inflections.

Figure 4.14 shows the implicit v-speed derivative values obtained from trimming/linearizing the stitched model, configured separately with quartering data and with forward/sideward data only, in 45-deg quartering flight from hover through 20 kn total airspeed as compared to the FORECAST truth values. Also shown are data labeled "stitching in U only" which are results from the stitched model configured without y-body airspeed V trim data. The quasi-steady, implicit derivative values from the stitched model configured with quartering data track very well with the truth values over the quartering flight airspeed range. Gross inflections in key derivatives Y_v, Z_v, and L_v are effectively captured. Results of the stitched model configured with forward/sideward-only data roughly capture the truth data near hover, but inflections are not represented well. Moreover, results of "stitching in U only" follow a linear trend as a function of forward airspeed U (the cosine component of the 45-deg quartering flight), between the two anchor point models at hover and 40 kn, and do not capture any inflections in the truth data. These results support the need to capture quartering flight trim data trends around hover for accurate simulation of quartering flight.

71
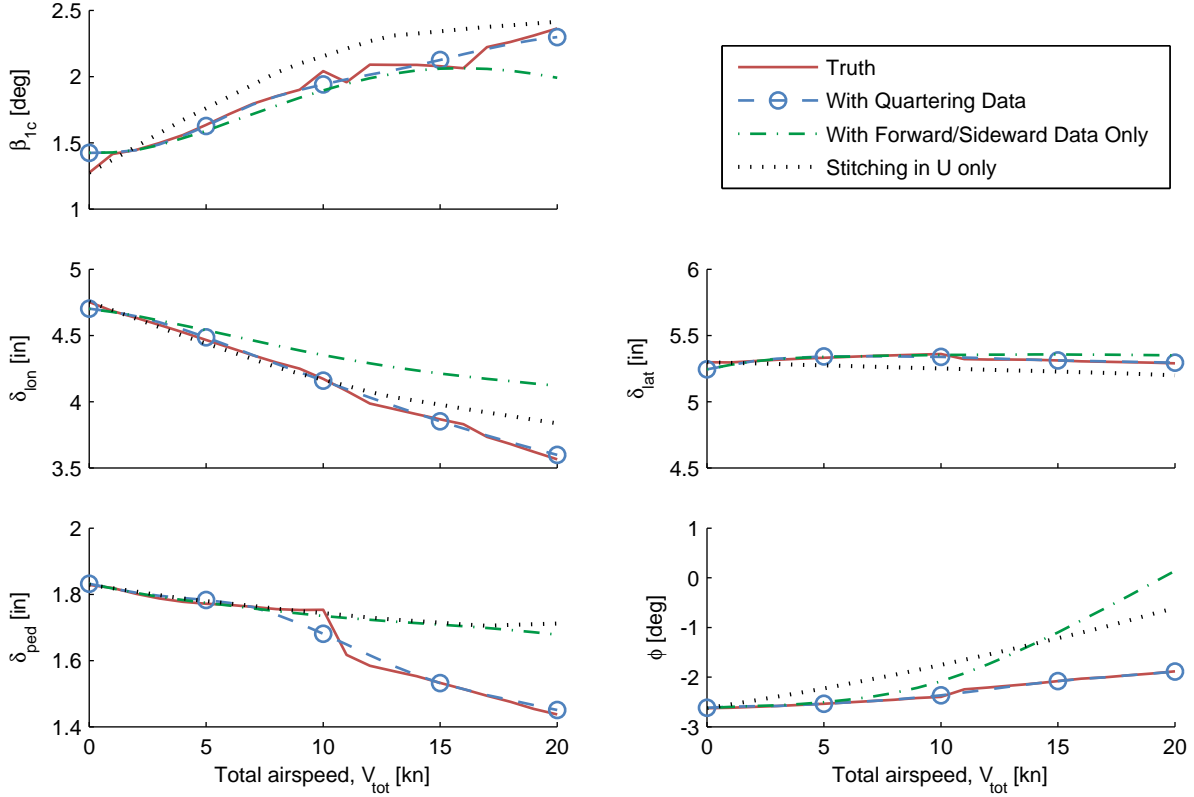
Figure 4.13: Trim values for 45-deg quartering flight up to 20 kn.

The dynamic response of the high-order stitched model was checked at 10-kn V_{tot}, 45-deg quartering flight. Figures 4.15 and 4.16 show the frequency response comparisons between the stitched model configured with quartering flight trim data, the stitched model configured with forward/sideward-only trim data, and the FORECAST point model for the 10-kn, 45-deg quartering flight condition. For the stitched model configured with quartering flight trim data there is very good agreement in the low-frequency portion of the responses, including the Pitch and Roll Phugoid modes, and excellent agreement over the remainder of the displayed frequency range. The agreement between the stitched model configured with forward/sideward-only trim data and the truth point model is degraded in the low-frequency portion of the responses.

The natural modes of the three systems compared in Figures 4.15 and 4.16 are provided in Table 4.3. The stitched model, configured with 45-deg quartering trim data and linearized at the 10-kn, 45-deg quartering condition, is in excellent agreement with the truth point model at the same 10-kn, 45-deg quartering condition. The low-frequency Pitch and Roll Phugoid modes, which are heavily affected by the implicit speed derivative values, are in close agreement. Note that the stitched model predicts two real Yaw and Heave poles, whereas the modes are combined into two complex poles in the truth point model. Results of the stitched model configured with forward/sideward-only trim data and linearized at the 10-kn, 45-deg quartering condition are satisfactory, but show larger discrepancies in the low-frequency Pitch and Roll Phugoid modes. These results verify the advantage of collecting and including quartering flight trim data in the stitched model for improved accuracy in the simulation of quartering flight.
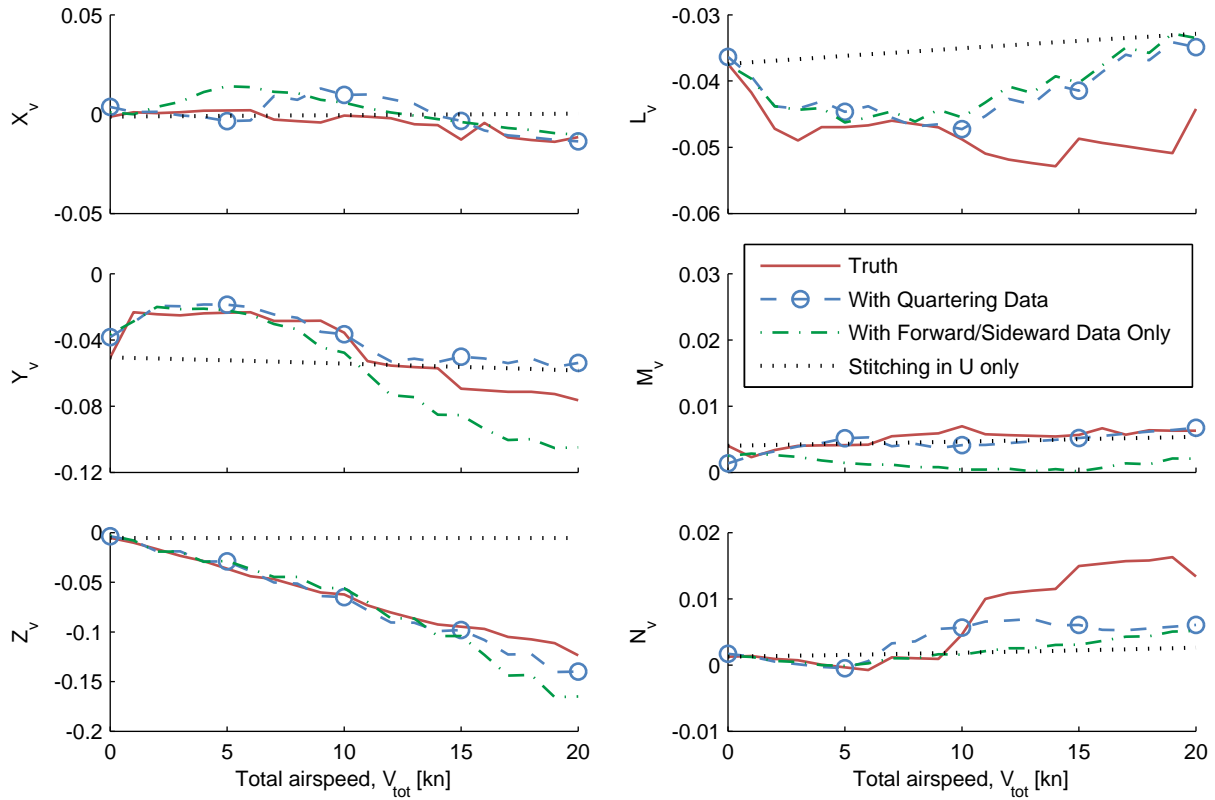
Figure 4.14: Implicit v-speed derivative values for 45-deg quartering flight up to 20 kn.
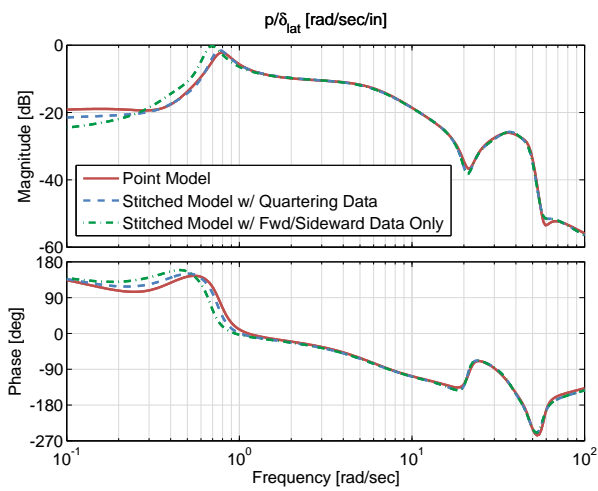
Figure 4.15: Roll rate response to lateral cyclic input for 10-kn, 45-deg quartering flight.
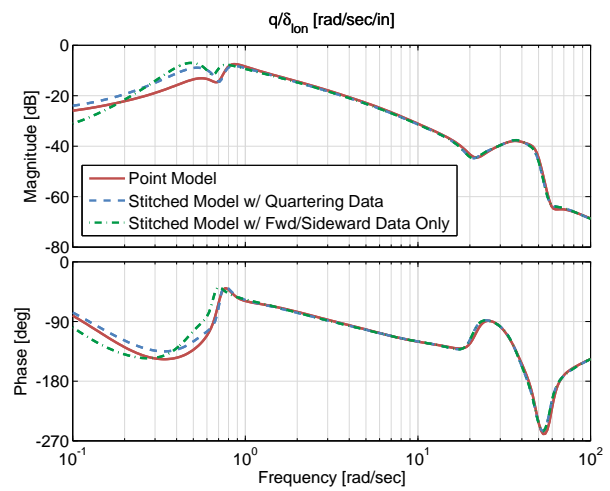
Figure 4.16: Pitch rate response to longitudinal cyclic input for 10-kn, 45-deg quartering flight.

Table 4.3: Modes – 10-kn, 45-deg quartering flight

Mode	Parameter	Stitched Model with fwd/sideward data only	Stitched Model with quartering data	Point Model
Yaw/Heave	ω_n [rad/sec] ζ	0.2273/0.2681 1.0000/1.0000	0.2143/0.2663 1.0000/1.0000	0.2262 0.8668
Pitch Phugoid	ω_n [rad/sec] ζ	0.4758 −0.3314	0.5496 −0.4014	0.6252 −0.4012
Roll Phugoid	ω_n [rad/sec] ζ	0.6799 0.1215	0.7491 0.1268	0.7751 0.1443
Pitch Aperiodic	$1/\tau$ [rad/sec]	1.1934	1.2971	1.5352
Collective Lead/Lag	ω_n [rad/sec] ζ	2.4455 0.8601	2.4445 0.8601	2.5040 0.8752
Rotor RPM	$1/\tau$ [rad/sec]	3.8432	3.8453	3.1485
Roll Aperiodic	$1/\tau$ [rad/sec]	4.6227	4.6224	4.3797
Regressive Flap	ω_n [rad/sec] ζ	6.3264 0.6729	6.3249 0.6726	6.2485 0.6440
Constant Inflow	$1/\tau$ [rad/sec]	11.3716	11.3701	11.3475
Regressive Lead/Lag	ω_n [rad/sec] ζ	20.3266 0.2570	20.3258 0.2569	21.3182 0.2830
1st Harmonic Inflow	ω_n [rad/sec] ζ	22.2268 0.9031	22.2255 0.9032	21.7088 0.8929
Collective Flap	ω_n [rad/sec] ζ	27.1492 0.3491	27.1491 0.3491	27.1355 0.3478
Progressive Lead/Lag	ω_n [rad/sec] ζ	37.8272 0.2043	37.8278 0.2043	37.3950 0.2404
Tail Rotor Inflow	$1/\tau$ [rad/sec]	38.8634	38.8615	43.5981
Progressive Flap	ω_n [rad/sec] ζ	48.7096 0.0987	48.7090 0.0987	48.7416 0.0961

Constant Airspeed, Varying Wind Direction

Hovering flight in the presence of steady winds is demonstrated for the UH-60 stitched model by trimming the model in a position-held/heading-held hover with a 10-kn wind of varying direction through a complete 360 degrees. These analyses employ the steady wind simulation element described in Section 2.4.1. The stitched model was configured with three separate trim data sets with radial increments of 30 deg, 45 deg, and 90 deg (i.e., no quartering data), all at 5-kn total airspeed V_{tot} increments, as depicted in Figure 4.17. The 10-kn wind magnitude is also depicted. Stability and control derivative values (i.e., point models) are again included only at hover and 40 kn forward airspeed.
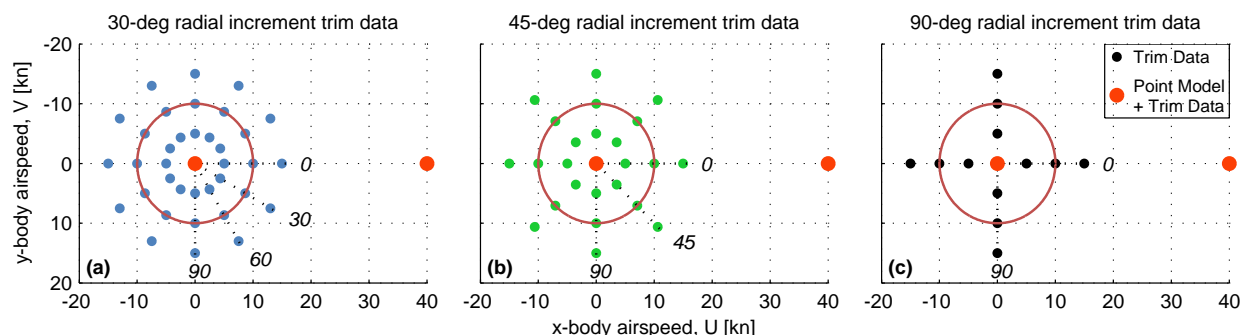
Figure 4.17: Trim data points at 30-, 45-, and 90-deg radial increments, with 10-kn magnitude indicated, and point models at hover and 40 kn.

Figure 4.18 presents the results of trimming the stitched model in hover with the presence of a steady 10-kn wind of varying direction. The wind vector was rotated in direction through 360 degrees as the stitched model held the aircraft's position and Northerly (0-deg) heading. The mapping of the trim cyclic stick position for all wind directions is shown in lateral (δ_{lat}) and longitudinal (δ_{lon}, positive *aft*) components, with winds from the cardinal directions of 0, 90, 180, and 270 deg indicated. The trim values of the remaining two controls, collective stick δ_{col} and pedals δ_{ped}, as well as the trim aircraft bank angle ϕ and pitch angle θ are plotted against wind direction in degrees. Note that indicated wind direction is *from* a specified heading, and is analogous to flight toward that heading.

The stitched model configured with quartering trim data (i.e., 30- and 45-deg radial increment data) tracks very well with the FORECAST truth data throughout the entire wind rotation. Although the trim results of the stitched model configured without quartering data (i.e., the 90-deg radial increment data) capture the gross trends in δ_{col}, δ_{ped}, and pitch angle over the wind direction range, subtle inflections are missed, most noticeably in the bank angle trend. Furthermore, there are disparities in the mapping of trim cyclic stick position from the stitched model configured with the 90-deg radial data, including discrepancies in the shape and magnitude of the mapping between 0 and 180 deg, and a reversal of the trends between 180 deg and 270 deg. These results support the need for radial trim data for the accurate simulation of hovering flight in the presence of quartering winds. The 45-deg radial increment data set produces results that are very close to those of the 30-deg radial increment set, and capture all critical inflections in the truth data.

Based on these and previous results, radial trim data every 45 degrees, with 5-kn V_{tot} spacing, is recommended for accurate simulation in low-speed forward, rearward, sideward, and quartering flight, as well as accurate simulation of hover/low-speed flight in the presence of winds. These trim data points are used to configure the hover/low-speed flight conditions of the UH-60 stitched model, as presented in Section 4.5, and are recommended in flight testing for the development of rotorcraft stitched models (see Section 4.9).
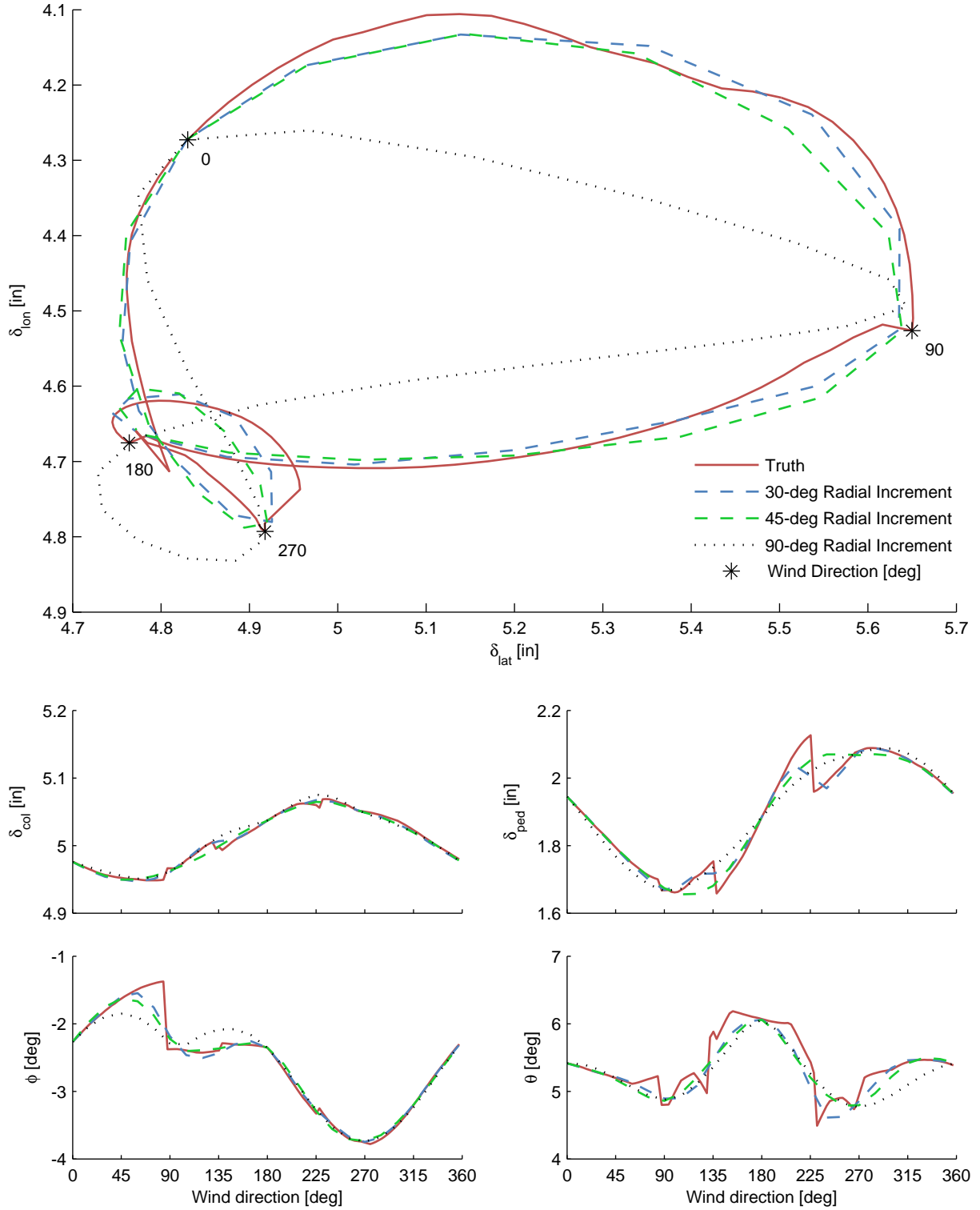
Figure 4.18: Stitched model trim results of position-held/heading-held hovering flight in the presence of a rotating 10-knot wind through 360 degrees.

4.4 Forward-Flight Trim Data

In the forward-flight regime of the UH-60 stitched model, "stitching in U" alone is applied, necessitating the collection of forward-flight trim data as a function of x-body airspeed U only. Analogous to the hover/low-speed trim data analyses presented in Section 4.3, the effects of the spacing of forward-flight trim data points on the accuracy of the implicit u-speed derivatives and the dynamic responses at the forward-flight identification points are presented in this section.

Trim data points as a function of x-body airspeed U at increments of 10 and 20 knots, covering a range of airspeed from 20 kn to 160 kn, were investigated in the stitched model. These data points are shown graphically in Figure 4.19. Also included and shown graphically in Figure 4.19 are point models at the following airspeeds in this forward-flight regime: 40, 80, and 120 kn. The trim data were fit with shape-preserving piecewise cubic splines (i.e., MATLAB function `interp1` with method '`pchip`' [12]) to interpolate the data to fine 1-kn increment sets over the airspeed range of the data. The stitched model, configured with the two different trim data sets of 10- and 20-kn x-body airspeed increment, was then retrimmed and linearized over the 20–160 knot airspeed range.

Figure 4.20 shows trim values of the controls, attitude, and longitudinal rotor flapping angle β_{1c} from the stitched model configured for each of the trim data sets as compared to truth values from FORECAST. Square and triangle symbols indicate the original data points of the 10- and 20-kn sets, respectively, used as anchor points for the spline fits. The truth trim data from FORECAST are nearly-perfectly captured with the 10-kn spacing over the investigated forward-flight airspeed range. The 20-kn spacing captures the data above 80 kn very well, but somewhat misses subtle inflections in the trends of pitch attitude θ, longitudinal cyclic stick δ_{lon}, and longitudinal rotor flapping angle up to 80kn.

The implicit u-speed derivative values, due to the x-body airspeed U trim data of different spacing, are shown in Figure 4.21 and compared to FORECAST truth data over the same airspeed range of 20–160 knots. Overall there is very good agreement between the quasi-steady, implicit u-speed derivative values and the truth data, with the 10-kn-increment data most-closely matching the truth data over the airspeed range. The 20-kn-increment data also match well, but show a slightly degraded agreement up through 80 kn and in regions of subtle inflection. Additionally, the derivative values at the point model airspeeds of 40, 80 and 120 kn are affected by the spacing of the data, due to the gradients between the data to either side of each point model. In general, the 10-kn-increment data most-closely match the truth values at the identification point airspeeds.

To quantify the effects of the implicit u-speed derivative values on the dynamic response at each identification point, the inverse time constant or natural frequency and damping ratio values of the low-frequency modes at 40, 80, and 120 kn are tabulated in Table 4.4, in which values of the linearized stitched model for the 10- and 20-kn trim data increment sets are compared to values from the truth FORECAST point model at each of the three airspeeds. The corresponding primary on-axis roll and pitch frequency response comparisons between the high-order stitched model and the truth point model at 40, 80, and 120 kn are presented in Figures 4.22–4.27. The values of the u-speed derivatives affect the low-frequency dynamics, as
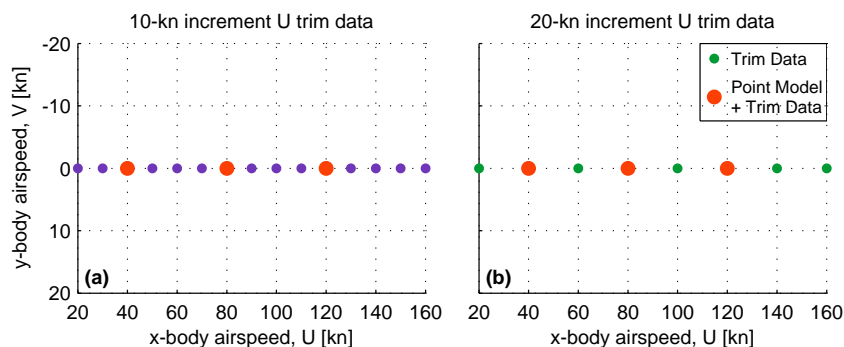

Figure 4.19: Forward-flight trim data points at 10- and 20-kn x-body airspeed U increments, and point models at 40, 80, and 120 kn.
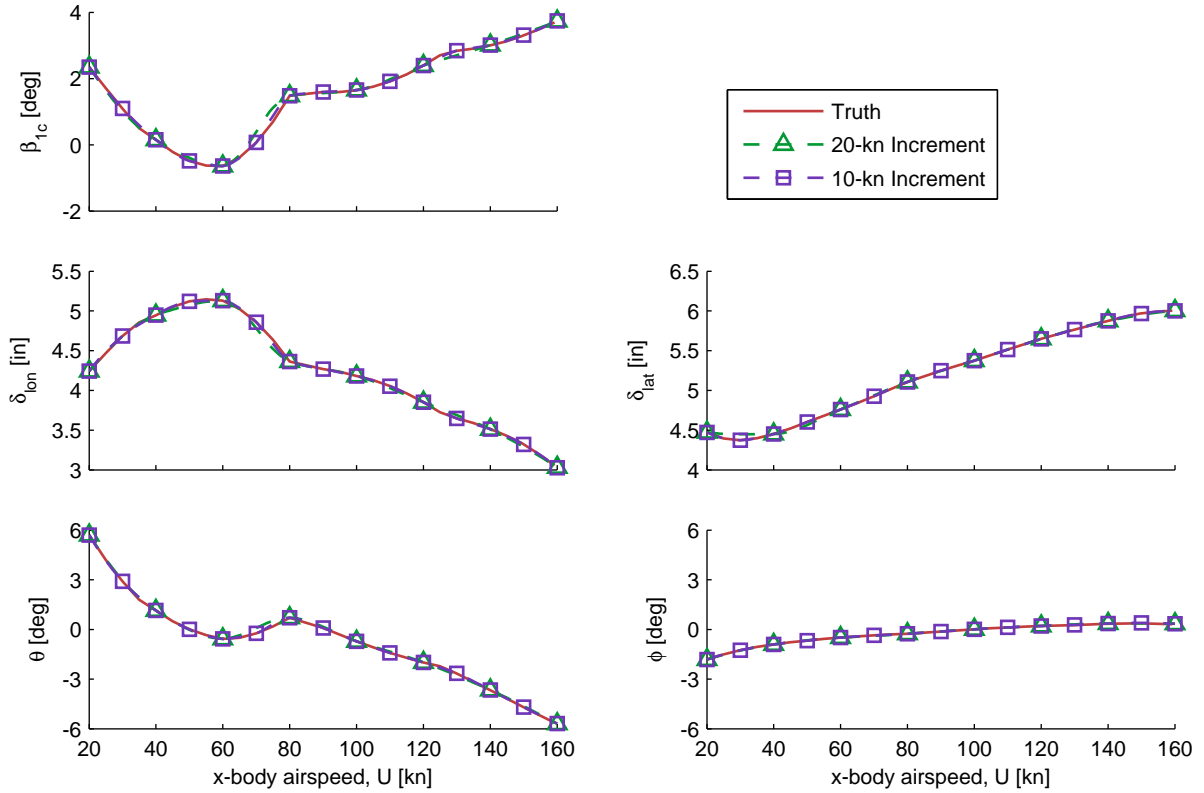
Figure 4.20: Spline-fit forward-flight trim values with 10- and 20-kn spacing.

seen in the frequency responses below approximately 0.5 rad/sec. The largest differences between results of the 10- and 20-kn increment trim data sets are seen for the 40-kn point model, with the 10-kn-increment data more-closely matching the truth modes. The 10-kn-increment data produce somewhat better results for the 80-kn point model, and acceptable results are seen from both sets of data for the 120-kn point.

Overall, the 10-kn-increment x-body airspeed U trim data track very well with the FORECAST truth data through 80 kn, and yield excellent dynamic response results at the 40- and 80-kn point models. The 20-kn-increment trim data have satisfactory agreement with the truth data above 80 kn, and the dynamic response at 120 kn is captured well by both 10- and 20-kn increment data sets. Therefore, for the collection of forward-flight trim data for use in the stitched model, a 10-kn x-body airspeed U spacing is recommended from 20 kn through 80 kn, and thereafter a 20-kn spacing is satisfactory.

In total, the overall recommended hover/low-speed (Section 4.3) and forward-flight trim data points are used for the UH-60 stitched model anchor points, as presented in Section 4.5. These recommendations are also summarized in the flight-test implications for the development of rotorcraft stitched models in Section 4.9.
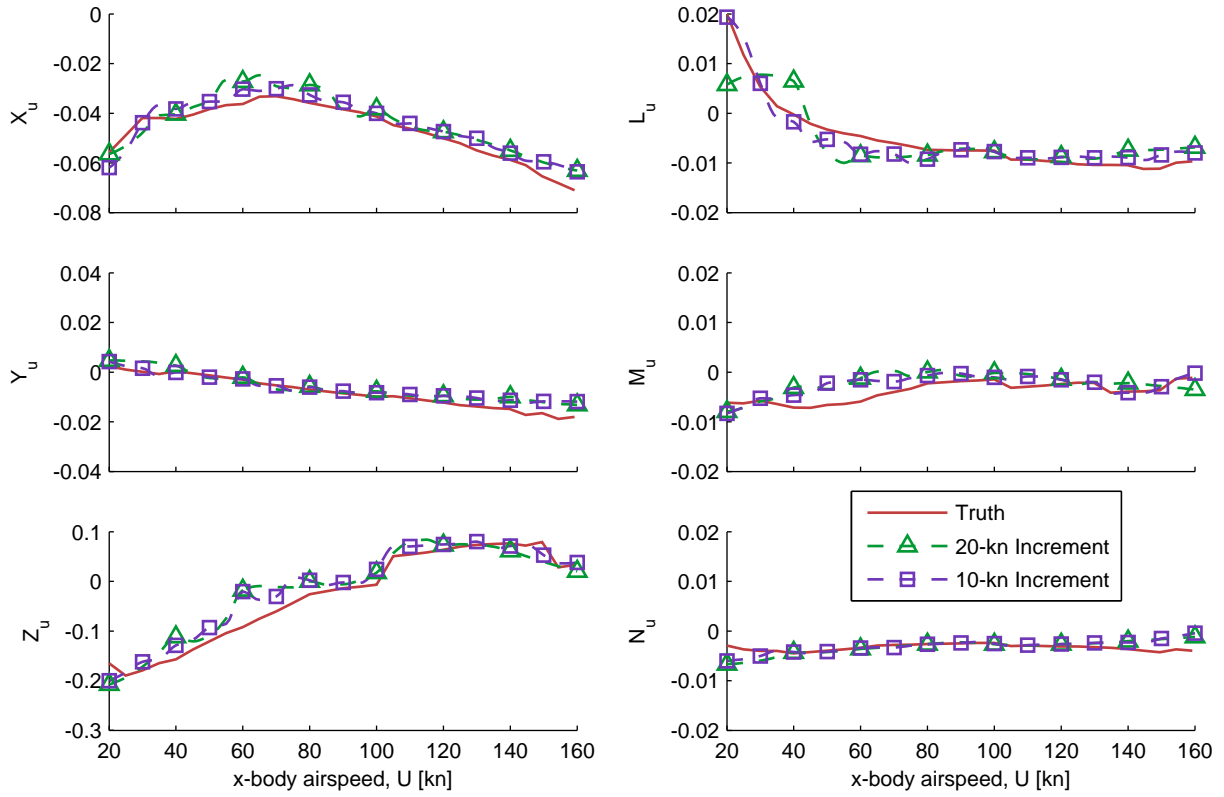
Figure 4.21: Implicit u-speed derivative values due to forward-flight trim data of 10- and 20-kn spacing.

Table 4.4: Low-frequency modes at 40, 80, and 120 kn for forward-flight trim data of 10- and 20-kn x-body airspeed U increments

ID Point	Mode	Parameter	Stitched Model 20-kn inc.	10-kn inc.	Point Model
40 kn	Roll	$1/\tau$ [rad/sec]	0.2495	0.2328	0.1981
	Pitch Phugoid	ω_n [rad/sec] ζ	0.3060 0.4047	0.3613 0.4694	0.4387 0.5552
	Pitch	$1/\tau$ [rad/sec]	-0.3357	-0.3958	-0.4795
80 kn	Roll	$1/\tau$ [rad/sec]	0.1905	0.1870	0.1809
	Pitch Phugoid	ω_n [rad/sec] ζ	0.2522 0.1335	0.2611 0.1674	0.2665 0.1988
	Pitch	$1/\tau$ [rad/sec]	-0.4314	-0.4482	-0.4532
120 kn	Roll	$1/\tau$ [rad/sec]	0.2174	0.2291	0.2538
	Pitch Phugoid	ω_n [rad/sec] ζ	0.2760 0.2379	0.2701 0.1994	0.2613 0.1095
	Pitch	$1/\tau$ [rad/sec]	-0.4181	-0.4101	-0.3933
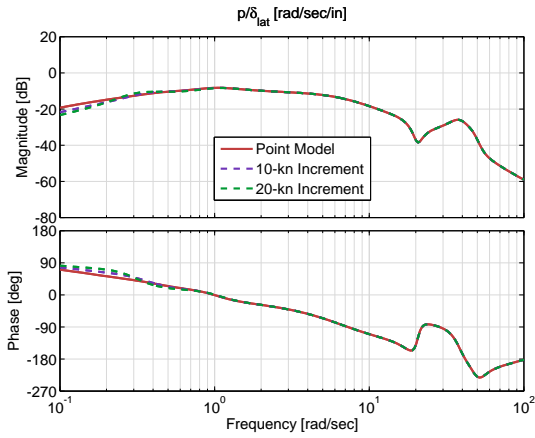
Figure 4.22: Roll rate response to lateral cyclic input comparison for forward-flight trim data of 10- and 20-kn spacing, 40 kn.
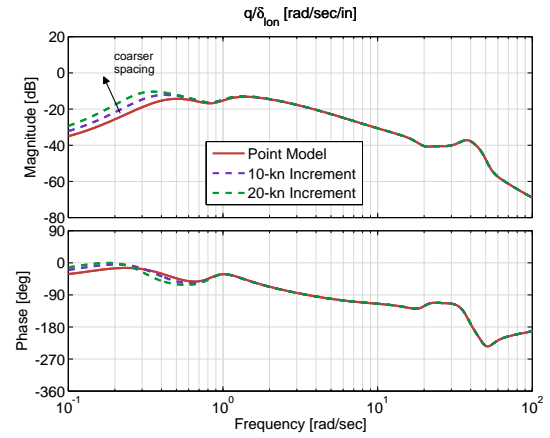
Figure 4.23: Pitch rate response to longitudinal cyclic input comparison for forward-flight trim data of 10- and 20-kn spacing, 40 kn.
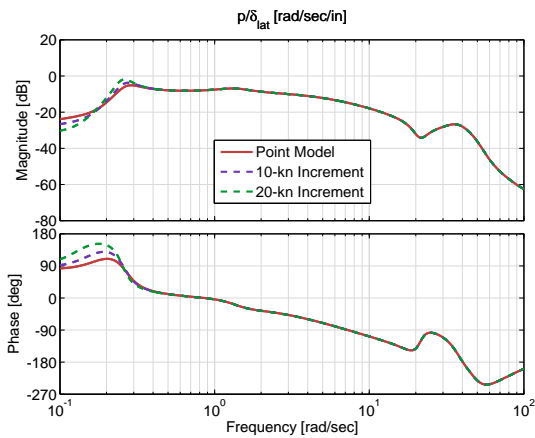
Figure 4.24: Roll rate response to lateral cyclic input comparison for forward-flight trim data of 10- and 20-kn spacing, 80 kn.
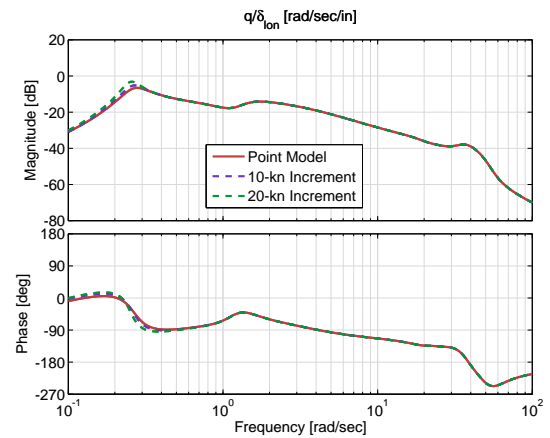
Figure 4.25: Pitch rate response to longitudinal cyclic input comparison for forward-flight trim data of 10- and 20-kn spacing, 80 kn.
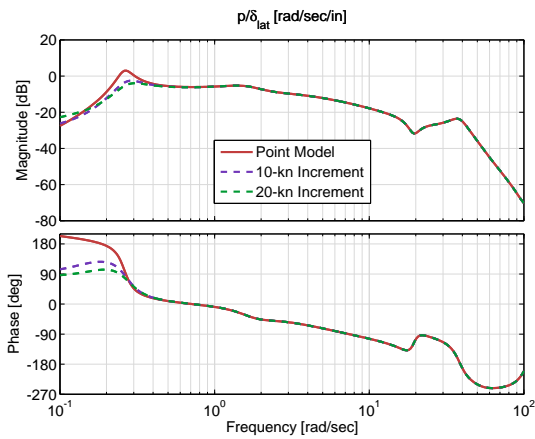
Figure 4.26: Roll rate response to lateral cyclic input comparison for forward-flight trim data of 10- and 20-kn spacing, 120 kn.
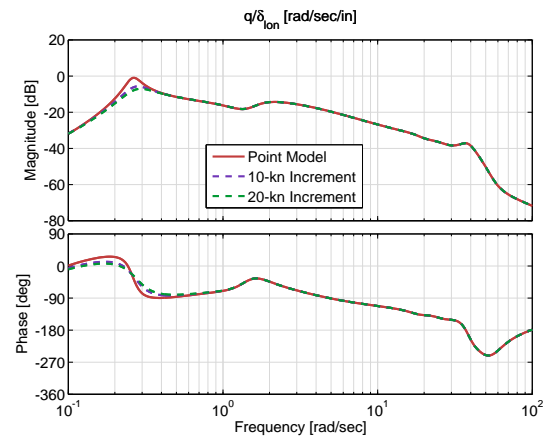
Figure 4.27: Pitch rate response to longitudinal cyclic input comparison for forward-flight trim data of 10- and 20-kn spacing, 120 kn.

4.5 Flight Condition Anchor Points

A series of linear point models and a collection of trim data were generated in FORECAST to be used as anchor points in the UH-60 stitched model. Naturally, a very large collection of point models and trim data could be used in the stitched model; however, based on the findings presented in Sections 4.3 and 4.4, flight conditions for the point models and trim points were selected to allow the accurate simulation of the dynamic response of the helicopter over the airspeed envelope while considering practical flight-test implications. Thus, four state-space point models (with corresponding trim data) of the following airspeeds are included in the stitched model: hover, 40, 80, and 120 knots.

Fine-increment trim points around hover are necessary to accurately capture the migration of controls and helicopter attitude for the simulation of low-speed forward, rearward, sideward, and quartering flight, as well as the simulation of hovering flight in the presence of winds. These hover/low-speed trim data are included in the stitched model as a function of both x-body airspeed U *and* y-body airspeed V; therefore, "stitching in U and V" is applied in the hover/low-speed regime. This results in the implicit representation of the v-speed derivatives (e.g., Y_v and L_v) in addition to the implicit u-speed derivatives. Forward-flight trim data are included in the stitched model as a function of x-body airspeed U alone; therefore, "stitching in U" is applied in the forward-flight regime.

Based on the analyses presented in Section 4.3.1, low-speed forward and rearward flight trim data with x-body airspeed U increments of 5 knots were found to produce implicit u-speed derivative values in close agreement with those from FORECAST truth data at hover and over the investigated airspeed range. Similarly, based on the analyses presented in Section 4.3.2, sideward flight trim data with y-body airspeed V increments of 5 knots were found to produce implicit v-speed derivative values in close agreement with those from truth data at hover and over the sideward flight airspeed range. Additionally, per analyses presented in Section 4.3.3, 45-deg radial increment quartering flight trim points, with total airspeed increments of 5 knots, were also included to adequately cover the entire hover/low-speed flight regime, and to allow accurate simulation of low-speed flight in the presence of winds. This 5-kn spacing was therefore employed herein for the selection of forward, rearward, sideward, and quartering trim data points for the UH-60 stitched model around hover. At forward airspeeds above 20 knots, trim points are included in the stitched model with a 10-kn spacing up to 80 knots and a coarser 20-kn spacing to high speed to effectively capture critical inflections in forward-flight trim controls and attitude, as presented in Section 4.4.

The flight conditions of the four state-space point models and all trim points included in the UH-60 stitched model are illustrated in Figure 4.28 on a U,V airspeed grid. Units are displayed in ft/sec and knots. The hover/low-speed (stitching in U and V) and forward-flight (stitching in U only) regimes are denoted.
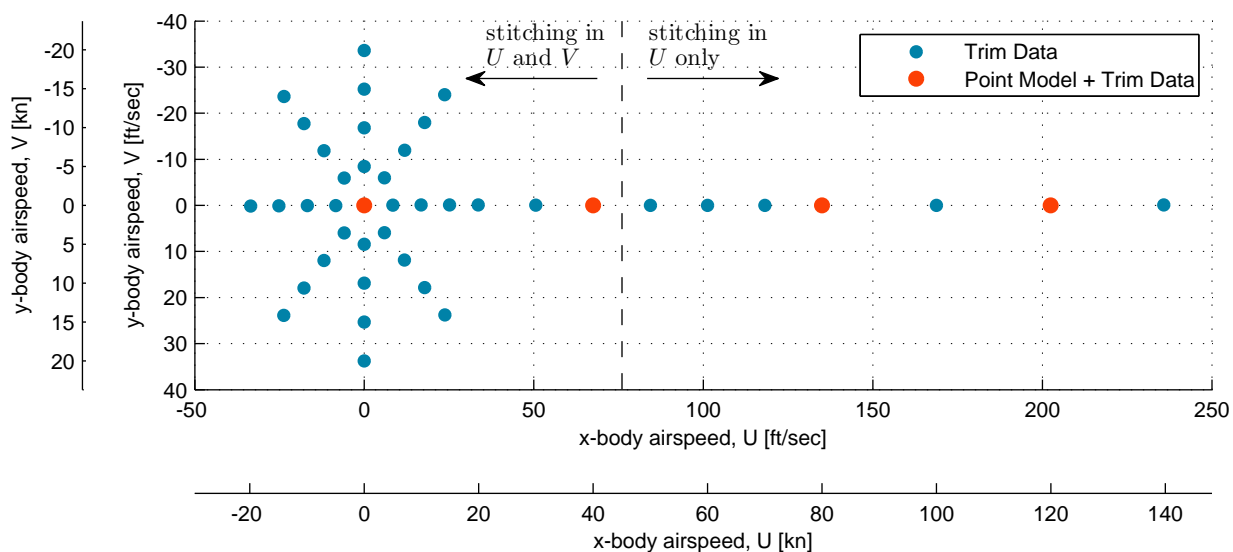

Figure 4.28: U,V airspeed points for anchor trim data and point models included in the stitched model.

Two-dimensional interpolation of the hover/low-speed trim data was utilized to construct a full rectangular grid of data with uniformly-spaced x-body airspeed U in one dimension and uniformly-spaced y-body airspeed V in the second dimension, per requirements of the model stitching architecture interpolation scheme (see Section 2.9.1). The 2-D interpolation of the data was performed using the MATLAB function `griddata` with method '`v4`', which interpolates a scattered data set over a uniform grid using biharmonic spline interpolation [12]. Specifically, the hover/low-speed rectangular grid is defined by a uniform increment of 2 ft/sec (approximately 1.2 kn) in both U and V dimensions, covering -40 to 80 ft/sec (-24 to 47 kn) x-body airspeed U, and -40 to 40 ft/sec (-24 to 24 kn) y-body airspeed V.

Sample interpolated data are displayed in Figure 4.29 as 3-D mesh surface plots, showing the interpolated values of trim control positions versus x-body airspeed U and y-body airspeed V over the defined rectangular grid. Values at the anchor trim points, shown previously in Figure 4.28, are depicted by blue spheres. The interpolated mesh data are smooth and precisely capture critical inflections in the anchor trim data.
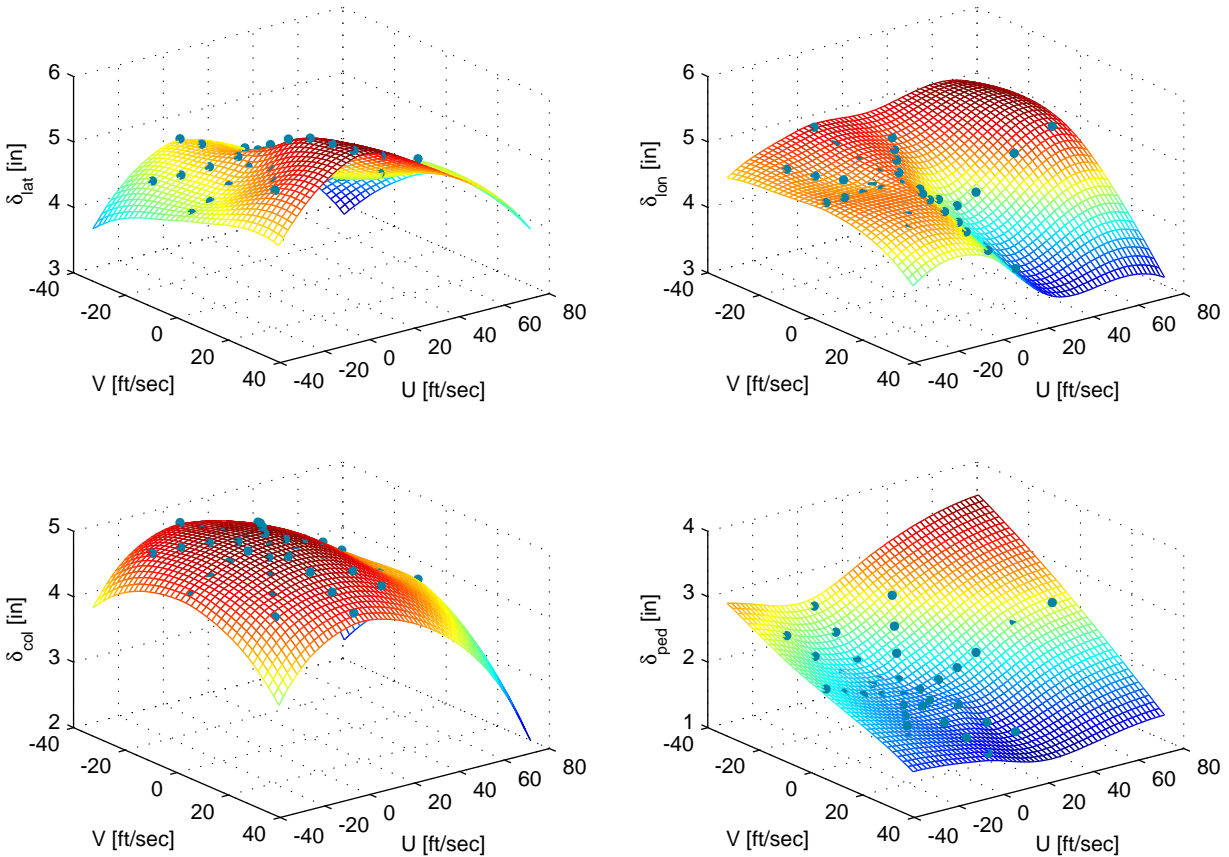
Figure 4.29: Two-dimensional interpolation of trim control values to U,V airspeed full rectangular grid – hover/low-speed regime.

4.6 Verification of Extrapolation Methods

Ranges of airspeed, gross weight, inertia, and CG location were investigated in the UH-60 stitched model in order to verify the off-nominal extrapolation methods used. A baseline configuration of 16,000 lb, mid CG was chosen for all FORECAST point models used in the stitched model. The stitched model was retrimmed (using the MATLAB function `findop` [12]) and relinearized (using the MATLAB function `linearize` [12]) at each verification point, with the results verified against a large database of off-nominal truth FORECAST point models. The results verify the built-in accommodation in the model stitching architecture for simulating off-nominal values of weight and inertia (Section 2.5.1) and CG location (Section 2.5.2).

Variations in altitude were also investigated. Due to the complexity of the rotor system, many stability and control derivatives do not scale linearly with air density, so utilizing the fixed-wing altitude extrapolation method (see Section 2.6) for a rotorcraft application does not fully predict results for alternate altitudes. Rather, it has been shown herein that linearly interpolating between point models and trim data at different altitudes yields very good results for rotorcraft.

For all comparisons of stability and control derivative values presented herein for the rotorcraft example, the full 26-state FORECAST truth models and high-order stitched model were first reduced to *quasi-steady* 6-DOF models. Quasi-steady derivative values are shown for meaningful comparisons and interpretation of the stability and control derivatives. Additional off-nominal verification results are provided in Appendix C.

4.6.1 Weight

The method for off-nominal weight extrapolation incorporated in the model stitching simulation architecture, as presented in Section 2.5.1, was utilized on the UH-60 stitched model. Key results of simulating off-nominal gross weights are shown in Figure 4.30. The stitched model, configured only with anchor point models and trim data of the nominal 16,000-lb configuration (solid symbols), was retrimmed and relinearized for three simulation values of gross weight over the full range of airspeed (dashed lines) and compared with FORECAST truth data (solid lines). Overall there is excellent agreement between the values from the stitched model and the truth data.

A change in gross weight mainly affects trim collective δ_{col} around hover and low speed, and has a noticeable effect on trim pitch attitude in the mid- to high-speed range, which are both captured nearly perfectly by the stitched model. The corresponding longitudinal cyclic stick position δ_{lon} (positive *aft*), affected mainly by trim pitch attitude, is predicted very well by the stitched model. Significant shifts of the primary heave-axis control derivative $Z_{\delta_{\mathrm{col}}}$ values are seen with change in weight, where a heavier weight results in a smaller vertical net force for a given collective input, and thus a derivative value of smaller magnitude (z-axis positive *down*). This effect is represented very well by the stitched model; values over the airspeed range for the anchor weight configuration are in good agreement, and the values from retrimming/relinearizing the stitched model for the off-nominal weights are also in good agreement over the airspeed range.

These results verify the capability to extrapolate to off-nominal values of weight using only anchor point data of a nominal weight. See Section C.1 for additional off-nominal weight verification results.

4.6.2 Inertia

The method for off-nominal inertia extrapolation incorporated in the model stitching simulation architecture, as presented in Section 2.5.1, was utilized on the UH-60 stitched model. Variations in the simulation values of the moments of inertia I_{xx}, I_{yy}, and I_{zz} were investigated individually within the UH-60 stitched model. The results are discussed over the succeeding subsections. See Section C.2 for the complete set of off-nominal inertia verification results.

Roll Inertia

Results of varying roll inertia I_{xx} are shown by the quasi-steady stability and control derivatives in Figure 4.31. The stitched model, configured with only anchor point models and trim data of the nominal configuration (solid symbols), was retrimmed and relinearized for three simulation values of roll inertia over the full range of airspeed (dashed lines) and compared with FORECAST truth data (solid lines). The baseline roll inertia value of 4659 slug-ft^2 is that of the nominal 16,000-lb configuration, a value of 4077 slug-ft^2 corresponds to a weight of 14,000 lb, and a value of 5824 slug-ft^2 corresponds to a weight of 20,000 lb, which were the weight values presented in Section 4.6.1.

The values of key roll control derivative $L_{\delta_{\mathrm{lat}}}$ are inversely proportional to values of I_{xx}, where an increase in roll inertia yields a lesser external roll moment for a given lateral cyclic stick input. Cross-coupling lateral/directional control derivatives $L_{\delta_{\mathrm{ped}}}$ and $N_{\delta_{\mathrm{lat}}}$ are similarly affected. This inversely proportional characteristic is seen also in stability derivative L_p. There is excellent agreement overall between the values from the stitched model and the FORECAST truth data. See Section C.2.1 for additional off-nominal roll inertia verification results.
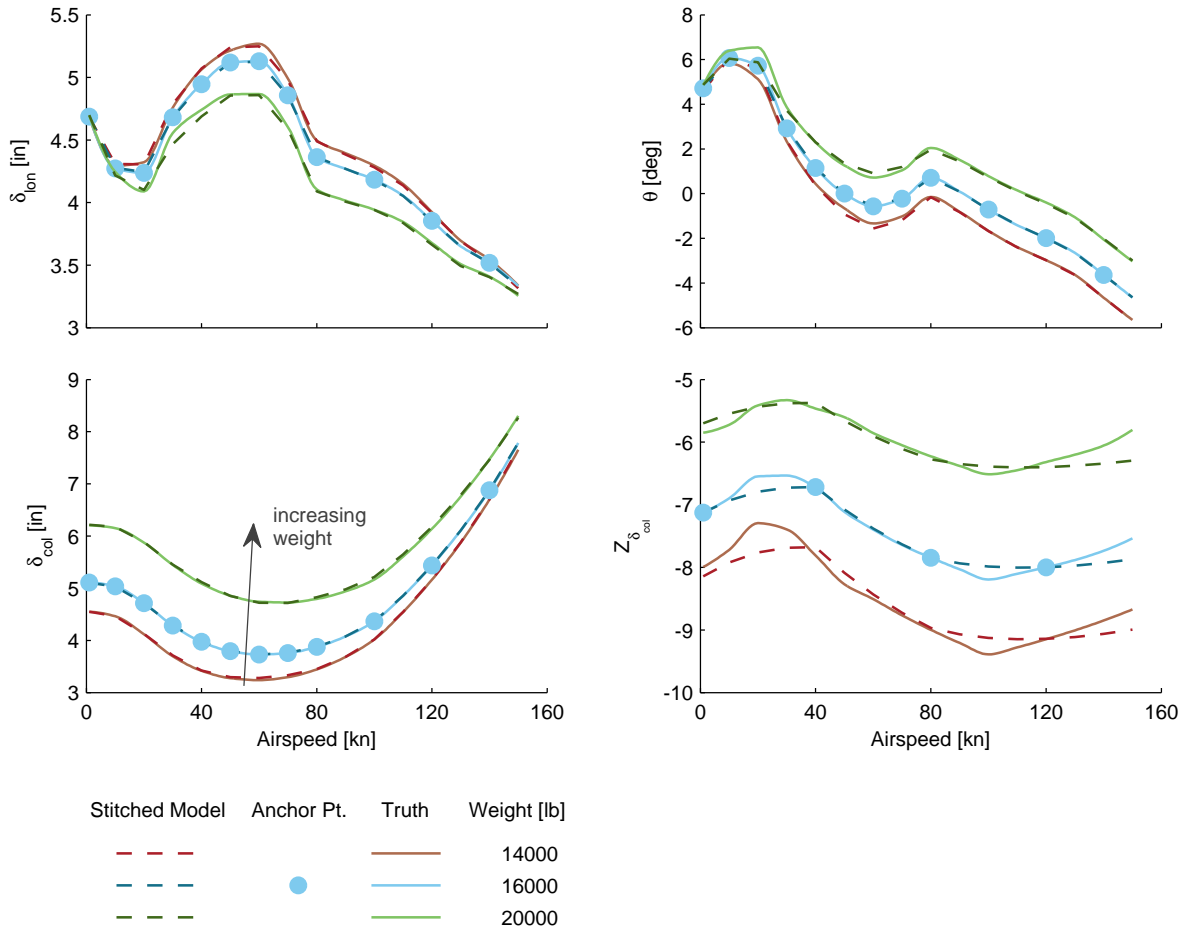
Figure 4.30: Verification of off-nominal weight extrapolation.

Pitch Inertia

Results of varying pitch inertia I_{yy} are shown in Section C.2.2. Like the roll inertia case, the values of pitch inertia presented correspond to aircraft gross weights of 14,000, 16,000, and 20,000 lb. The values of the primary pitch control derivative $M_{\delta_{\text{lon}}}$ are inversely proportional to values of I_{yy}, where an increase in pitch inertia yields a smaller external pitch moment for a given longitudinal cyclic stick input. Similar relations are seen in the values of the pitch damping derivative M_q and pitching moment due to yaw rate derivative M_r. There is excellent agreement overall between the stitched model and the truth data.

Yaw Inertia

Results of varying yaw inertia I_{zz} are shown in Section C.2.3. Again, the values of yaw inertia presented correspond to aircraft gross weights of 14,000, 16,000, and 20,000 lb. Overall there is excellent agreement between the values from the stitched model and the truth data. The values of the primary yaw control derivative $N_{\delta_{\text{ped}}}$ are inversely proportional to values of I_{zz}, where an increase in yaw inertia results in a smaller external yaw moment for a given pedal input. A similar relation is seen in the values of the yaw damping derivative N_r. Yaw inertia has a relatively small effect on cross derivative N_p and cross control derivative $N_{\delta_{\text{lat}}}$.
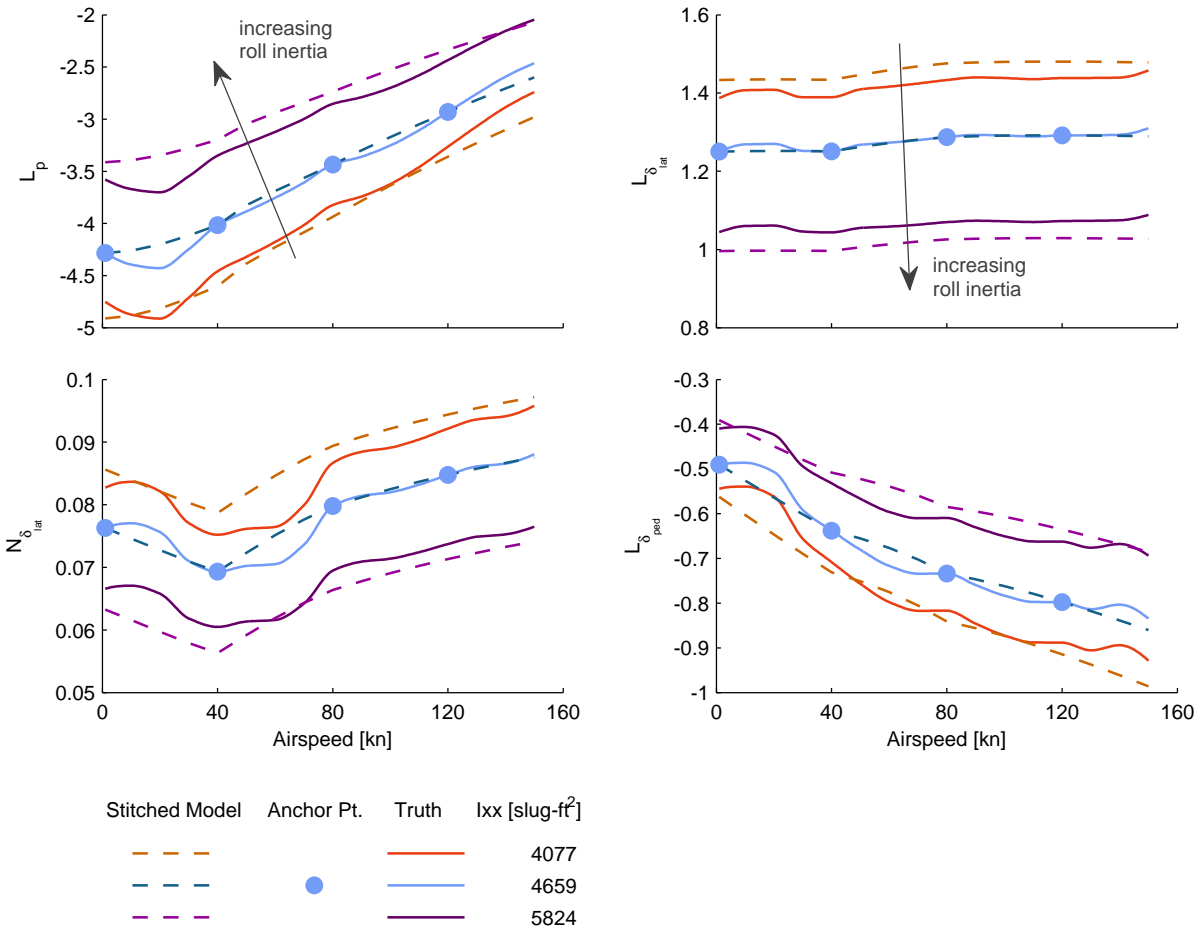
Figure 4.31: Verification of off-nominal inertia extrapolation, roll inertia I_{xx}.

4.6.3 Center of Gravity

Off-nominal center of gravity (CG) positions were simulated in the UH-60 stitched model by employing the CG extrapolation method presented in Section 2.5.2. Changes in fuselage-station CG location (x-body axis, positive *aft*) and buttline CG location (y-body axis, positive *right*) were investigated. See Section C.3 for the complete set of off-nominal CG verification results.

Station CG

Results of variations in fuselage-station CG location (x-body axis, positive *aft*) are shown in Figure 4.32. The stitched model, configured only with anchor point models and trim data of the nominal mid-CG configuration (solid symbols), was retrimmed and relinearized for three simulation values of station CG over the full range of airspeed (dashed lines) and compared with FORECAST truth data (solid lines).

A change in fuselage-station CG mainly affects the trim pitch attitude and corresponding trim longitudinal cyclic stick position. An increase in value of station CG indicates movement aft, thus resulting in a more nose-up pitch attitude and a more forward cyclic stick position (δ_{lon} is defined positive *aft*). Key stability derivative M_w (analogous to M_α) increases slightly in value as the CG progresses aft, indicating reduced static stability in high-speed forward flight and increased static instability around hover and mid-speed forward flight. These key effects are captured very well by the stitched model. Additionally, pitching moment due to collective control derivative $M_{\delta_{\text{col}}}$ is affected by the varying offset between CG and rotor hub. See Section C.3.1 for additional off-nominal fuselage-station CG verification results.
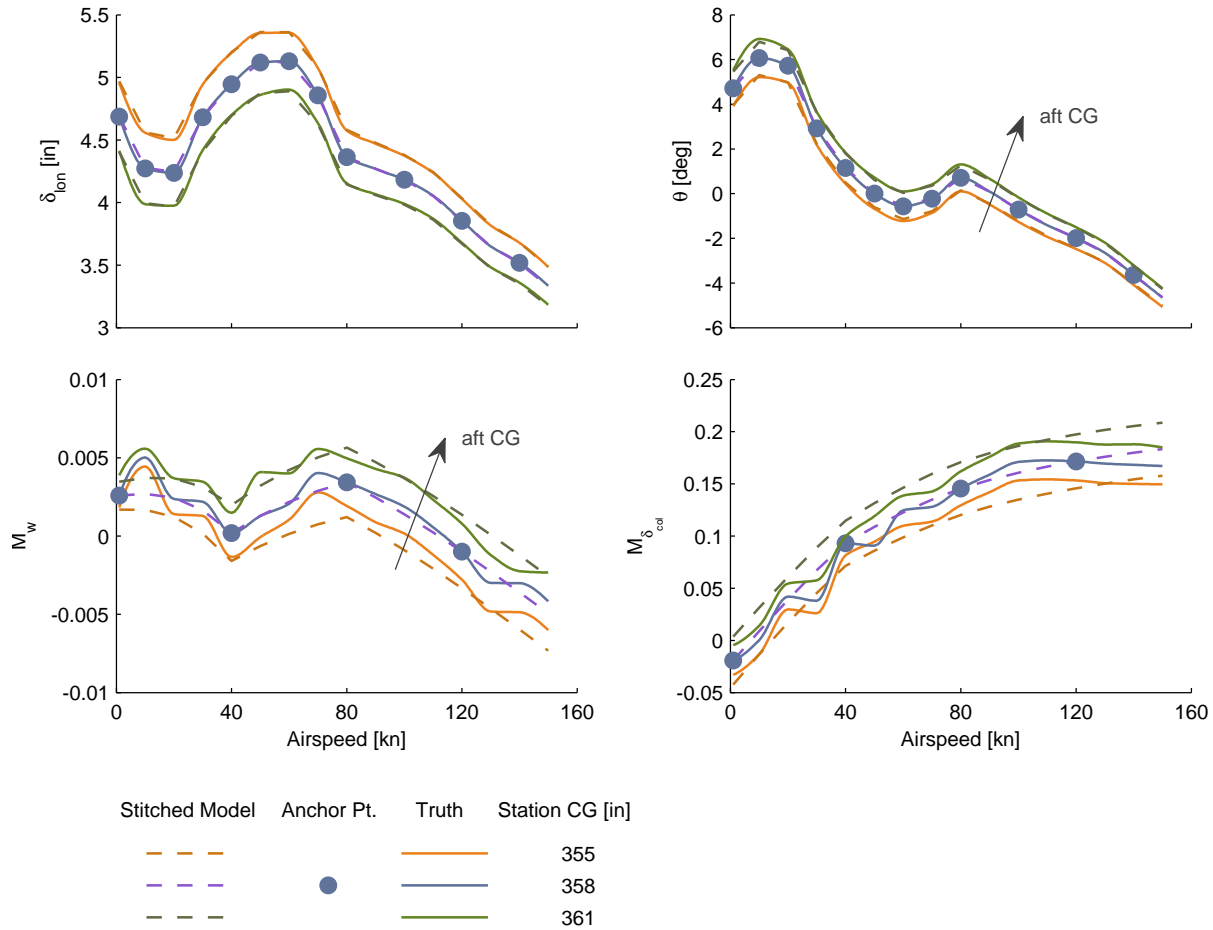
Figure 4.32: Verification of off-nominal CG extrapolation, fuselage station.

Buttline CG

Results of a six-inch offset in buttline CG location (*y*-body axis, positive *right*) are shown in Section C.3.2. Overall, the extrapolated simulation values track the verification points well. The reasonably-large six-inch CG offset to the right results in a trim bank angle difference of approximately 2 deg over the airspeed envelope, which is somewhat underpredicted in simulation. The more-right trim bank angle results in a more-left required lateral cyclic stick position, which is slightly overpredicted by the simulation model. The values of the rolling moment due to collective derivative $L_{\delta_{col}}$ are greater in magnitude than those of the baseline configuration due to the significant moment arm created by the lateral offset between the rotor hub and the CG; thus an increase in collective (increased thrust) creates a positive rolling moment. A similar outcome is seen with the values of the rolling moment due to pedal derivative $L_{\delta_{ped}}$, in which an increase in pedal displacement (increased tail rotor thrust) yields a greater rolling moment. These trends are captured by the stitched model.

4.6.4 Altitude

Variations in simulation altitude were investigated in the UH-60 stitched model. The stitched model was configured with anchor point models and trim data from only two altitudes: sea level (0 ft) and 6000 ft. Unlike the fixed-wing model, air density-ratio scaling of the aerodynamic forces and moments was not performed because not all rotorcraft derivatives scale correctly with air density. Instead, linear interpolation/extrapolation was performed on the trim data and derivative values from the two anchor altitudes, and

86

the stitched model was retrimmed and relinearized to generate results at alternate altitudes of 3000 ft and 10,000 ft.

Figure 4.33 shows key results of simulating alternate altitudes in the UH-60 stitched model over the full airspeed envelope. The stitched model, configured only with anchor point models and anchor trim points at sea level and 6000 ft (solid symbols), was retrimmed and relinearized for a variety of simulation altitudes over the full range of airspeed (dashed lines) and compared with FORECAST truth data (solid lines). Trim collective stick position δ_{col} is significantly impacted by altitude, especially around hover and low speed, because a greater collective pitch is required to maintain lift in the reduced air density; this effect is captured very well by the stitched model. The on-axis heave control derivative $Z_{\delta_{col}}$ is similarly impacted, in which a change in collective pitch results in less of a vertical force at higher altitude. Additionally, tail rotor effectiveness is reduced with increase in altitude, as shown by control derivative $N_{\delta_{ped}}$; this key effect is well represented in the stitched model.

Overall, applying this technique of linear interpolation/extrapolation of the anchor points at altitudes of sea level and 6000 ft yields very good agreement of the UH-60 stitched model with FORECAST truth data over a broad altitude range of sea level through 10,000 ft. These results validate the use of linear interpolation/extrapolation of trim data and derivatives from two altitudes for rotorcraft stitched model applications. See Section C.4 for additional off-nominal altitude verification results.
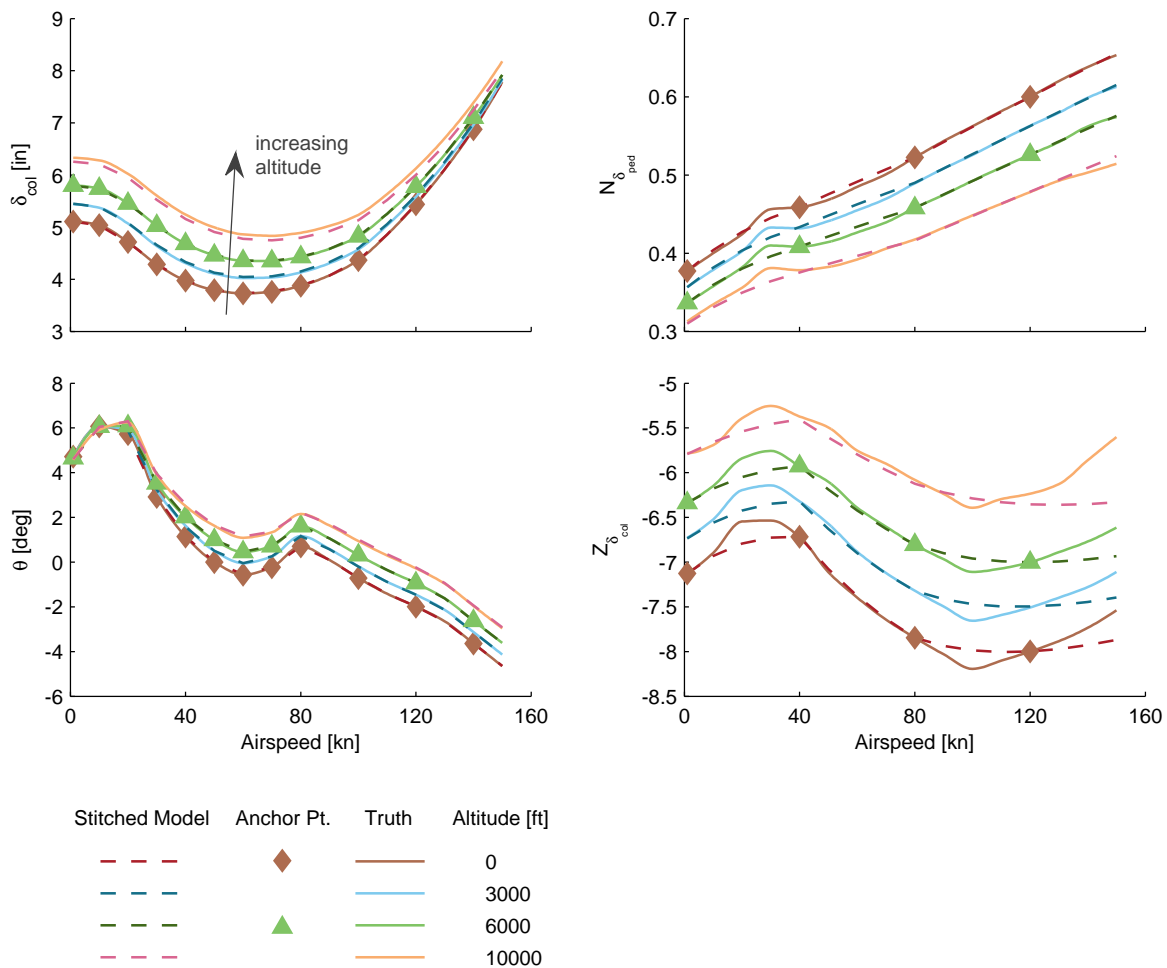
Figure 4.33: Verification of altitude extrapolation.

4.7 Dynamic Response Check Cases

This section presents two check cases in order to verify the dynamic response of the UH-60 Black Hawk stitched model at a particular flight condition and configuration against the corresponding FORECAST truth point model. Frequency responses, time-history plots, modes, and derivative values are discussed for each case.

4.7.1 Case 1: Hover, 2000 ft, Design Weight

This section presents the results of check case 1, which represents a typically-loaded UH-60 with a gross weight of 16,825 lb hovering at a field elevation of 2000 ft. This case mainly exercises extrapolation to an alternate altitude (see Section 4.6.4), with a slight weight extrapolation, as well. A summary of the simulation loading configuration values compared to those of the nominal configuration, and the simulation flight condition values compared to the nearest anchor point values are provided in Table 4.5.

Table 4.5: Simulation loading configuration and flight condition – Case 1

	Parameter	Simulation Value	Nominal/Anchor Value(s)	Off-Nominal
Loading Configuration	Weight [lb]	16825	16000	✓
	CG [in]	358	358	
Flight Condition	Airspeed	*hover*	*hover*	
	Altitude [ft]	2000	0, 6000	✓

Two primary frequency response comparisons between the high-order stitched model and the FORECAST truth model for each of the four controls are presented in Figures 4.34–4.41. A summary of the natural frequency and damping values for most modes of the high-order stitched model versus truth point model is presented in Table 4.6. Values of quasi-steady 6-DOF and higher-order stability and control derivatives are given in Tables 4.7 and 4.8, respectively.

Figures 4.34 and 4.35 show responses to longitudinal cyclic input. There is near perfect agreement in the mid- to high-frequency range, with a slight disparity in the low-frequency portion due to the implicit speed derivative values resulting from trim extrapolation. The key low-frequency unstable Pitch Phugoid mode, however, is satisfactorily captured by the stitched model ($\omega_n = 0.55$ versus $\omega_n = 0.49$ of the point model) with good match in unstable damping ratio ($\zeta = -0.49$ versus $\zeta = -0.51$ of the point model).
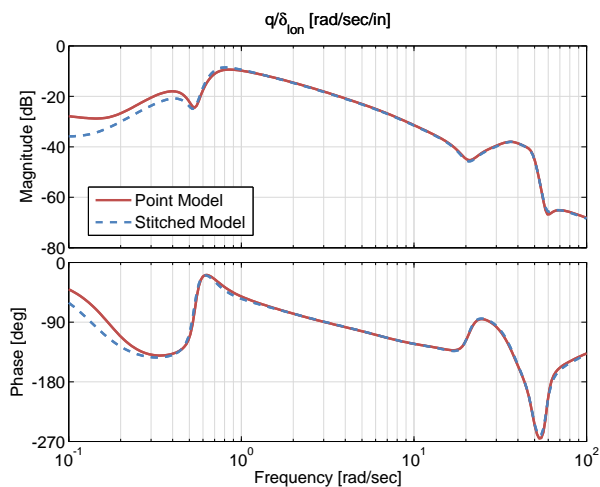
Figure 4.34: Case 1: pitch rate response to longitudinal cyclic input comparison.
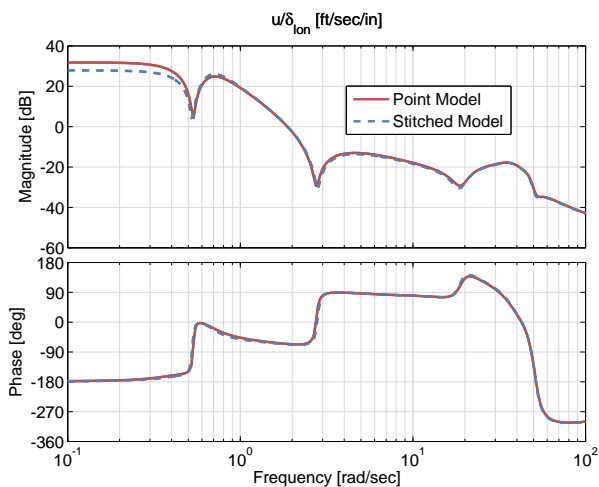
Figure 4.35: Case 1: x-body airspeed response to longitudinal cyclic input comparison.

Figures 4.36 and 4.37 show responses to lateral cyclic input. As with the primary pitch responses, these primary roll responses have near perfect agreement in the mid- to high-frequency range, with some discrepancy in the low-frequency portion also due to the inaccuracy in trim extrapolation and the resultant effect on the implicit speed derivatives. The primary low-frequency Roll Phugoid mode is well captured in natural frequency by the stitched model ($\omega_n = 0.66$ versus $\omega_n = 0.64$ of the point model), however, with a modest difference in damping ($\zeta = 0.25$ versus $\zeta = 0.30$ of the point model).
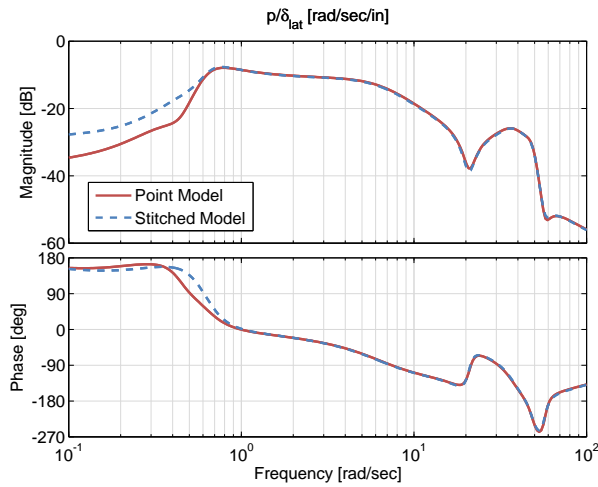
Figure 4.36: Case 1: roll rate response to lateral cyclic input comparison.
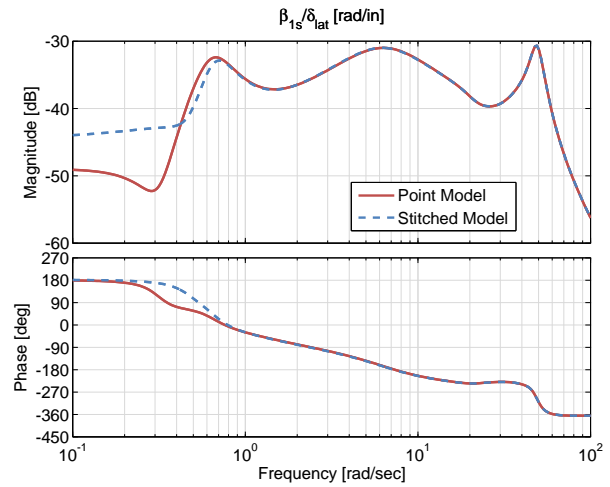
Figure 4.37: Case 1: lateral flapping angle to lateral cyclic input comparison.

The primary heave response comparison is shown in Figure 4.38 and the coupled yaw-to-collective response comparison is shown in Figure 4.39. There is near perfect agreement in the heave response over the displayed frequency range, and excellent agreement in the yaw-to-collective response, with a small disparity in low-frequency magnitude.

Figures 4.40 and 4.41 show yaw rate and main rotor rotational speed responses to pedal input. There is excellent agreement between the stitched model and the point model for the primary yaw response and high-order main rotor speed response over the full frequency range of interest.
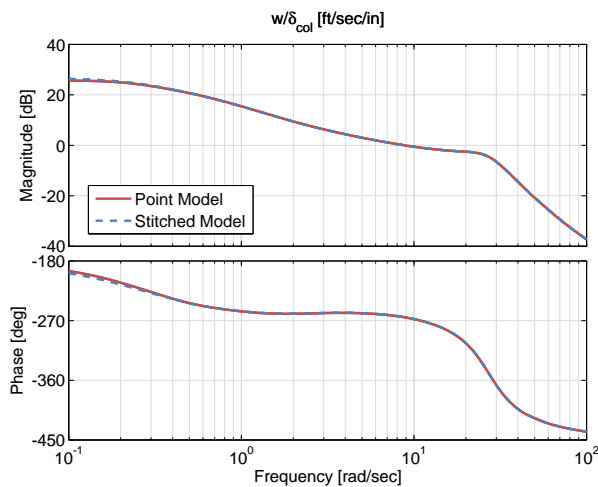
Figure 4.38: Case 1: z-body airspeed response to collective input comparison.
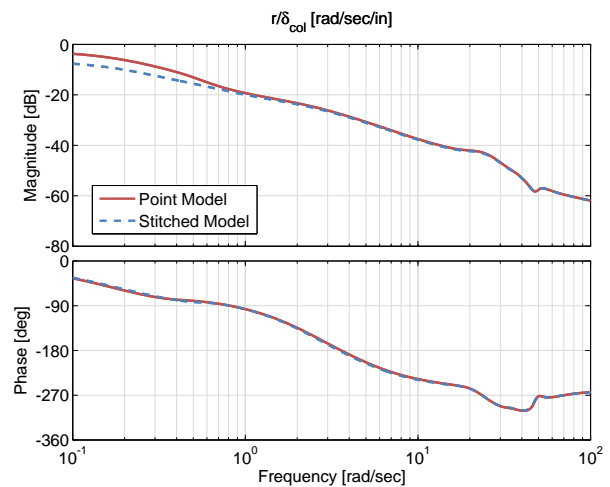
Figure 4.39: Case 1: yaw rate response to collective input comparison.
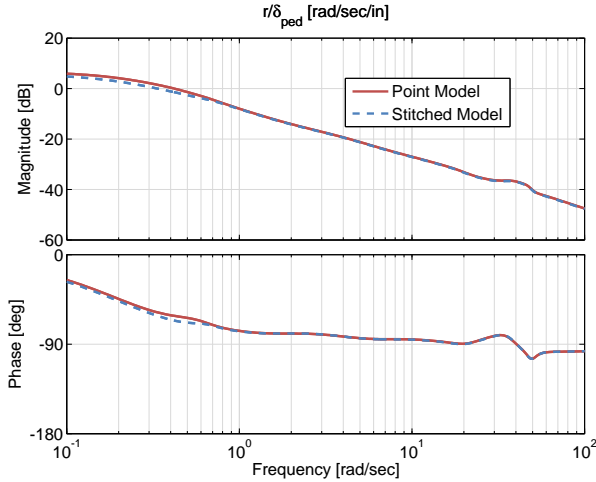
Figure 4.40: Case 1: yaw rate response to pedal input comparison.
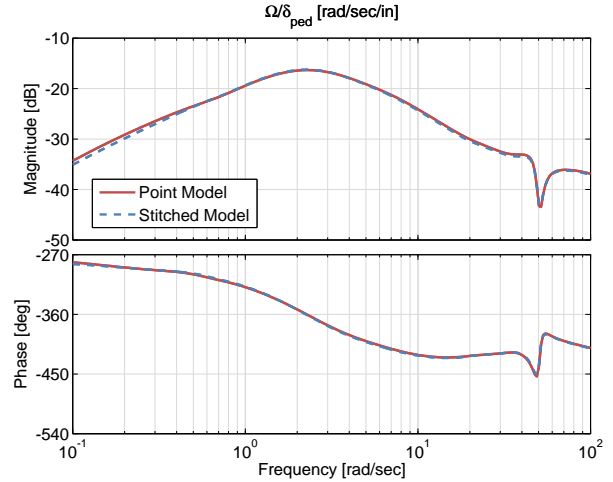
Figure 4.41: Case 1: main rotor rotational speed to pedal input comparison.

A summary of most modes of the high-order stitched model versus truth point model for this hover check case is given in Table 4.6, with complex modes expressed by natural frequency ω_n and damping ratio ζ, and real poles expressed by inverse time constant $1/\tau$. There is excellent agreement in the natural frequency and damping of all mid- to high-frequency modes, including those of the high-order Lead/Lag, Flap, and Inflow states. There are small differences in the damping of the low-frequency Phugoid modes due to small errors in the implicit speed derivatives. Values of quasi-steady 6-DOF and higher-order stability and control derivatives are given in Tables 4.7 and 4.8, respectively. The values of the implicit u- and v-speed derivatives predominately affect the low-frequency Pitch and Roll Phugoid modes, and are in satisfactory agreement. The implicit v-speed derivatives, in particular, show excellent agreement with the FORECAST point model; the value of the key v-speed derivative Y_v is within 4% of the value from the point model.

Short-term time-history results for three separate control doublets are presented in Figures 4.42–4.44. Figure 4.42 shows the x-body airspeed U and pitch rate response comparisons for a 1-inch longitudinal cyclic input doublet. The short-term responses of the stitched model agree very well with those of the point model, with a slight divergence in airspeed due to the implicit u-speed derivatives. Figure 4.43 shows the roll rate and lateral flapping angle response comparisons for a 1-inch lateral cyclic input doublet. Near-perfect agreement is seen between the responses of the stitched model and those of the point model. Figure 4.44 shows the y-body airspeed V and yaw rate comparisons for a 1-inch pedal input doublet. The short-term responses of the stitched model are in very good agreement with those of the point model, with a slight divergence in y-body airspeed due to the implicit v-speed derivatives. Overall, the stitched model tracks very well with the point model at this off-nominal flight condition and loading configuration.

Table 4.6: Modes – Case 1

Mode	Parameter	Stitched Model	Point Model
Yaw/Heave	ω_n [rad/sec]	0.2182	0.2199
	ζ	0.9904	0.9663
Pitch Phugoid	ω_n [rad/sec]	0.5465	0.4856
	ζ	-0.4898	-0.5111
Roll Phugoid	ω_n [rad/sec]	0.6581	0.6436
	ζ	0.2473	0.2960
Pitch Aperiodic	$1/\tau$ [rad/sec]	1.2035	1.0970
Collective Lead/Lag	ω_n [rad/sec]	2.5076	2.5989
	ζ	0.8743	0.8878
Rotor RPM	$1/\tau$ [rad/sec]	3.6071	3.2853
Roll Aperiodic	$1/\tau$ [rad/sec]	4.5859	4.6449
Regressive Flap	ω_n [rad/sec]	6.4493	6.5523
	ζ	0.6358	0.6341
Constant Inflow	$1/\tau$ [rad/sec]	11.8134	11.9830
Regressive Lead/Lag	ω_n [rad/sec]	20.4532	20.7526
	ζ	0.2627	0.2717
1st Harmonic Inflow	ω_n [rad/sec]	21.3999	21.5513
	ζ	0.9050	0.9087
Collective Flap	ω_n [rad/sec]	27.2335	27.2034
	ζ	0.3339	0.3333
Progressive Lead/Lag	ω_n [rad/sec]	37.6998	37.4706
	ζ	0.2114	0.2227
Tail Rotor Inflow	$1/\tau$ [rad/sec]	38.5564	39.7850
Progressive Flap	ω_n [rad/sec]	49.0633	49.0918
	ζ	0.0898	0.0896

Table 4.7: Stability and Control Derivatives, Quasi-Steady 6-DOF – Case 1

Derivative	Stitched Model	Point Model
X_u	0.0099	0.0063
Z_u	0.0325	0.0242
L_u	0.0413	0.0362
M_u	0.0147	0.0063
X_w	0.0199	0.0184
Z_w	-0.2538	-0.2541
M_w	0.0027	0.0031
X_q	1.1391	1.1159
Z_q	-0.0490	0.0284
L_q	1.1035	1.1022
M_q	-0.7858	-0.7669
Y_v	-0.0476	-0.0495
L_v	-0.0373	-0.0390
M_v	0.0040	0.0039
N_v	0.0012	0.0011
X_p	-0.2047	-0.1768
Y_p	-0.1018	-0.1995
L_p	-4.4383	-4.4883
M_p	-0.2489	-0.2492
N_p	-0.3191	-0.3292
Y_r	0.3629	0.3593
Z_r	1.9213	2.0382
L_r	-0.1354	-0.1385
N_r	-0.2197	-0.2254
$X_{\delta_{\mathrm{lon}}}$	-1.5000	-1.5742
$Z_{\delta_{\mathrm{lon}}}$	-0.0099	-0.0157
$L_{\delta_{\mathrm{lon}}}$	0.0732	0.0646
$M_{\delta_{\mathrm{lon}}}$	0.3718	0.3769
$X_{\delta_{\mathrm{col}}}$	0.8157	0.8403
$Z_{\delta_{\mathrm{col}}}$	-6.5305	-6.5625
$M_{\delta_{\mathrm{col}}}$	-0.0202	-0.0216
$N_{\delta_{\mathrm{col}}}$	0.0614	0.0667
$L_{\delta_{\mathrm{lat}}}$	1.2437	1.2682
$M_{\delta_{\mathrm{lat}}}$	0.0123	0.0135
$N_{\delta_{\mathrm{lat}}}$	0.0757	0.0775
$Y_{\delta_{\mathrm{ped}}}$	-0.8333	-0.8324
$L_{\delta_{\mathrm{ped}}}$	-0.4674	-0.4674
$N_{\delta_{\mathrm{ped}}}$	0.3634	0.3679

Table 4.8: Stability and Control Derivatives, Higher-Order – Case 1

Derivative	Stitched Model	Point Model
$L_{\beta_{1s}}$	-56.0670	-57.5310
$M_{\beta_{1c}}$	-7.7823	-7.9256
Z_{β_0}	-530.9641	-529.1161
$L_{f\delta_{\mathrm{lat}}}$	-11.9275	-11.8894
$M_{f\delta_{\mathrm{lon}}}$	-22.4010	-22.3387
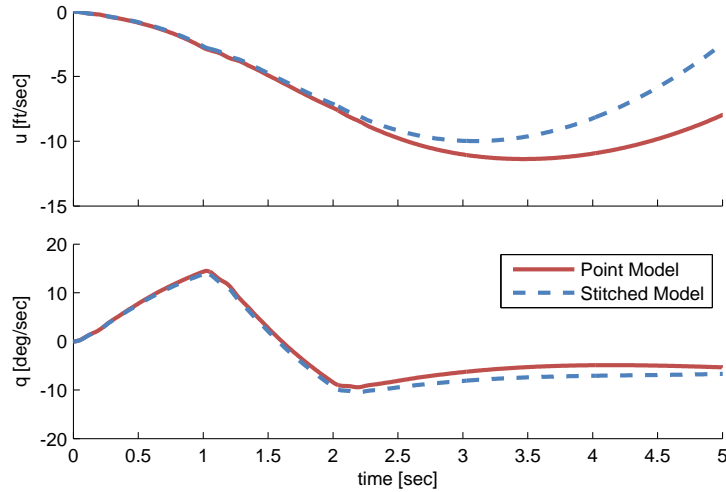
Figure 4.42: Case 1: short-term time history responses, longitudinal cyclic doublet.
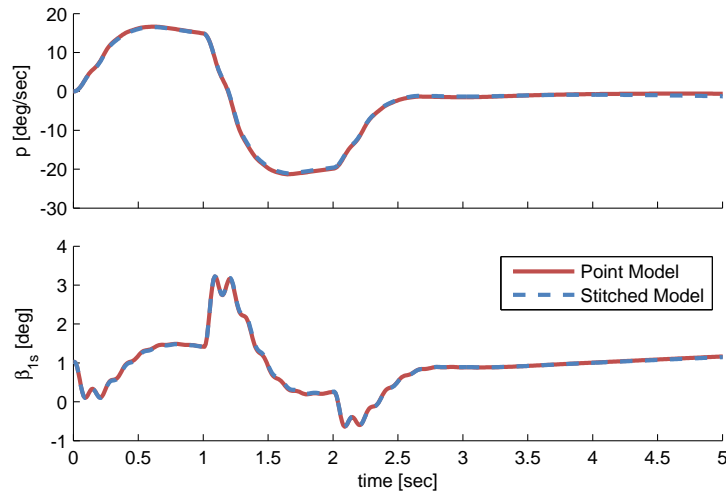
Figure 4.43: Case 1: short-term time history responses, lateral cyclic doublet.
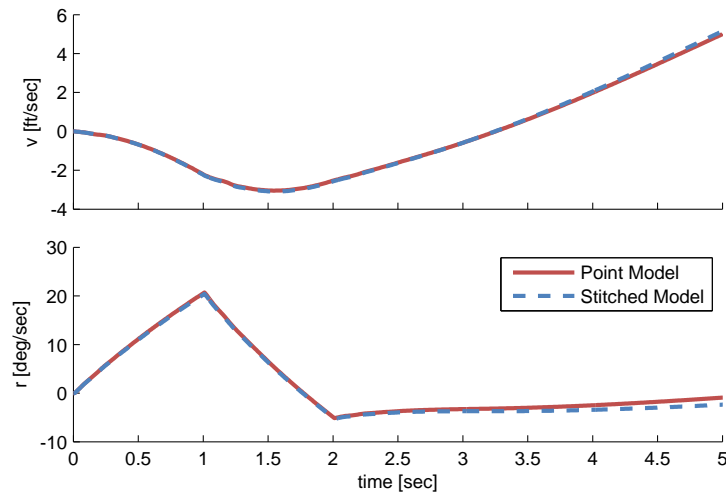
Figure 4.44: Case 1: short-term time history responses, pedal doublet.

93

4.7.2 Case 2: 100 kn, 500 ft, Heavy Weight

This section presents the results of check case 2, which represents a heavily-loaded (20,000-lb), aft-CG UH-60 performing contour flight at an altitude of 500 feet and an airspeed of 100 knots. This case exercises significant weight and CG extrapolation, slight altitude interpolation, and is at an airspeed between anchor points. A summary of the simulation loading configuration values compared to those of the nominal configuration, and the simulation flight condition values compared to the nearest anchor point values are provided in Table 4.9.

Table 4.9: Simulation loading configuration and flight condition – Case 2

	Parameter	Simulation Value	Nominal/Anchor Value(s)	Off-Nominal
Loading Configuration	Weight [lb]	20000	16000	✓
	CG [in]	359	358	✓
Flight Condition	Airspeed [kn]	100	80, 120	✓
	Altitude [ft]	500	0, 6000	✓

Two primary frequency responses for each of the four controls are presented in Figures 4.45–4.52. A summary of the natural frequency and damping values for key modes of the high-order stitched model versus truth point model is presented in Table 4.10. Values of quasi-steady 6-DOF and higher-order stability and control derivatives are given in Tables 4.11 and 4.12, respectively.

Figures 4.45 and 4.46 show responses to longitudinal cyclic input. There is excellent agreement in the mid- to high-frequency range, with a slight disparity in the low-frequency portion due to the implicit u-speed derivative values resulting from trim extrapolation. The lightly-damped Pitch Phugoid mode of the FORECAST point model is well captured in natural frequency by the stitched model ($\omega_n = 0.23$ rad/sec versus $\omega_n = 0.22$ of the point model) but predicts somewhat more damping ($\zeta = 0.195$ versus $\zeta = 0.130$ of the point model).

Responses to lateral cyclic input are shown in Figures 4.47 and 4.48. As with the longitudinal responses, there is excellent agreement overall in the mid- to high-frequency range. The discrepancy in Phugoid damping manifests as a low-frequency disparity in the lateral responses, as well. Also, the difference in Regressive Lead/Lag damping ($\zeta = 0.228$ versus $\zeta = 0.157$ of the point model) can be seen in the v/δ_{lat} response around 19 rad/sec. There is also a slight difference in damping of the Progressive Lead/Lag mode ($\zeta = 0.167$ versus $\zeta = 0.104$ of the point model) at 38 rad/sec.
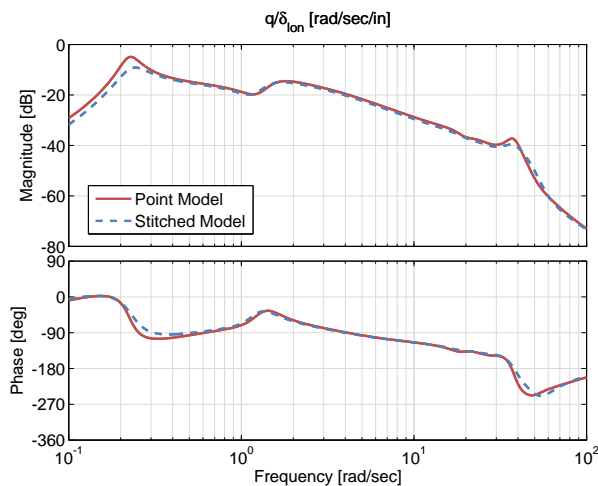
Figure 4.45: Case 2: pitch rate response to longitudinal cyclic input comparison.
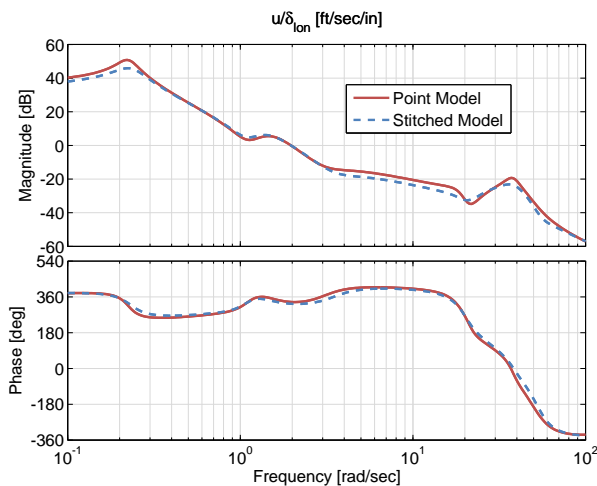
Figure 4.46: Case 2: x-body airspeed response to longitudinal cyclic input comparison.
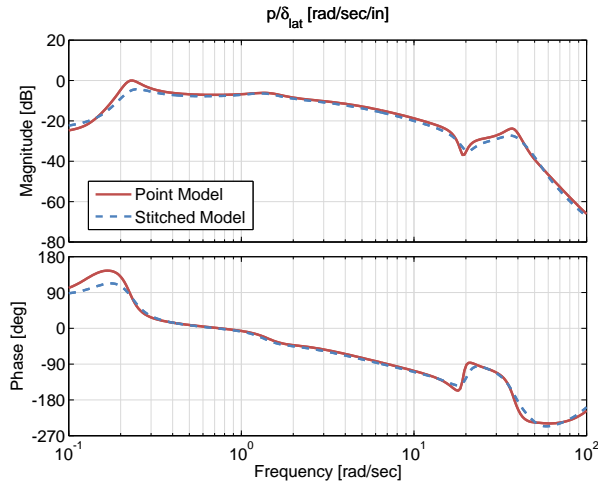
Figure 4.47: Case 2: roll rate response to lateral cyclic input comparison.
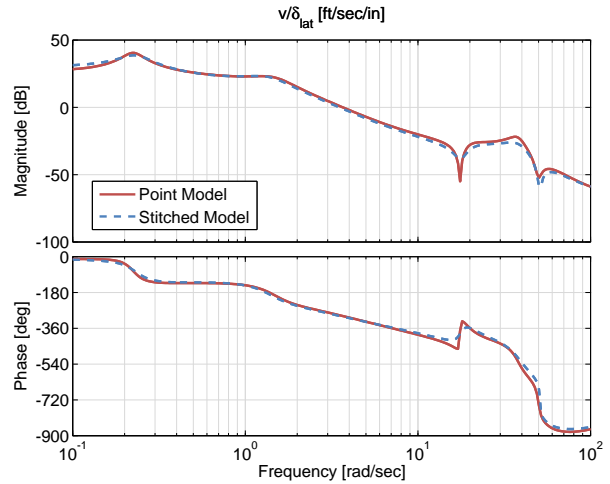
Figure 4.48: Case 2: y-body airspeed response to lateral cyclic input comparison.

Responses to collective input are shown in Figures 4.49 and 4.50. There is very good agreement overall, with the Phugoid mode slightly affecting the low-frequency agreement, as well.

Figures 4.51 and 4.52 show responses to pedal input. The y-body airspeed response (analogous to sideslip angle β) to pedal input comparison is shown in Figure 4.51, and there is excellent agreement overall. Again, the Phugoid mode damping disparity appears in the low-frequency portion of the responses. The mismatch in Progressive Lead/Lag damping can be seen in the v/δ_{ped} response around 38 rad/sec, as was seen previously in the v/δ_{lat} response of Figure 4.48. The apparent large discrepancy in the phase response of v/δ_{ped} in Figure 4.51 is actually just 360 degrees, and is due to a slight shift in the relative pole-zero configuration of the Progressive Lead/Lag mode.
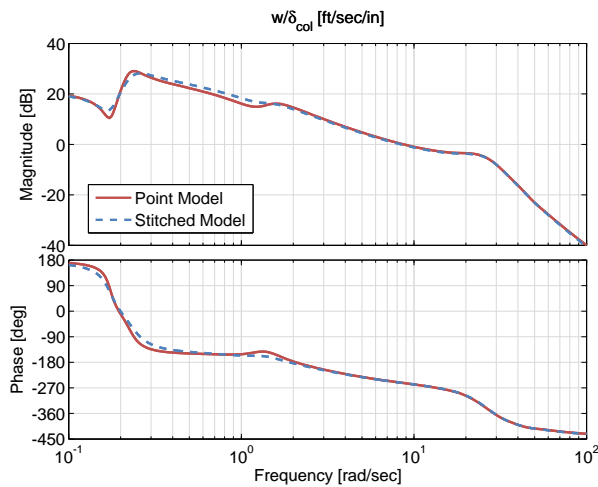
Figure 4.49: Case 2: z-body airspeed response to collective input comparison.
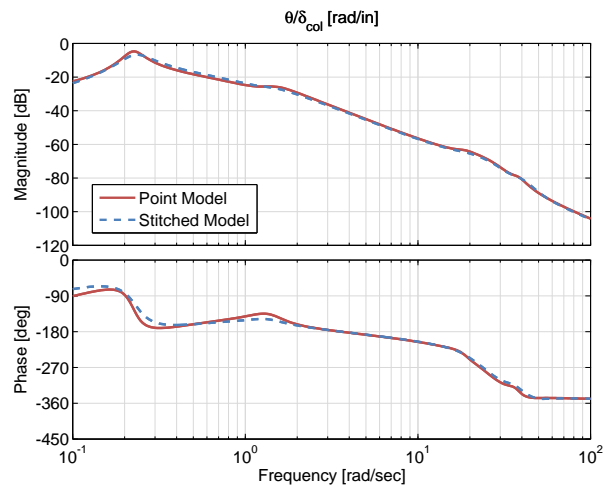
Figure 4.50: Case 2: pitch angle response to collective input comparison.

95
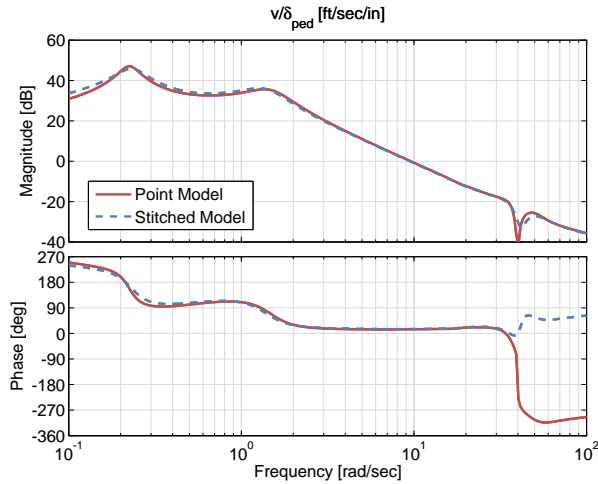
Figure 4.51: Case 2: y-body airspeed response to pedal input comparison.
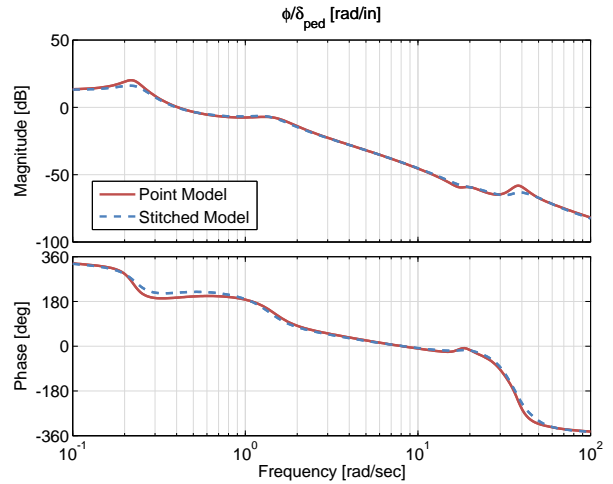
Figure 4.52: Case 2: bank angle response to pedal input comparison.

A summary of the key modes of the high-order stitched model versus truth point model for this forward-flight check case is given in Table 4.10. Once again, the notable disparities between the stitched model and the FORECAST point model for this off-nominal check case are in the damping ratio values of the Pitch Phugoid, Regressive Lead/Lag, and Progressive Lead/Lag modes. All other key modes are in excellent agreement. Values of quasi-steady 6-DOF and higher-order stability and control derivatives are given in Tables 4.11 and 4.12, respectively. The differences in values of quasi-steady Z_u and M_u between the stitched model and the truth point model are main contributing factors to the disagreement in Phugoid damping, whereas the differences in values of higher-order $L_{\beta_{1s}}$ and $L_{\beta_{1c}}$ are the cause of the mismatch in Regressive and Progressive Lead/Lag damping ratios.

Short-term time-history results for three separate control doublets are presented in Figures 4.53–4.55. Figure 4.53 shows the x-body airspeed and pitch rate response comparisons for a 1-inch longitudinal cyclic input doublet. The short-term responses of the stitched model agree well with those of the point model, with a divergence in pitch rate due to the disparity in Phugoid damping. This disparity also accounts for the slight divergence in the airspeed response. Figure 4.54 shows the roll rate and y-body airspeed response comparisons for a 1-inch lateral cyclic input doublet. The short-term lateral responses are in very good agreement, with a small divergence seen in y-body airspeed. Figure 4.55 shows y-body airspeed and yaw rate responses due to a 1-inch pedal input doublet. Very good agreement is seen in these lateral/directional responses, again with a small drift in y-body airspeed and subsequently in yaw rate. Overall, the stitched model tracks very well with the FORECAST point model for this forward flight check case.

Table 4.10: Modes – Case 2

Mode	Parameter	Stitched Model	Point Model
Roll	$1/\tau$ [rad/sec]	0.1626	0.1521
Pitch Phugoid	ω_n [rad/sec]	0.2319	0.2244
	ζ	0.1950	0.1301
Pitch	$1/\tau$ [rad/sec]	-0.5141	-0.4887
Dutch Roll	ω_n [rad/sec]	1.3881	1.4790
	ζ	0.2872	0.2767
Roll/Lateral Flap	ω_n [rad/sec]	2.2037	2.1524
	ζ	0.9784	0.9800
Collective Lead/Lag	ω_n [rad/sec]	2.8427	3.1655
	ζ	0.8361	0.8534
Regressive Flap	ω_n [rad/sec]	15.3042	15.2740
	ζ	0.9739	0.9761
Regressive Lead/Lag	ω_n [rad/sec]	19.7530	18.7387
	ζ	0.2282	0.1568
Collective Flap	ω_n [rad/sec]	26.8930	26.6137
	ζ	0.3140	0.3249
Progressive Lead/Lag	ω_n [rad/sec]	38.3364	38.0198
	ζ	0.1671	0.1044
Progressive Flap	ω_n [rad/sec]	49.8271	49.8898
	ζ	0.1917	0.1972

Table 4.11: Stability and Control Derivatives, Quasi-Steady 6-DOF – Case 2

Derivative	Stitched Model	Point Model
X_u	-0.0320	-0.0373
Z_u	0.0209	-0.0042
L_u	-0.0057	-0.0069
M_u	-0.0001	-0.0027
X_w	0.0281	0.0313
Z_w	-0.5632	-0.5774
M_w	0.0018	0.0017
X_q	1.3372	1.9259
Z_q	-0.5683	-0.5783
L_q	-0.1752	-0.1814
M_q	-1.2264	-1.2848
Y_v	-0.0926	-0.0975
L_v	-0.0212	-0.0259
M_v	0.0110	0.0113
N_v	0.0058	0.0058
X_p	-0.3674	-0.5514
Y_p	-0.2360	-0.7180
L_p	-2.5688	-2.8734
M_p	0.1897	0.2183
N_p	-0.1412	-0.1836
Y_r	1.4393	1.4508
Z_r	1.4883	1.8380
L_r	0.2157	0.1885
N_r	-0.5686	-0.5995
$X_{\delta_{\text{lon}}}$	-0.9061	-1.2267
$Z_{\delta_{\text{lon}}}$	-4.1872	-4.3375
$L_{\delta_{\text{lon}}}$	0.1012	0.0491
$M_{\delta_{\text{lon}}}$	0.4272	0.4601
$X_{\delta_{\text{col}}}$	0.3518	0.3417
$Z_{\delta_{\text{col}}}$	-6.3197	-6.4522
$M_{\delta_{\text{col}}}$	0.1345	0.1405
$N_{\delta_{\text{col}}}$	-0.0415	-0.0323
$L_{\delta_{\text{lat}}}$	1.0324	1.1592
$M_{\delta_{\text{lat}}}$	0.0047	0.0056
$N_{\delta_{\text{lat}}}$	0.0663	0.0755
$Y_{\delta_{\text{ped}}}$	-1.0308	-1.0271
$L_{\delta_{\text{ped}}}$	-0.6027	-0.5989
$N_{\delta_{\text{ped}}}$	0.4433	0.4748

Table 4.12: Stability and Control Derivatives, Higher-Order – Case 2

Derivative	Stitched Model	Point Model
$L_{\beta_{1s}}$	-41.9441	-47.4337
$M_{\beta_{1c}}$	-6.1765	-6.9337
Z_{β_0}	-447.5597	-440.5828
$L_{f\delta_{\text{lat}}}$	-7.5670	-7.1547
$M_{f\delta_{\text{lon}}}$	-15.8057	-15.1098
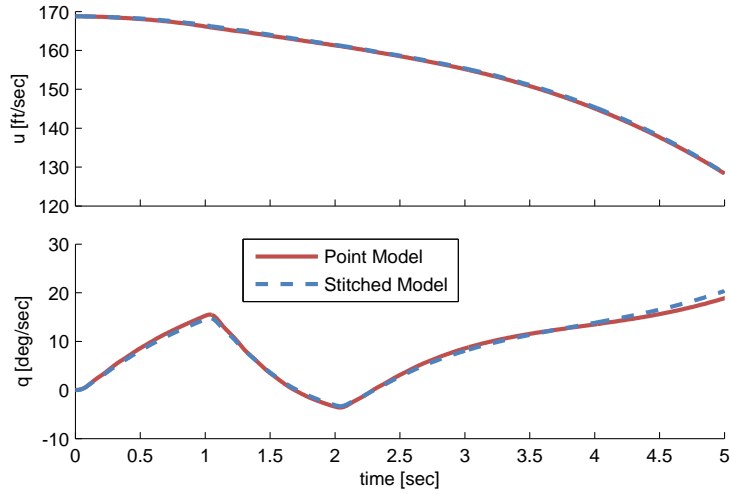
Figure 4.53: Case 2: short-term time history responses, longitudinal cyclic doublet.
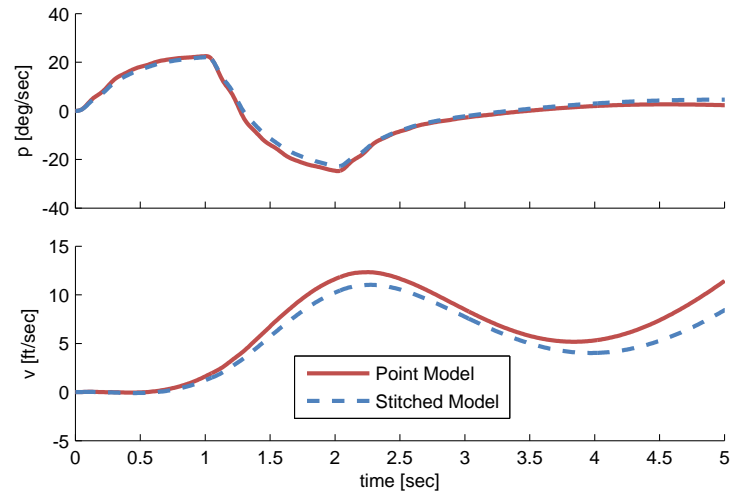
Figure 4.54: Case 2: short-term time history responses, lateral cyclic doublet.
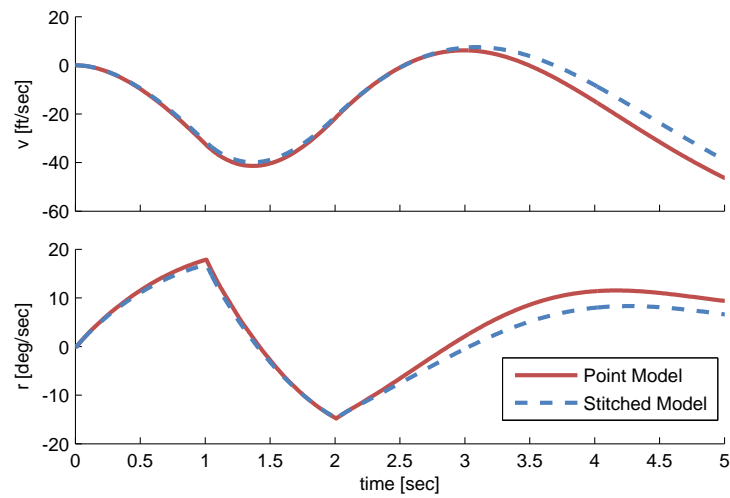
Figure 4.55: Case 2: short-term time history responses, pedal doublet.

4.8 Simulation of Alternate Configurations – Sling Loads

To demonstrate the simulation of alternate vehicle configurations by linearly interpolating the trim data and dimensional stability and control derivatives between known configurations, results of retrimming and relinearizing the UH-60 stitched model for alternate sling-load weights are presented in this section. A sling load is an external load that is hung by a cable attached to a cargo hook on the underside of the helicopter's fuselage. The presence of the sling load significantly affects the bare-airframe dynamics and adversely affects pilot handling qualities, particularly in the hover/low-speed regime [22]. Because of its unique characteristics, the helicopter/sling-load system can be considered an alternate configuration to the unloaded aircraft.

A nondimensional Load Mass Ratio (LMR) is commonly used to express the mass of the sling load in relation to the mass of the total helicopter/sling-load system [22]:

$$\text{LMR} = \frac{m_{\text{load}}}{m_{\text{load}} + m_{\text{aircraft}}} \tag{4.11}$$

For the demonstration herein, the stitched model was configured with anchor point models and trim data of the baseline aircraft (16,000 lb gross weight) with two separate sling-load configurations: 1) a load weight of 1778 lb (LMR = 0.1); and 2) a load weight of 4000 lb (LMR = 0.2). Linear interpolation between (and extrapolation beyond) the trim data and dimensional stability and control derivatives of the two anchor configurations within the stitched model was then performed to simulate alternate sling-load weight configurations. For verification, the stitched model configured with data from the two anchor load configurations was retrimmed and relinearized over a range of airspeed and compared against FORECAST truth points for the following load configurations: 1) a load weight of 2824 lb (LMR = 0.15); and 2) a load weight of 5918 lb (LMR = 0.27), which is just within the maximum total gross weight limitation of 22,000 lb for the UH-60. A summary of the load weight and corresponding Load Mass Ratio for the anchor configurations and interpolated/extrapolated alternate configurations is provided in Table 4.13.

Table 4.13: Sling-load weight configurations

	Load Weight [lb]	LMR
Anchor Configurations	1778	0.10
	4000	0.20
Interpolated/Extrapolated Configurations	2824	0.15
	5918	0.27

Results of simulating alternate sling-load weight configurations in the UH-60 stitched model over a broad airspeed range are shown in Figure 4.56 with comparisons of values of trim pitch attitude, trim collective stick position, quasi-steady stability derivative X_q, and quasi-steady control derivative $Z_{\delta_{\text{col}}}$. The stitched model, configured only with anchor point models and trim data of the two anchor configurations (solid symbols), was retrimmed and relinearized for two alternate load configurations over the range of airspeed (dashed lines) and compared with FORECAST truth data (solid lines).

The primary effect on trim is the increased required collective stick position δ_{col} with increased weight of the system, which is nearly-perfectly captured by the stitched model for all configurations. Heave control derivative $Z_{\delta_{\text{col}}}$ is affected by load weight, as the vertical acceleration from a given collective input is reduced as weight is increased. Overall there is excellent agreement between the stitched model and the truth points for the interpolated/extrapolated sling-load configurations, thus validating the technique of linear interpolation/extrapolation of trim data and dimensional stability and control derivatives of configurations for rotorcraft stitched model applications. Additional verification results for the simulation of alternate sling-load weight configurations in the UH-60 stitched model are provided in Section C.5.
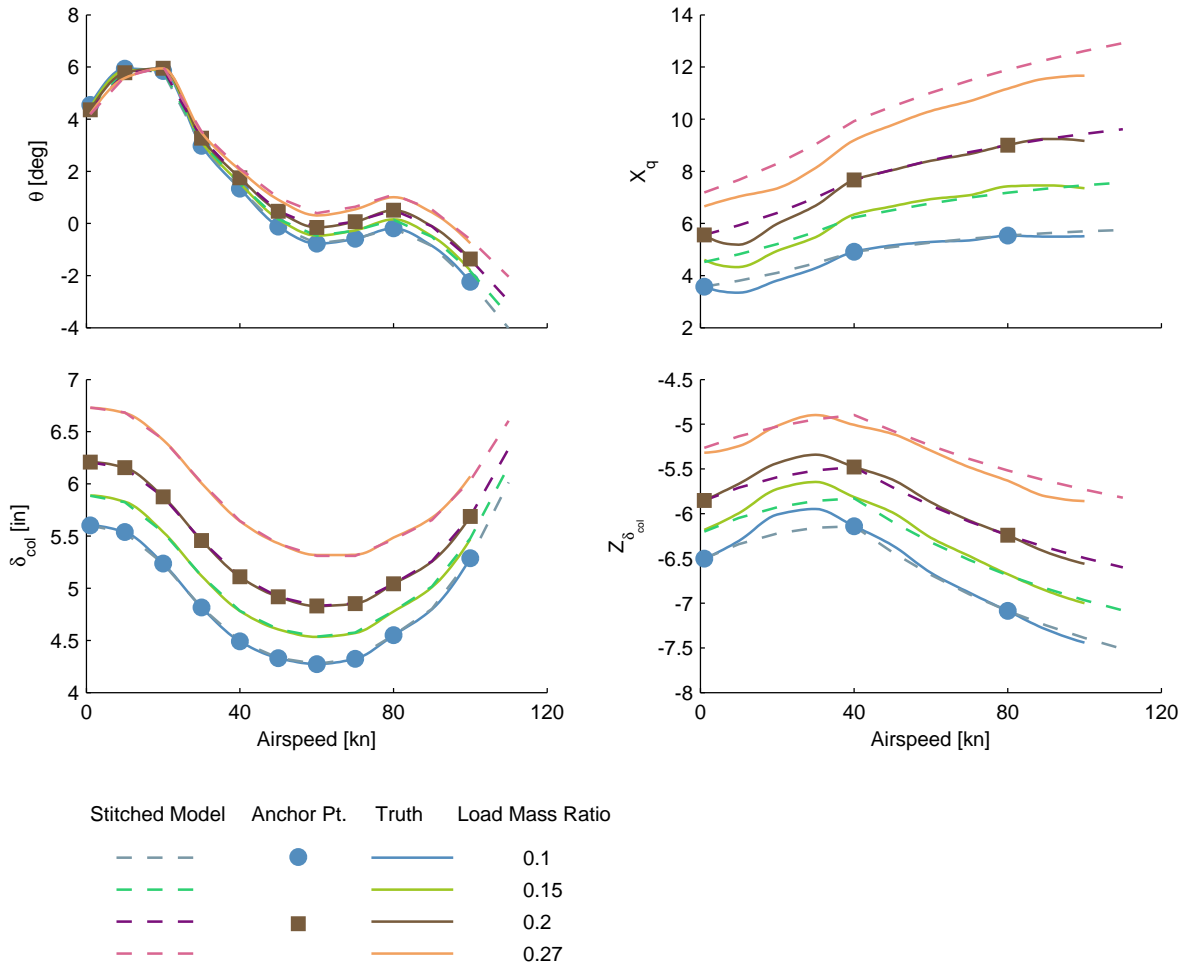
Figure 4.56: Alternate configuration verification, sling-load weight.

4.9 Flight-Test Implications for Rotorcraft

A key application of the model stitching architecture is the development of full flight-envelope stitched simulation models from flight-identified point models using system identification methods and associated flight-test trim data. This section covers the overall considerations for planning and conducting a flight test involving rotorcraft for the development of stitched simulation models. The techniques and requirements presented in this section follow closely to those for fixed-wing applications presented earlier in Section 3.9, with the pertinent material referenced throughout. Analyses of the FORECAST UH-60 simulation model data trends discussed herein and lessons learned are applied to provide specific guidance for rotorcraft on the spacing and quantity of trim data, point models, and static stability data to be obtained in flight testing. A summary of the overall flight-test recommendations for rotorcraft is provided in Table 4.14.

4.9.1 Flight-Test Data Collection

Trim Data

The collection of trim test data is accomplished by trimming the rotorcraft at the desired flight condition and recording data for a duration of approximately 3–5 seconds. Post-flight processing of the data is done to determine the average trim values of the controls, aircraft attitude, and any additional desired states for the particular flight-test point. As with fixed-wing aircraft, it is important to know the helicopter loading

configuration at each test point (e.g., from measurements of the fuel load at each test point for use with a fuel-burn data sheet post-flight) as the trim points are then collectively *baselined* to a nominal loading during data processing, as discussed in Section 4.9.2.

It is necessary to collect fine-increment trim points around hover to accurately capture the migration of controls and helicopter attitude for the simulation of low-speed forward, rearward, sideward, and quartering flight, as well as the simulation of hovering flight in the presence of winds. The spacing and corresponding gradients between the trim data affect the accuracy of the implicit speed derivatives of the hover identification point model, as presented in Section 4.3, so a fine spacing of 3–5 kn is recommended for pure forward (i.e., 0 deg), rearward (i.e., 180 deg), and sideward (i.e., 90 and 270 deg) flight up to approximately 20 kn. Additionally, quartering flight points should be collected at 45-deg radial increments (i.e., 45, 135, 225, and 315 deg) at a fine airspeed increment of 5 kn total airspeed.

In forward flight, it is important to capture critical inflections in the trim curves (e.g., bottom of the power curve) for accurate simulation over the forward-flight airspeed envelope. Collecting trim data at a somewhat-fine 10-kn speed increment up to a forward airspeed of 80 knots is recommended to ensure the capture of key trim trends (see Section 4.4). Collecting trim data at a coarser 20-kn speed increment at higher airspeeds (i.e., > 80 kn) is satisfactory, as was done for the UH-60 stitched model presented herein.

Identification Point Models

The process of identifying point models in rotorcraft is identical to that for fixed-wing aircraft (see Section 3.9.1), and involves performing frequency sweeps in each primary axis and processing the flight-test data to extract state-space models at each flight-test condition. The analyses of the FORECAST UH-60 model stability and control derivative trends over ranges of airspeed (Section 4.6) show that 4 identified point models are sufficient to accurately represent the dynamic response of the rotorcraft over the entire airspeed range for a particular altitude. Identification point models are typically valid over ±20 kn from the ID airspeed, so a 40-kn spacing is recommended. Identification point models were therefore included at hover, 40, 80, and 120 knots for the UH-60 stitched model presented herein. As with the collection of trim data, it is important to note the loading configuration at the start of each frequency sweep run, as this information is used during the baselining process.

Static Stability Data

When performing system identification it is common for speed derivatives to be insensitive due to lack of frequency response data at low frequencies. Therefore it is recommended that longitudinal and lateral/directional static stability data be collected around each point for which a model is identified, which can be used to explicitly calculate speed derivatives M_u and L_v, and static-stability derivative N_v [1].

For hover/low-speed flight the "collective-fixed" [23] method for obtaining longitudinal and lateral static stability data is suggested. Here, the collective is held constant at "power for level flight" (i.e., zero climb rate) while the cyclic stick is used to vary forward/rearward airspeed for longitudinal data, and sideward airspeed for lateral data. Collecting the static stability data over a range of approximately −15 to +15 knots around the hover point model flight condition, at an increment of approximately 5 knots, is suggested to accurately capture the M_u, L_v, and N_v derivatives.

In forward flight, the above "collective-fixed" method is equally applicable for obtaining longitudinal static stability data. It is recommended that longitudinal static stability data be collected around each forward-flight flight condition for which a point model is identified, using the above guidance on airspeed change and spacing. Lateral/directional static stability data should be collected in forward flight using the "steady heading sideslip" [23] technique.

While the primary purpose of the static stability data is for accurate identification of the M_u, L_v, and N_v derivatives in the point models, these data do provide an additional, finely-spaced source of trim data around the identification flight conditions. However, these collected data must be processed (i.e., retrimmed) to a level flight path angle using the model stitching architecture to be combined with the collected trim data, as discussed in Section 4.9.2.

Verification Doublets

Performing piloted doublets at each point for which a model is identified is useful for time-domain verification of the identified point models and the final stitched model at the anchor point flight conditions. Two doublets, one each for a positive and negative input, in each of the primary axes at each identified point model flight condition are required for verification.

4.9.2 Data Processing

Baselining

Typically during flight testing there will be a natural variance in helicopter weight between test points due to fuel burn-off, which will also affect the inertia values and CG location. As a result, the precise loading configuration will likely vary among the anchor points. To remove the effects of loading configuration on trim and dynamics, a method was introduced in Section 3.9.2 in which the anchor trim data and identified point models are *baselined* to a nominal, or baseline, loading configuration using the model stitching simulation architecture. In this process, the integrated extrapolation methods (Section 2.5) are employed to accurately retrim the anchor trim points and relinearize the anchor point models to a common loading configuration. These *baselined* anchor points are then used to construct the final stitched model.

As with fixed-wing applications, static stability data collected using the collective-fixed method must also be baselined (i.e., retrimmed) to a level flight path angle using the model stitching architecture to employ the data as additional trim points. This is accomplished by ensuring the climb or descent rate is captured in the collected flight-test data, then simply retrimming each data point to level flight.

Interpolation

Upon completion of the *baselining* processing step, the full collection of data is then further processed for direct use in the model stitching architecture. These processing steps include the fitting of splines to the data and interpolating the data to a fine grid. Trim data must be formatted as a full rectangular grid, which is a grid constructed from defined axis values for each interpolation dimension, per requirements of the model stitching architecture interpolation scheme (see Section 2.9). Typically, the grid will be defined for a set range of x-body airspeed U (and y-body airspeed V in the hover/low-speed regime) and a set range of altitude, covering the entire flight envelope. Employing 2-D spline interpolation around hover, for example, as discussed in Section 4.5, allows the collected data to be interpolated to the defined grid while retaining critical inflections in the data.

4.9.3 Rotorcraft Configurations

The extrapolation methods integrated into the model stitching architecture were shown to very accurately simulate loading configurations with off-nominal values of weight, CG, and inertia (see Section 4.6). Therefore, collecting trim data and identifying point models is necessary using only the nominal (baseline) rotorcraft configuration. If the simulation of additional off-nominal configurations is desired, such as the aircraft configured with an external sling load, that configuration would need to be identified or sufficiently modeled by the user for accurate simulation results.

4.9.4 Altitude

Collecting trim data and identifying models at two altitudes is essential for capturing the behavior of rotorcraft trim and key stability and control derivatives over a reasonable operational altitude envelope. For the UH-60 stitched model example presented herein, the technique of linear interpolation/extrapolation of the anchor points at altitudes of sea level and 6000 ft yielded very good agreement over a broad altitude range of sea level through 10,000 ft (see Section 4.6.4). Based on these results, it is suggested that trim is collected and models are identified at sea level and 6000 feet. A 6000-ft spacing was also chosen when identifying models of the Bell 206 at 1000 ft and 7000 ft for the development of a stitched simulation model, as presented in Ref. [5], which yielded good results.

4.9.5 Summary of Recommendations

The overall flight-test recommendations for the development of a rotorcraft stitched simulation model are summarized in Table 4.14. These recommendations are based on the analyses of the FORECAST UH-60 stitched simulation model presented herein, and are appropriate for military and civilian conventional helicopter applications. The table provides recommended airspeed increments, quantity of points, and example profile at which to identify point models and collect trim data. Trim data recommendations are further organized into forward/rearward points for hover/low-speed through forward flight, and sideward/quartering points for hover/low-speed. Recommended altitudes at which to perform the data collection are provided.

Table 4.14: Summary of flight-test recommendations for development of rotorcraft stitched models

Interpolation Dimension	Parameter	ID Point Models	Trim Data	
			Forward/Rearward	Sideward/Quartering
Airspeed	# of airspeeds	3–5	15–20	15–25
	Increment [kn]	40–60	5–20[a,b]	3–5[c]
	Example profile	[*hover* 40 80 120]	[−20 −15 −10 −5 *hover* 5 10 15 20 30 40 50 60 70 80 100 120 140 160]	[5 10 15 20] kn @ [45 90 135 225 270 315] deg
Altitude	# of altitudes	2		2
	Increment [ft]	5000–7000		5000–7000
	Example profile	[*sea level* 6000]		[*sea level* 6000]

[a] Fine 5-kn increment around hover (≤ 20 kn), 10-kn increment at low/mid speed (≤ 80 kn), and coarser 20-kn increment out to high speed (> 80 kn)

[b] Can include baselined longitudinal static stability data as fine-increment trim data around ID points

[c] Can include baselined lateral static stability data as fine-increment sideward trim data around the hover ID point

4.10 Chapter Summary

Application of the model stitching architecture for a rotorcraft was demonstrated in this chapter using FORECAST high-order linear models of the UH-60 Black Hawk helicopter. In addition to demonstrating the use of high-order models in the model stitching architecture, this example application also demonstrated the storing and subsequent look-up of trim data in multiple dimensions. *Stitching* in x-body axis airspeed U and y-body axis airspeed V allowed for accurate simulation in the hover/low-speed regime. Scenarios were investigated to determine recommended spacing and strategies for the collection of trim data in the hover/low-speed and forward-flight regimes.

Verification results of the off-nominal extrapolation methods were presented comparing outputs of the stitched model to values from point models for off-nominal configurations and conditions. Two check cases were provided to verify overall simulation fidelity at two discrete flight conditions and configurations. Findings and implications were considered to provide guidance on future flight testing for the development of stitched models involving rotorcraft.

5 Conclusions

Model stitching is a technique that allows continuous, full flight-envelope flight dynamics simulation of fixed-wing aircraft and rotorcraft using only a small number of discrete-point linear models and trim data. A model stitching simulation architecture has been developed, which allows flight-identified models to be used directly, and incorporates additional features and extrapolation methods for the simulation of off-nominal loading configurations and alternate altitudes. The model stitching simulation architecture is applicable to any flight vehicle configuration for which point-wise linear models and trim data can be obtained, and is demonstrated herein for a fixed-wing aircraft model representative of the Cessna Citation CJ1 and a rotorcraft model representative of the UH-60 Black Hawk.

The following general conclusions were determined from the current effort:

1. The model stitching simulation architecture provides a quasi-nonlinear, time varying model that is accurate for flight dynamics and control applications over the operational envelope, with good accuracy maintained in the frequency- and time-domain.

2. For both the fixed-wing CJ1 and the UH-60 rotorcraft application, configuring the stitched simulation models with 8 discrete-point linear models (4 point models each at two altitudes) plus additional trim data, and employing the appropriate altitude extrapolation technique for each case, was found to allow accurate simulation over the full airspeed and altitude range.

3. Accurate simulation of off-nominal aircraft configurations (i.e., values of gross weight, inertia, and CG location that differ from those of the identified/baseline configuration) is accomplished by real-time extrapolation methods within the model stitching architecture. The off-nominal extrapolation methods necessitate only the baseline aircraft loading configuration to be flight tested, which significantly reduces required flight-test points and associated flight costs.

Fixed-Wing Aircraft

The following conclusions were determined from the analyses of the Cessna Citation CJ1 stitched model:

i. The model stitching technique of combining linear point models and trim data for discrete flight conditions allows for accurate, full flight-envelope simulation of a business jet. Eight discrete point models (4 at 10,000 ft and 4 at 30,000 ft) over the airspeed range and at a nominal weight/CG are needed to cover the flight envelope and accurately predict off-nominal trends. More finely-spaced trim data are also needed to correctly capture trends and key inflections.

ii. Point models and trim data at two altitudes provides for an accurate simulation of altitude effects using air density-ratio scaling. Extrapolating models to off-nominal altitudes using air density-ratio scaling was found to be highly accurate over a range of ±10,000 ft for the CJ1 stitched model application. Extrapolation on two sets of point models and trim data were performed; the 10,000-ft data were extrapolated to sea level and 20,000 ft, and the 30,000-ft data were extrapolated to 40,000 ft, covering the entire altitude envelope in 10,000-ft increments. Air density-ratio scaling produced more accurate results than linearly interpolating between the two altitudes.

iii. Analyses of the nondimensional stability and control derivatives from the AAA CJ1 model have indicated that some nondimensional derivatives are significantly affected by Mach and angle-of-attack effects, and are not necessarily constant over the flight envelope. As such, the flight-test recommendations for the identification of 4 point models each at two altitudes is appropriate using either dimensional derivatives or nondimensional derivatives.

iv. Analyses of variations in trim and derivative values from the AAA CJ1 model as a function of flap deflection indicate significant changes in trim angle of attack, elevator deflection, and thrust for deployed flaps at a given airspeed. Although some stability and control derivatives are affected, the largest

and most significant variations with flap deflection are seen in trim angle of attack and longitudinal controls. Herein, the flap deflection implementation was confined to changes in trim only; the stability and control derivatives remain at the nominal (i.e., flaps-up) configuration. This approach ensures that trim with flap deflection is correct, which is important for piloted simulation, and allows for efficient flight testing while satisfactorily preserving the dynamic response.

Rotorcraft

The following conclusions were determined from the analyses of the UH-60 Black Hawk stitched model:

i. Full flight-envelope simulation using the model stitching simulation architecture was demonstrated for a rotorcraft application, requiring only 8 discrete point models (4 at sea level and 4 at 6000 ft) at a nominal weight/CG. More finely-spaced trim data are also needed to correctly capture trends and key inflections.

ii. Storing and subsequent look-up of trim data in multiple simultaneous dimensions, i.e., stitching in x-body airspeed U and y-body airspeed V, has been demonstrated to yield good accuracy of the UH-60 stitched simulation model in the hover/low-speed regime. Low-speed forward, rearward, and sideward trim data at a fine 5-kn increment, as well as quartering flight trim at 45-deg radial spacing, was found to accurately preserve the implicit u- and v-speed derivative values, and thus the dynamic response, around hover. Additionally, hovering flight in the presence of steady winds was accurately simulated using the above trim data collection strategy.

iii. High-order linear models can be effectively utilized in the model stitching architecture. Dynamic response check cases provided verification of the higher-order rotor dynamics for two flight conditions at off-nominal loading configurations.

iv. Linear interpolation, as opposed to air density-ratio scaling, between data at anchor altitudes is recommended for simulating off-nominal altitudes for rotorcraft, as certain derivatives do not scale directly with altitude. Herein, linear interpolation was performed on trim data and derivatives between the sea-level and 6000-ft anchor data, and the data were also linearly extrapolated to 10,000 ft, which yielded good results.

Appendix A   Stability and Control Derivatives for Fixed-Wing Aircraft

Contents

This Appendix provides stability and control derivative definitions and conversions used in the development of the bare-airframe models for the Cessna Citation CJ1 stitched model presented in Chapter 3. The bare-airframe linear point models were first formulated in stability axes then transformed into body axes for use in the model stitching simulation architecture. Section A.1 provides equations for the calculation of stability-axes inertias, dimensional derivatives from nondimensional derivatives, and primed derivatives. Section A.2 provides transformation equations to obtain body-axes dimensional derivatives given the stability-axes dimensional derivatives. Equations for the thrust control derivatives are given in Section A.2.2.

A.1   Stability Axes Coordinate System

A.1.1   Inertias

Given the values of the aircraft moments of inertia (I_{xx}, I_{yy}, and I_{zz}) and cross-product of inertia I_{xz} in body axes, the values of the *stability-axes* inertias are found following Ref. [13]:

$$I_{xx_s} = I_{xx} \cos^2 \alpha_0 + I_{zz} \sin^2 \alpha_0 - I_{xz} \sin 2\alpha_0 \tag{A.1}$$

$$I_{yy_s} = I_{yy} \tag{A.2}$$

$$I_{zz_s} = I_{xx} \sin^2 \alpha_0 + I_{zz} \cos^2 \alpha_0 + I_{xz} \sin 2\alpha_0 \tag{A.3}$$

$$I_{xz_s} = \tfrac{1}{2} \left(I_{xx} - I_{zz} \right) \sin 2\alpha_0 + I_{xz} \cos 2\alpha_0 \tag{A.4}$$

where α_0 is the trim angle of attack. The stability-axes inertias are used in the calculation of the dimensional stability-axes derivatives, as presented in Sections A.1.2 and A.1.3.

A.1.2   Unprimed Dimensional Derivatives

Dimensional stability and control derivatives in *stability axes* are found from the nondimensional derivatives and aircraft properties [13]:

$$X_u = \frac{-\bar{q}S}{mV_{\text{tot}_0}} \left(2C_D + C_{D_u} \right) \tag{A.5}$$

$$X_{T_u} = \frac{\bar{q}S}{mV_{\text{tot}_0}} \left(2C_T + C_{T_u} \right) \tag{A.6}$$

$$X_\alpha = \frac{\bar{q}S}{m} \left(C_L - C_{D_\alpha} \right) \tag{A.7}$$

$$X_w = \frac{X_\alpha}{V_{\text{tot}_0}} \tag{A.8}$$

$$X_{\delta_e} = \frac{-\bar{q}S}{m} C_{D_{\delta_e}} \tag{A.9}$$

$$Z_u = \frac{-\bar{q}S}{mV_{\text{tot}_0}} \left(2C_L + C_{L_u}\right) \tag{A.10}$$

$$Z_\alpha = \frac{-\bar{q}S}{m} \left(C_D + C_{L_\alpha}\right) \tag{A.11}$$

$$Z_w = \frac{Z_\alpha}{V_{\text{tot}_0}} \tag{A.12}$$

$$Z_{\dot{\alpha}} = \frac{-\bar{q}S\bar{c}}{2mV_{\text{tot}_0}} C_{L_{\dot{\alpha}}} \tag{A.13}$$

$$Z_{\dot{w}} = \frac{Z_{\dot{\alpha}}}{V_{\text{tot}_0}} \tag{A.14}$$

$$Z_q = \frac{-\bar{q}S\bar{c}}{2mV_{\text{tot}_0}} C_{L_q} \tag{A.15}$$

$$Z_{\delta_e} = \frac{-\bar{q}S}{m} C_{L_{\delta_e}} \tag{A.16}$$

$$M_u = \frac{\bar{q}S\bar{c}}{I_{yy}V_{\text{tot}_0}} \left(2C_m + C_{m_u}\right) \tag{A.17}$$

$$M_{T_u} = \frac{\bar{q}S\bar{c}}{I_{yy}V_{\text{tot}_0}} \left(2C_{m_T} + C_{m_{T_u}}\right) \tag{A.18}$$

$$M_\alpha = \frac{\bar{q}S\bar{c}}{I_{yy}} C_{m_\alpha} \tag{A.19}$$

$$M_w = \frac{M_\alpha}{V_{\text{tot}_0}} \tag{A.20}$$

$$M_{\dot{\alpha}} = \frac{\bar{q}S\bar{c}}{I_{yy}} \frac{\bar{c}}{2V_{\text{tot}_0}} C_{m_{\dot{\alpha}}} \tag{A.21}$$

$$M_{\dot{w}} = \frac{M_{\dot{\alpha}}}{V_{\text{tot}_0}} \tag{A.22}$$

$$M_q = \frac{\bar{q}S\bar{c}}{I_{yy}} \frac{\bar{c}}{2V_{\text{tot}_0}} C_{m_q} \tag{A.23}$$

$$M_{\delta_e} = \frac{\bar{q}S\bar{c}}{I_{yy}} C_{m_{\delta_e}} \tag{A.24}$$

$$Y_\beta = \frac{\bar{q}S}{m} C_{Y_\beta} \tag{A.25}$$

$$Y_v = \frac{Y_\beta}{V_{\text{tot}_0}} \tag{A.26}$$

$$Y_p = \frac{\bar{q}Sb}{2mV_{\text{tot}_0}} C_{Y_p} \tag{A.27}$$

$$Y_r = \frac{\bar{q}Sb}{2mV_{\text{tot}_0}} C_{Y_r} \tag{A.28}$$

$$Y_{\delta_r} = \frac{\bar{q}S}{m} C_{Y_{\delta_r}} \tag{A.29}$$

$$Y_{\delta_a} = \frac{\bar{q}S}{m} C_{Y_{\delta_a}} \tag{A.30}$$

$$L_\beta = \frac{\bar{q}Sb}{I_{xx_s}} C_{l_\beta} \tag{A.31}$$

$$L_v = \frac{L_\beta}{V_{\text{tot}_0}} \tag{A.32}$$

$$L_p = \frac{\bar{q}Sb}{I_{xx_\mathrm{s}}} \frac{b}{2V_{\mathrm{tot}_0}} C_{l_p} \tag{A.33}$$

$$L_r = \frac{\bar{q}Sb}{I_{xx_\mathrm{s}}} \frac{b}{2V_{\mathrm{tot}_0}} C_{l_r} \tag{A.34}$$

$$L_{\delta_\mathrm{a}} = \frac{\bar{q}Sb}{I_{xx_\mathrm{s}}} C_{l_{\delta_\mathrm{a}}} \tag{A.35}$$

$$L_{\delta_\mathrm{r}} = \frac{\bar{q}Sb}{I_{xx_\mathrm{s}}} C_{l_{\delta_\mathrm{r}}} \tag{A.36}$$

$$N_\beta = \frac{\bar{q}Sb}{I_{zz_\mathrm{s}}} C_{n_\beta} \tag{A.37}$$

$$N_v = \frac{N_\beta}{V_{\mathrm{tot}_0}} \tag{A.38}$$

$$N_p = \frac{\bar{q}Sb}{I_{zz_\mathrm{s}}} \frac{b}{2V_{\mathrm{tot}_0}} C_{n_p} \tag{A.39}$$

$$N_r = \frac{\bar{q}Sb}{I_{zz_\mathrm{s}}} \frac{b}{2V_{\mathrm{tot}_0}} C_{n_r} \tag{A.40}$$

$$N_{\delta_\mathrm{a}} = \frac{\bar{q}Sb}{I_{zz_\mathrm{s}}} C_{n_{\delta_\mathrm{a}}} \tag{A.41}$$

$$N_{\delta_\mathrm{r}} = \frac{\bar{q}Sb}{I_{zz_\mathrm{s}}} C_{n_{\delta_\mathrm{r}}} \tag{A.42}$$

A.1.3 Primed Dimensional Derivatives

Primed derivatives [11], which account for the influence of the cross-product of inertia I_{xz}, are defined as:

$$L'_i = \frac{L_i + (I_{xz_\mathrm{s}}/I_{xx_\mathrm{s}}) N_i}{1 - \left[I_{xz_\mathrm{s}}^2 / (I_{xx_\mathrm{s}} I_{zz_\mathrm{s}})\right]} \tag{A.43}$$

$$N'_i = \frac{N_i + (I_{xz_\mathrm{s}}/I_{zz_\mathrm{s}}) L_i}{1 - \left[I_{xz_\mathrm{s}}^2 / (I_{xx_\mathrm{s}} I_{zz_\mathrm{s}})\right]} \tag{A.44}$$

for $i = \alpha, \beta, u, v, w, p, q, r, \delta_\mathrm{a}, \delta_\mathrm{e}, \delta_\mathrm{r}, \delta_\mathrm{t}$.

A.2 Body Axes Coordinate System

A.2.1 Derivative Transformations

Transformations of the dimensional derivatives from stability axes to *body axes*, as provided in Ref. [11], are as follows:

$$(X_u)_\mathrm{b} = X_u \cos^2 \alpha_0 - (X_w + Z_u) \sin \alpha_0 \cos \alpha_0 + Z_w \sin^2 \alpha_0 \tag{A.45}$$

$$(X_w)_\mathrm{b} = X_w \cos^2 \alpha_0 + (X_u - Z_w) \sin \alpha_0 \cos \alpha_0 - Z_u \sin^2 \alpha_0 \tag{A.46}$$

$$(X_{\dot{w}})_\mathrm{b} = X_{\dot{w}} \cos^2 \alpha_0 - Z_{\dot{w}} \sin \alpha_0 \cos \alpha_0 \tag{A.47}$$

$$(X_q)_\mathrm{b} = X_q \cos \alpha_0 - Z_q \sin \alpha_0 \tag{A.48}$$

$$(X_{\delta_\mathrm{e}})_\mathrm{b} = X_{\delta_\mathrm{e}} \cos \alpha_0 - Z_{\delta_\mathrm{e}} \sin \alpha_0 \tag{A.49}$$

$$(Z_u)_\mathrm{b} = Z_u \cos^2 \alpha_0 - (Z_w - X_u) \sin \alpha_0 \cos \alpha_0 - X_w \sin^2 \alpha_0 \tag{A.50}$$

$$(Z_w)_\mathrm{b} = Z_w \cos^2 \alpha_0 + (Z_u + X_w) \sin \alpha_0 \cos \alpha_0 + X_u \sin^2 \alpha_0 \tag{A.51}$$

$$(Z_{\dot{w}})_\mathrm{b} = Z_{\dot{w}} \cos^2 \alpha_0 + X_{\dot{w}} \sin \alpha_0 \cos \alpha_0 \tag{A.52}$$

$$(Z_q)_\mathrm{b} = Z_q \cos \alpha_0 + X_q \sin \alpha_0 \tag{A.53}$$

$$(Z_{\delta_\mathrm{e}})_\mathrm{b} = Z_{\delta_\mathrm{e}} \cos \alpha_0 + X_{\delta_\mathrm{e}} \sin \alpha_0 \tag{A.54}$$

$$(M_u)_{\mathrm{b}} = M_u \cos\alpha_0 - M_w \sin\alpha_0 \tag{A.55}$$

$$(M_w)_{\mathrm{b}} = M_w \cos\alpha_0 + M_u \sin\alpha_0 \tag{A.56}$$

$$(M_{\dot{w}})_{\mathrm{b}} = M_{\dot{w}} \cos\alpha_0 \tag{A.57}$$

$$(M_q)_{\mathrm{b}} = M_q \tag{A.58}$$

$$(M_{\delta_{\mathrm{e}}})_{\mathrm{b}} = M_{\delta_{\mathrm{e}}} \tag{A.59}$$

$$(Y_v)_{\mathrm{b}} = Y_v \tag{A.60}$$

$$(Y_p)_{\mathrm{b}} = Y_p \cos\alpha_0 - Y_r \sin\alpha_0 \tag{A.61}$$

$$(Y_r)_{\mathrm{b}} = Y_r \cos\alpha_0 + Y_p \sin\alpha_0 \tag{A.62}$$

$$(Y_{\delta_{\mathrm{a}}})_{\mathrm{b}} = Y_{\delta_{\mathrm{a}}} \tag{A.63}$$

$$(Y_{\delta_{\mathrm{r}}})_{\mathrm{b}} = Y_{\delta_{\mathrm{r}}} \tag{A.64}$$

$$(L'_v)_{\mathrm{b}} = L'_v \cos\alpha_0 - N'_v \sin\alpha_0 \tag{A.65}$$

$$(L'_p)_{\mathrm{b}} = L'_p \cos^2\alpha_0 - \left(L'_r + N'_p\right)\sin\alpha_0\cos\alpha_0 + N'_r \sin^2\alpha_0 \tag{A.66}$$

$$(L'_r)_{\mathrm{b}} = L'_r \cos^2\alpha_0 - \left(N'_r - L'_p\right)\sin\alpha_0\cos\alpha_0 - N'_p \sin^2\alpha_0 \tag{A.67}$$

$$(L'_{\delta_{\mathrm{a}}})_{\mathrm{b}} = L'_{\delta_{\mathrm{a}}} \cos\alpha_0 - N'_{\delta_{\mathrm{a}}} \sin\alpha_0 \tag{A.68}$$

$$(L'_{\delta_{\mathrm{r}}})_{\mathrm{b}} = L'_{\delta_{\mathrm{r}}} \cos\alpha_0 - N'_{\delta_{\mathrm{r}}} \sin\alpha_0 \tag{A.69}$$

$$(N'_v)_{\mathrm{b}} = N'_v \cos\alpha_0 + L'_v \sin\alpha_0 \tag{A.70}$$

$$(N'_p)_{\mathrm{b}} = N'_p \cos^2\alpha_0 - \left(N'_r - L'_p\right)\sin\alpha_0\cos\alpha_0 - L'_r \sin^2\alpha_0 \tag{A.71}$$

$$(N'_r)_{\mathrm{b}} = N'_r \cos^2\alpha_0 + \left(L'_r + N'_p\right)\sin\alpha_0\cos\alpha_0 + L'_p \sin^2\alpha_0 \tag{A.72}$$

$$(N'_{\delta_{\mathrm{a}}})_{\mathrm{b}} = N'_{\delta_{\mathrm{a}}} \cos\alpha_0 + L'_{\delta_{\mathrm{a}}} \sin\alpha_0 \tag{A.73}$$

$$(N'_{\delta_{\mathrm{r}}})_{\mathrm{b}} = N'_{\delta_{\mathrm{r}}} \cos\alpha_0 + L'_{\delta_{\mathrm{r}}} \sin\alpha_0 \tag{A.74}$$

Note that the above body-axes notation $(\ )_{\mathrm{b}}$ is dropped elsewhere herein.

A.2.2 Thrust Control Derivatives

The dimensional thrust control derivatives are formulated based on the geometric placement and incidence of the engines, and the assumption that the produced thrust is concentrated at the center of the engine nacelle. The thrust derivatives are naturally defined in *body axes* as follows:

$$X_{\delta_{\mathrm{t}}} = \frac{1}{m}\cos\alpha_{\mathrm{t}} \tag{A.75}$$

$$Z_{\delta_{\mathrm{t}}} = -\frac{1}{m}\sin\alpha_{\mathrm{t}} \tag{A.76}$$

$$M_{\delta_{\mathrm{t}}} = \frac{1}{I_{yy}}\left(z_{\mathrm{t}}\cos\alpha_{\mathrm{t}} + x_{\mathrm{t}}\sin\alpha_{\mathrm{t}}\right) \tag{A.77}$$

where α_{t} is the thrust inclination angle, and x_{t} and z_{t} are the x- and z-axis offsets, respectively, between the thrust center and the aircraft CG. The thrust control input δ_{t} has units of pounds thrust, and an assumed range from 0 to maximum thrust.

Appendix B Verification Figures: CJ1 Stitched Model

Contents

This appendix provides additional off-nominal verification results for the Cessna Citation CJ1 business jet stitched model, as presented in Section 3.6. Stability and control derivative and trim comparisons are provided for a range of airspeed for off-nominal values of weight (Section B.1), inertia (Section B.2), center of gravity location (Section B.3), altitude (Section B.4), and flap setting (Section B.5). In all figures, the stitched model, configured only with the anchor point models and trim data indicated (solid symbols), was retrimmed and relinearized for various simulation values of each property over a range of airspeed (dashed lines) and compared with values from the AAA truth data (solid lines).

B.1 Weight

Figures B.1–B.3 show the complete trim and stability and control derivative comparison results for the CJ1 off-nominal weight verification presented in Section 3.6.1.
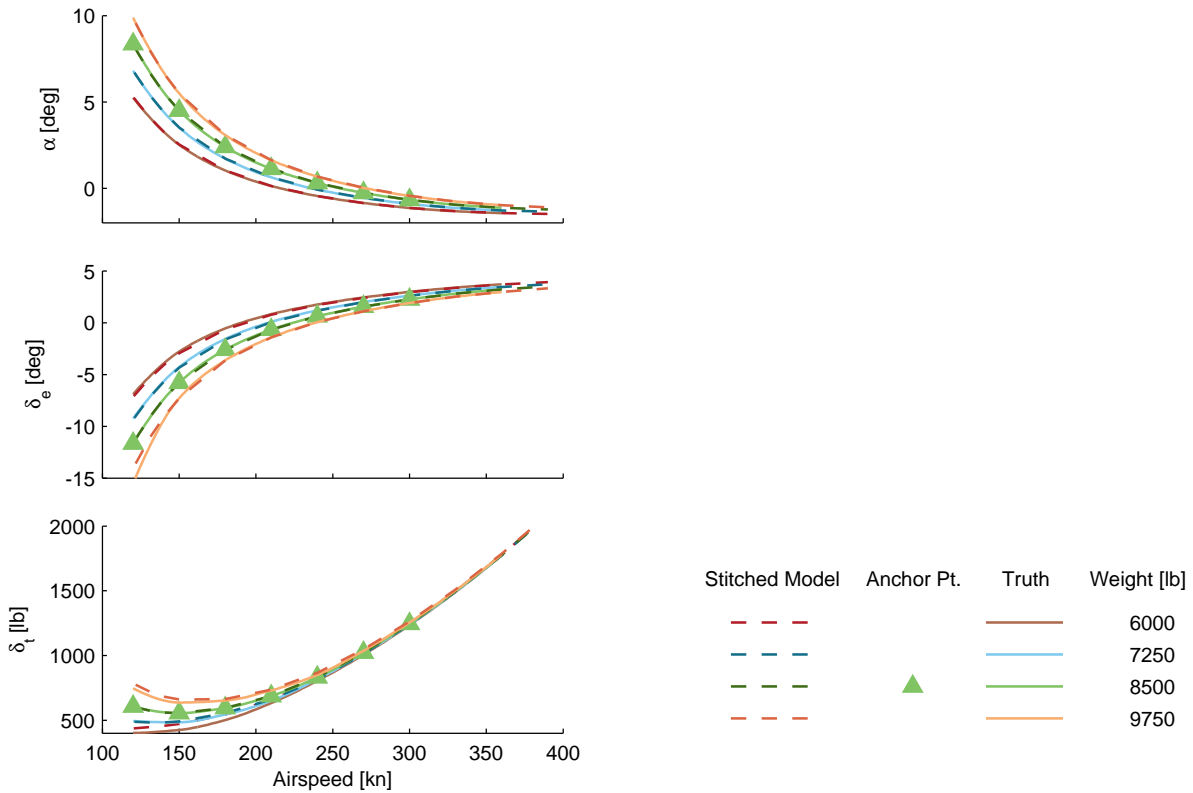
Figure B.1: Verification of off-nominal weight extrapolation, CJ1 stitched model, trim.
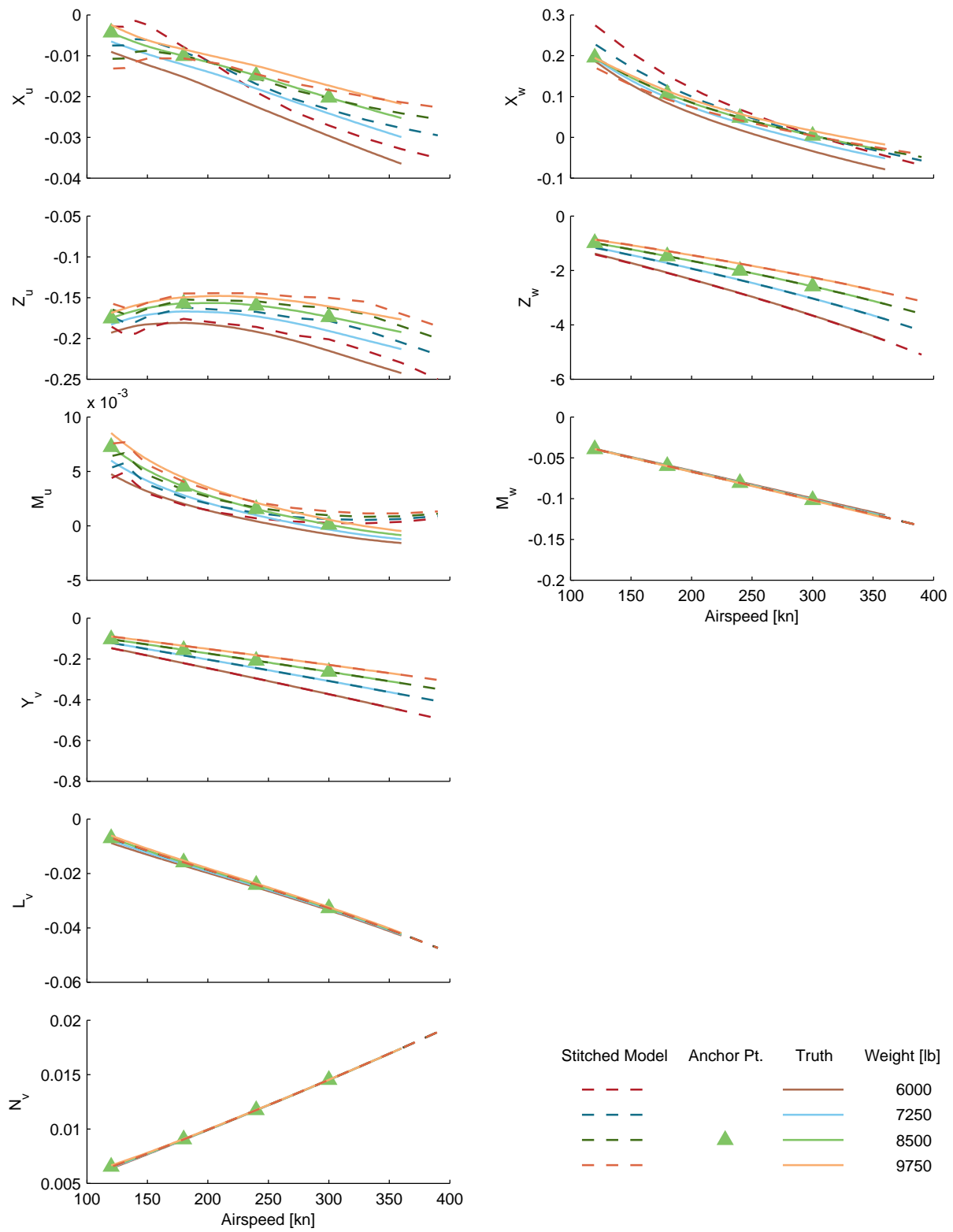
Figure B.2: Verification of off-nominal weight extrapolation, CJ1 stitched model, stability derivatives.
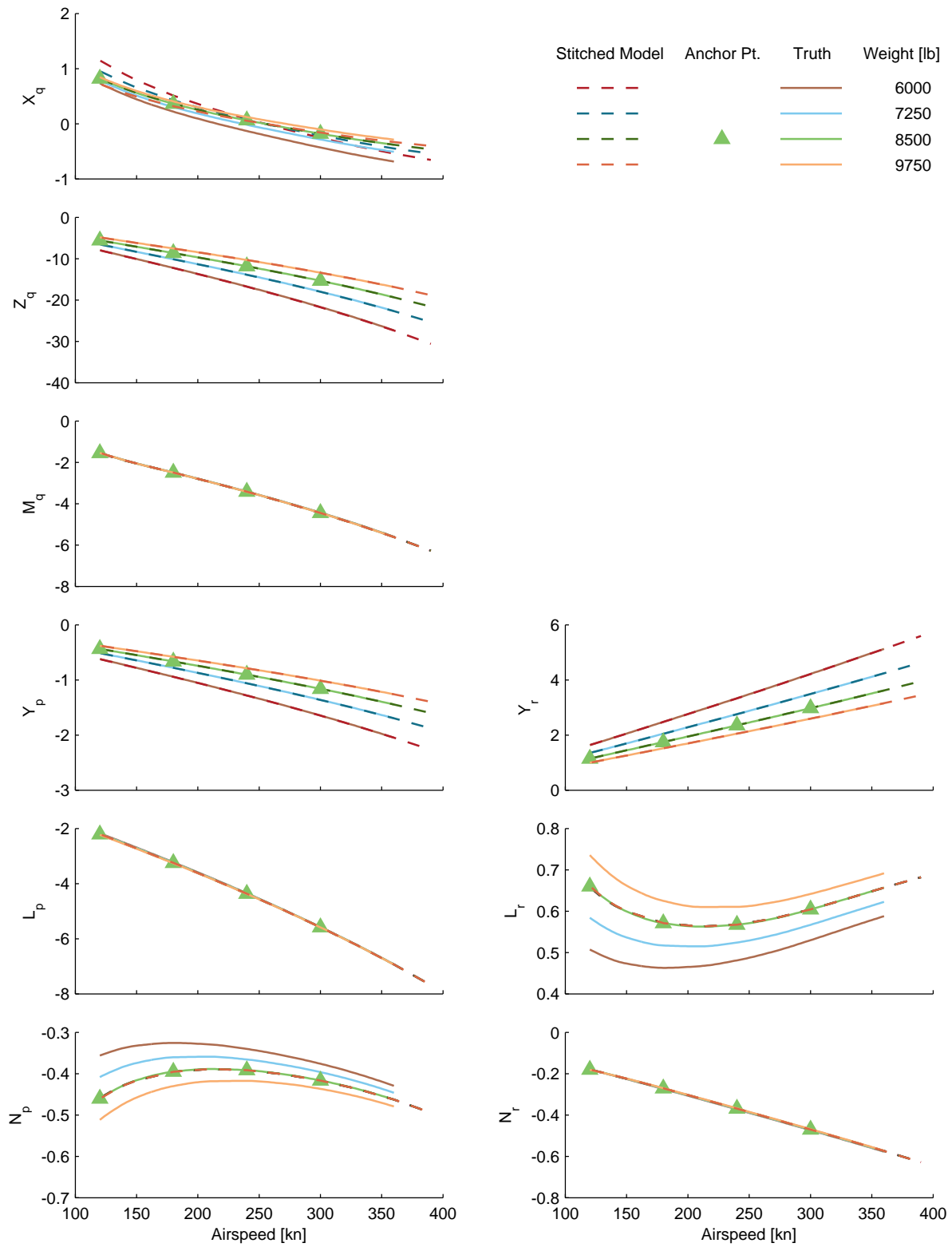
Figure B.2: Verification of off-nominal weight extrapolation, CJ1 stitched model, stability derivatives (cont.)
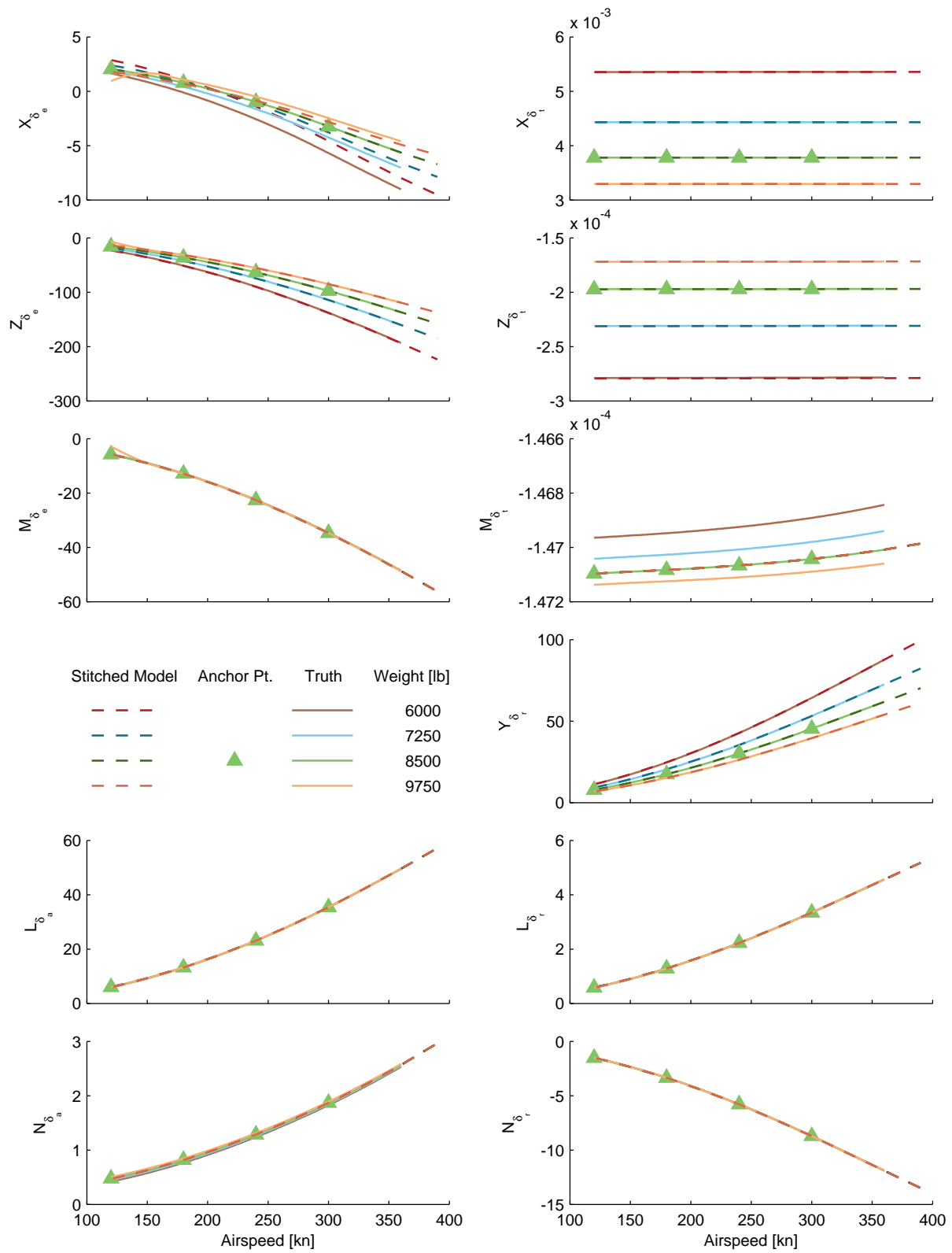
Figure B.3: Verification of off-nominal weight extrapolation, CJ1 stitched model, control derivatives.

B.2   Inertia

The CJ1 stitched model was configured with off-nominal inertia values and verified against AAA point models. Sections B.2.1–B.2.3 present the results for off-nominal values of I_{xx}, I_{yy}, and I_{zz} varied individually.

B.2.1   Roll Inertia

Figures B.4–B.6 show the complete trim and stability and control derivative comparison results for the CJ1 off-nominal roll inertia verification, as presented in Section 3.6.2. Note that changes in inertia have no effect on trim; only the dynamics are affected, as seen in the values of the stability and control derivatives. A plot of trim angle of attack and controls is shown for this inertia case only to verify the unchanged values of trim.
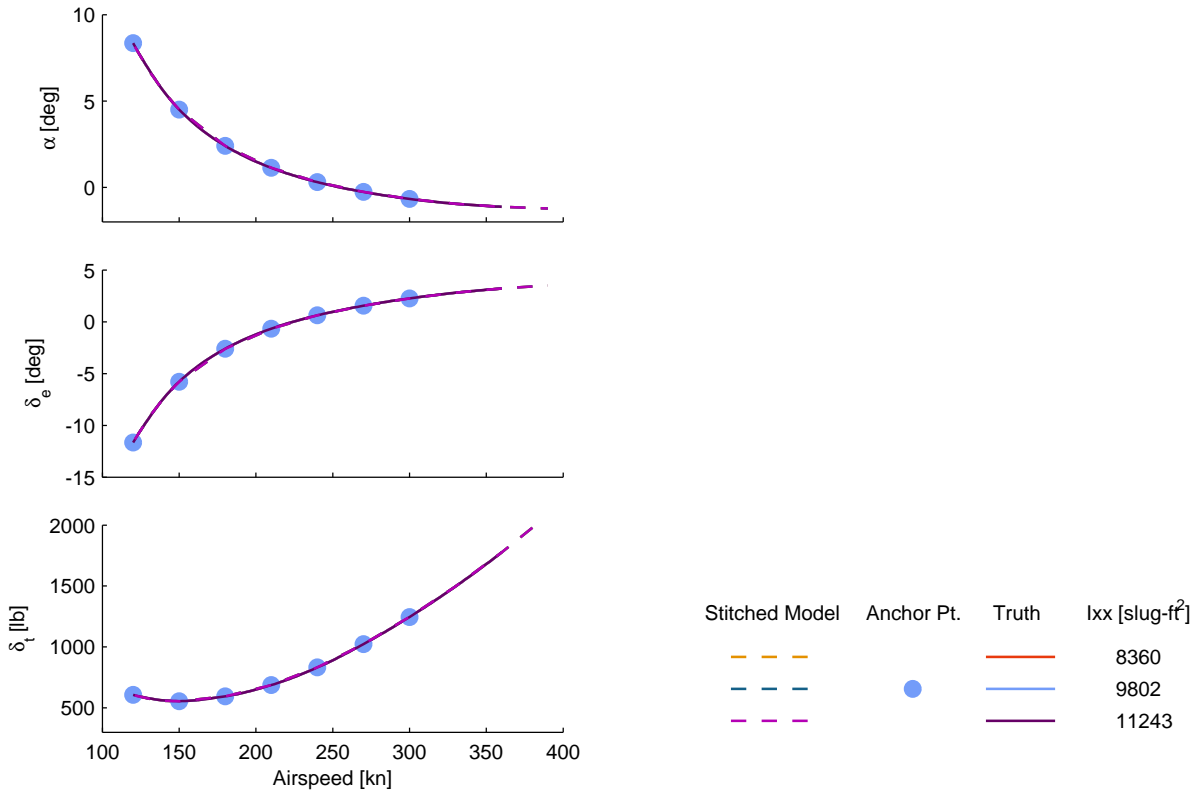
Figure B.4: Verification of off-nominal roll inertia extrapolation, CJ1 stitched model, trim.
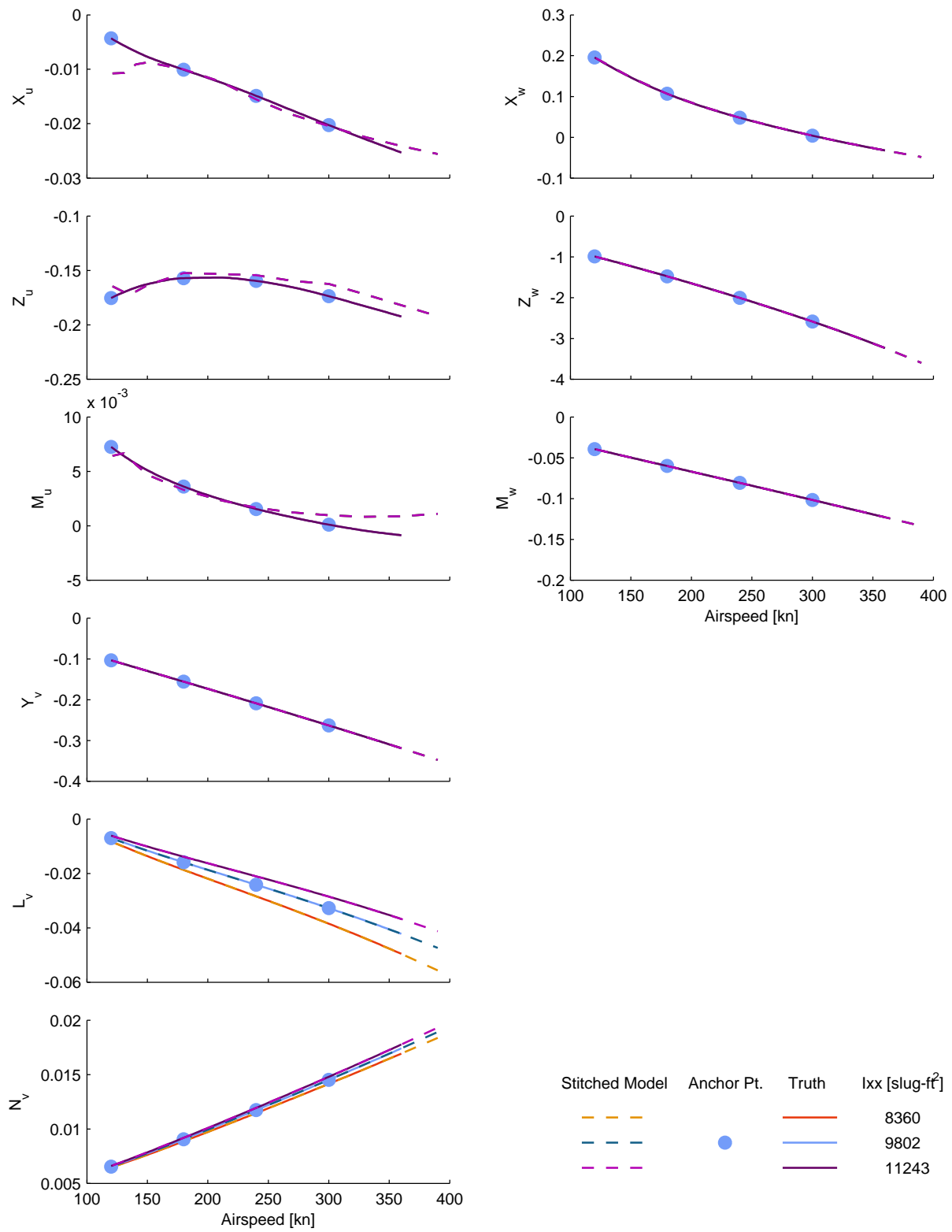
Figure B.5: Verification of off-nominal roll inertia extrapolation, CJ1 stitched model, stability derivatives.
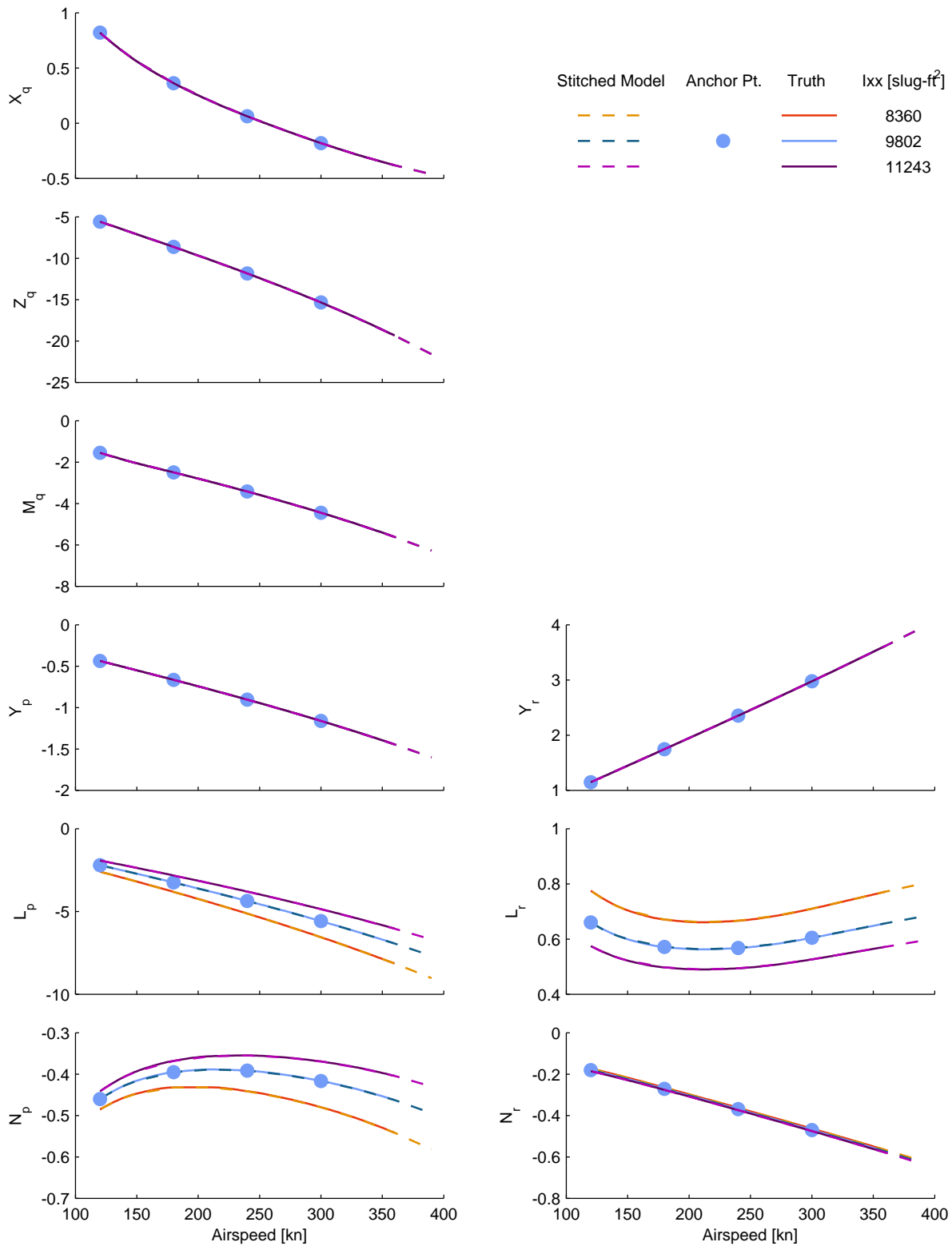
Figure B.5: Verification of off-nominal roll inertia extrapolation, CJ1 stitched model, stability derivatives (cont.)
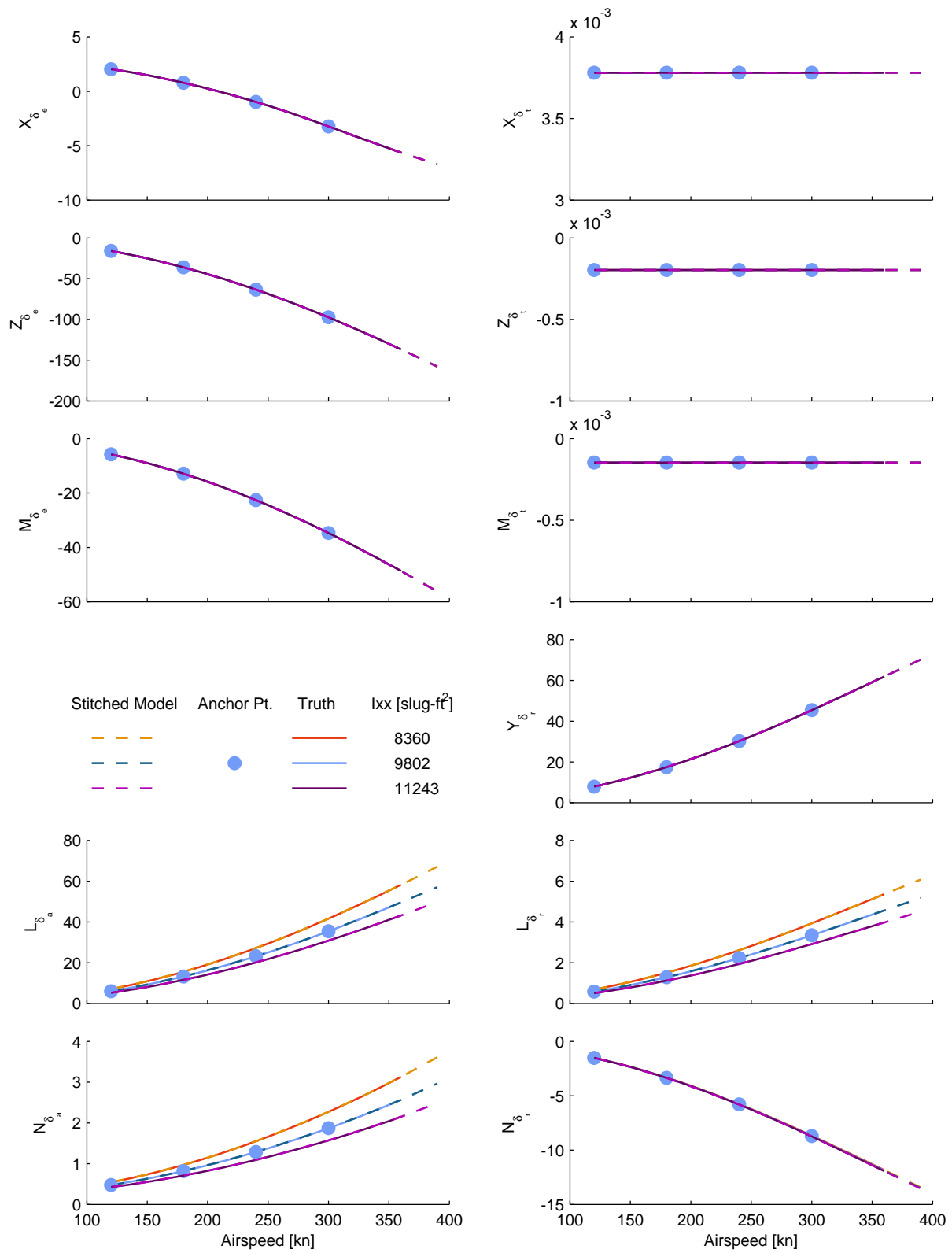
Figure B.6: Verification of off-nominal roll inertia extrapolation, CJ1 stitched model, control derivatives.

B.2.2 Pitch Inertia

Figures B.7 and B.8 show the complete stability and control derivative comparison results for the CJ1 off-nominal pitch inertia verification, as presented in Section 3.6.2. As noted and verified in the previous section, changes in inertia have no effect on trim; thus, the plot showing the unchanged values of trim has been omitted.
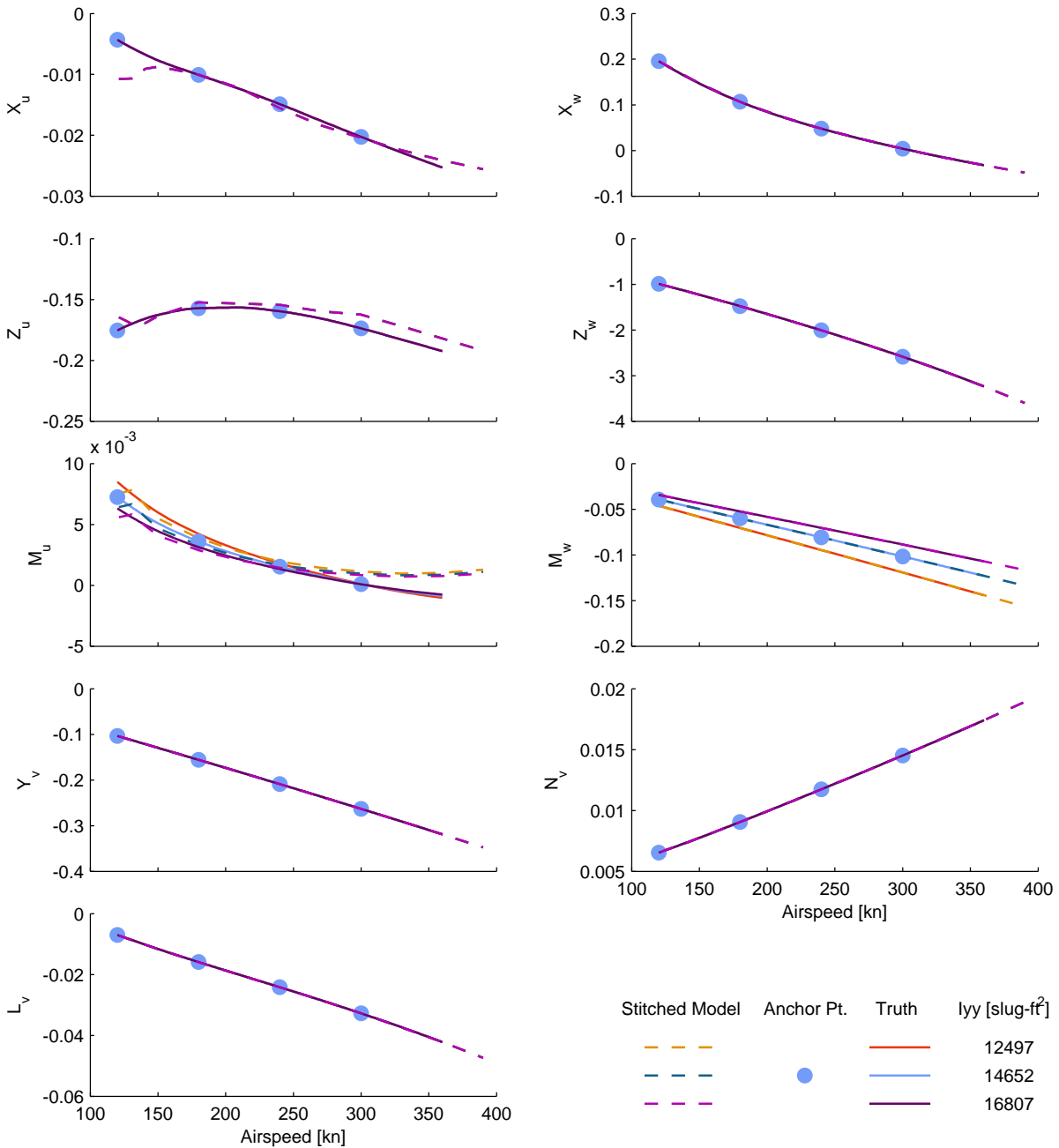
Figure B.7: Verification of off-nominal pitch inertia extrapolation, CJ1 stitched model, stability derivatives.
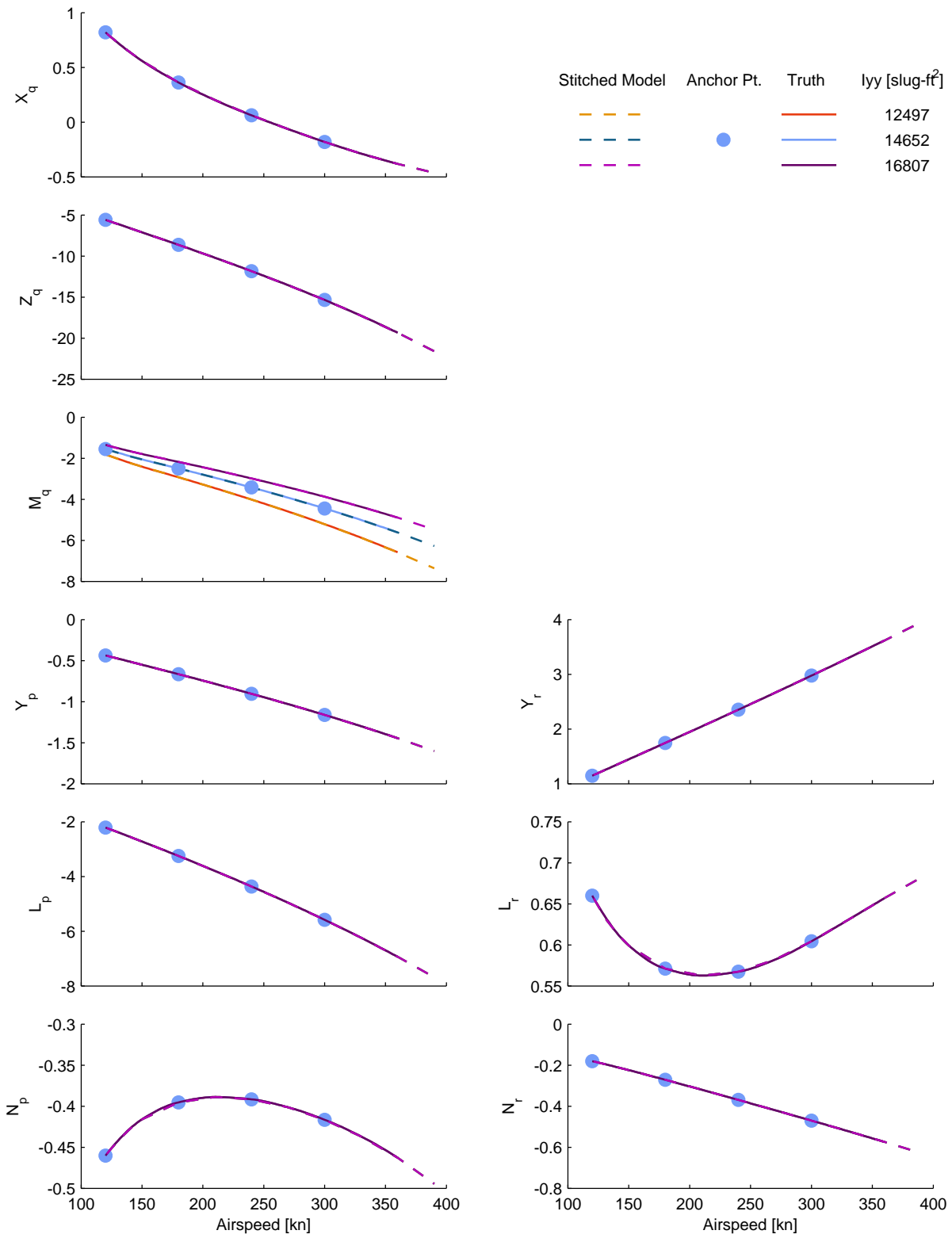
Figure B.7: Verification of off-nominal pitch inertia extrapolation, CJ1 stitched model, stability derivatives (cont.)
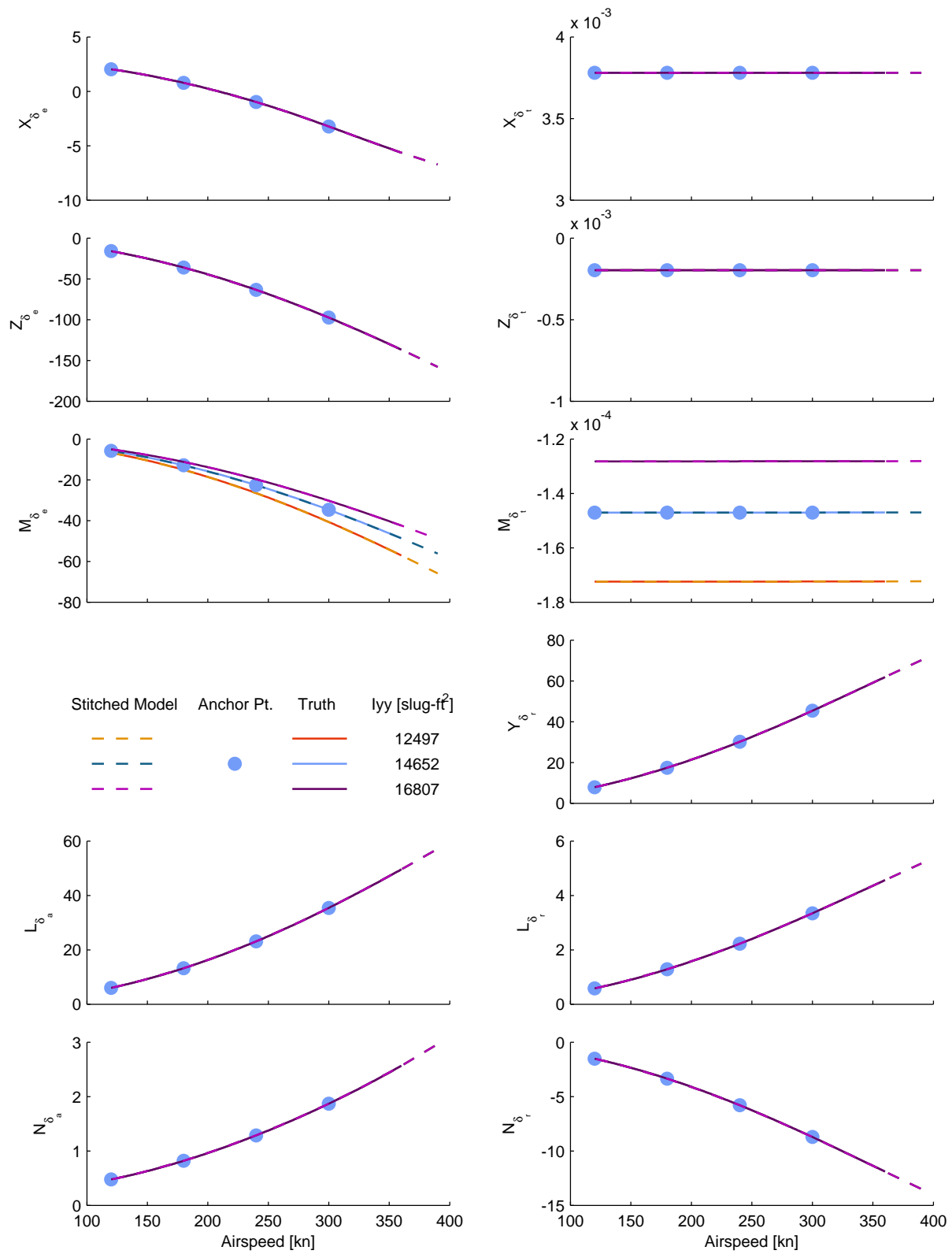
Figure B.8: Verification of off-nominal pitch inertia extrapolation, CJ1 stitched model, control derivatives.

B.2.3 Yaw Inertia

Figures B.9 and B.10 show the complete stability and control derivative comparison results for the CJ1 off-nominal yaw verification, as presented in Section 3.6.2. As noted and verified previously, changes in inertia have no effect on trim; thus, the plot showing the unchanged values of trim has been omitted from this section.
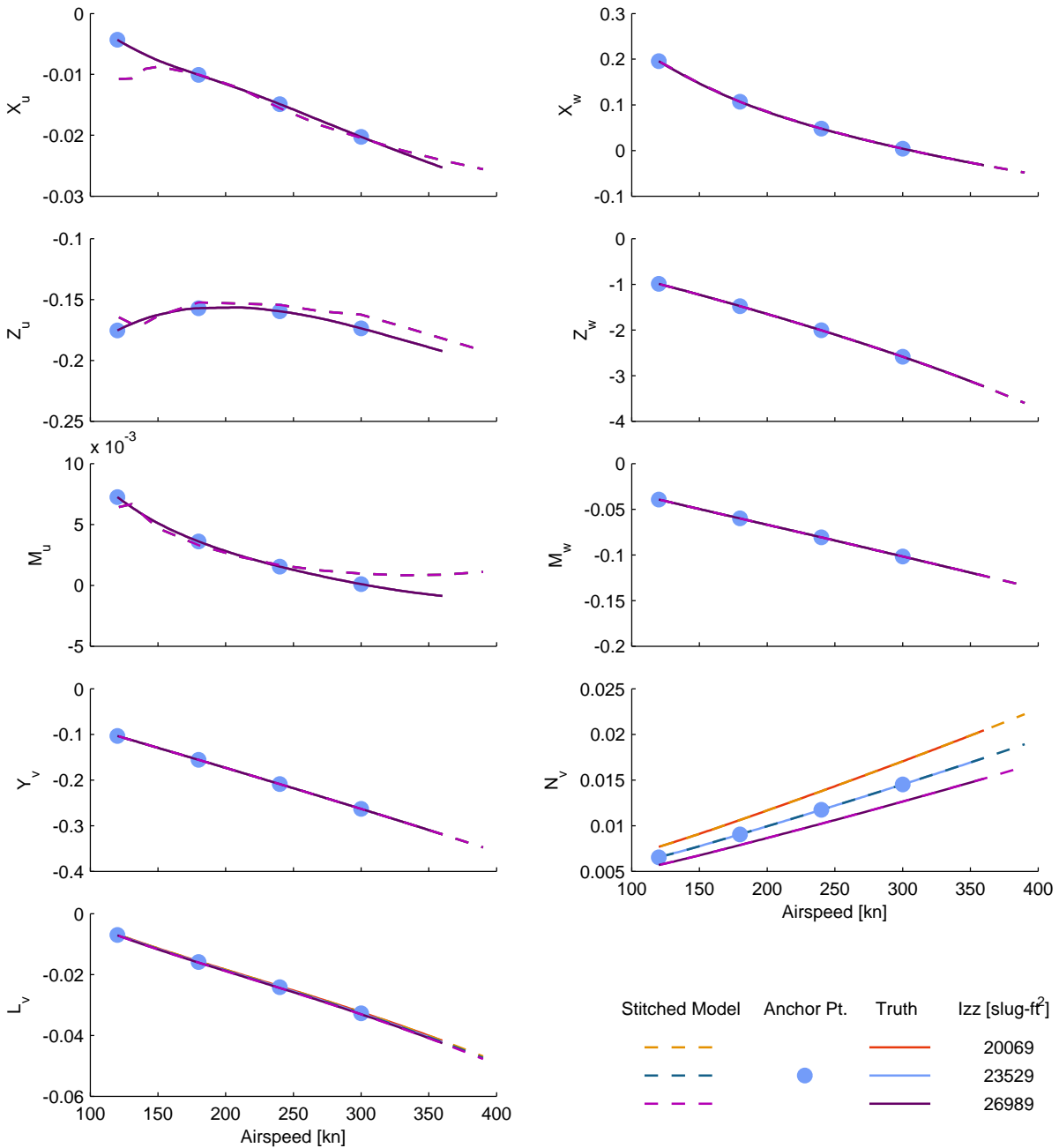
Figure B.9: Verification of off-nominal yaw inertia extrapolation, CJ1 stitched model, stability derivatives.
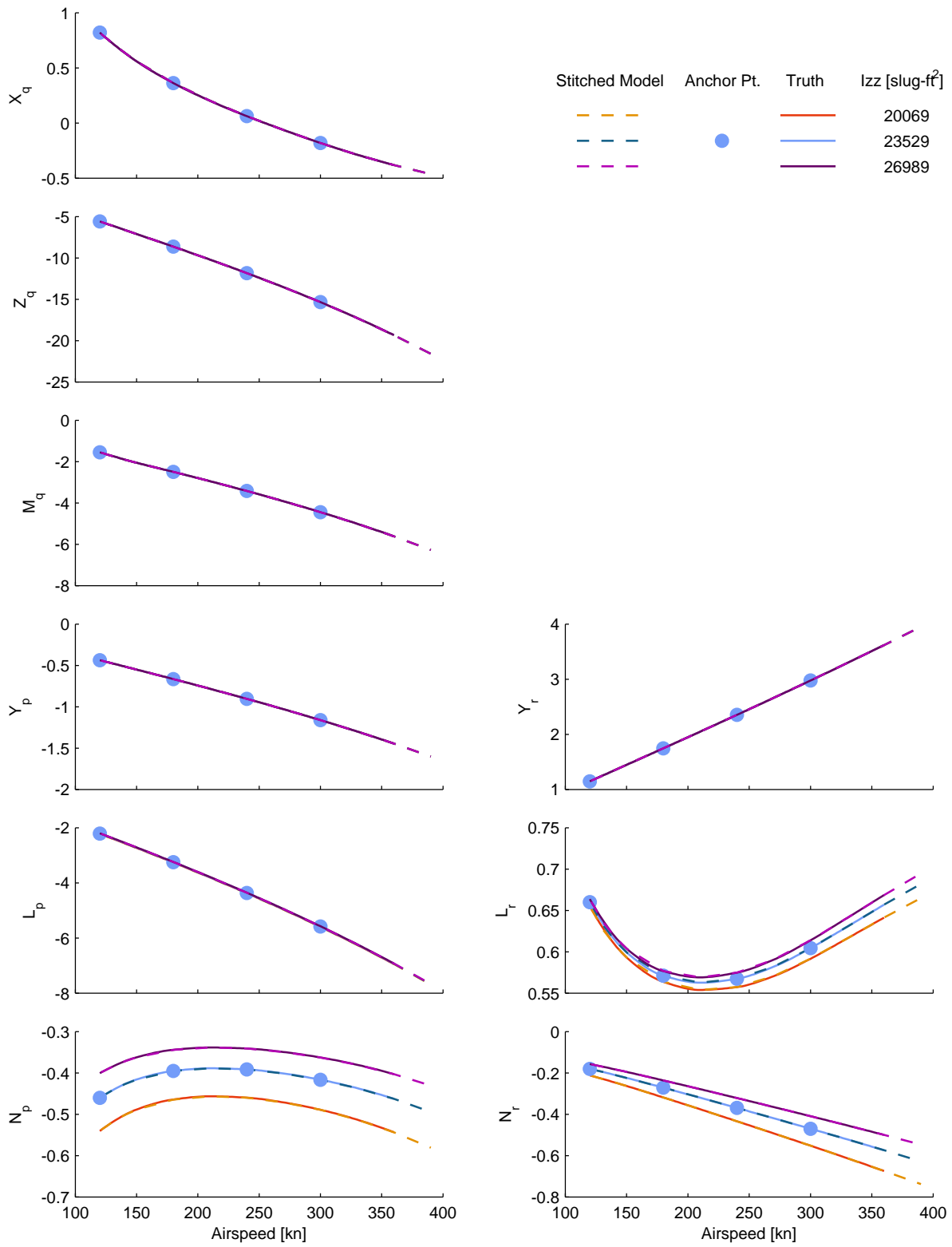
Figure B.9: Verification of off-nominal yaw inertia extrapolation, CJ1 stitched model, stability derivatives (cont.)
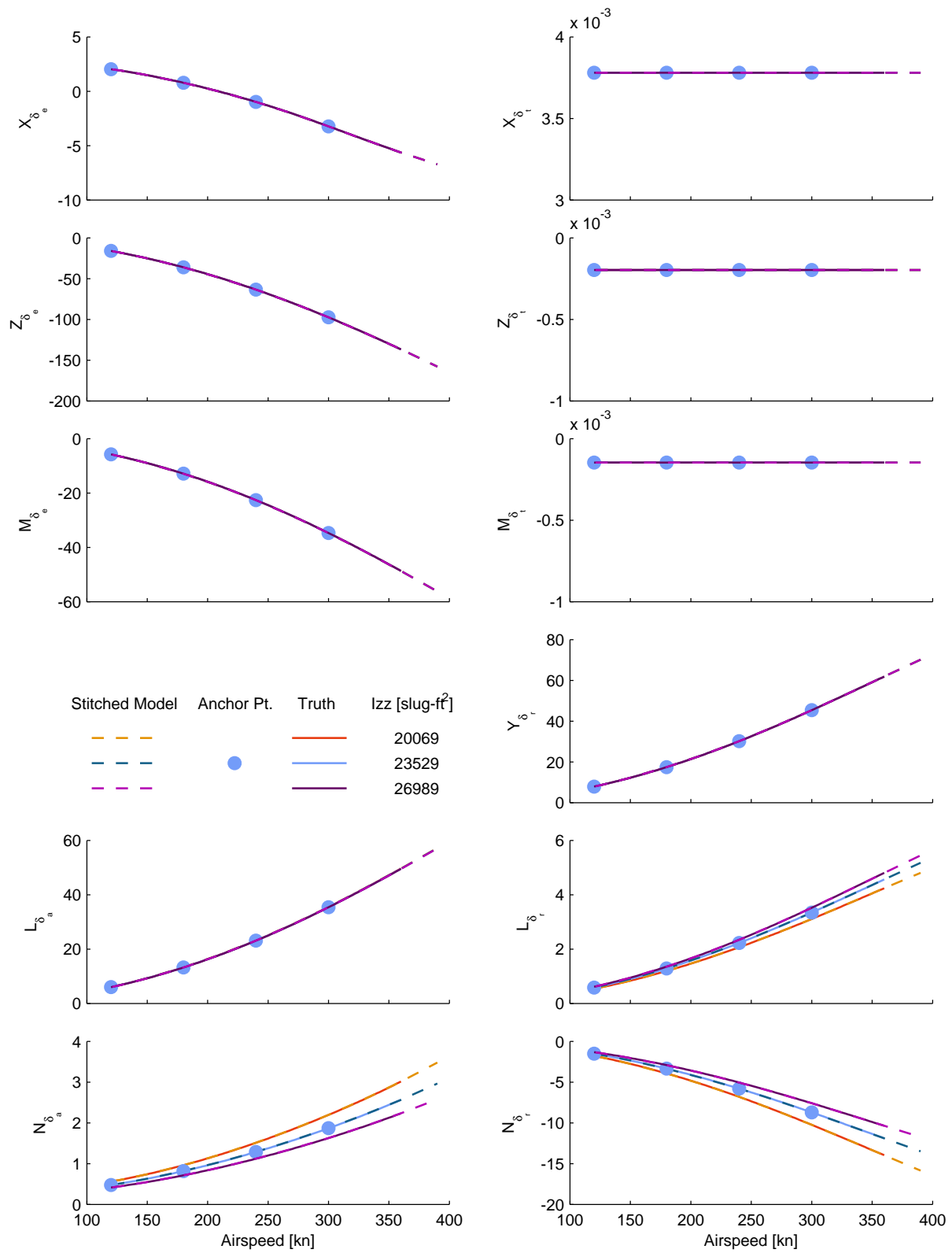
Figure B.10: Verification of off-nominal yaw inertia extrapolation, CJ1 stitched model, control derivatives.

B.3 Center of Gravity

The CJ1 stitched model was configured with off-nominal CG locations and verified against AAA point models. Section B.3.1 presents the results for off-nominal fuselage-station CG location (*x*-body axis, positive *aft*), and Section B.3.2 presents the results for off-nominal waterline CG location (*z*-body axis, positive *up*).

B.3.1 Station CG

Figures B.11–B.13 show the complete trim and stability and control derivative verification results for the CJ1 stitched model configured with fuselage-station CG offsets, as presented in Section 3.6.3.
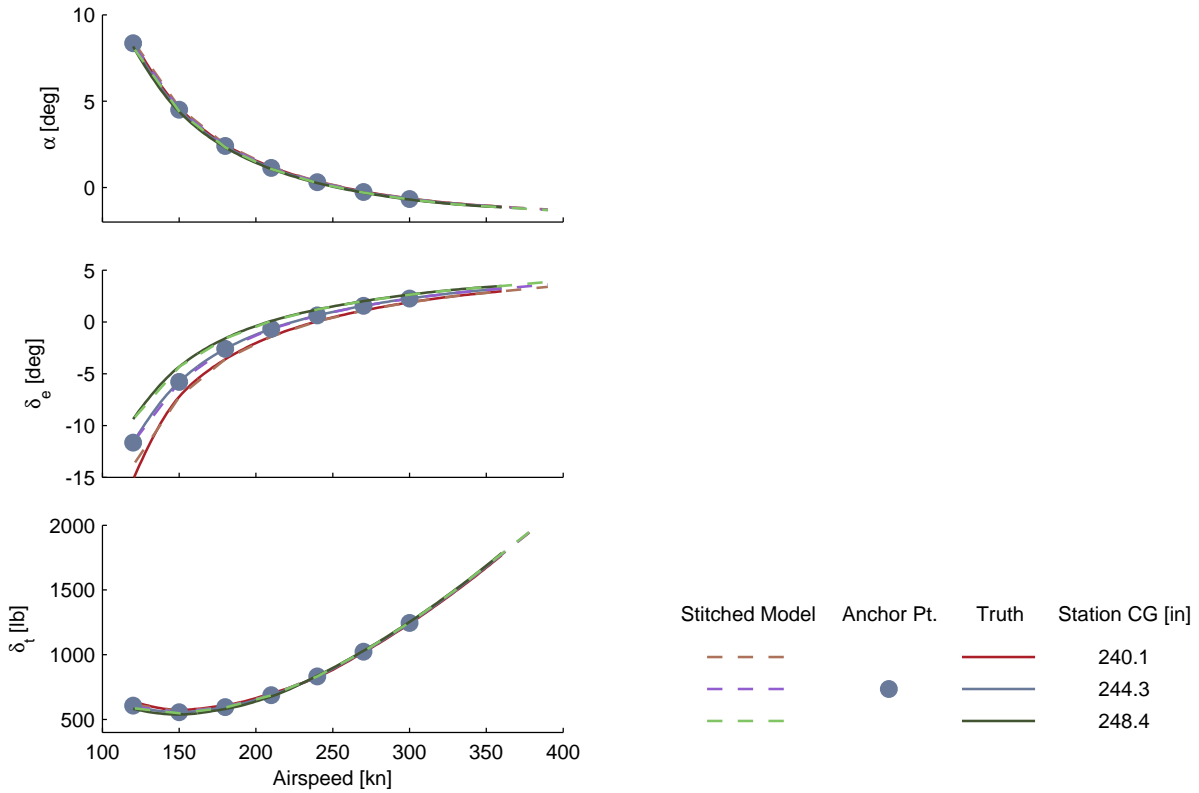
Figure B.11: Verification of off-nominal station CG extrapolation, CJ1 stitched model, trim.
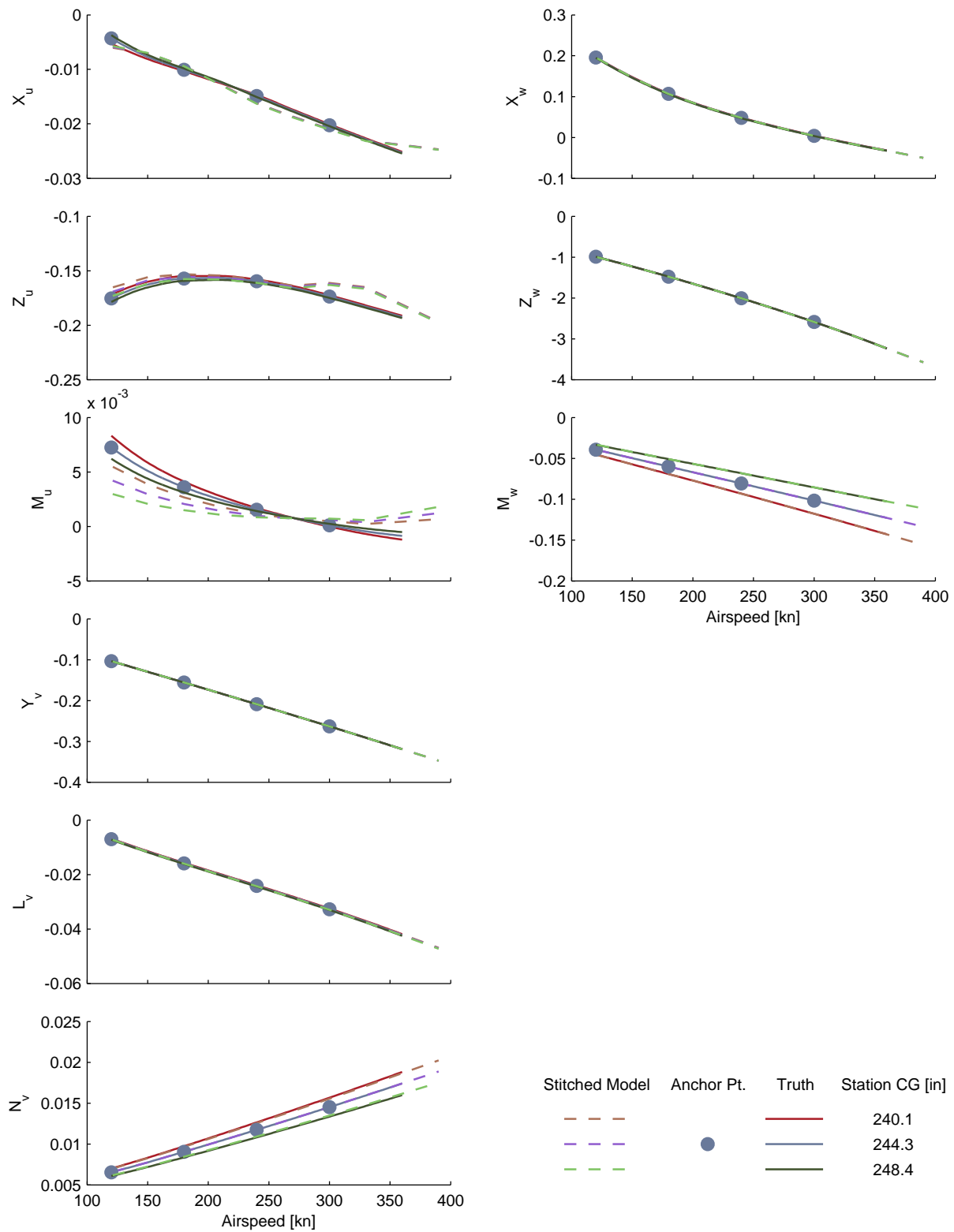
Figure B.12: Verification of off-nominal station CG extrapolation, CJ1 stitched model, stability derivatives.
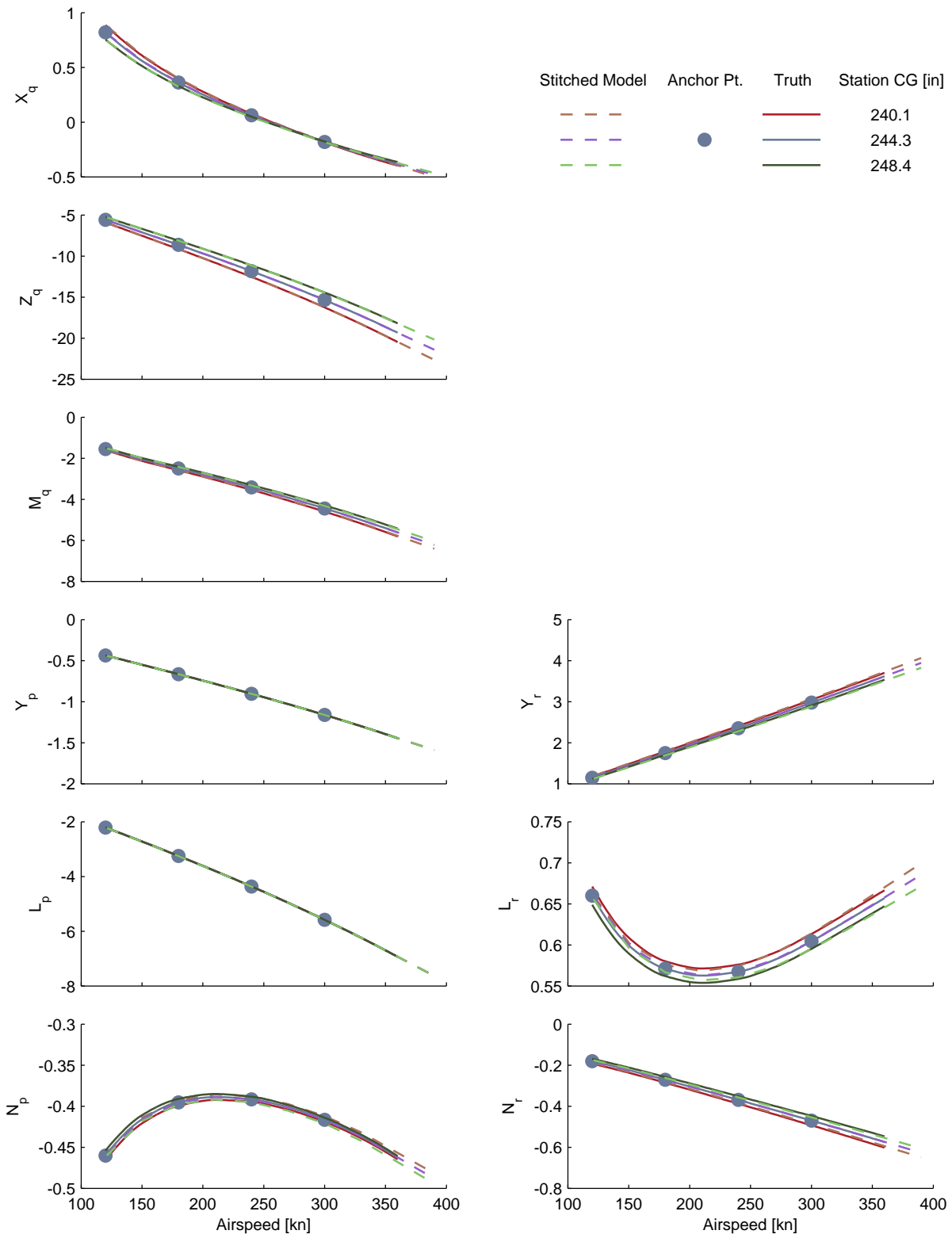
Figure B.12: Verification of off-nominal station CG extrapolation, CJ1 stitched model, stability derivatives (cont.)
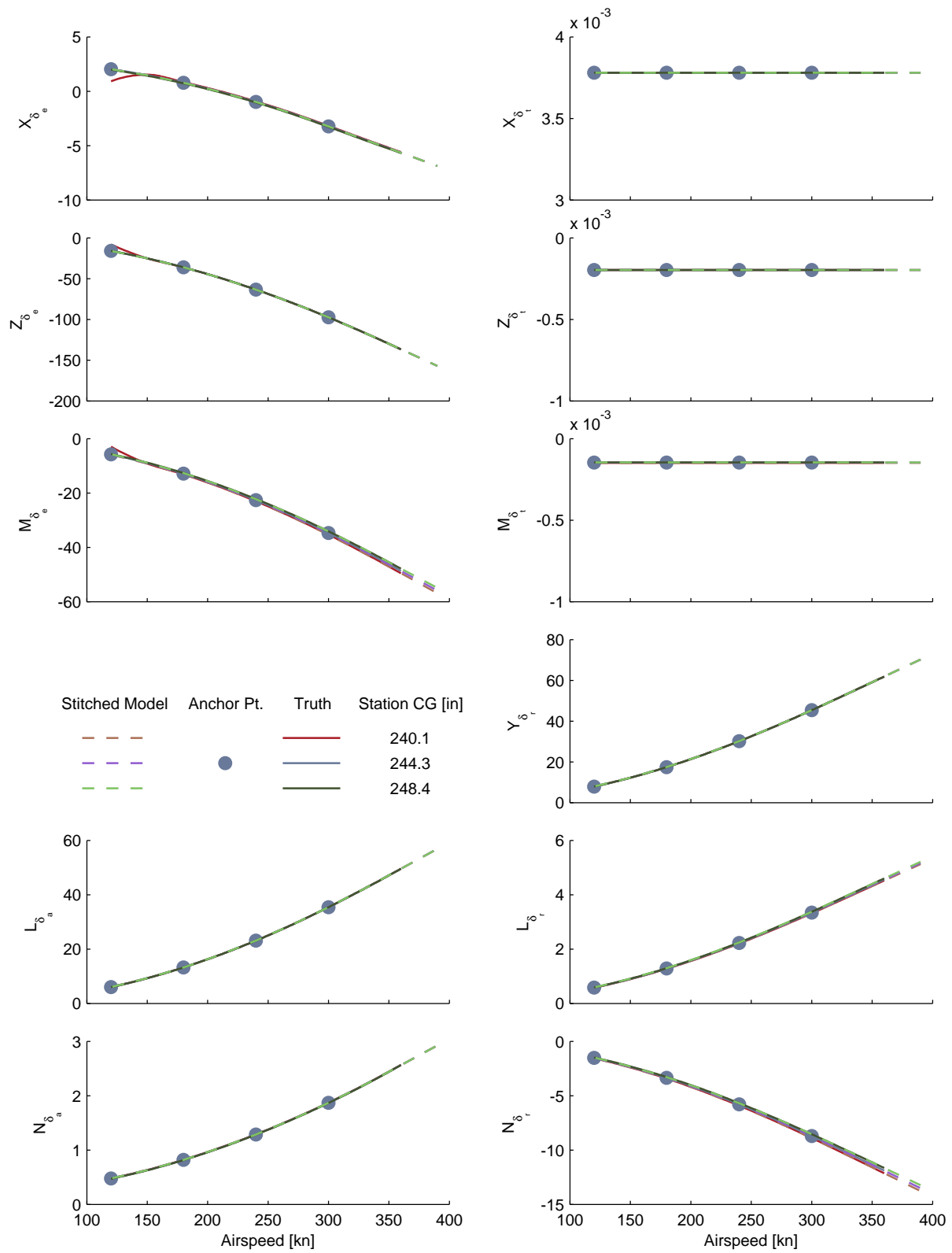
Figure B.13: Verification of off-nominal station CG extrapolation, CJ1 stitched model, control derivatives.

B.3.2 Waterline CG

Figures B.14–B.16 show the complete trim and stability and control derivative verification results for the CJ1 stitched model configured with waterline CG offsets, as presented in Section 3.6.3.
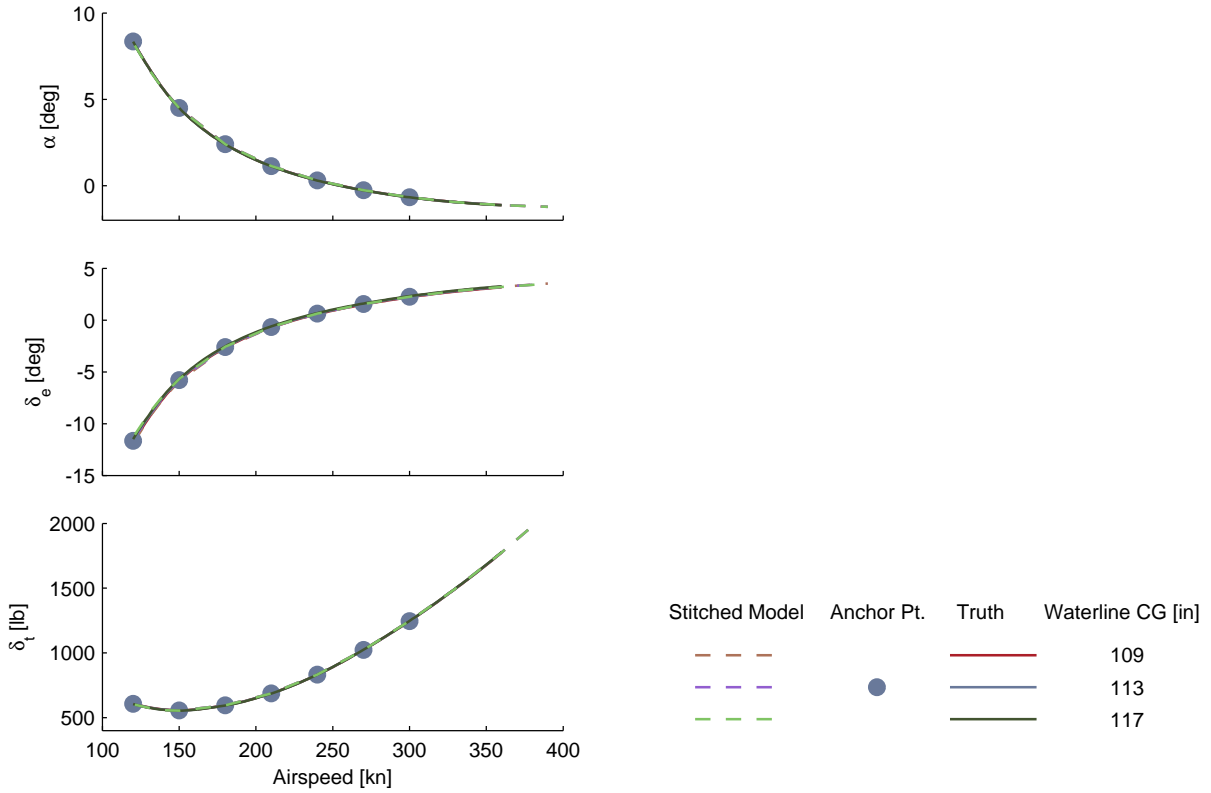
Figure B.14: Verification of off-nominal waterline CG extrapolation, CJ1 stitched model, trim.
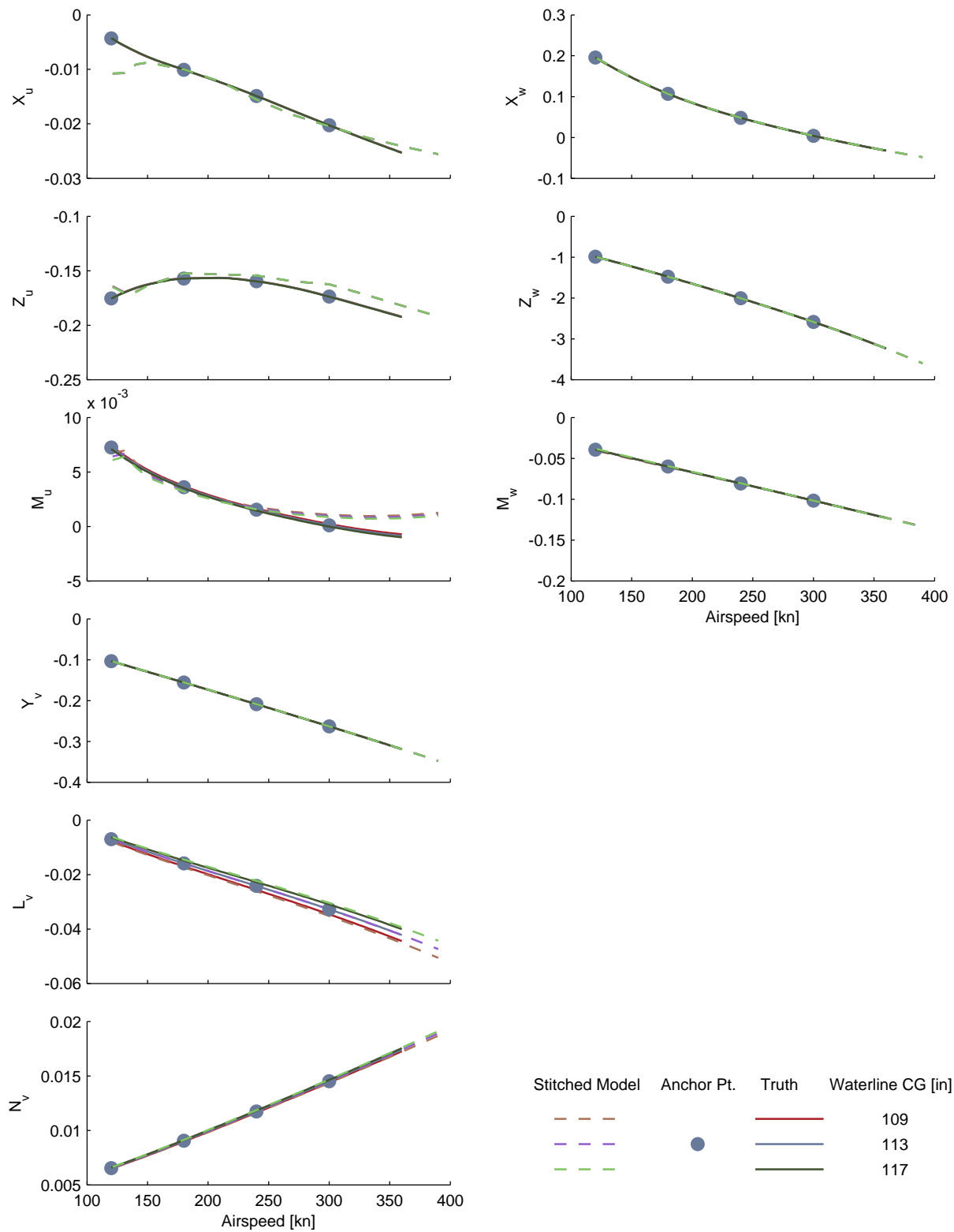
Figure B.15: Verification of off-nominal waterline CG extrapolation, CJ1 stitched model, stability derivatives.
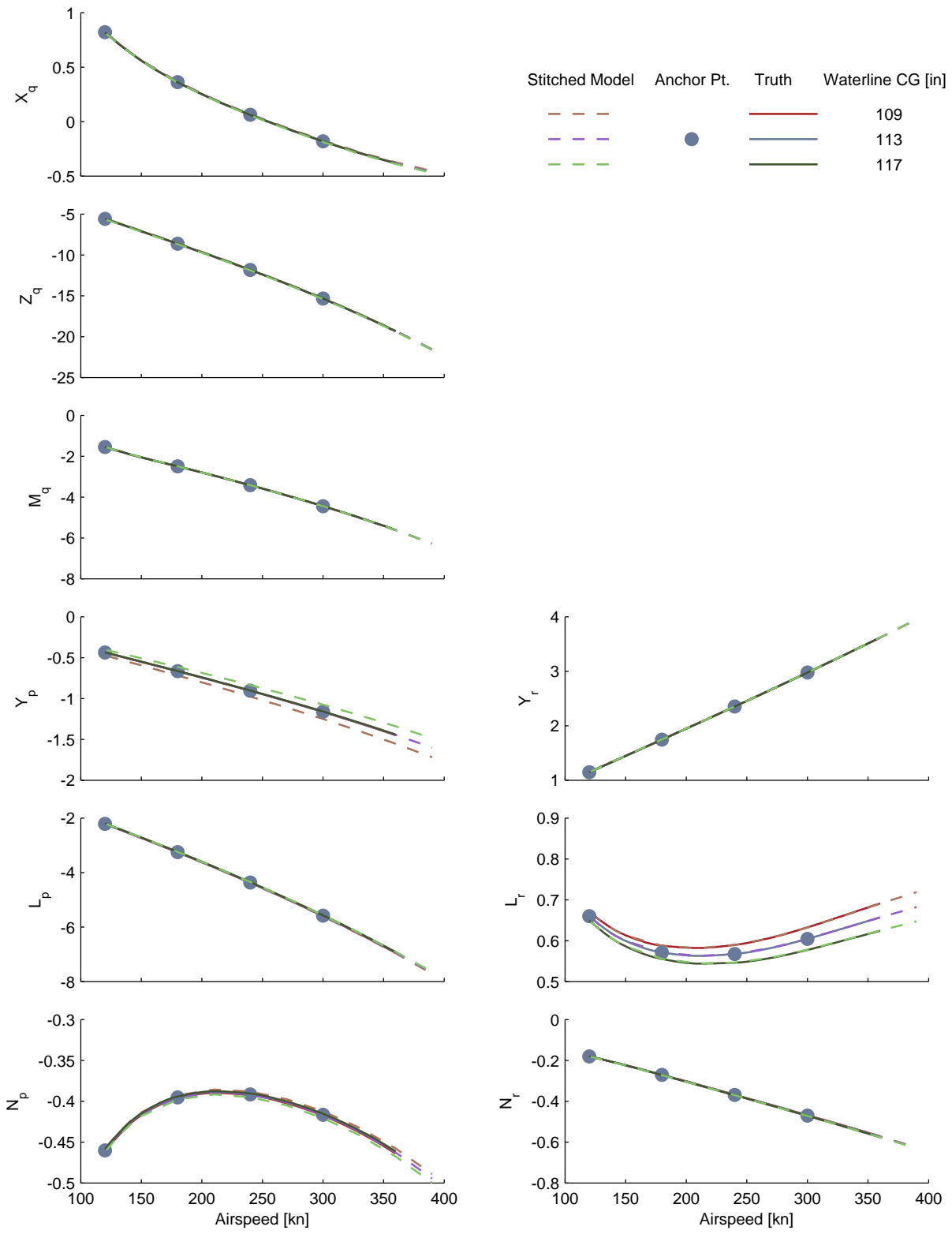
Figure B.15: Verification of off-nominal waterline CG extrapolation, CJ1 stitched model, stability derivatives (cont.)
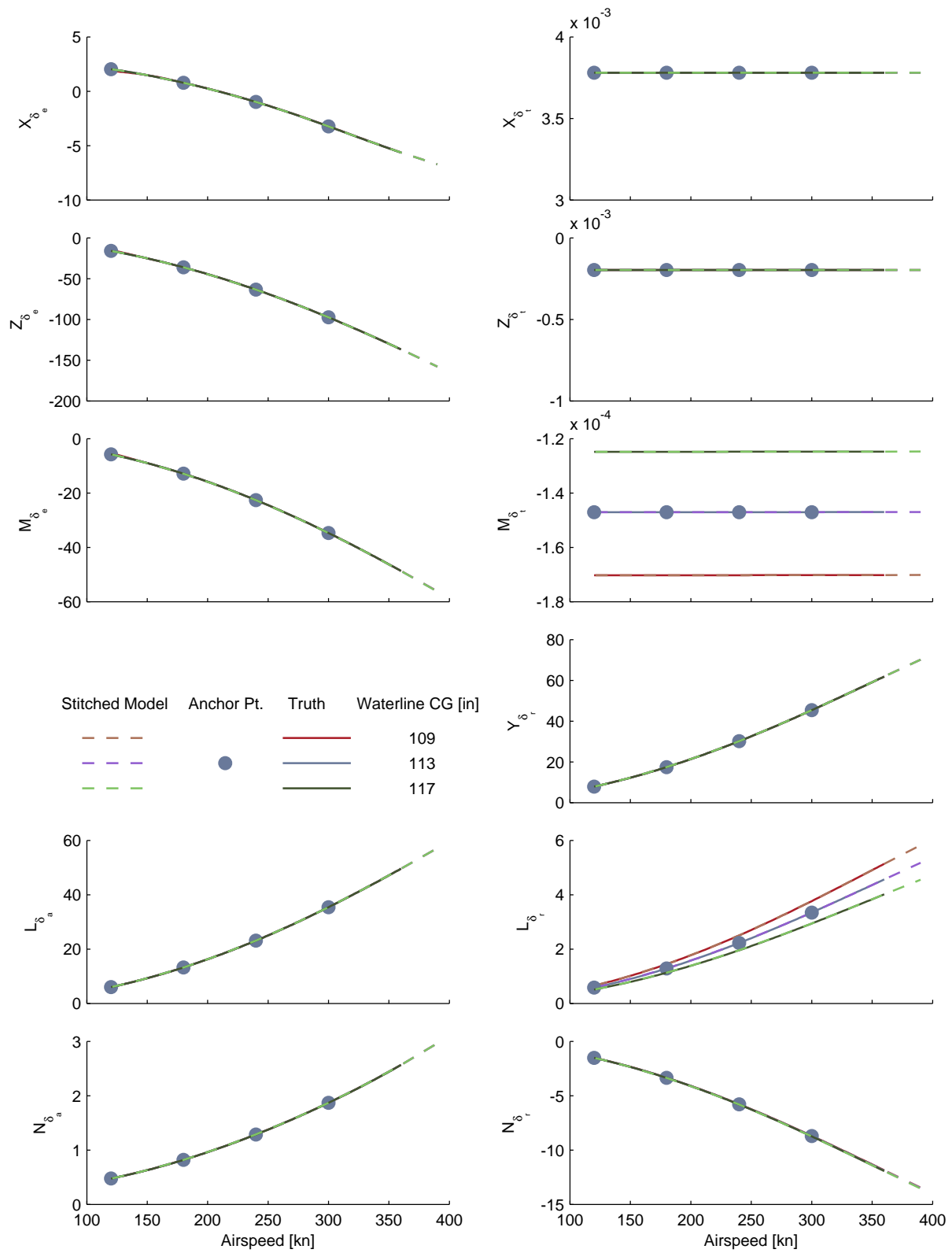
Figure B.16: Verification of off-nominal waterline CG extrapolation, CJ1 stitched model, control derivatives.

B.4 Altitude

The complete results of three strategies for altitude extrapolation within the CJ1 stitched model are presented in Sections B.4.1–B.4.3. The first strategy takes anchor point models and trim data from a single altitude (10,000 ft) and employs the density-ratio scaling extrapolation within the model stitching architecture to retrim and relinearize the data to cover the entire altitude envelope (sea level through 40,000 ft in 10,000-ft increments). The second strategy is identical to the first but utilizes anchor point data from 30,000 ft only. The third strategy combines results from the first two strategies, and demonstrates the advantage of employing models from two separate altitudes (10,000 ft and 30,000 ft). Extrapolation with altitude using anchor point data from two altitudes is the recommended strategy, and the results are discussed in Section 3.6.4.

B.4.1 Single-Altitude Data – 10,000 ft

Figures B.17–B.19 show trim and stability and control derivative comparison results for the CJ1 off-nominal altitude verification. The following results were generated by configuring the stitched model with the 10,000-ft altitude AAA models and trim data only. The stitched model was then retrimmed/relinearized at alternate altitudes over the full range of airspeed. Very close agreement between the stitched model and AAA is seen in the sea-level, 10,000-, and 20,000-ft altitude results, with degraded, but generally acceptable, agreement (largest discrepancies in trim thrust) for the 30,000- and 40,000-ft altitude results.
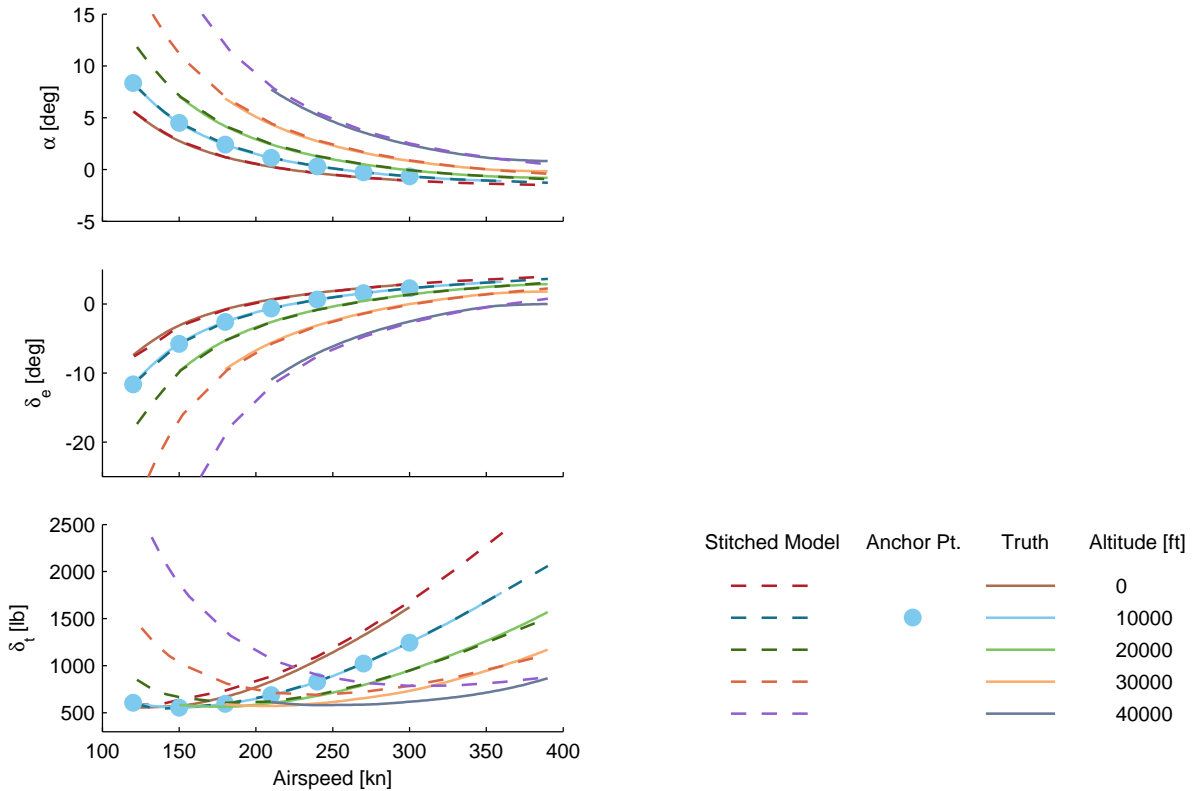
Figure B.17: Verification of single-altitude extrapolation, 10,000 ft, CJ1 stitched model, trim.
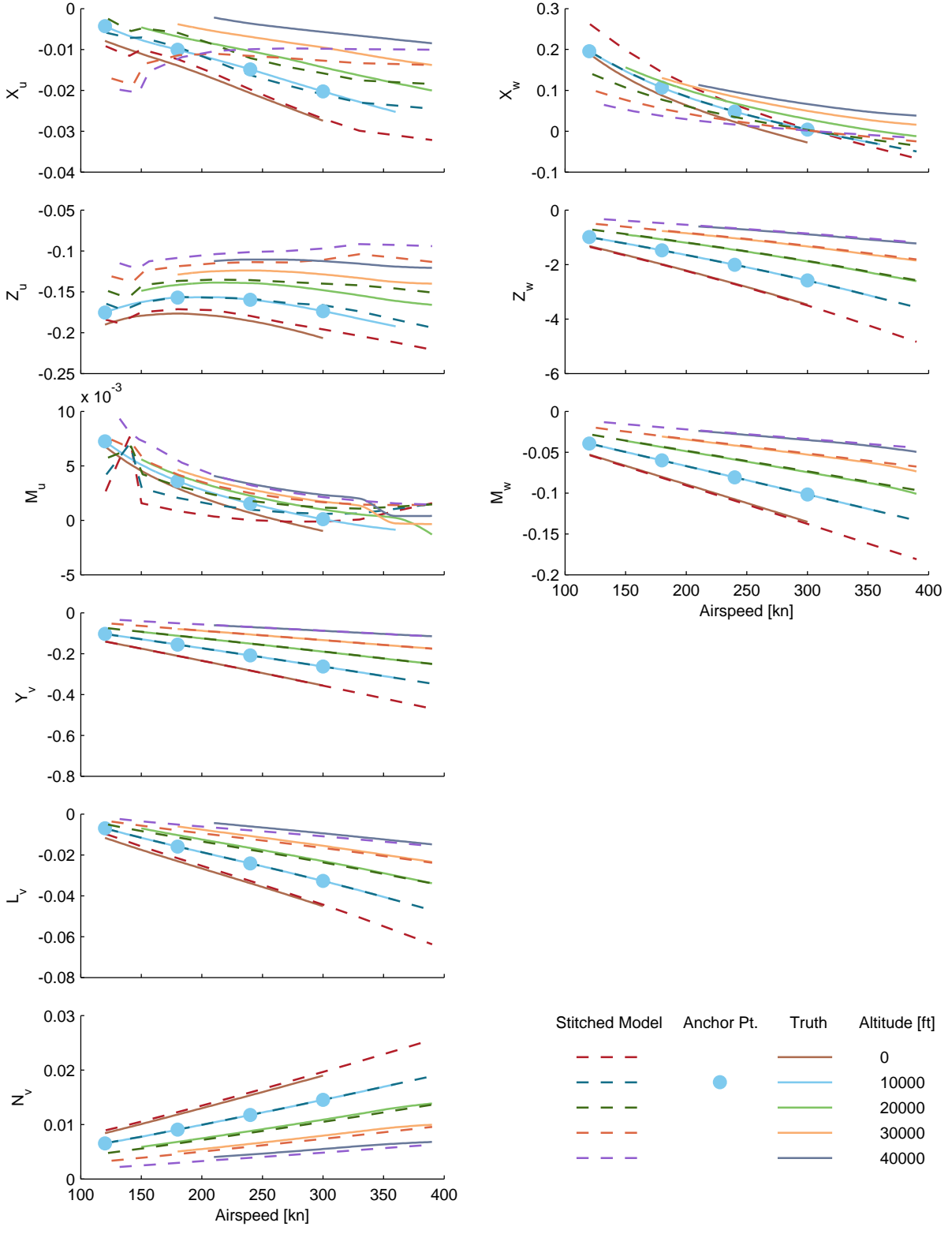
Figure B.18: Verification of single-altitude extrapolation, 10,000 ft, CJ1 stitched model, stability derivatives.
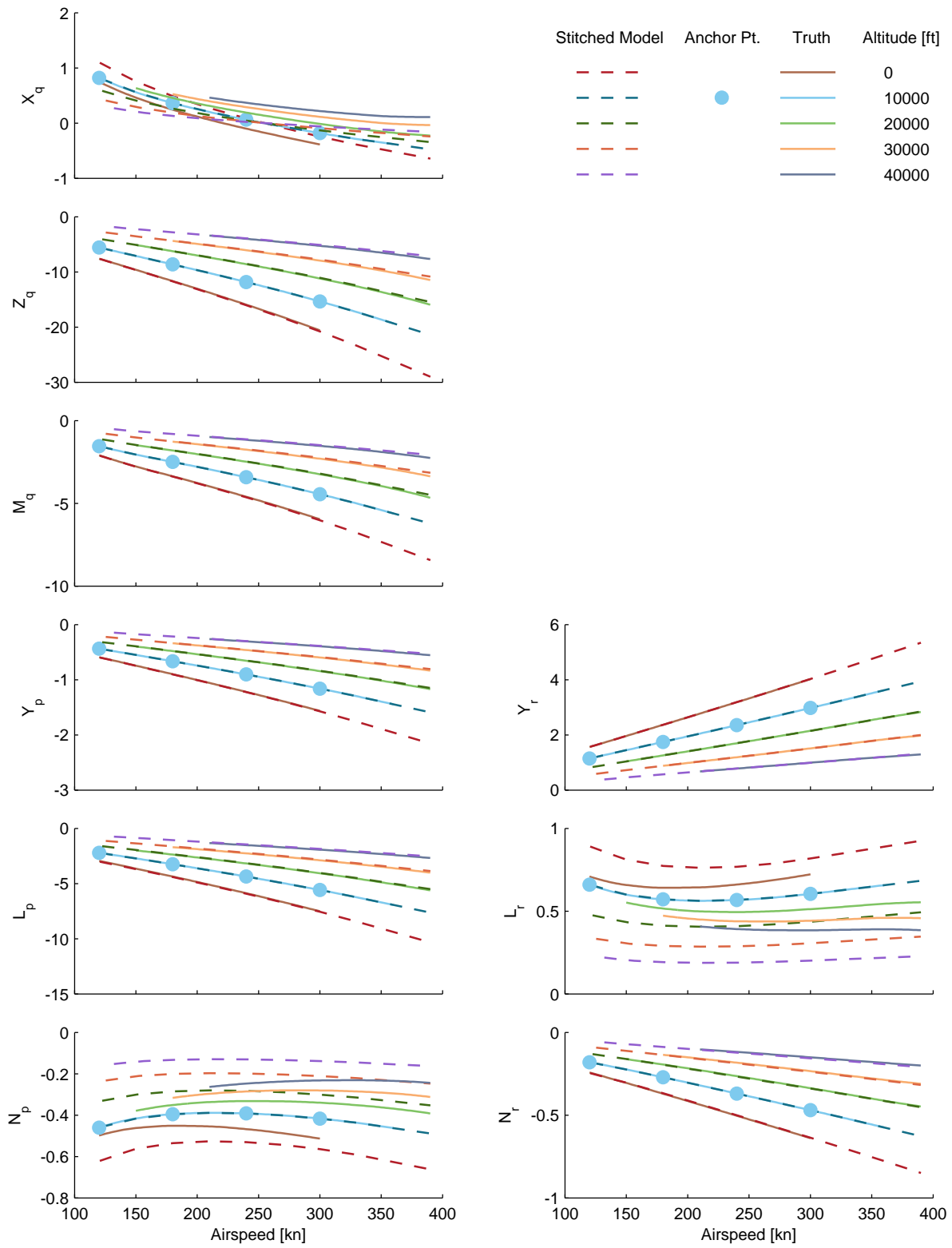
Figure B.18: Verification of single-altitude extrapolation, 10,000 ft, CJ1 stitched model, stability derivatives (cont.)
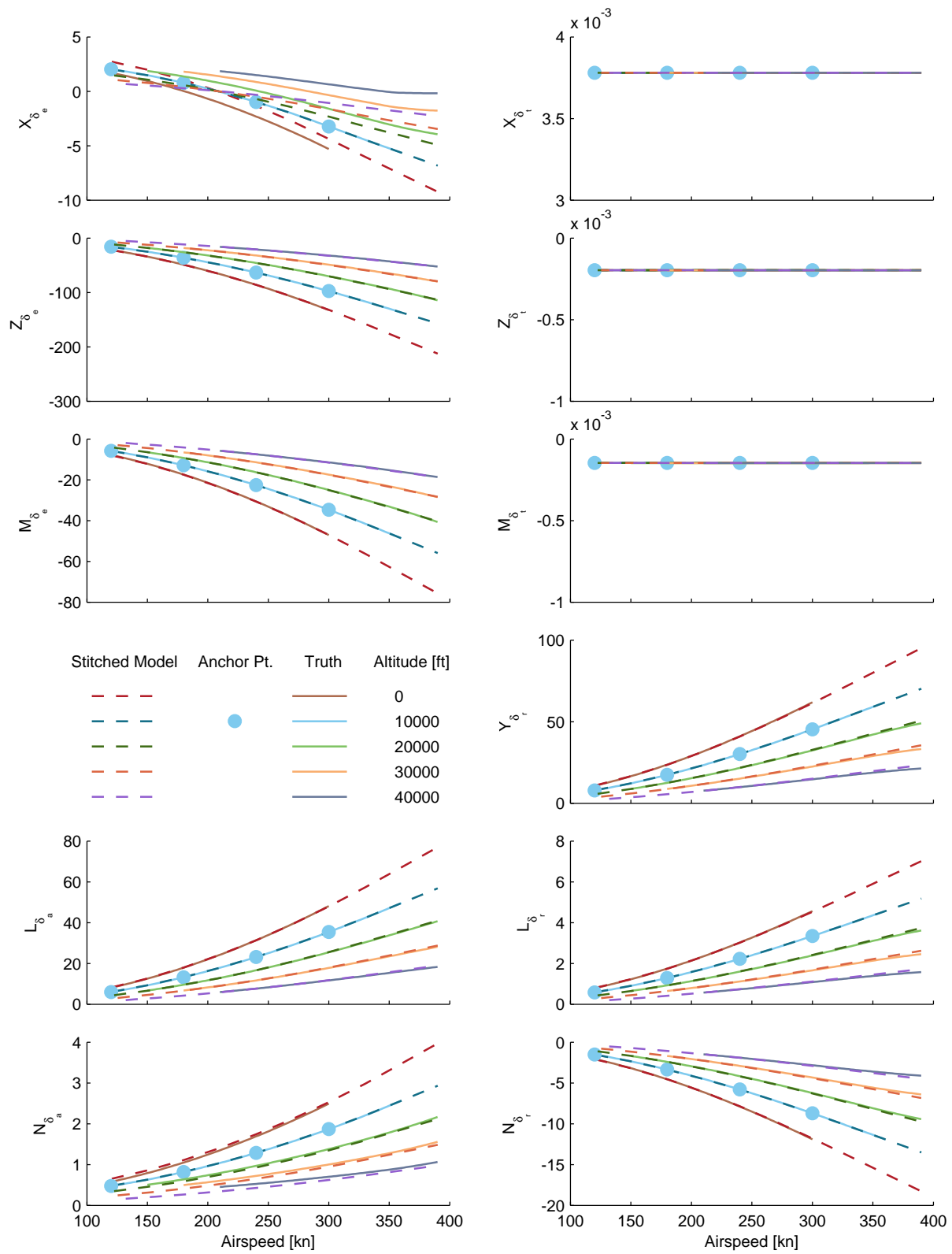
Figure B.19: Verification of single-altitude extrapolation, 10,000 ft, CJ1 stitched model, control derivatives.

B.4.2 Single-Altitude Data – 30,000 ft

Figures B.20–B.22 show trim and stability and control derivative comparison results for the CJ1 off-nominal altitude verification. The following results were generated by configuring the stitched model with the 30,000-ft altitude AAA models and trim data only. The stitched model was then retrimmed/relinearized at alternate altitudes over the full range of airspeed. Close agreement between the stitched model and AAA is seen in the 30,000- and 40,000-ft altitude results only, with significant discrepancies (largest discrepancies in trim thrust) for the sea-level through 20,000-ft altitude results.
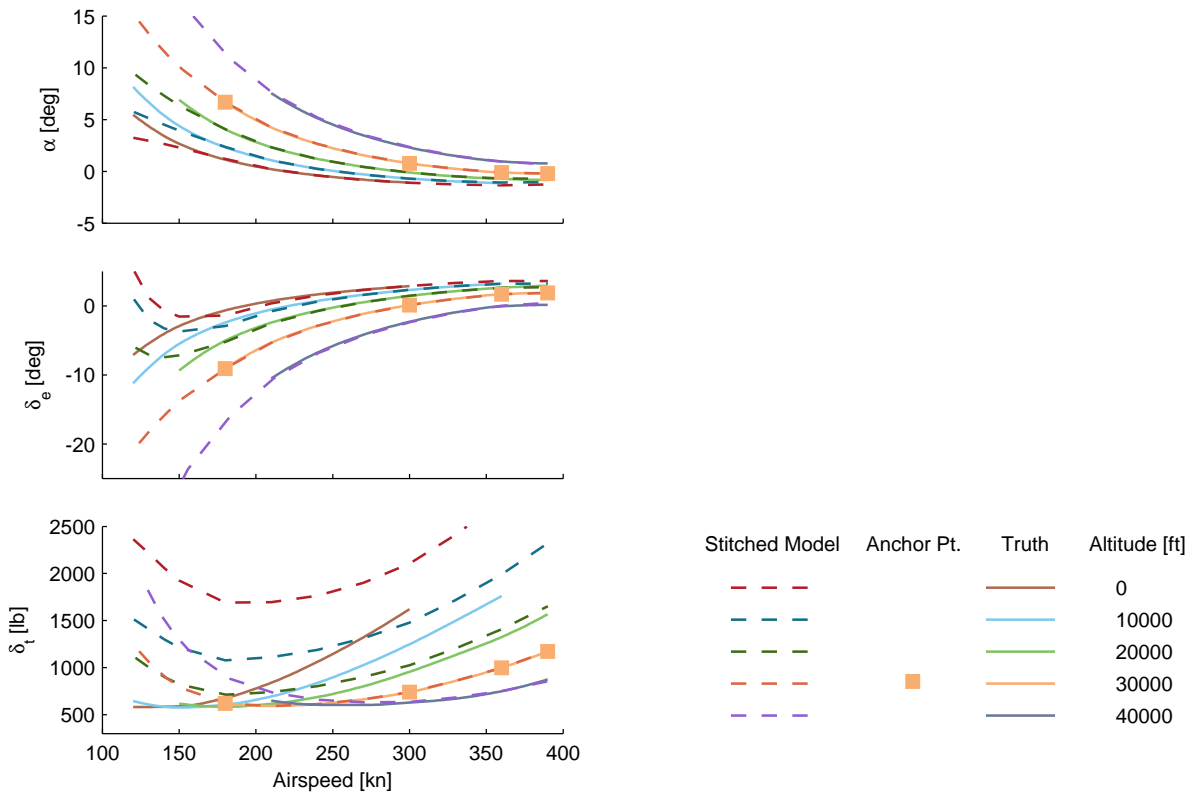
Figure B.20: Verification of single-altitude extrapolation, 30,000 ft, CJ1 stitched model, trim.
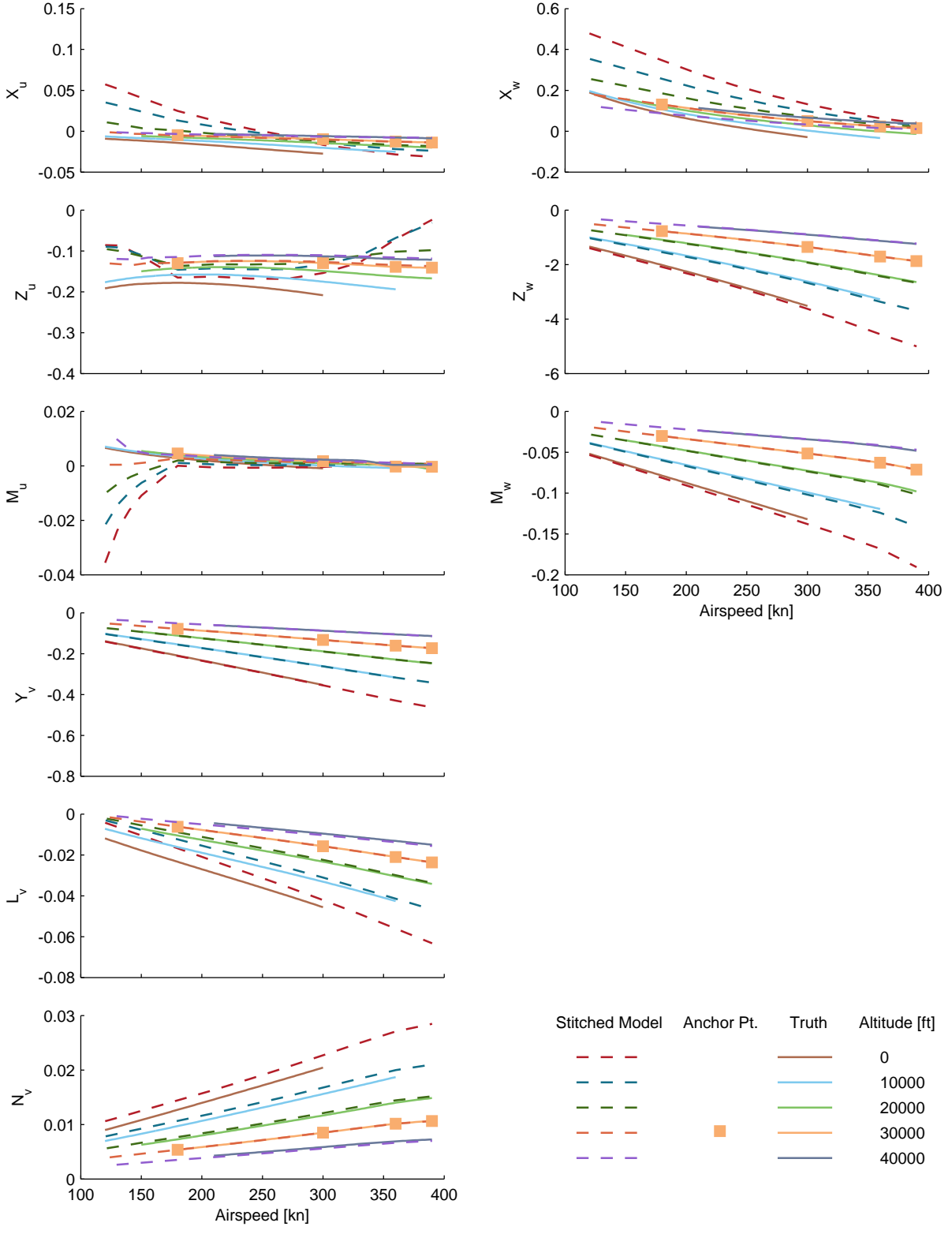
Figure B.21: Verification of single-altitude extrapolation, 30,000 ft, CJ1 stitched model, stability derivatives.
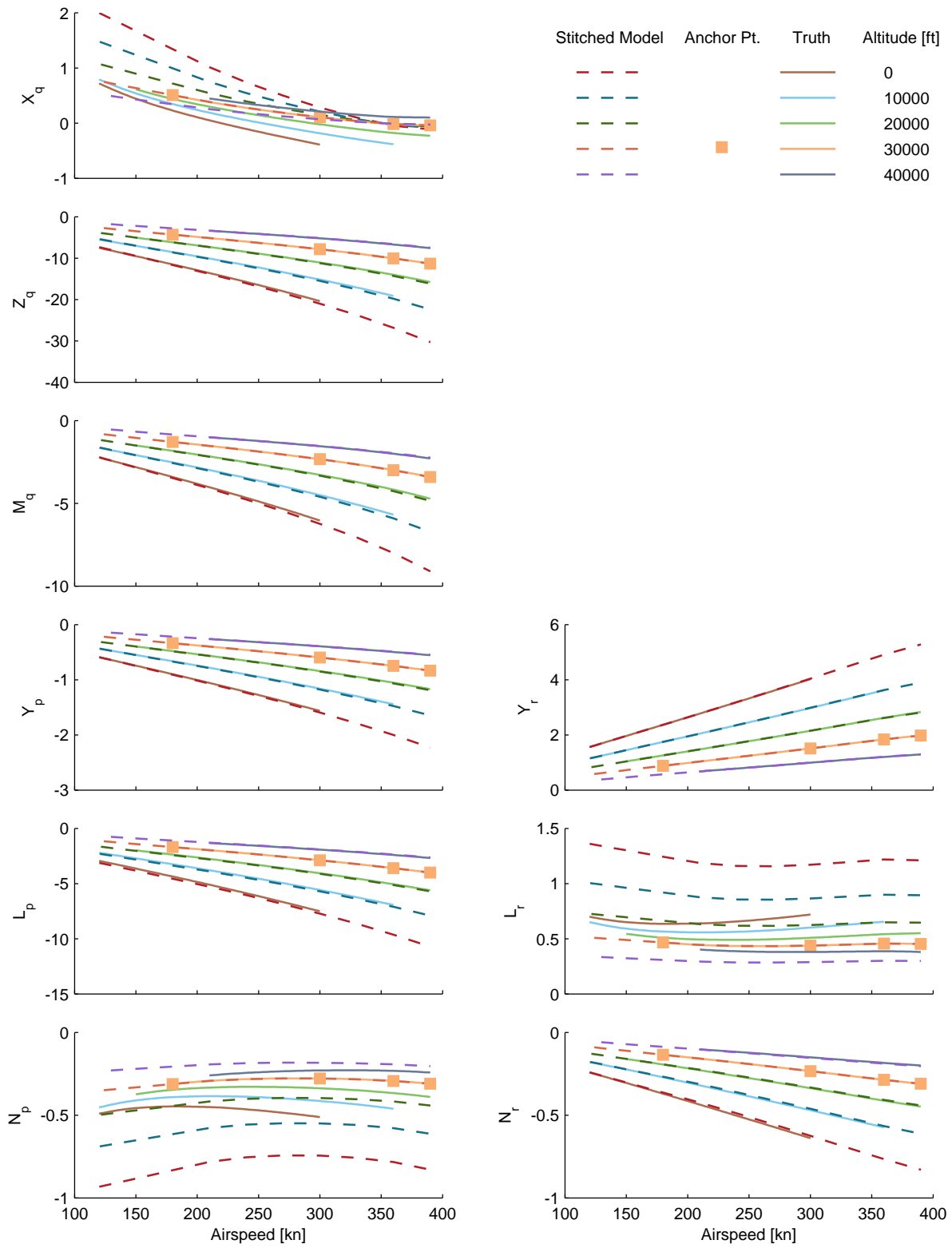
Figure B.21: Verification of single-altitude extrapolation, 30,000 ft, CJ1 stitched model, stability derivatives (cont.)
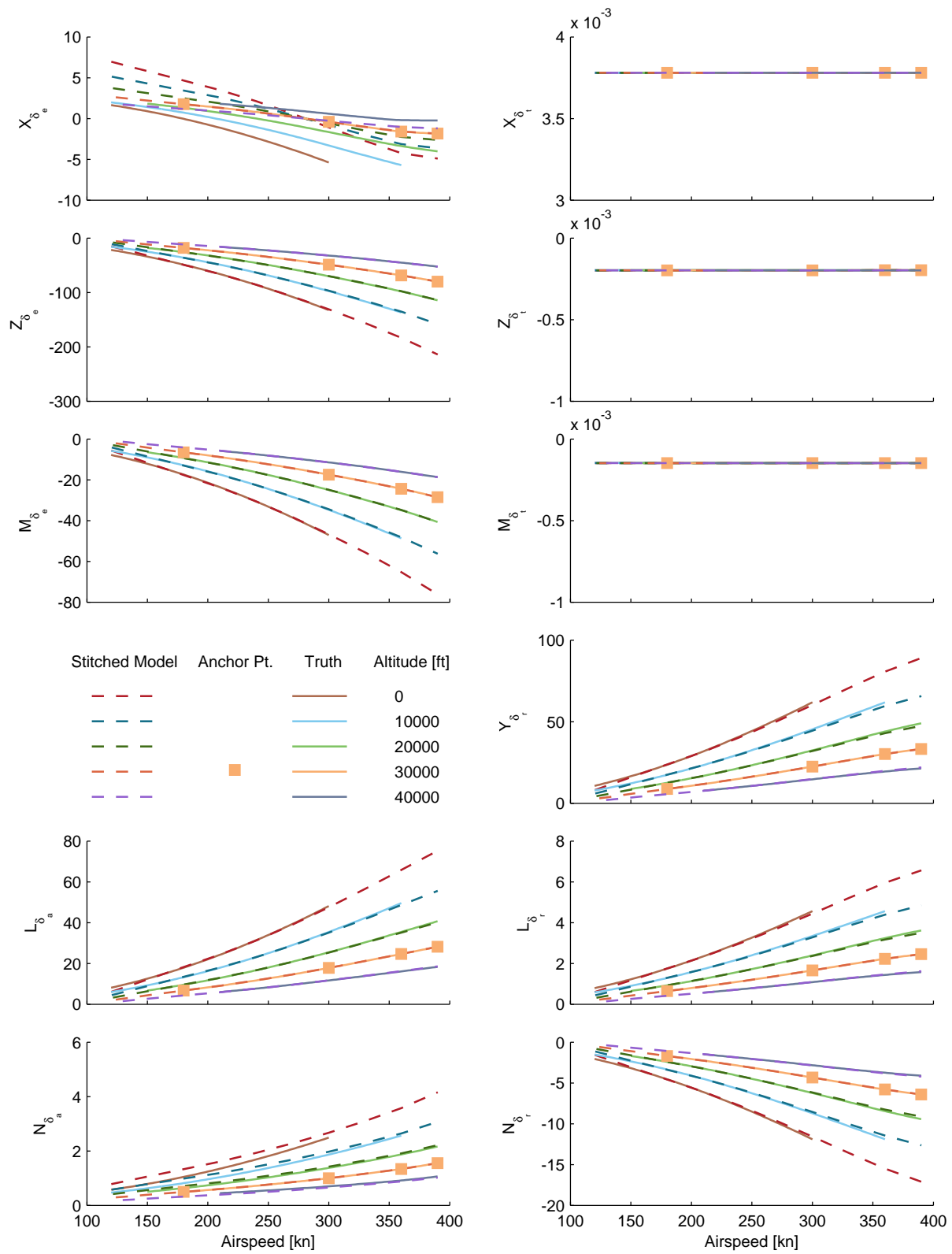
Figure B.22: Verification of single-altitude extrapolation, 30,000 ft, CJ1 stitched model, control derivatives.

B.4.3   Data from Two Altitudes – 10,000 ft and 30,000 ft

Figures B.23–B.25 show trim and stability and control derivative comparison results for the CJ1 off-nominal altitude verification. The following figures show the trim and linearization results for the stitched model configured with both the 10,000- and 30,000-ft altitude AAA models and trim data, as shown in the previous two sections. Specifically, the 10,000-ft models and trim data were used to retrim and relinearize the stitched model at sea level, 10,000, and 20,000 ft, and the 30,000-ft models and trim data were used to retrim and relinearize the stitched model at 30,000 and 40,000 ft. Generally excellent agreement is attained over the entire flight envelope. Further discussion of these results is presented in Section 3.6.4.
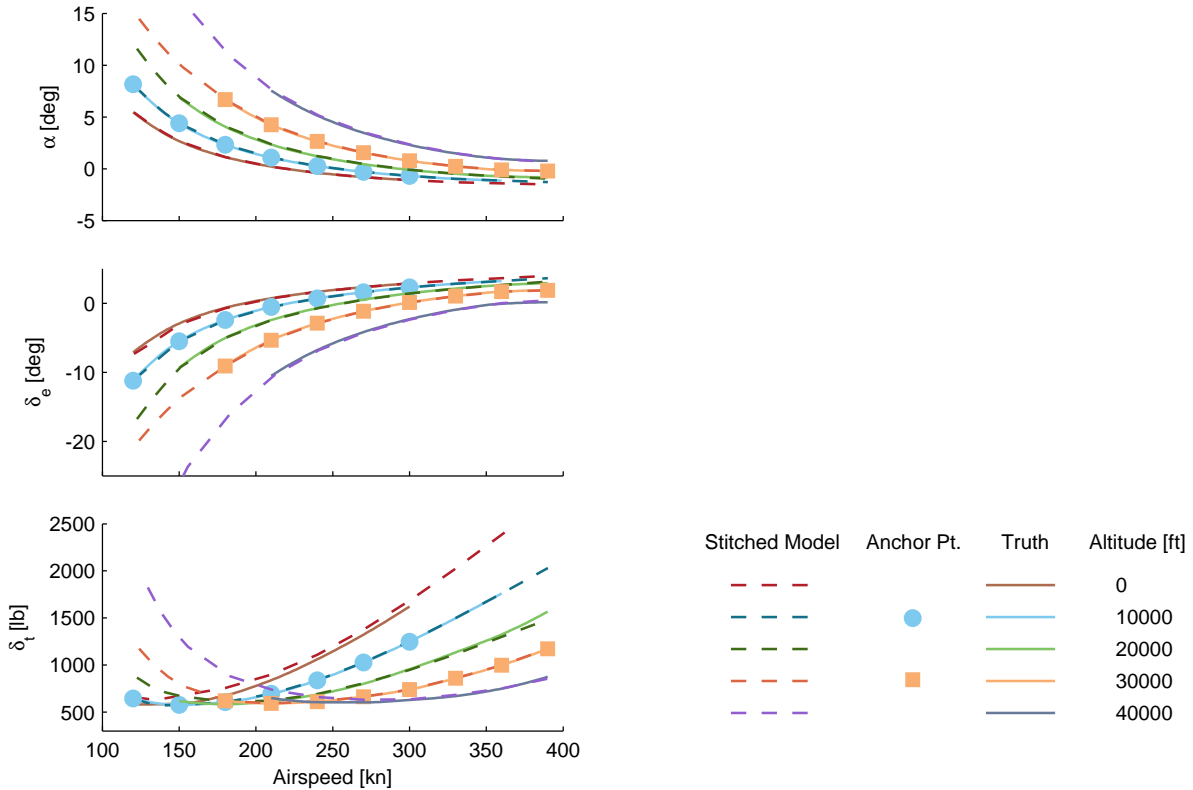
Figure B.23: Verification of altitude extrapolation, two altitudes, CJ1 stitched model, trim.
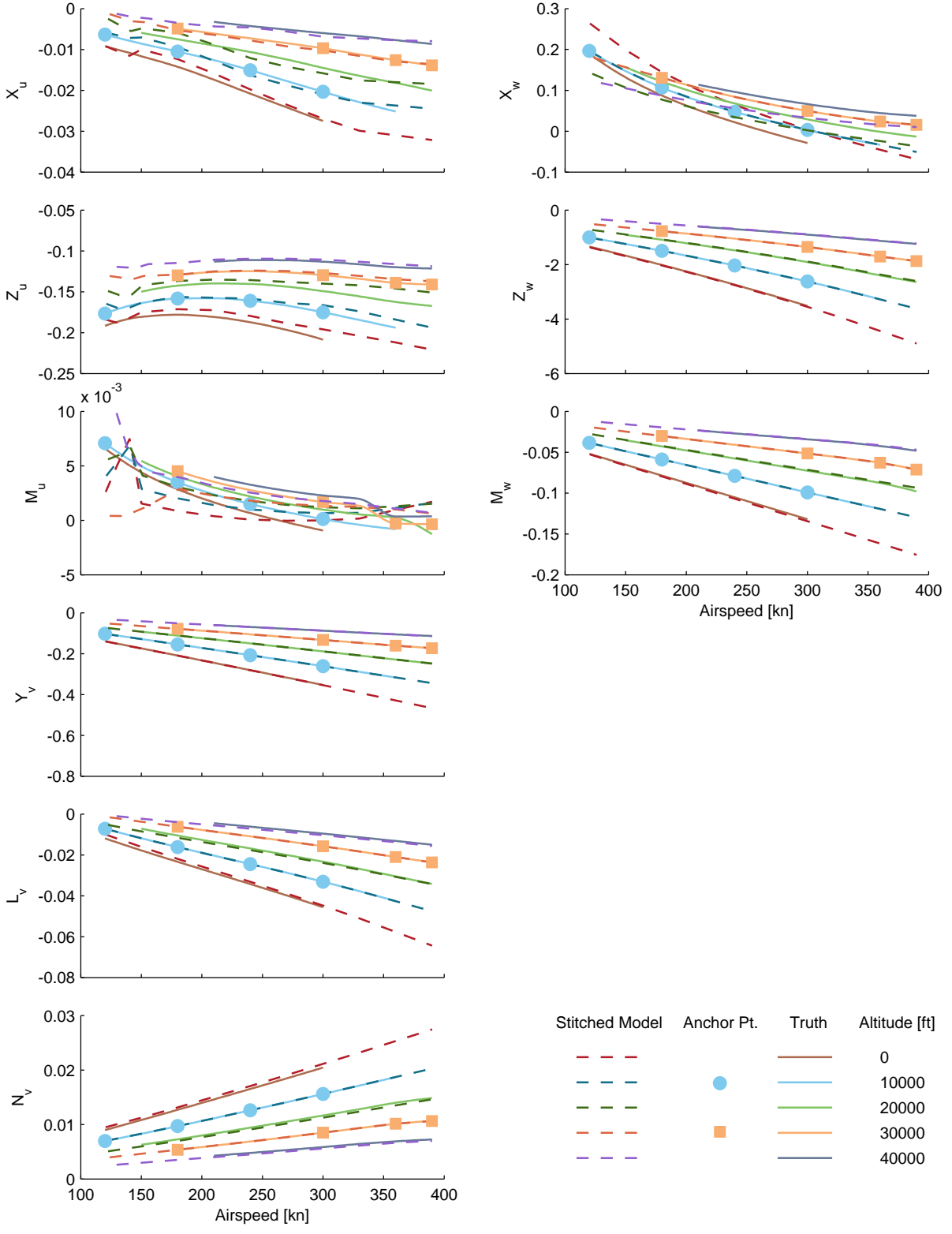
Figure B.24: Verification of altitude extrapolation, two altitudes, CJ1 stitched model, stability derivatives.
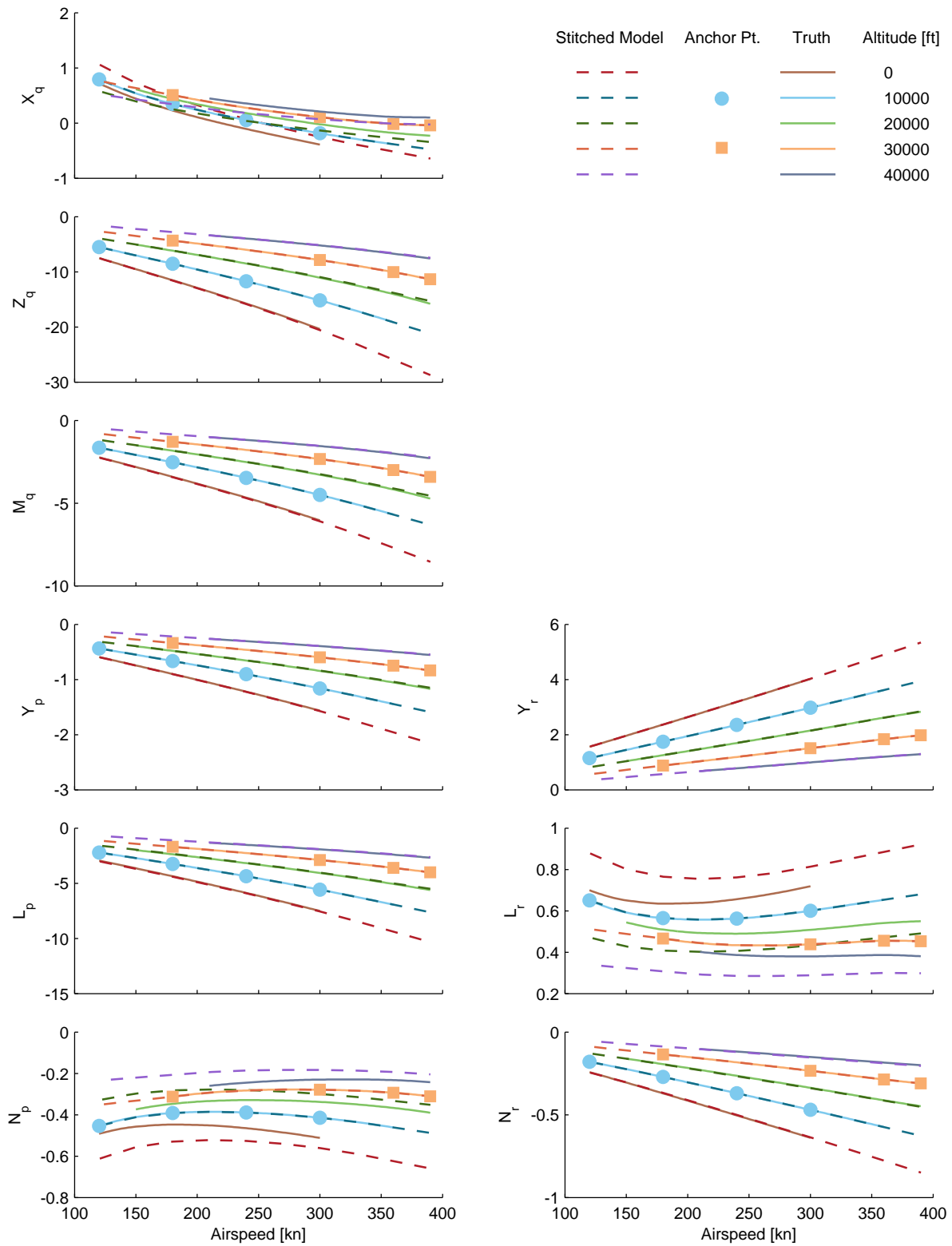
Figure B.24: Verification of altitude extrapolation, two altitudes, CJ1 stitched model, stability derivatives (cont.)
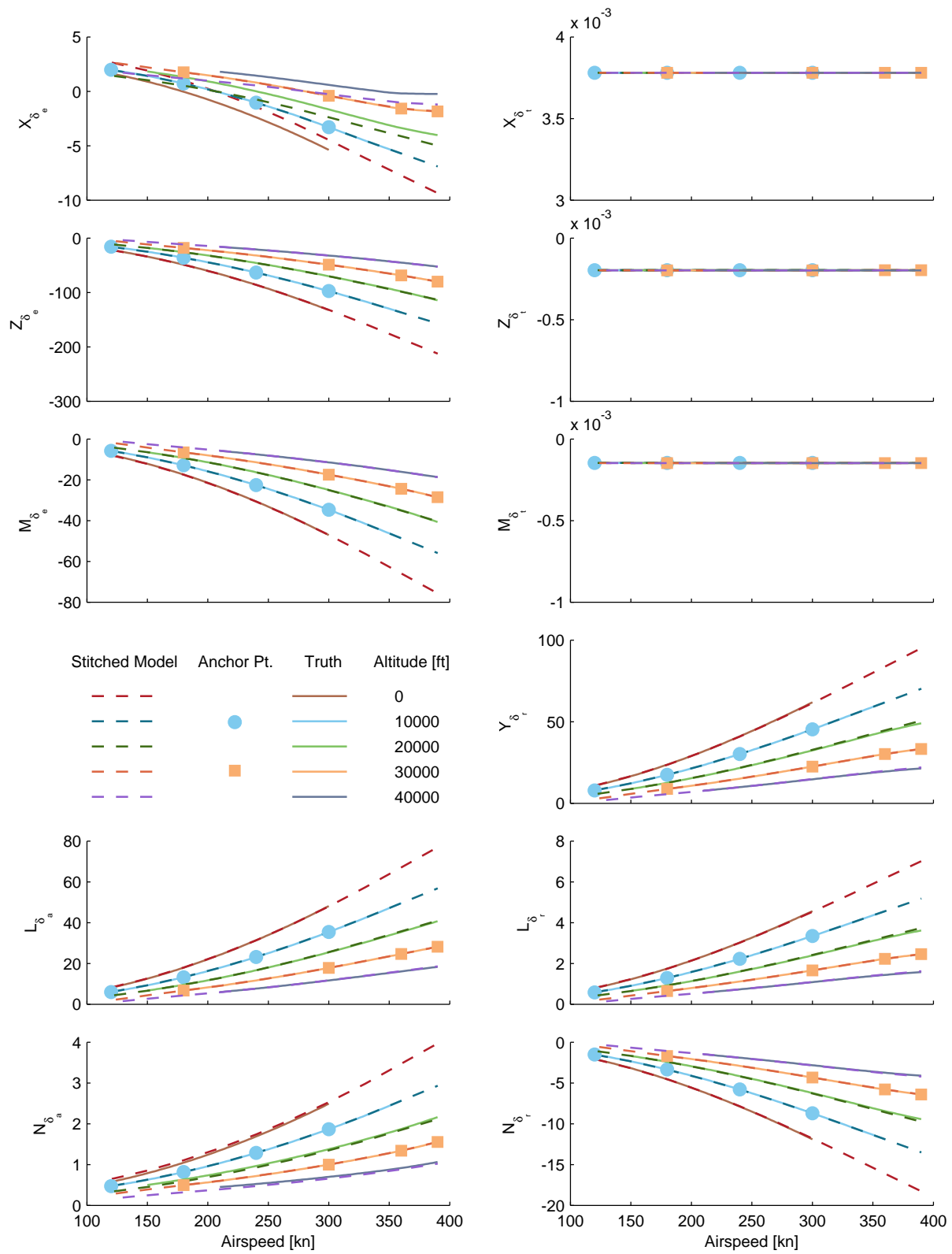
Figure B.25: Verification of altitude extrapolation, two altitudes, CJ1 stitched model, control derivatives.

B.5   Flap Setting

Figures B.26–B.28 show the complete trim and stability and control derivative comparison results for the CJ1 stitched model flap setting verification presented in Section 3.8. Herein, flap deflection effects were modeled as changes in trim only; the stability and control derivatives remain those of the nominal flaps-up configuration.
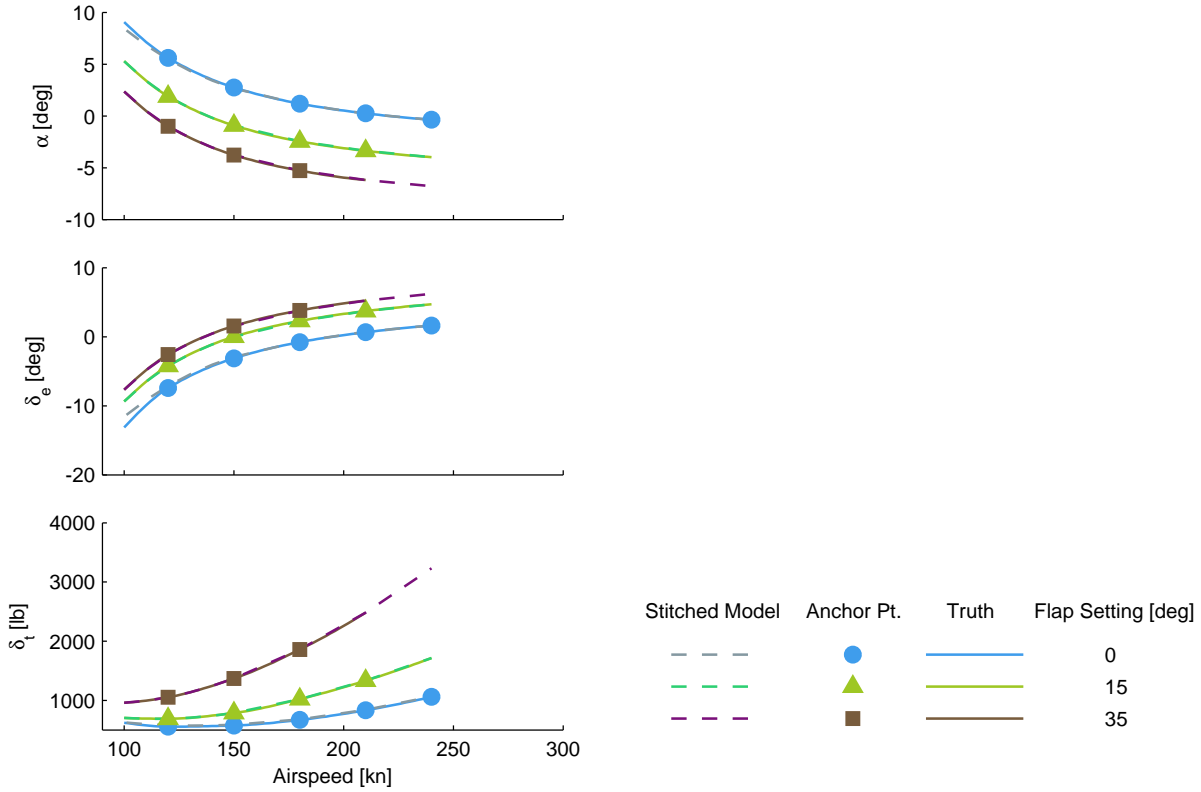
Figure B.26: Alternate configuration verification, flap setting, CJ1 stitched model, trim.
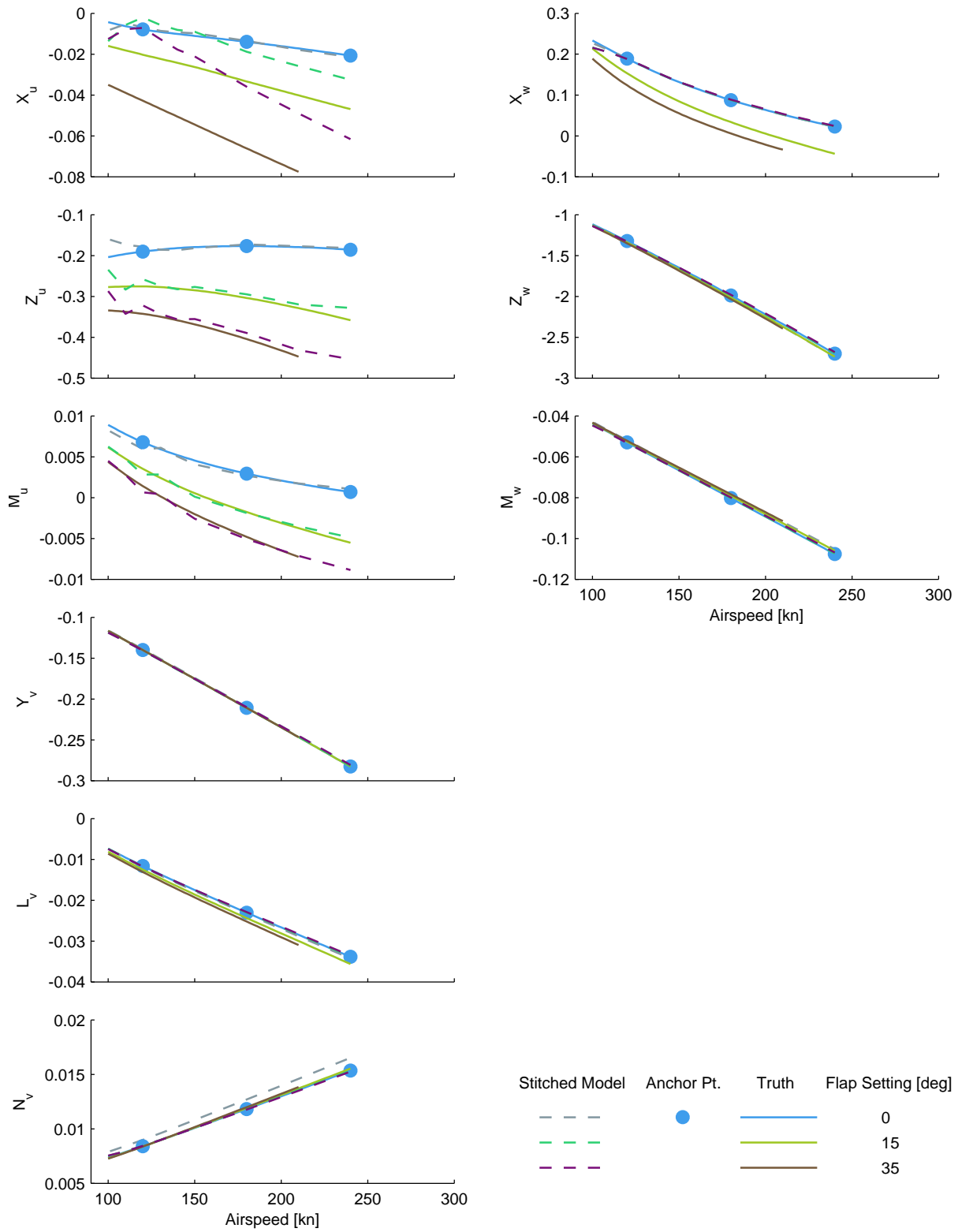
Figure B.27: Alternate configuration verification, flap setting, CJ1 stitched model, stability derivatives.
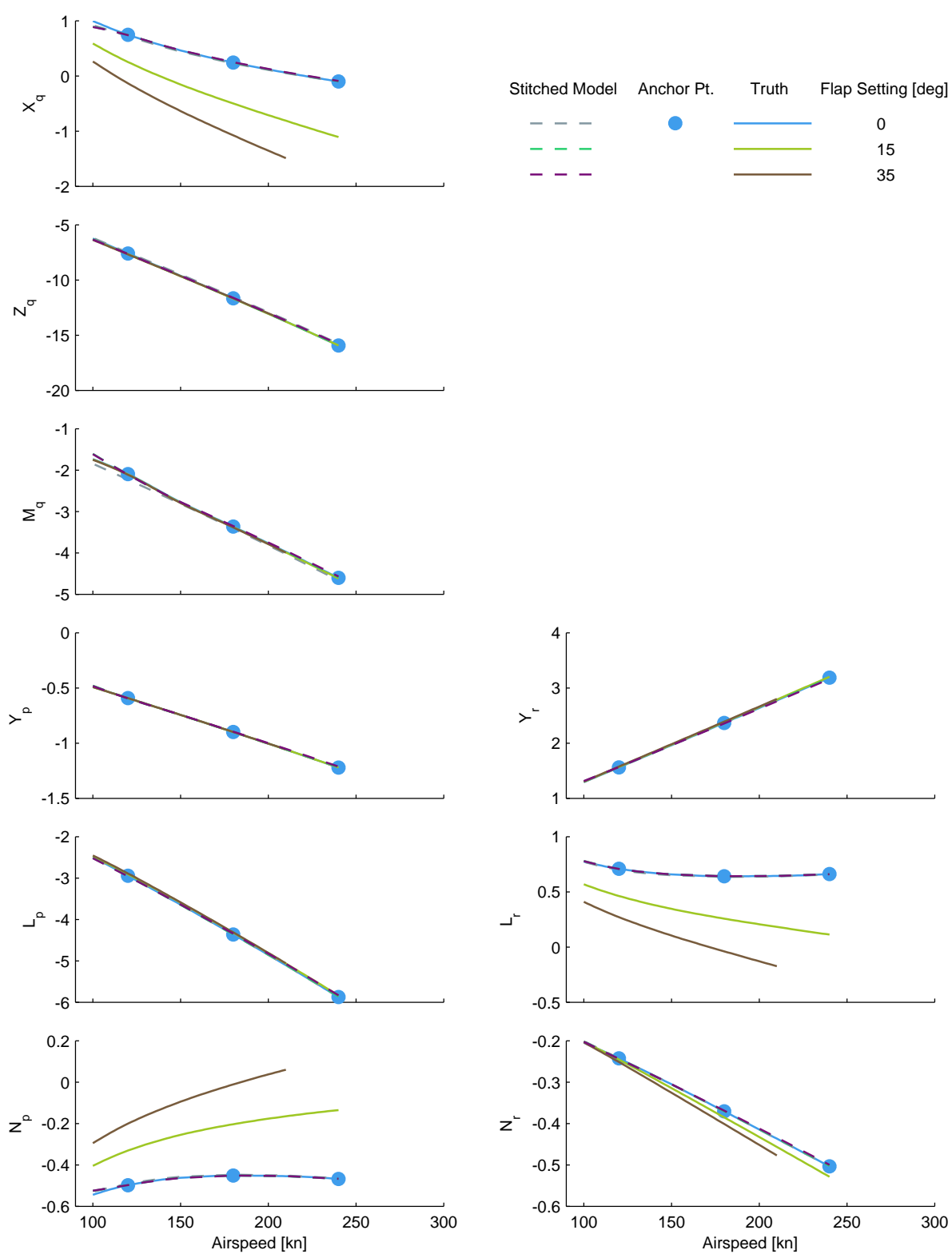
Figure B.27: Alternate configuration verification, flap setting, CJ1 stitched model, stability derivatives (cont.)
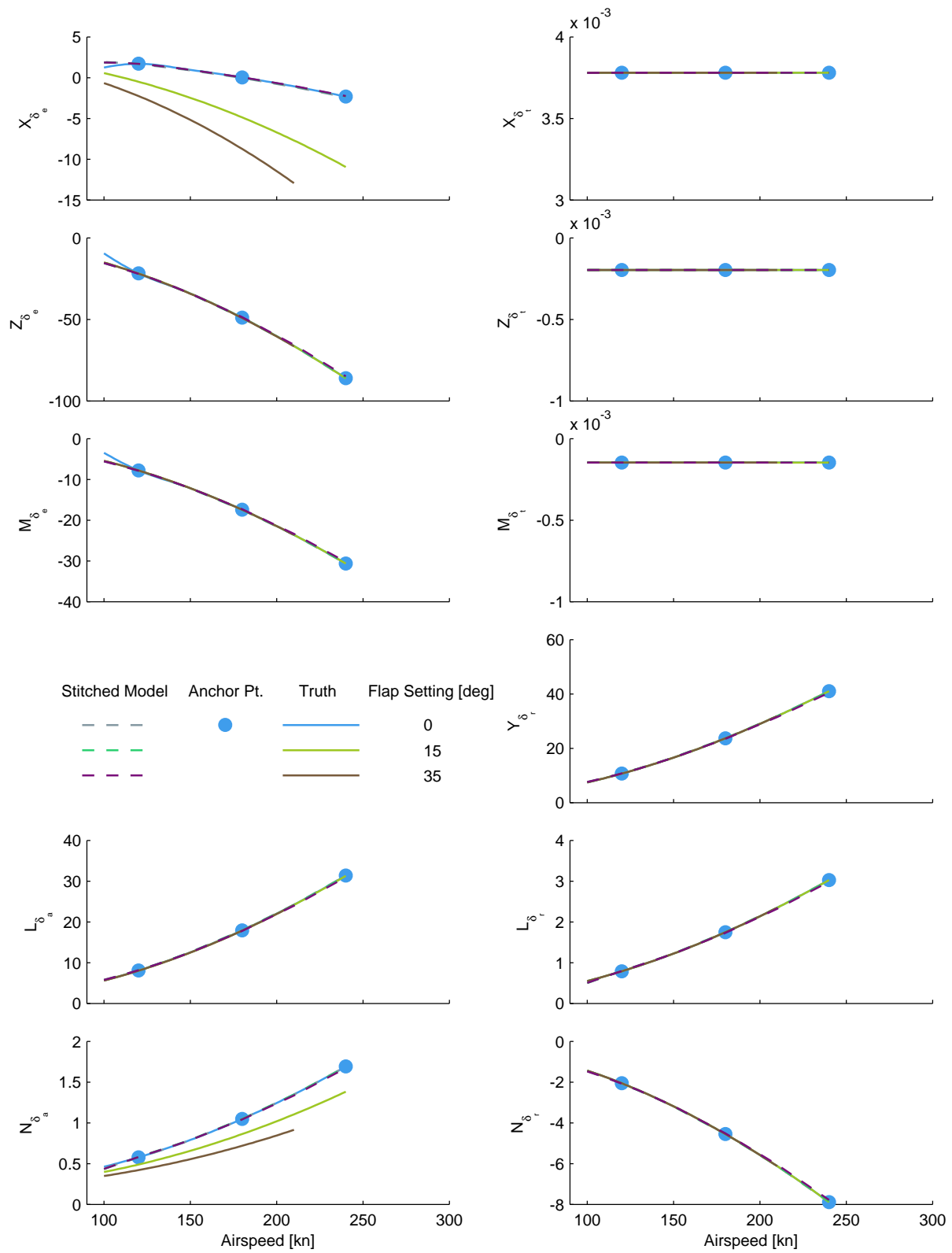
Figure B.28: Alternate configuration verification, flap setting, CJ1 stitched model, control derivatives.

Appendix C   Verification Figures: UH-60 Stitched Model

Contents

This appendix provides additional off-nominal verification results for the UH-60 Black Hawk helicopter stitched model, as presented in Section 4.6. For all comparisons of stability and control derivative values presented herein for the rotorcraft example, the full 26-state FORECAST truth models and high-order stitched model were first reduced to *quasi-steady* 6-DOF models. Quasi-steady derivative values are shown for meaningful comparisons and interpretation of the stability and control derivatives.

Quasi-steady stability and control derivative and trim comparisons are provided for a range of airspeeds for off-nominal values of weight (Section C.1), inertia (Section C.2), center of gravity location (Section C.3), altitude (Section C.4), and sling-load weight (Section C.5). In all figures, the stitched model, configured only with the anchor point models and trim data indicated (solid symbols), was retrimmed and relinearized for various simulation values of each property over a range of airspeed (dashed lines) and compared with values from the FORECAST truth data (solid lines).

C.1 Weight

Figures C.1–C.3 show the complete trim and quasi-steady stability and control derivative comparison results for the UH-60 off-nominal weight verification presented in Section 4.6.1.
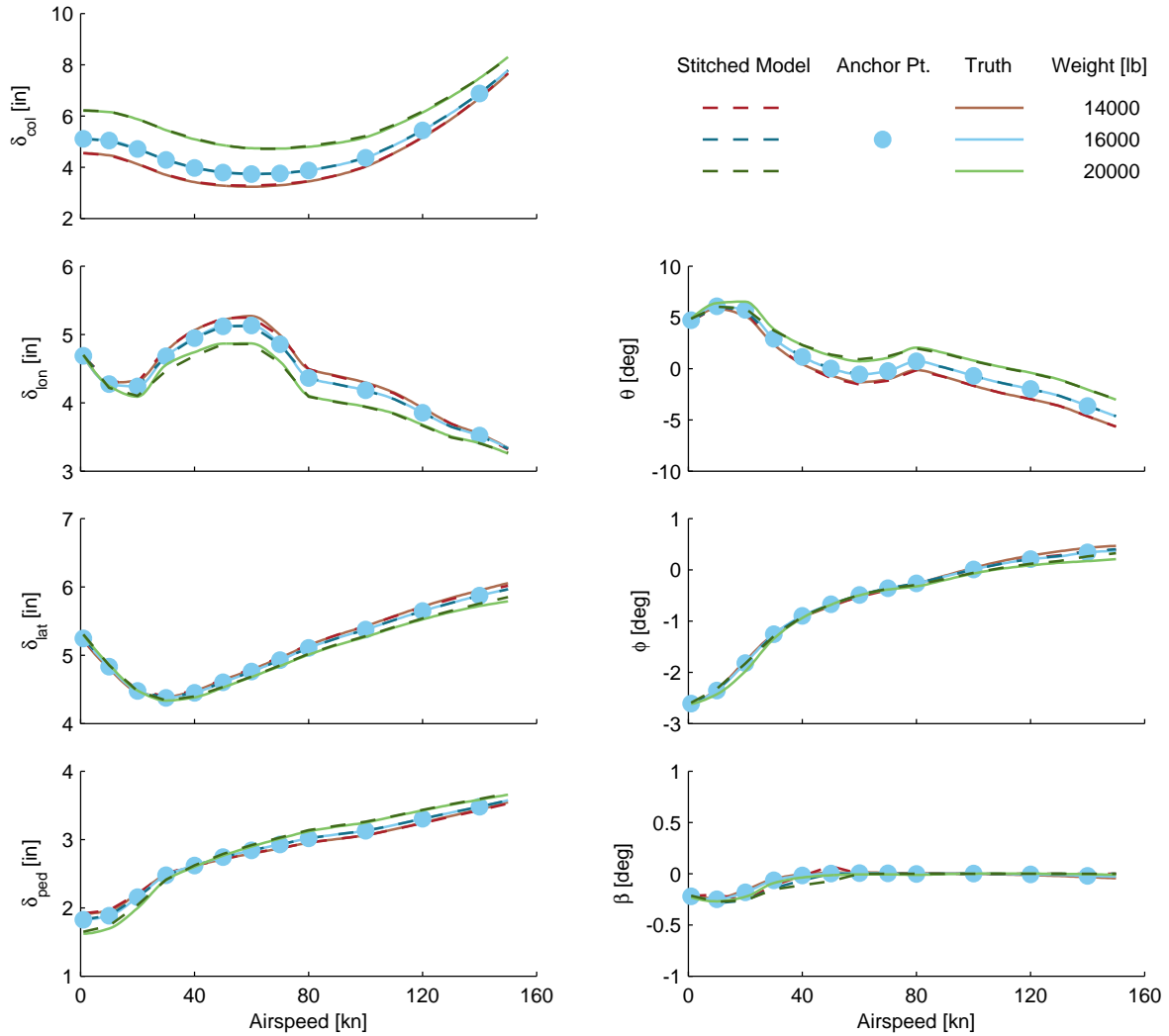
Figure C.1: Verification of off-nominal weight extrapolation, UH-60 stitched model, trim.
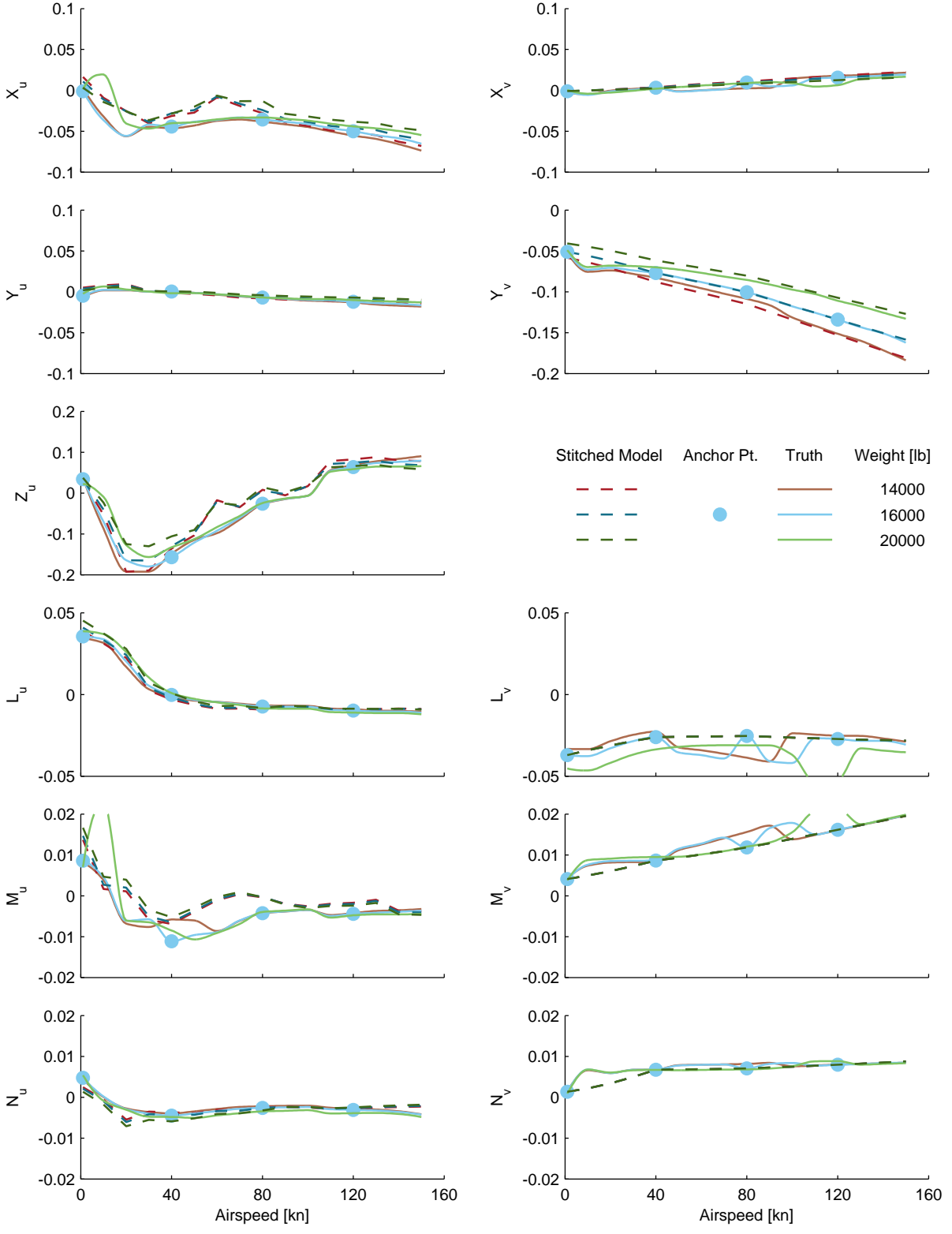
Figure C.2: Verification of off-nominal weight extrapolation, UH-60 stitched model, stability derivatives.
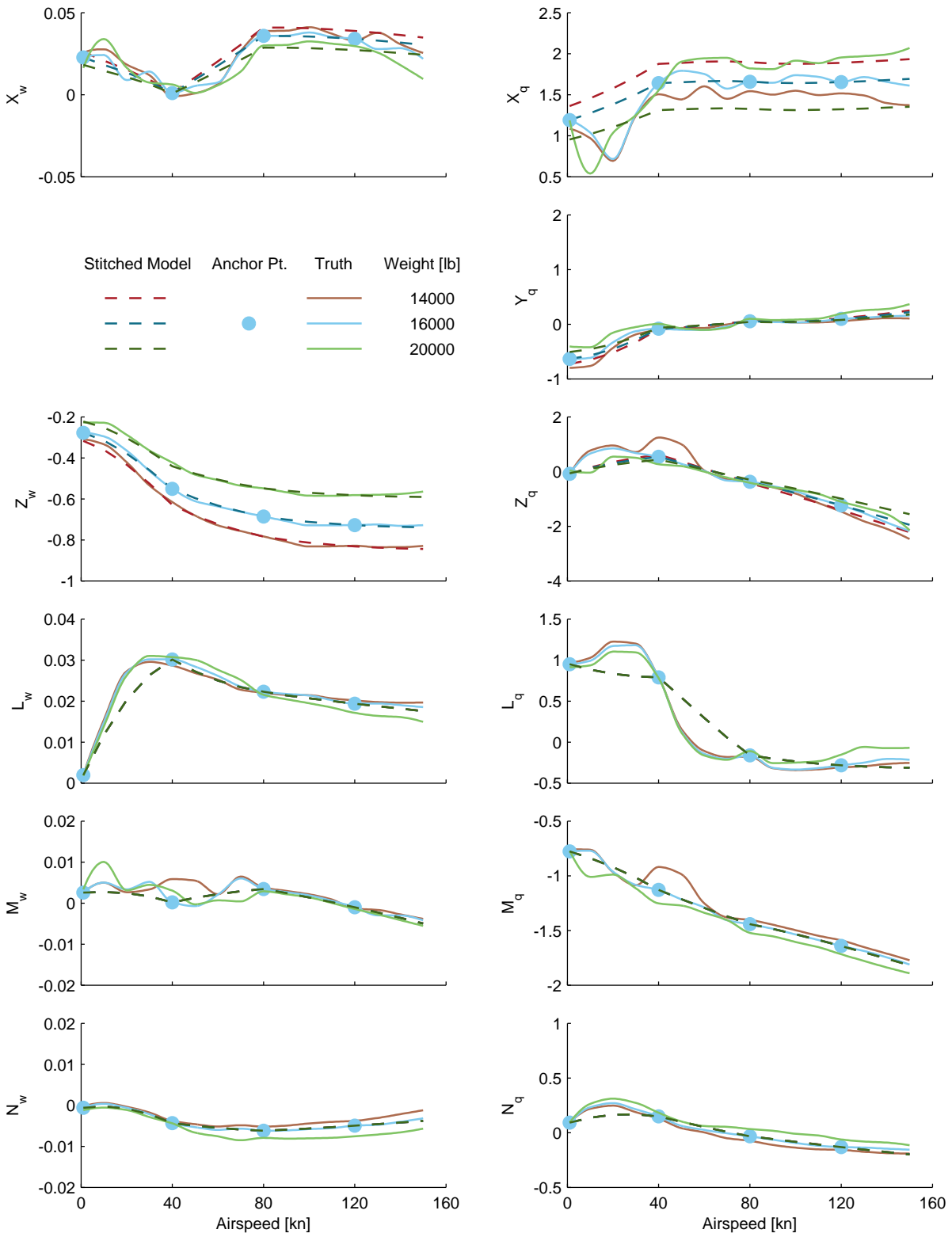
Figure C.2: Verification of off-nominal weight extrapolation, UH-60 stitched model, stability derivatives (cont.)
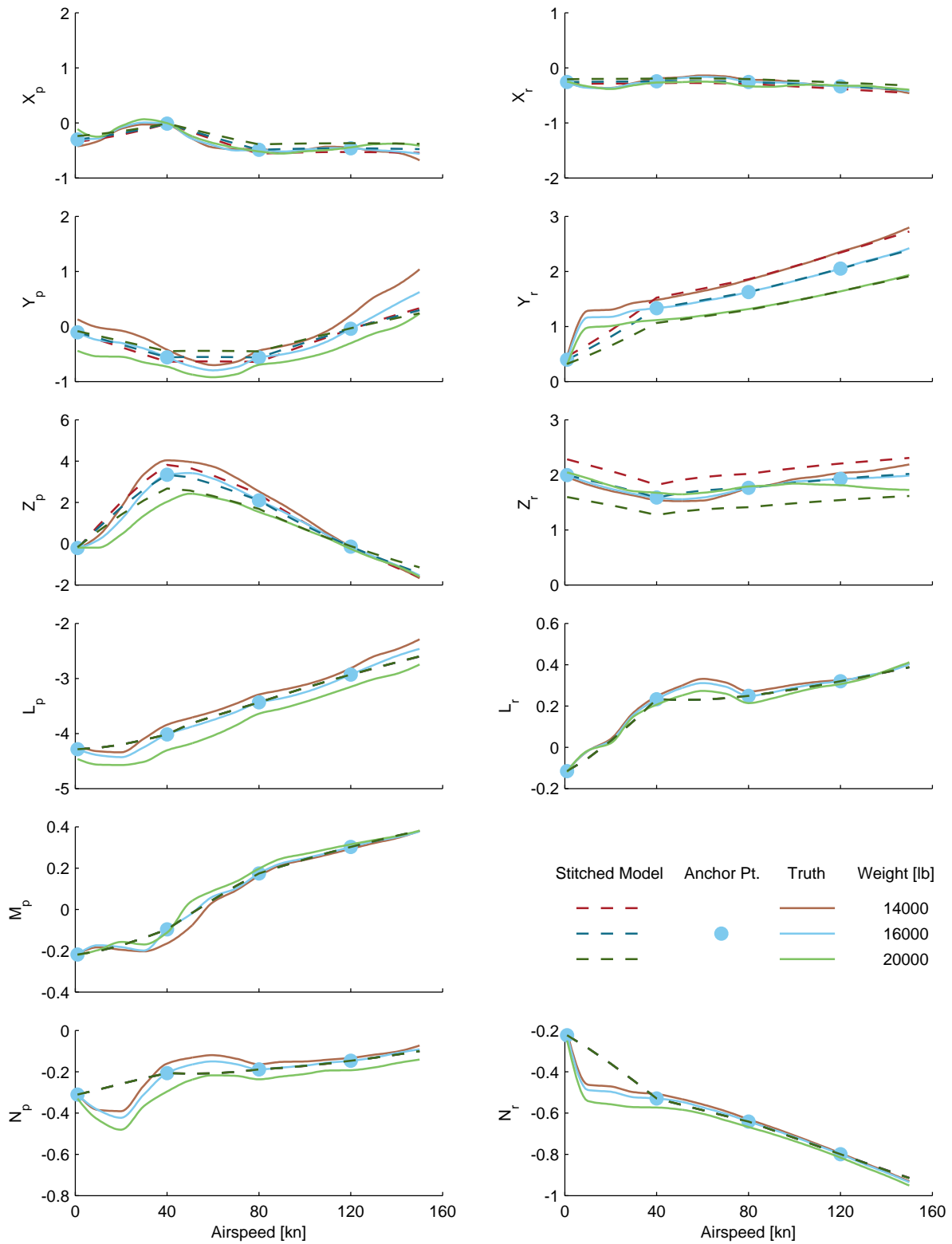
Figure C.2: Verification of off-nominal weight extrapolation, UH-60 stitched model, stability derivatives (cont.)
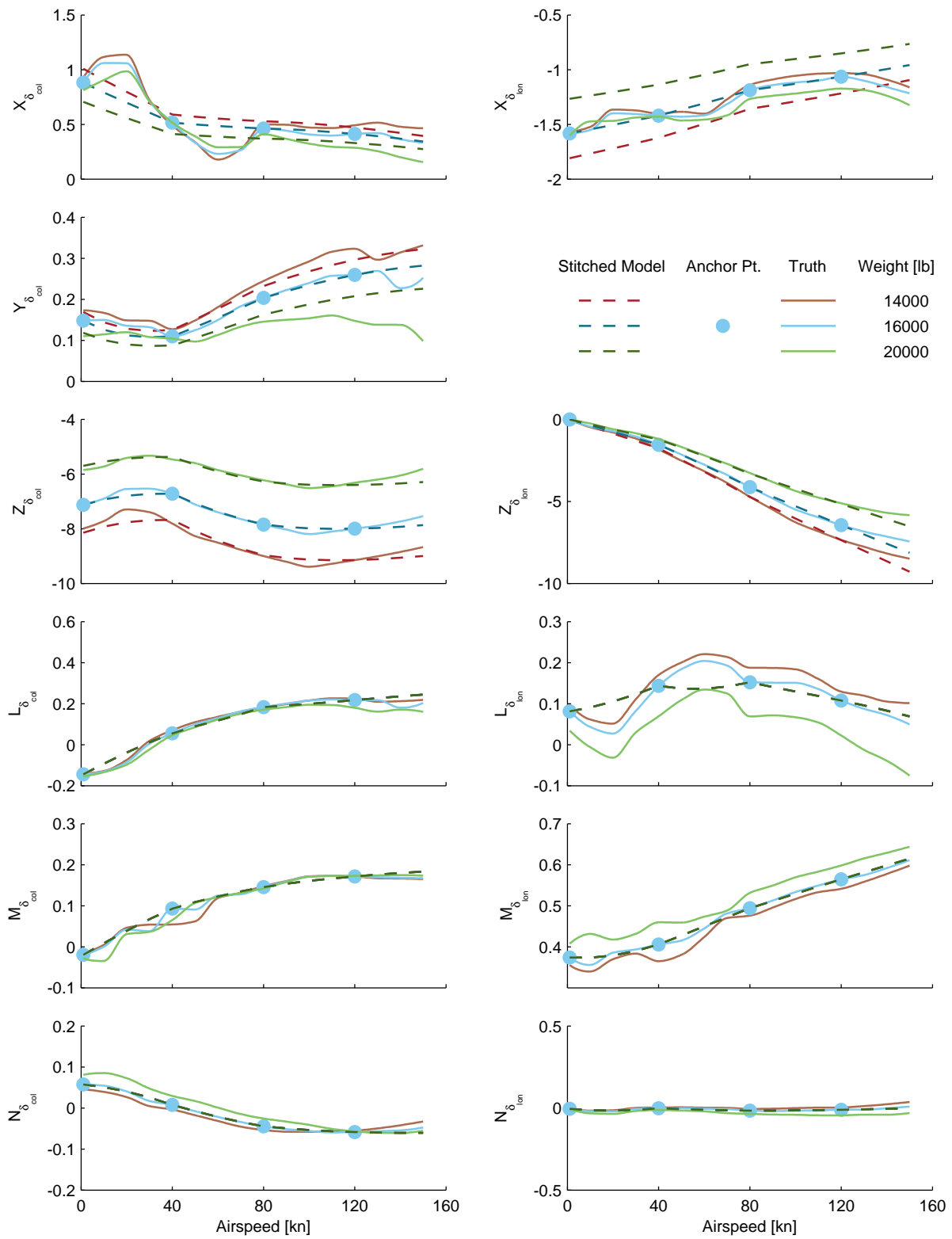
Figure C.3: Verification of off-nominal weight extrapolation, UH-60 stitched model, control derivatives.
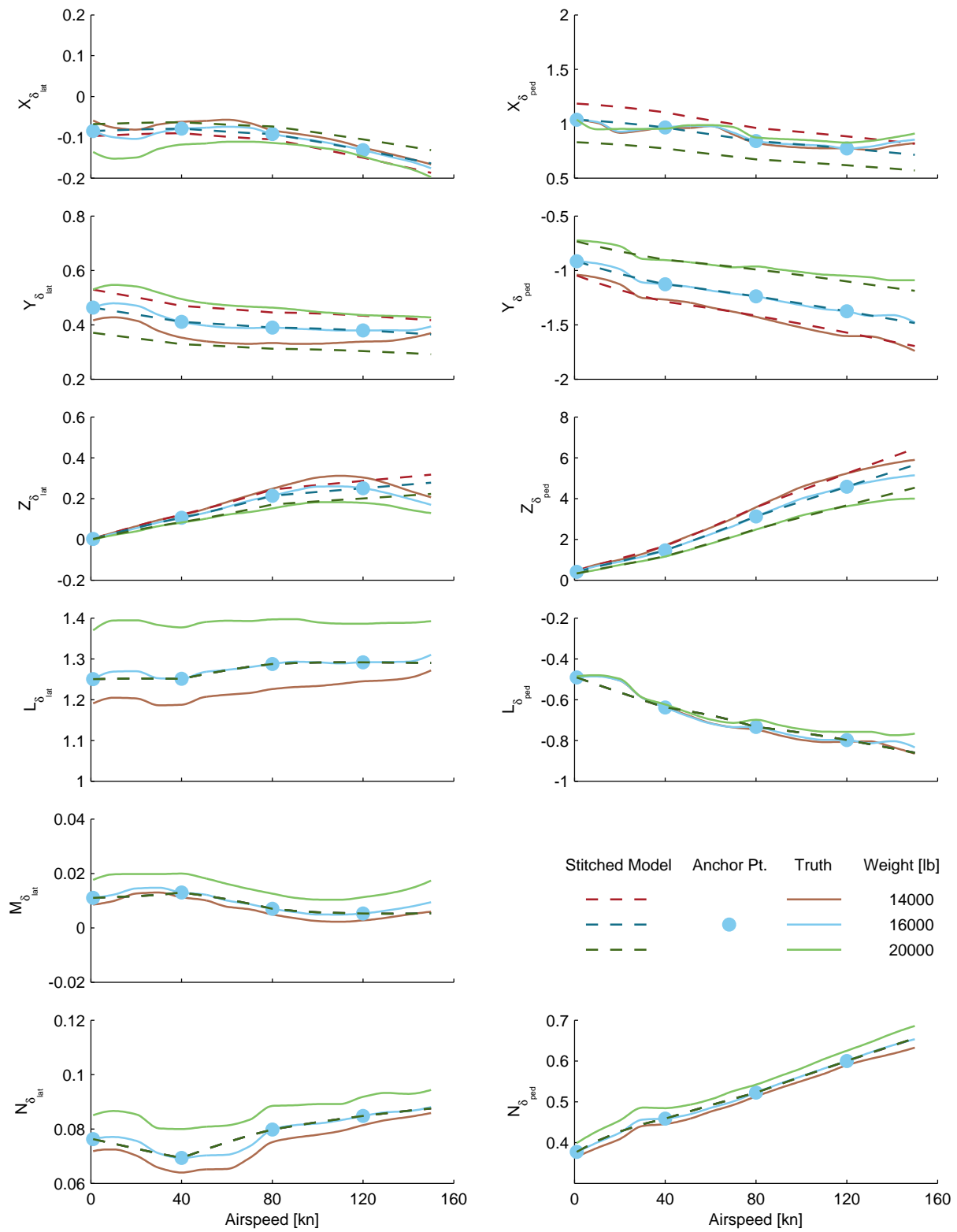
Figure C.3: Verification of off-nominal weight extrapolation, UH-60 stitched model, control derivatives (cont.)

C.2 Inertia

The UH-60 Black Hawk stitched model was configured with values of off-nominal inertia and verified against FORECAST point models. Sections C.2.1–C.2.3 present the results for off-nominal values of I_{xx}, I_{yy}, and I_{zz} varied individually.

C.2.1 Roll Inertia

Figures C.4–C.6 show the complete trim and quasi-steady stability and control derivative comparison results for the UH-60 off-nominal roll inertia verification, as presented in Section 4.6.2. Note that changes in inertia have no effect on trim; only the dynamics are affected, as seen in the values of the stability and control derivatives. A plot of the trim controls and attitude is shown for this inertia case only to verify the unchanged values of trim.
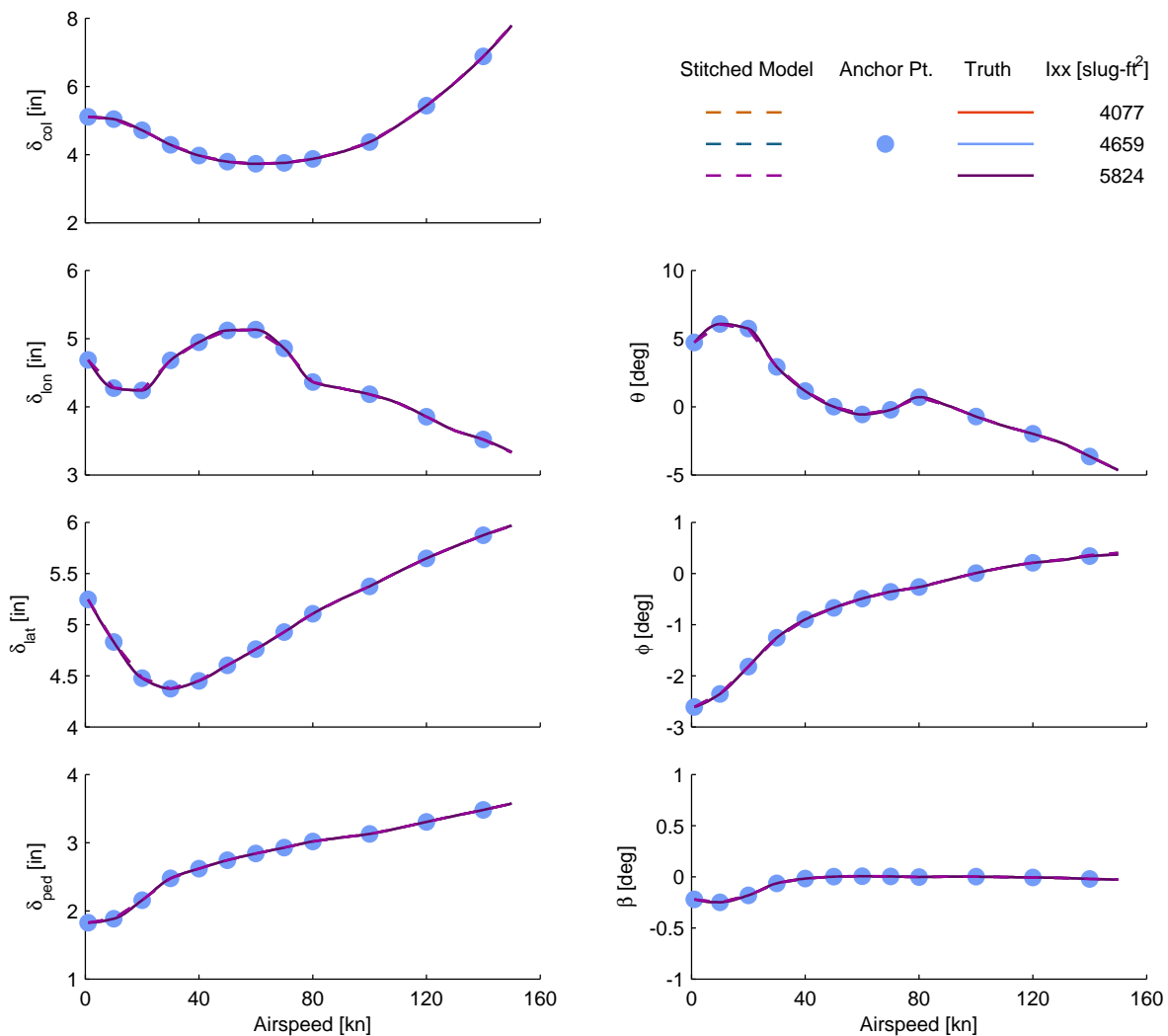
Figure C.4: Verification of off-nominal roll inertia extrapolation, UH-60 stitched model, trim.
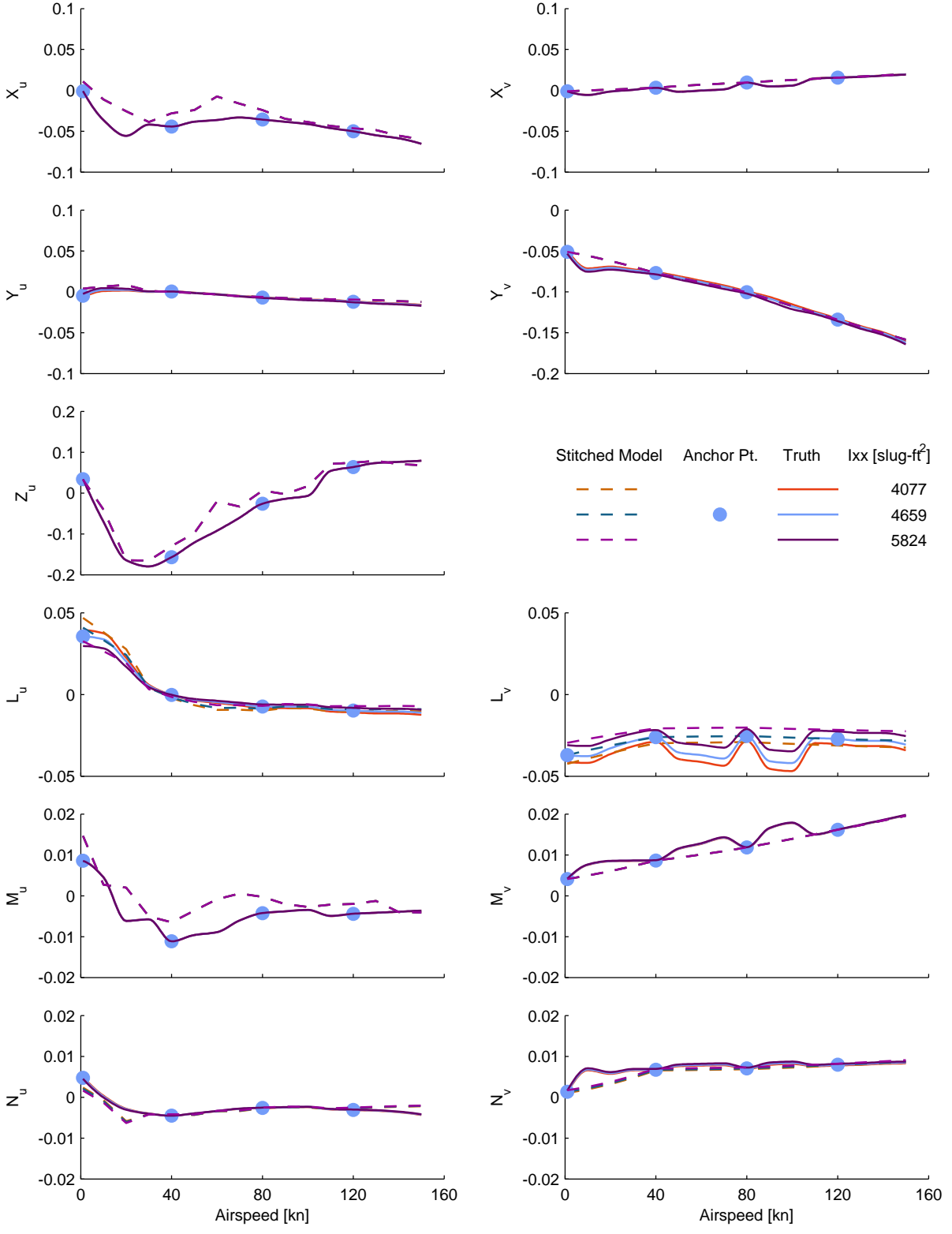
Figure C.5: Verification of off-nominal roll inertia extrapolation, UH-60 stitched model, stability derivatives.
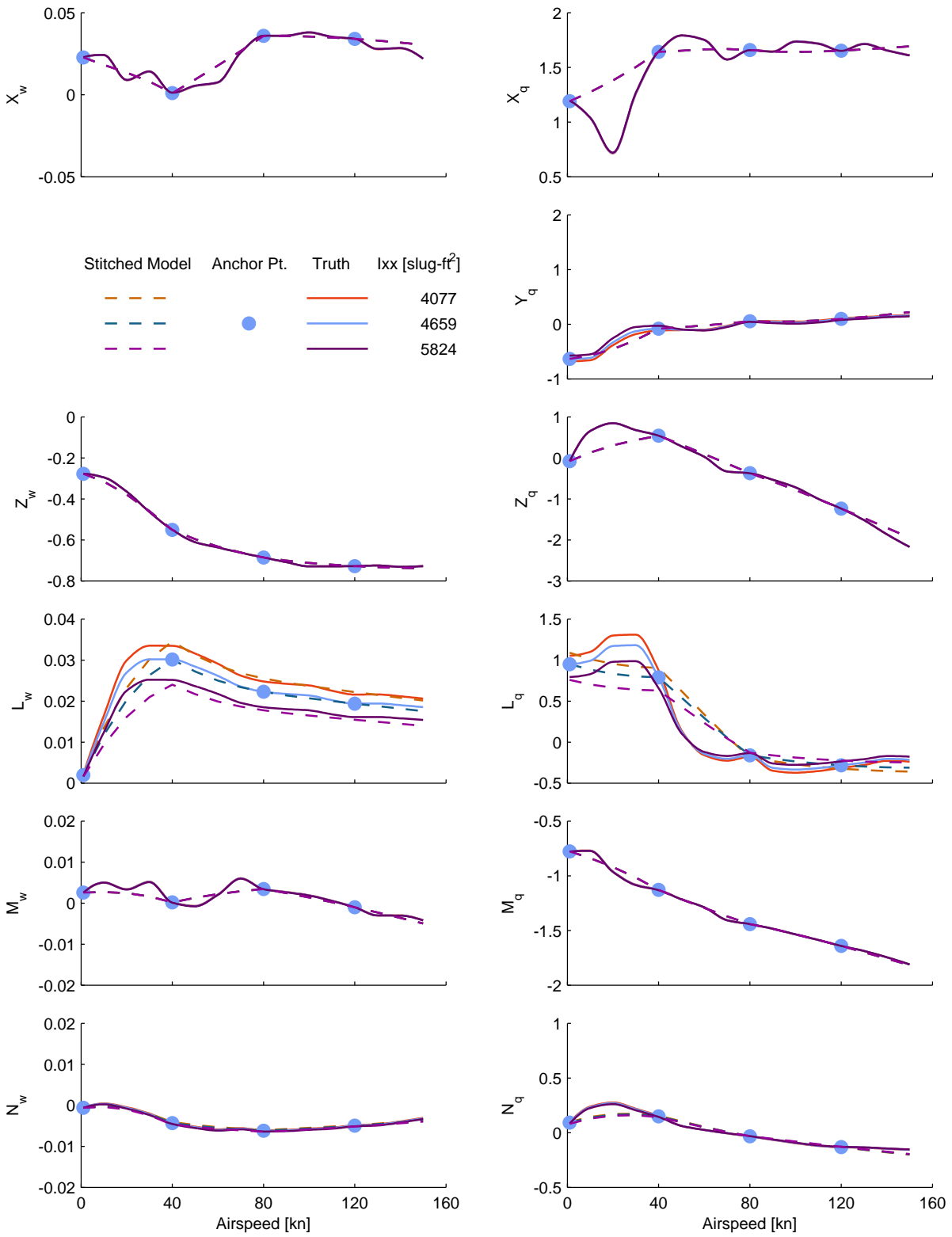
Figure C.5: Verification of off-nominal roll inertia extrapolation, UH-60 stitched model, stability derivatives (cont.)
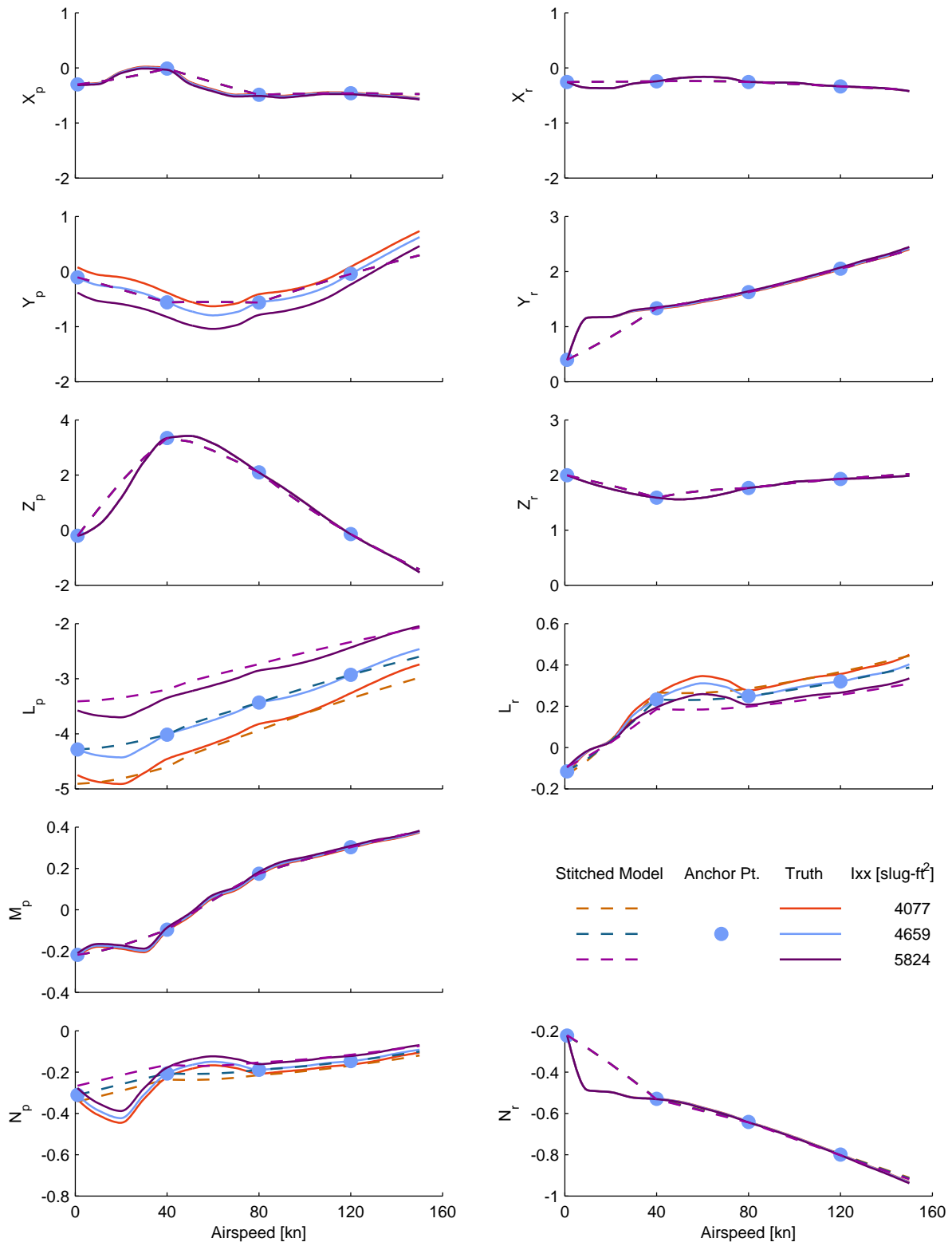
Figure C.5: Verification of off-nominal roll inertia extrapolation, UH-60 stitched model, stability derivatives (cont.)
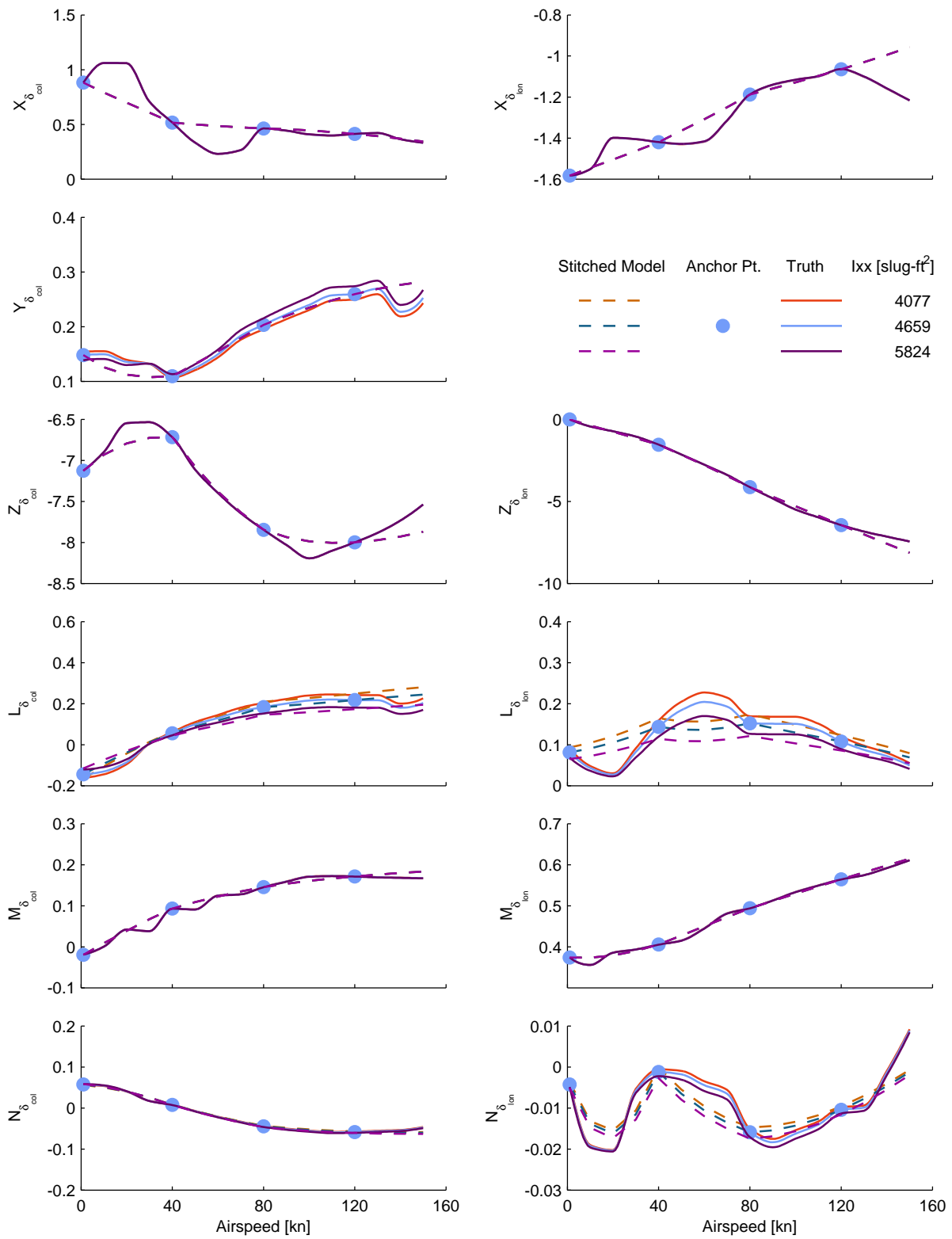
Figure C.6: Verification of off-nominal roll inertia extrapolation, UH-60 stitched model, control derivatives.
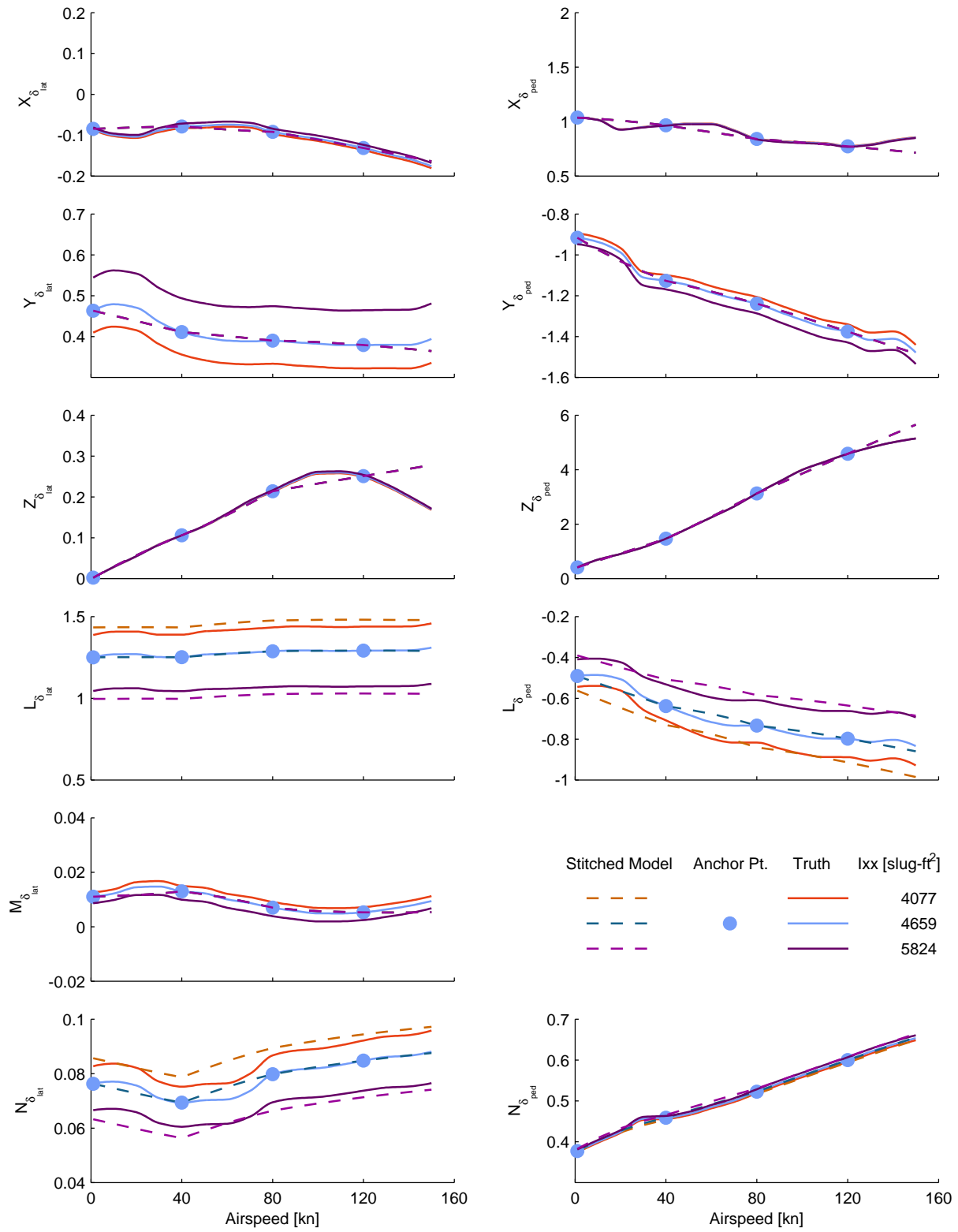
Figure C.6: Verification of off-nominal roll inertia extrapolation, UH-60 stitched model, control derivatives (cont.)

C.2.2   Pitch Inertia

Figures C.7 and C.8 show the complete quasi-steady stability and control derivative comparison results for the UH-60 off-nominal pitch inertia verification, as presented in Section 4.6.2. As noted and verified in the previous section, changes in inertia have no effect on trim; thus, the plot showing the unchanged values of trim has been omitted.
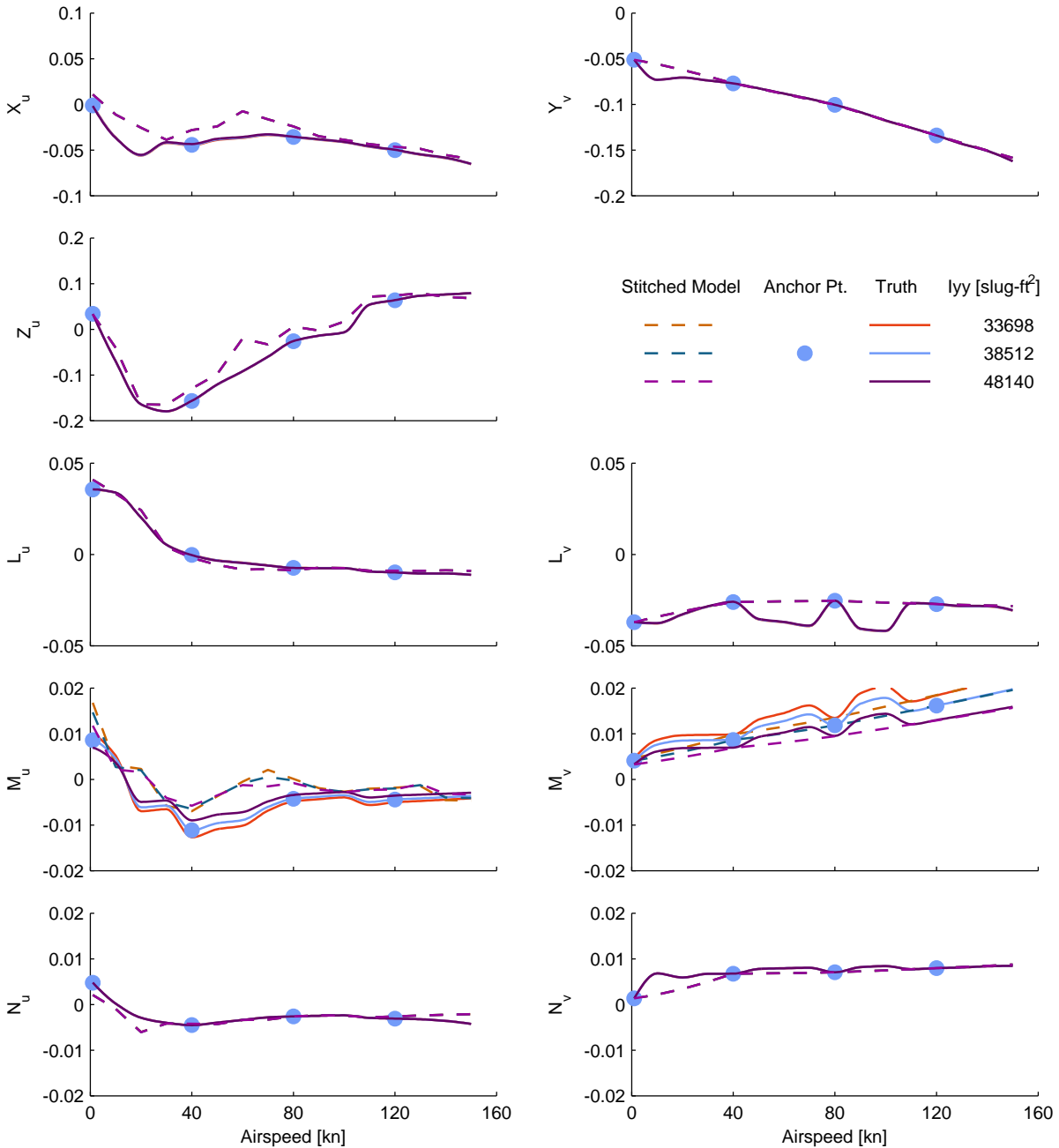

Figure C.7: Verification of off-nominal pitch inertia extrapolation, UH-60 stitched model, stability derivatives.
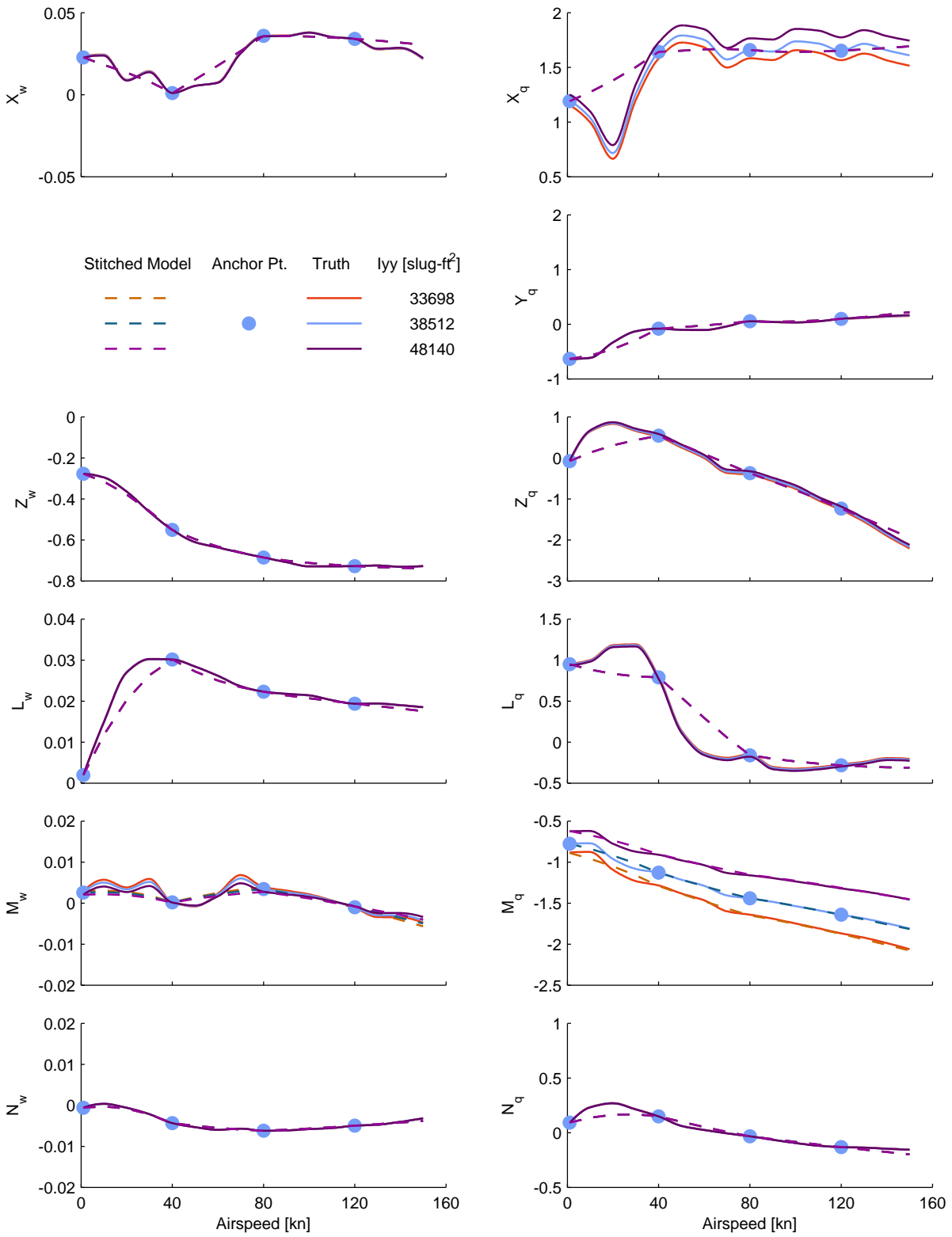
Figure C.7: Verification of off-nominal pitch inertia extrapolation, UH-60 stitched model, stability derivatives (cont.)
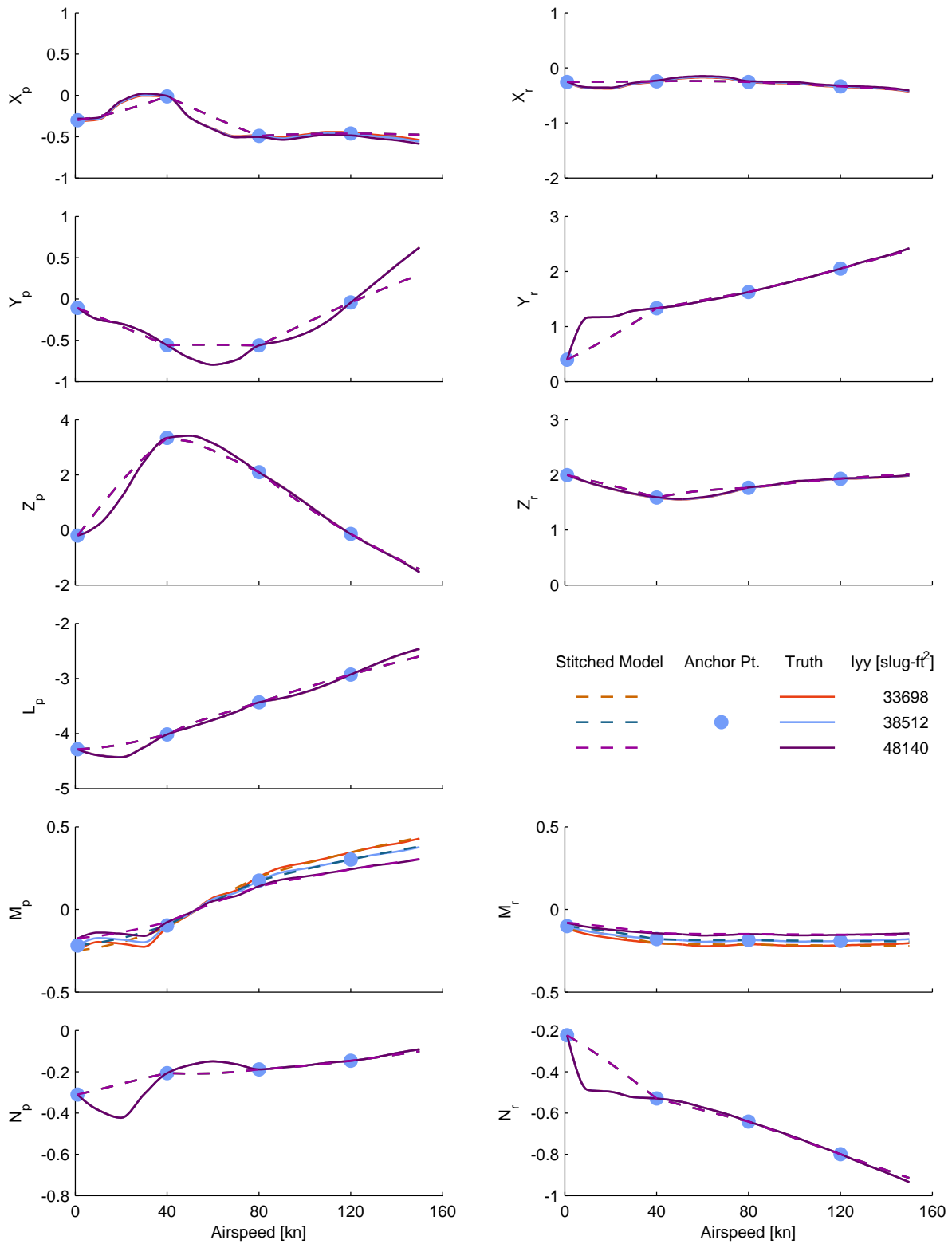
Figure C.7: Verification of off-nominal pitch inertia extrapolation, UH-60 stitched model, stability derivatives (cont.)
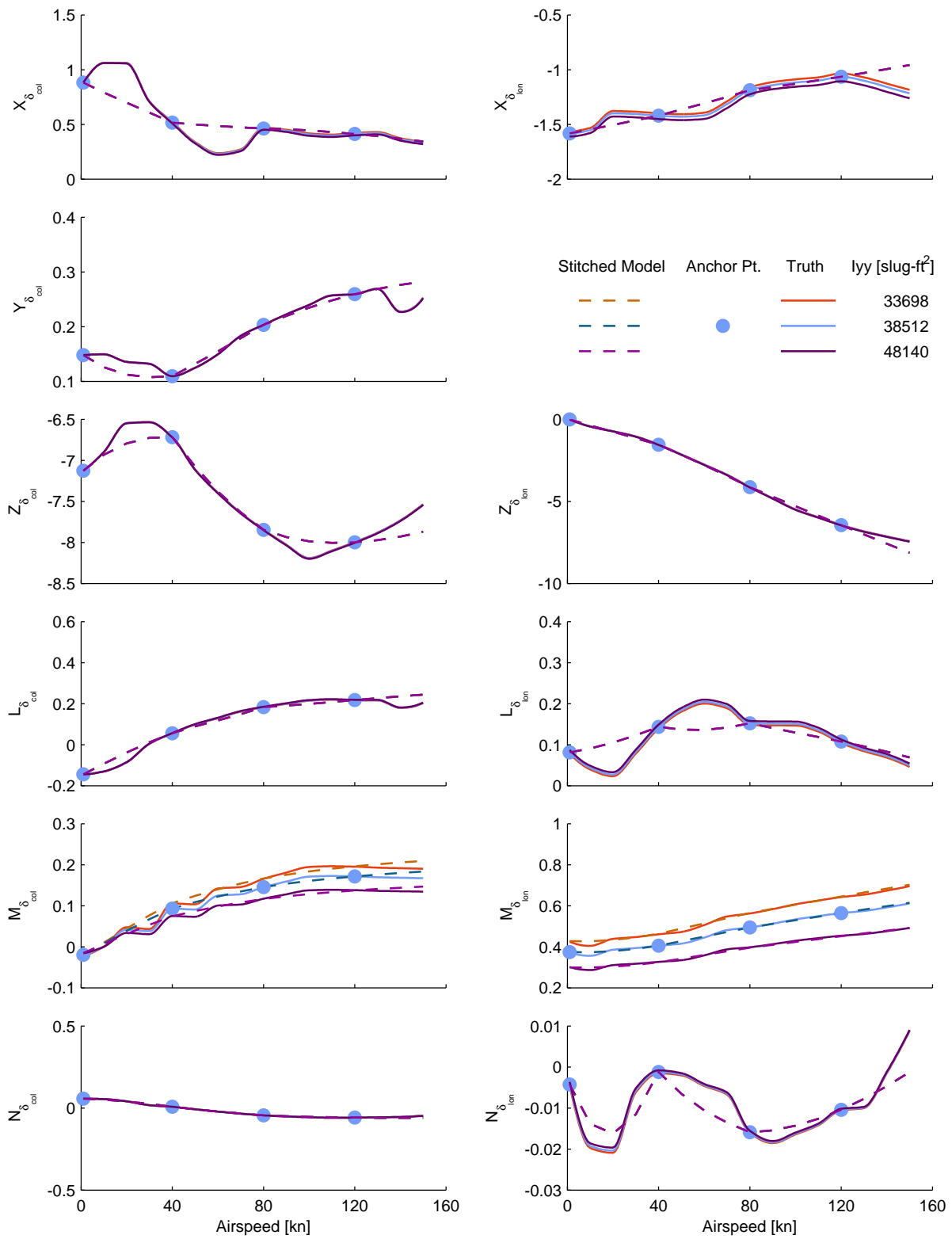
Figure C.8: Verification of off-nominal pitch inertia extrapolation, UH-60 stitched model, control derivatives.
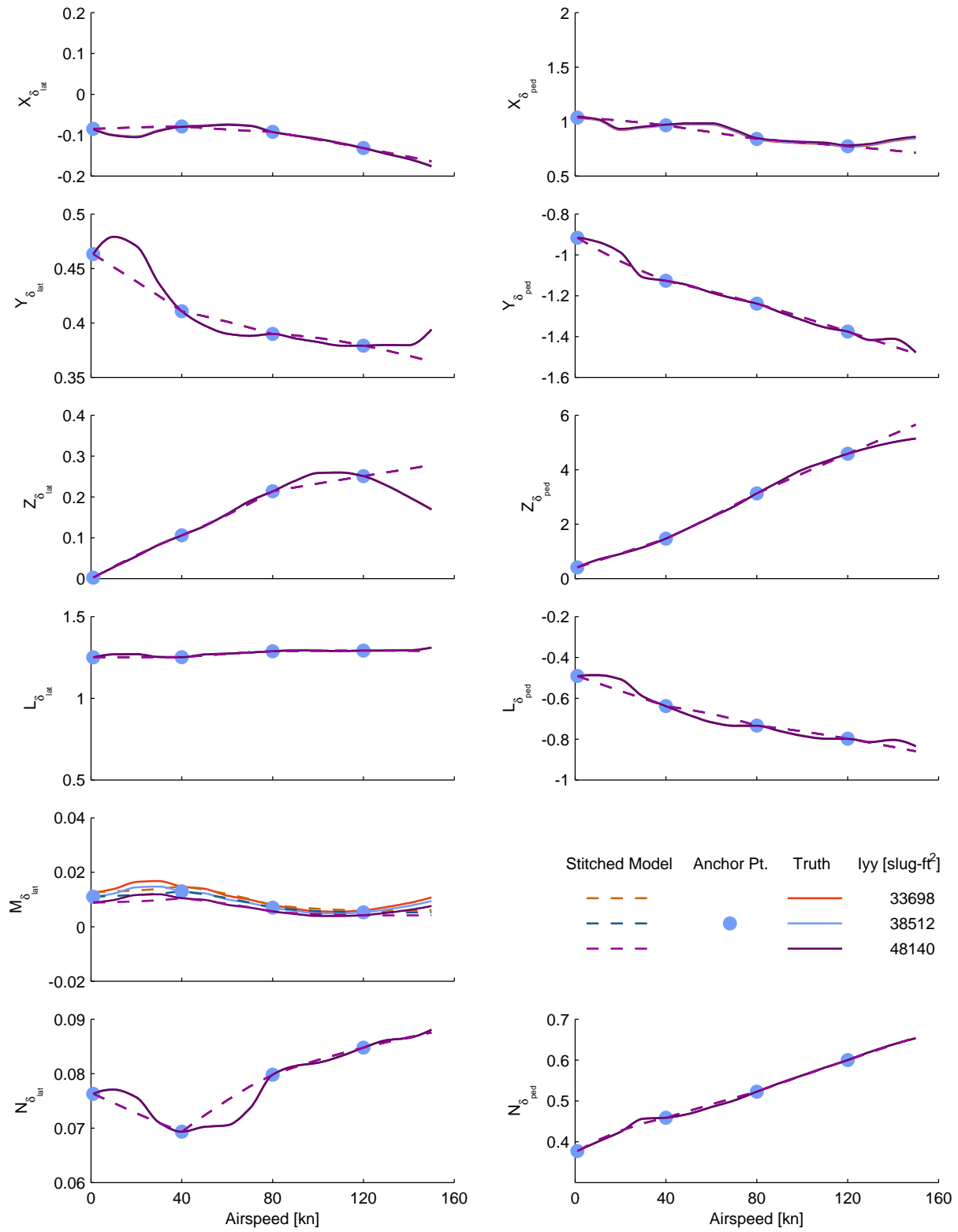
Figure C.8: Verification of off-nominal pitch inertia extrapolation, UH-60 stitched model, control derivatives (cont.)

C.2.3 Yaw Inertia

Figures C.9 and C.10 show the complete quasi-steady stability and control derivative comparison results for the UH-60 off-nominal yaw verification, as presented in Section 4.6.2. As noted and verified previously, changes in inertia have no effect on trim; thus, the plot showing the unchanged values of trim has been omitted from this section.
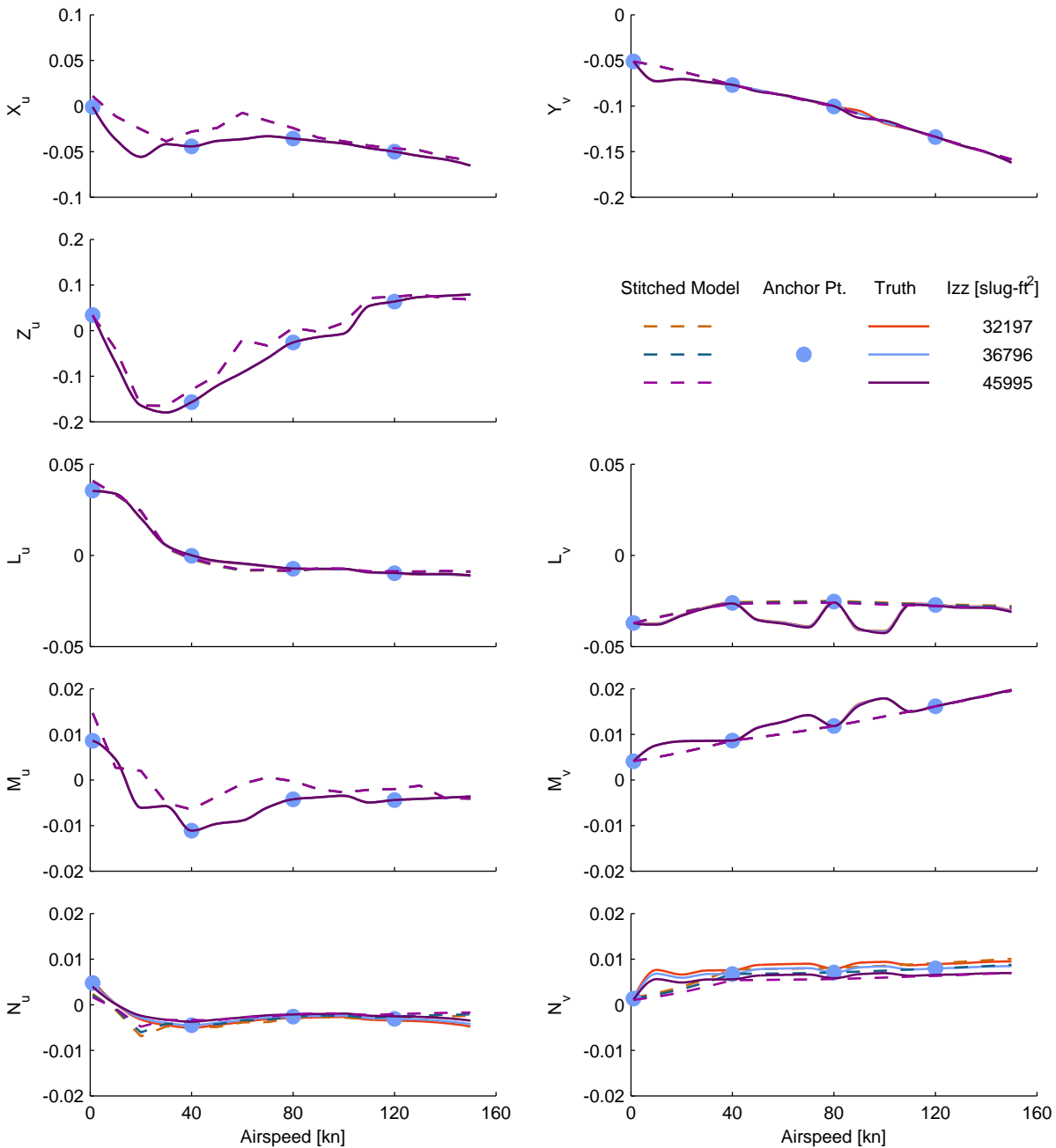
Figure C.9: Verification of off-nominal yaw inertia extrapolation, UH-60 stitched model, stability derivatives.
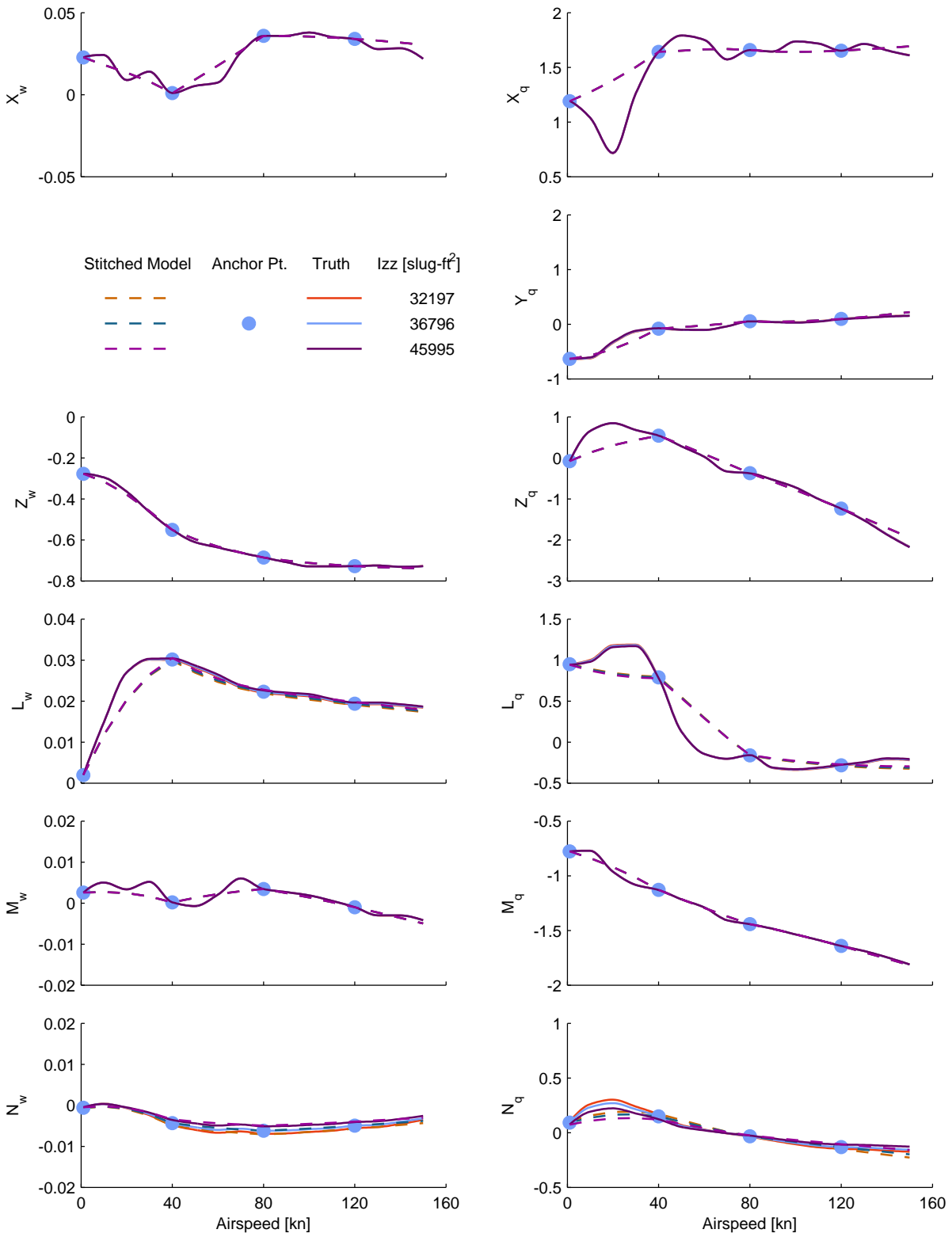
Figure C.9: Verification of off-nominal yaw inertia extrapolation, UH-60 stitched model, stability derivatives (cont.)

Figure C.9: Verification of off-nominal yaw inertia extrapolation, UH-60 stitched model, stability derivatives (cont.)

171
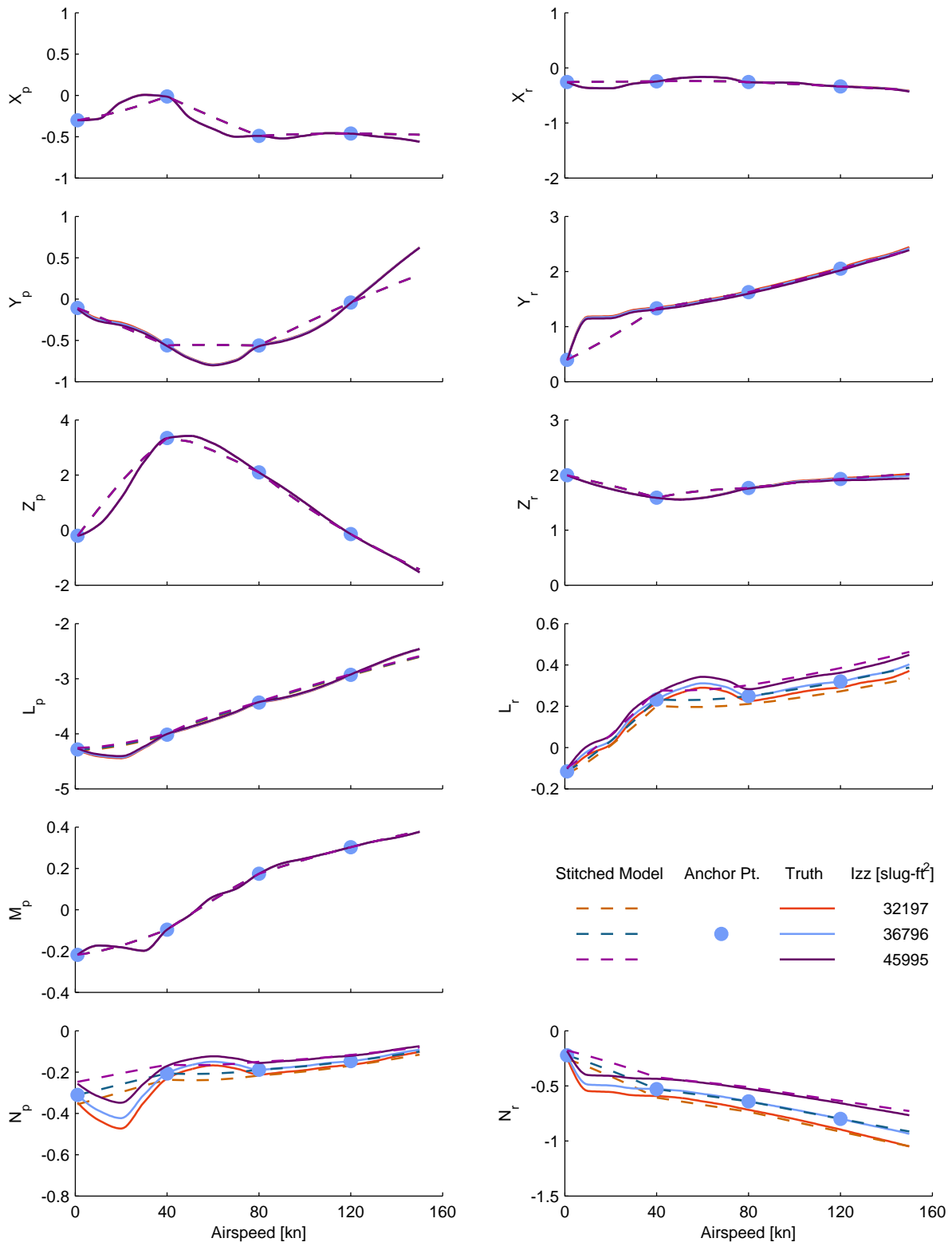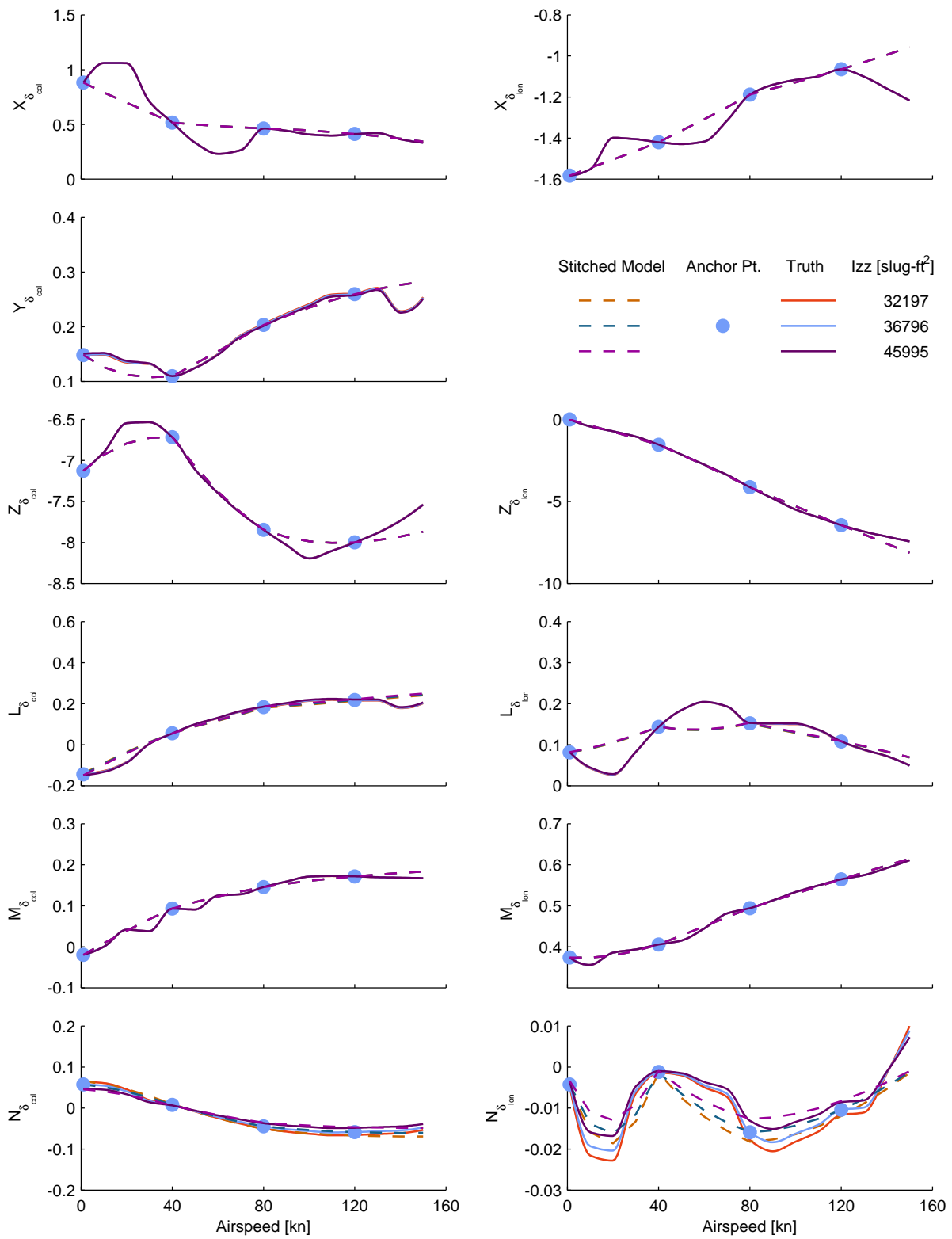
Figure C.10: Verification of off-nominal yaw inertia extrapolation, UH-60 stitched model, control derivatives.
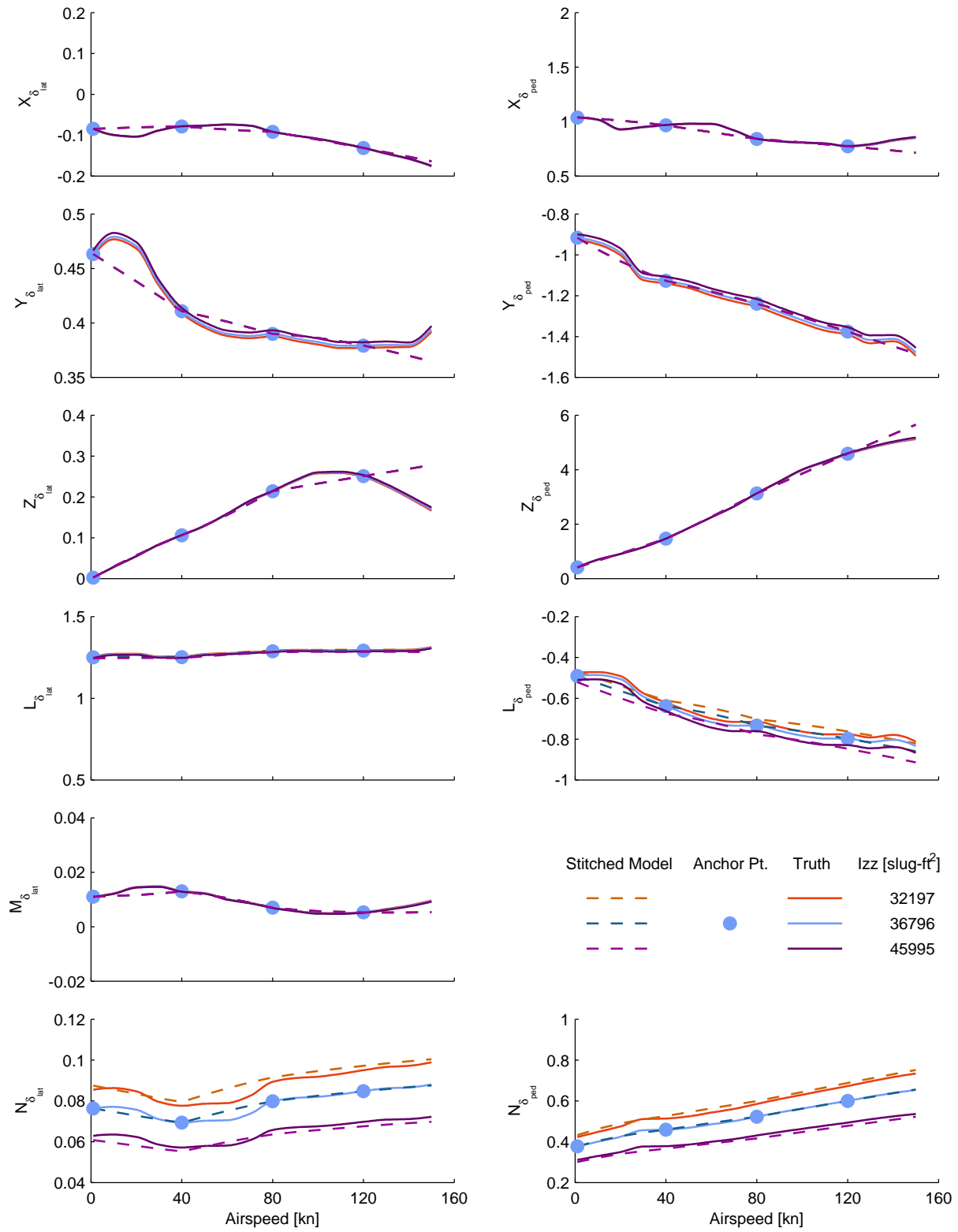
Figure C.10: Verification of off-nominal yaw inertia extrapolation, UH-60 stitched model, control derivatives (cont.)

C.3 Center of Gravity

The UH-60 stitched model was configured with off-nominal CG location values and verified against FORE-CAST point models. Section C.3.1 presents the results for off-nominal fuselage-station CG location, and Section C.3.2 presents the results for off-nominal buttline CG location.

C.3.1 Station CG

Figures C.11–C.13 show the complete trim and quasi-steady stability and control derivative verification results for the UH-60 stitched model configured with fuselage-station CG location (x-body axis, positive aft) offsets, as discussed in Section 4.6.3.
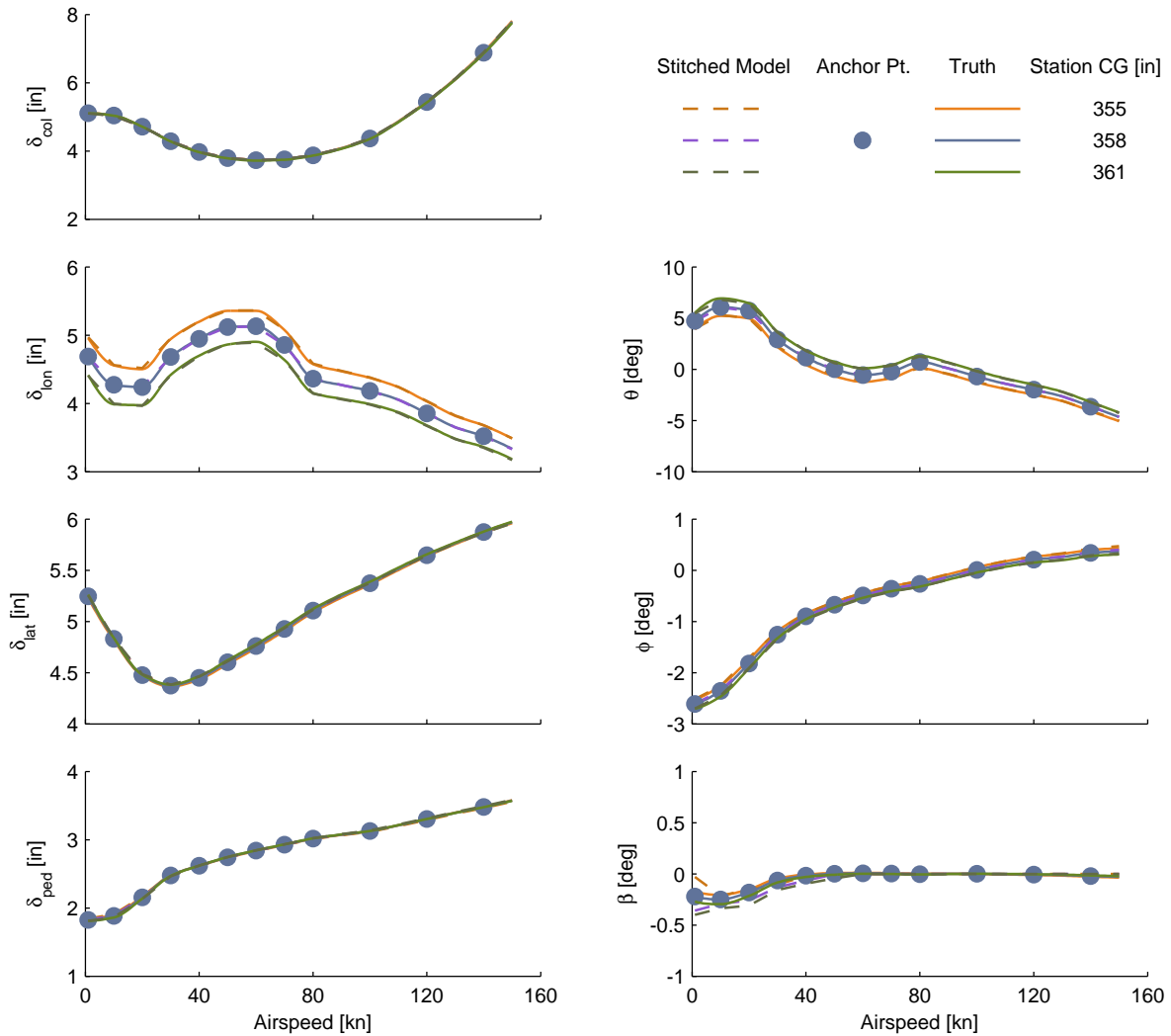
Figure C.11: Verification of off-nominal station CG extrapolation, UH-60 stitched model, trim.
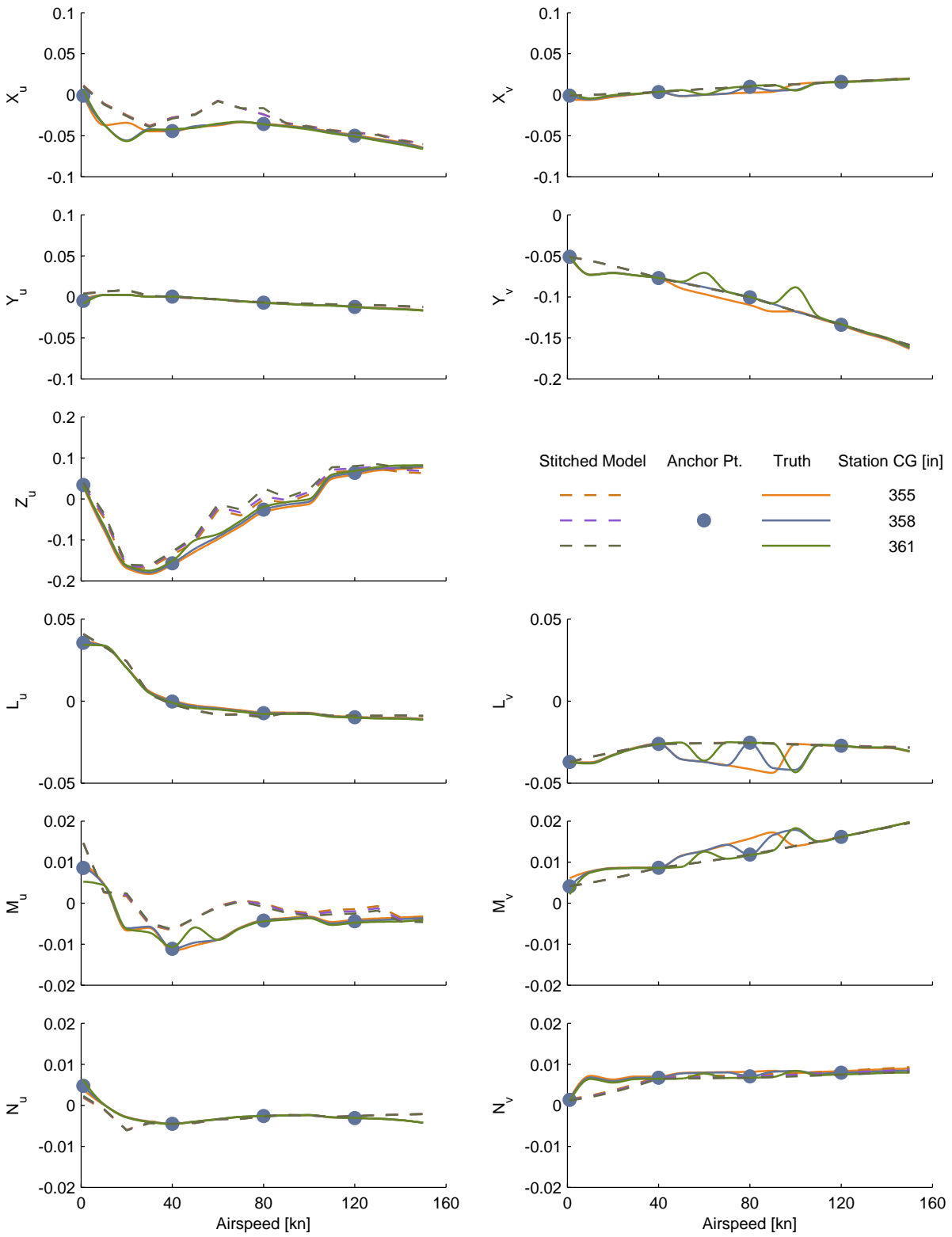
Figure C.12: Verification of off-nominal station CG extrapolation, UH-60 stitched model, stability derivatives.
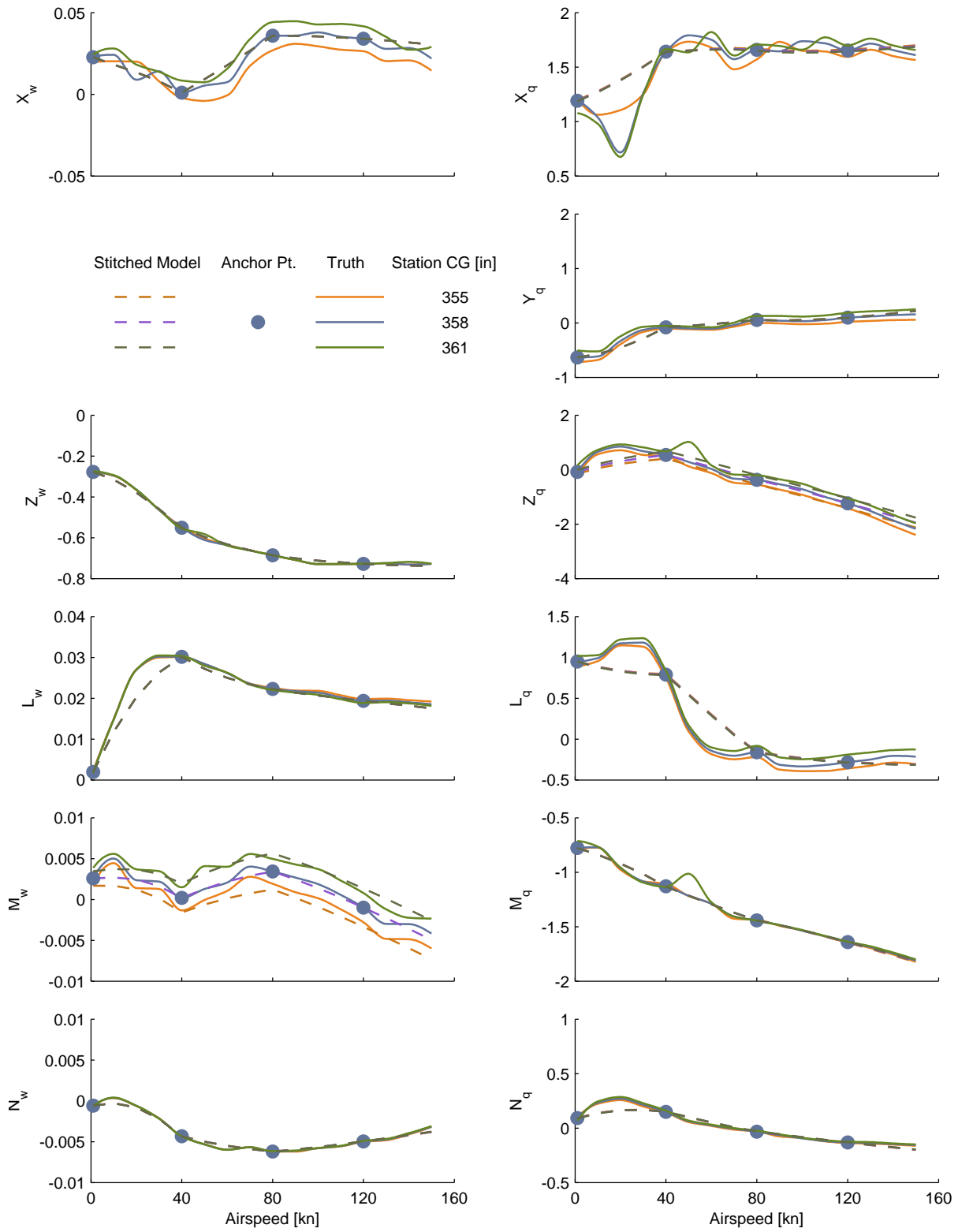
Figure C.12: Verification of off-nominal station CG extrapolation, UH-60 stitched model, stability derivatives (cont.)
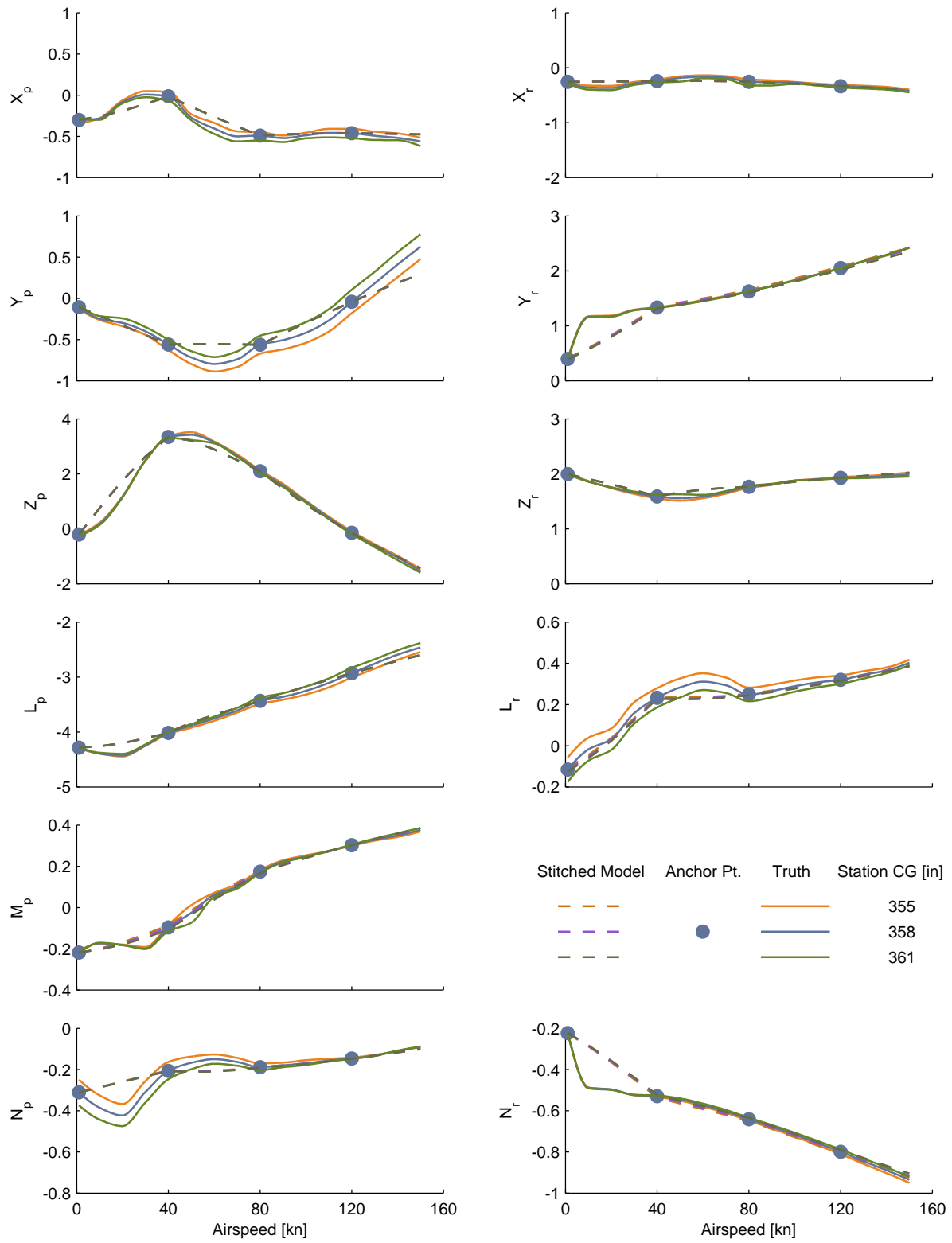
Figure C.12: Verification of off-nominal station CG extrapolation, UH-60 stitched model, stability derivatives (cont.)
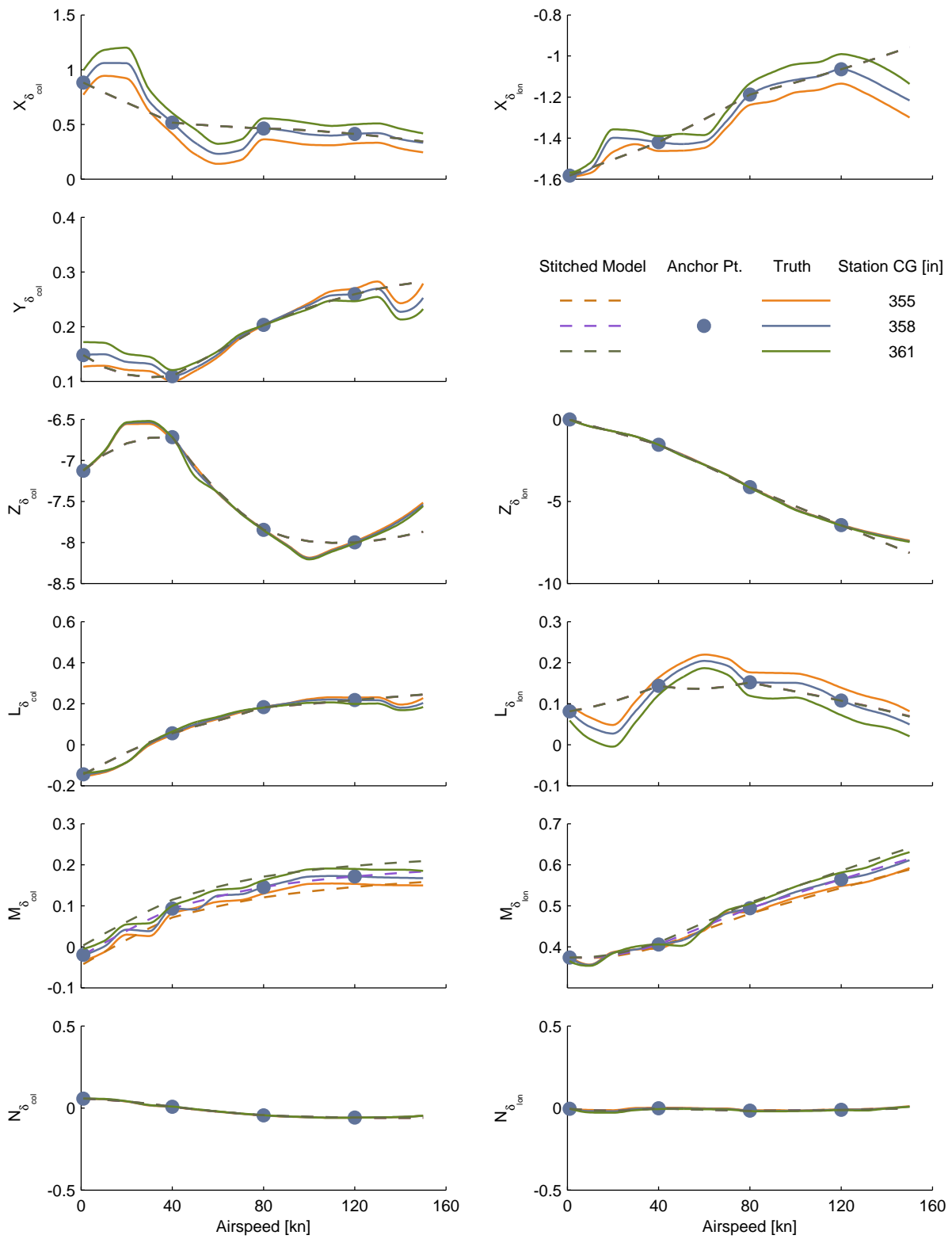
Figure C.13: Verification of off-nominal station CG extrapolation, UH-60 stitched model, control derivatives.
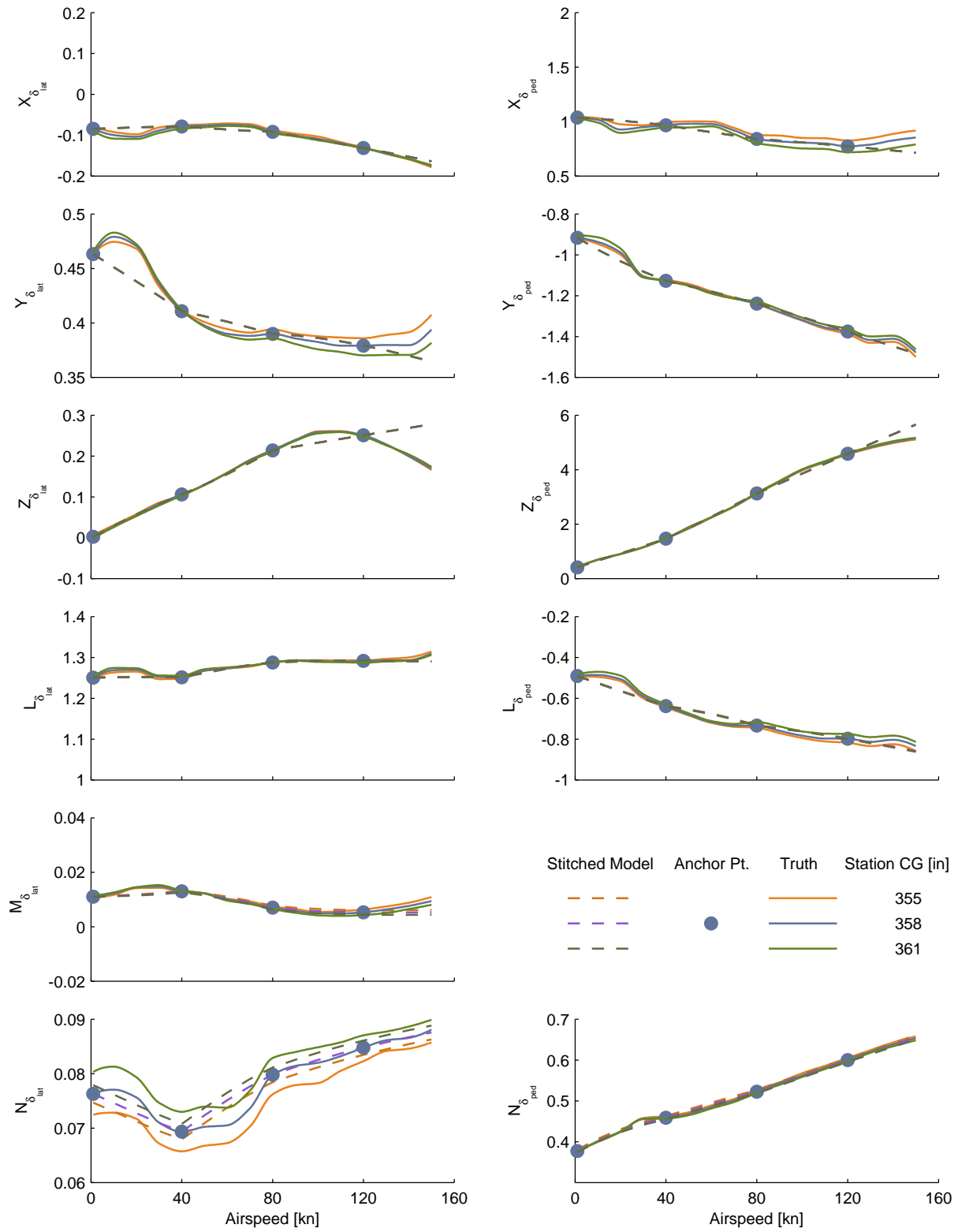
Figure C.13: Verification of off-nominal station CG extrapolation, UH-60 stitched model, control derivatives (cont.)

C.3.2 Buttline CG

Figures C.14–C.16 show the complete trim and quasi-steady stability and control derivative verification results for the UH-60 stitched model configured with a buttline CG location (*y*-body axis, positive right) offset, as discussed in Section 4.6.3.
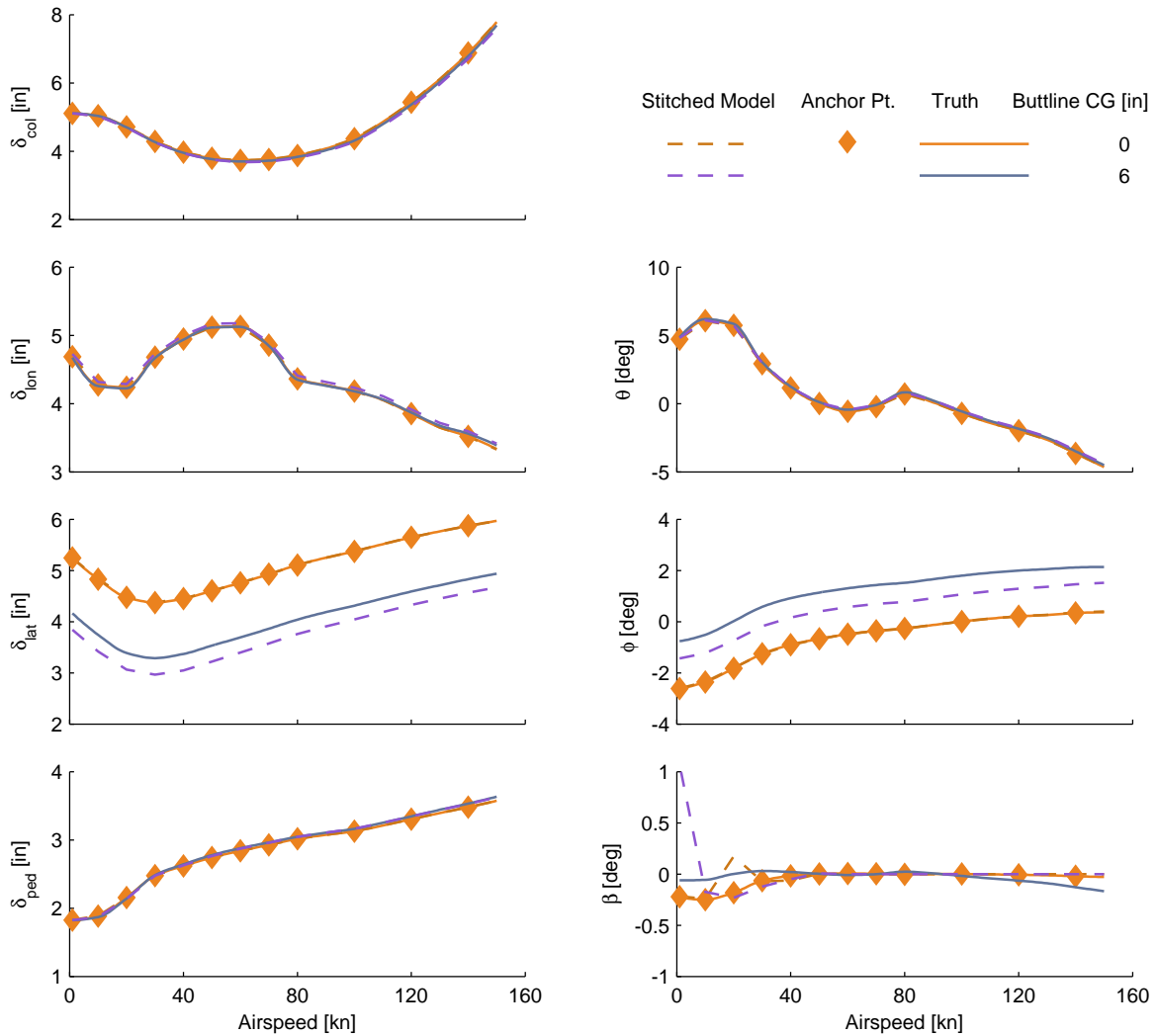
Figure C.14: Verification of off-nominal buttline CG extrapolation, UH-60 stitched model, trim.
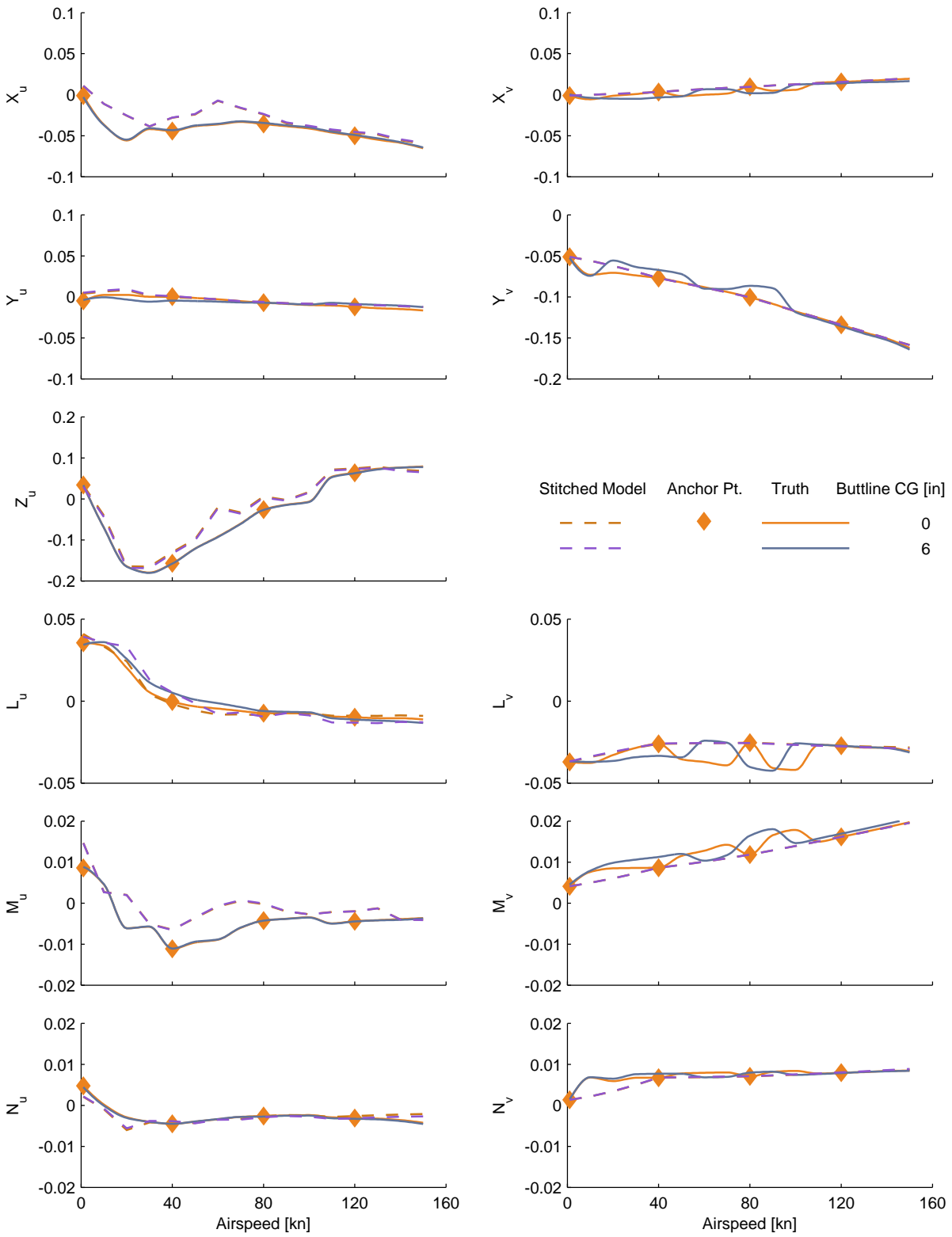
Figure C.15: Verification of off-nominal buttline CG extrapolation, UH-60 stitched model, stability derivatives.
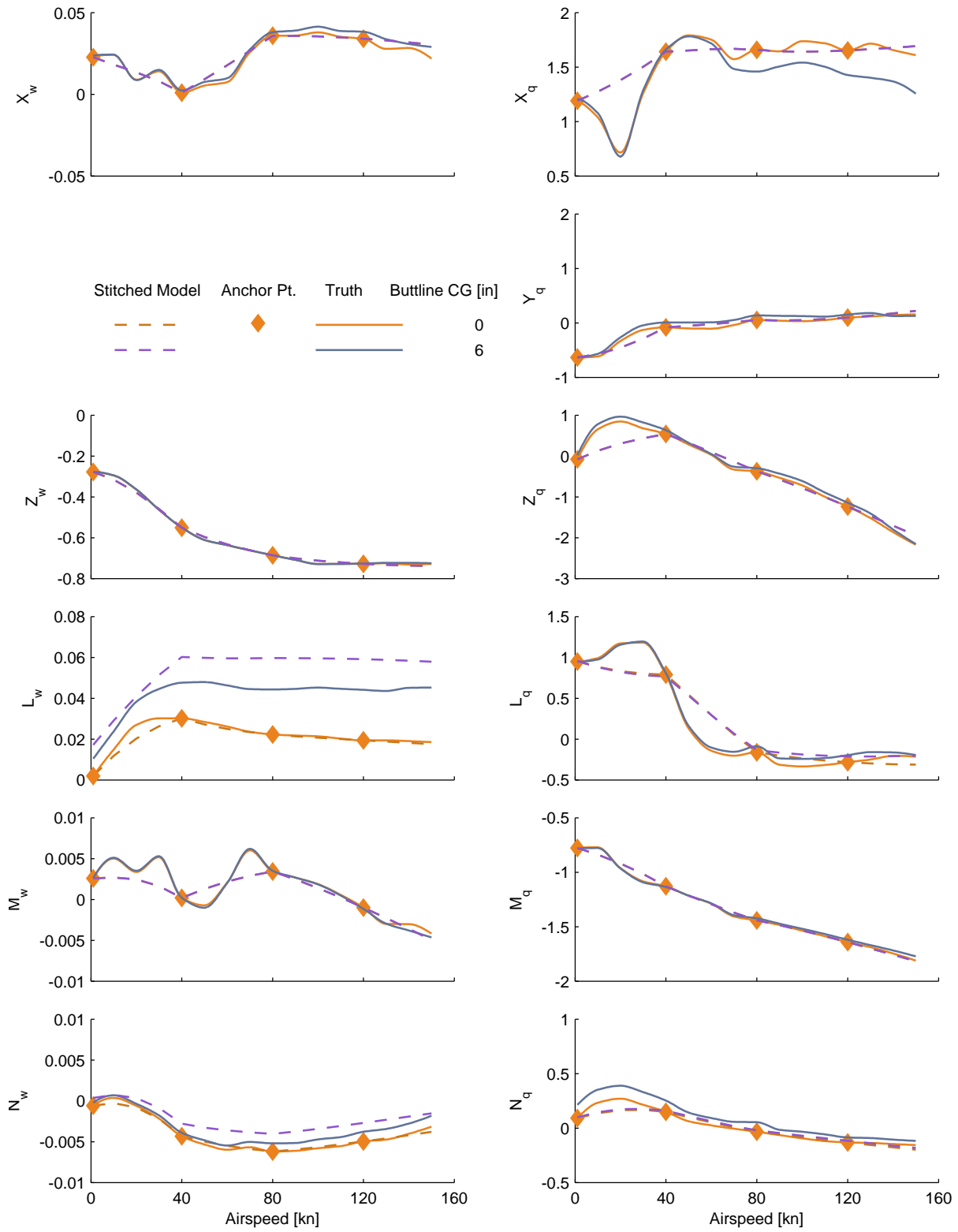
Figure C.15: Verification of off-nominal buttline CG extrapolation, UH-60 stitched model, stability derivatives (cont.)
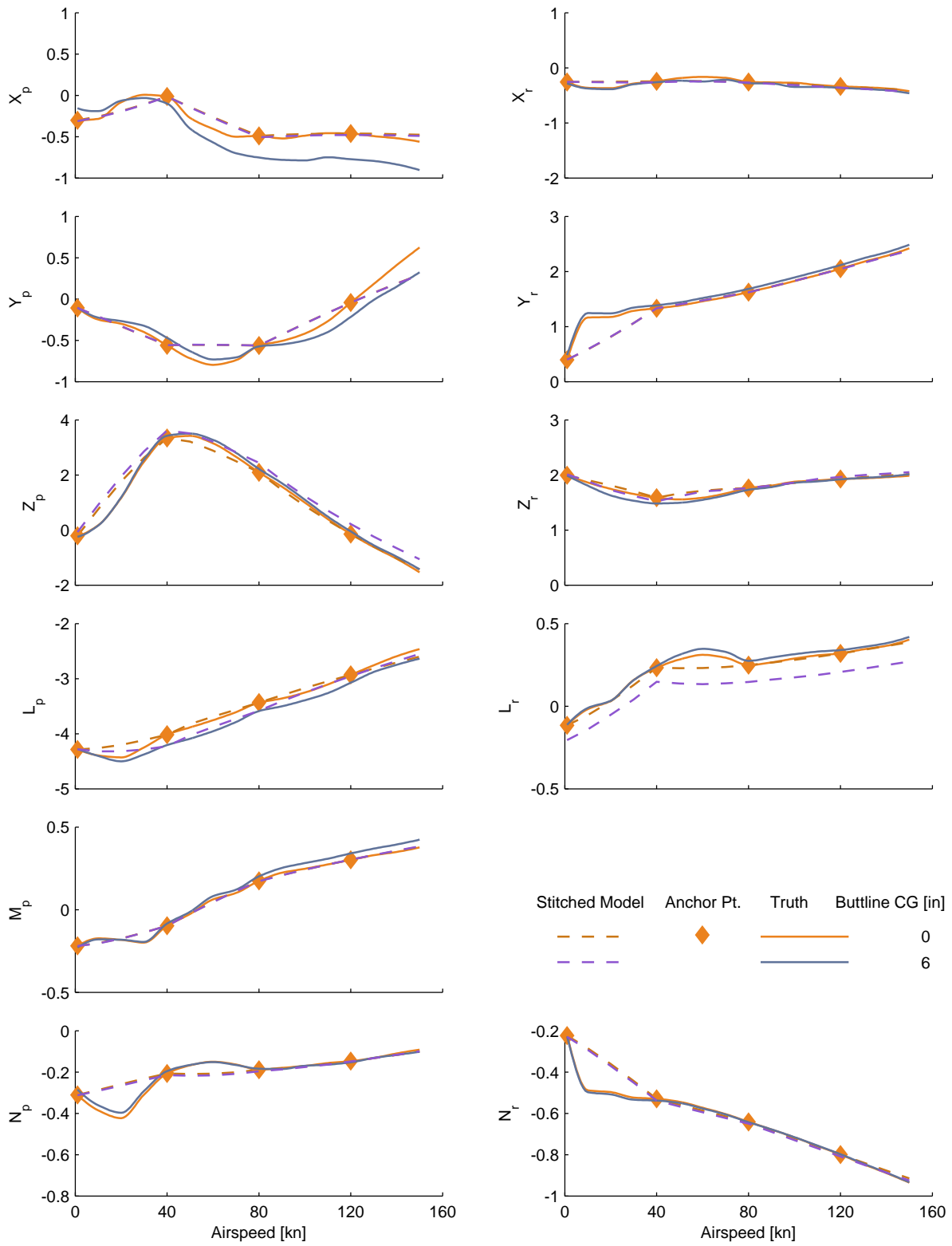
Figure C.15: Verification of off-nominal buttline CG extrapolation, UH-60 stitched model, stability derivatives (cont.)
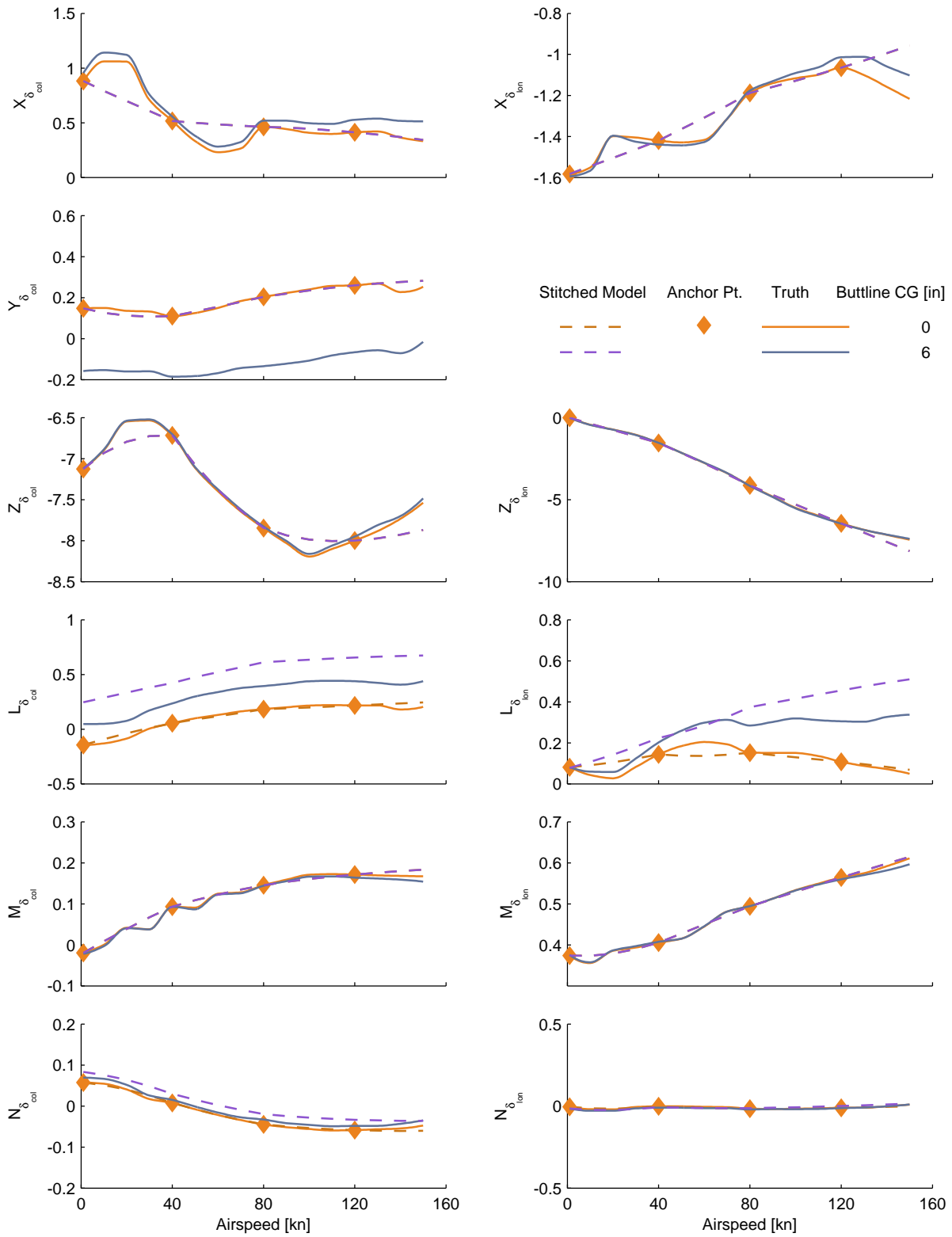
Figure C.16: Verification of off-nominal buttline CG extrapolation, UH-60 stitched model, control derivatives.
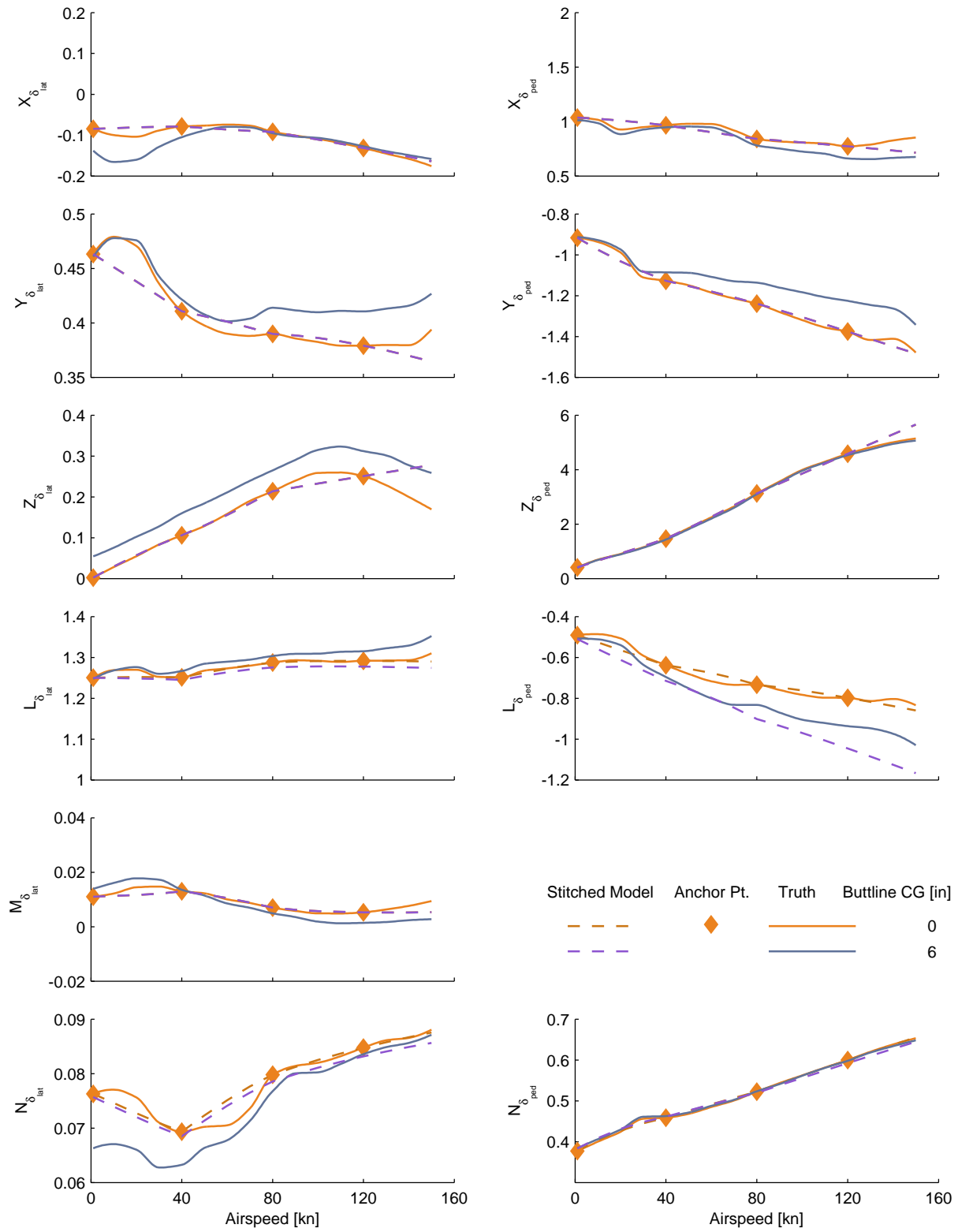
Figure C.16: Verification of off-nominal buttline CG extrapolation, UH-60 stitched model, control derivatives (cont.)

C.4 Altitude

Figures C.17–C.19 show the complete trim and quasi-steady stability and control derivative comparison results for the UH-60 off-nominal altitude verification, as presented in Section 4.6.4.
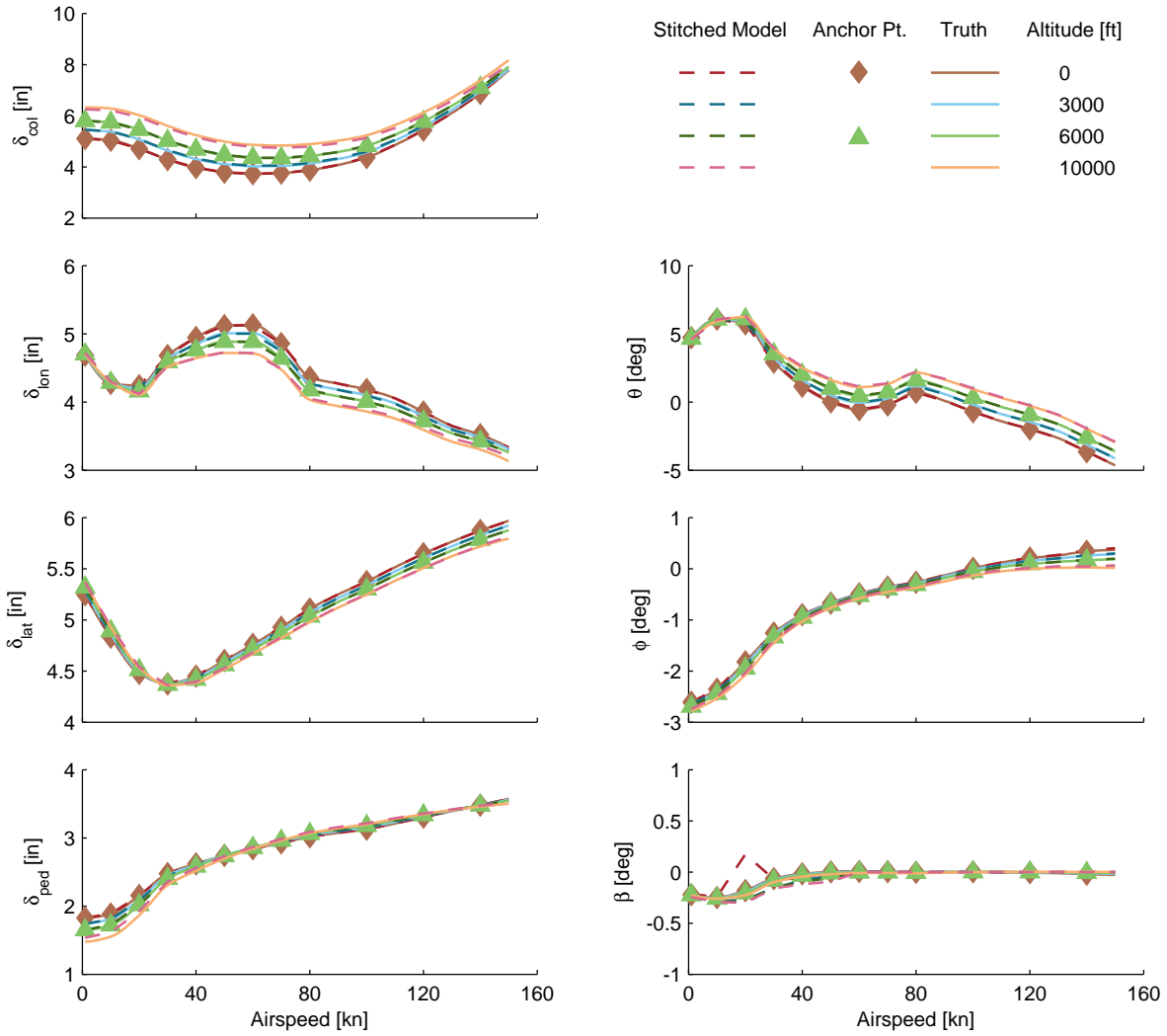
Figure C.17: Verification of altitude extrapolation, UH-60 stitched model, trim.
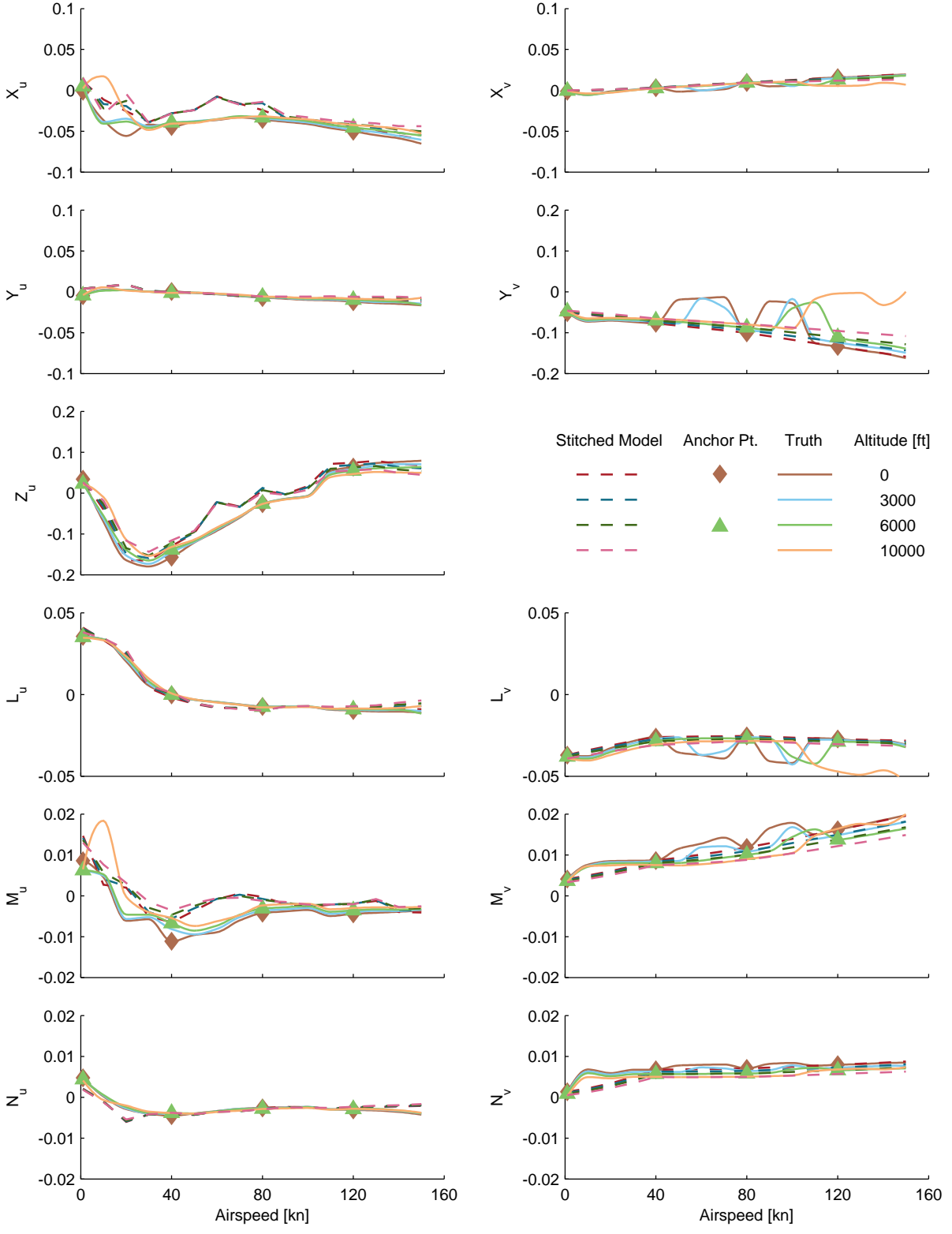
Figure C.18: Verification of altitude extrapolation, UH-60 stitched model, stability derivatives.
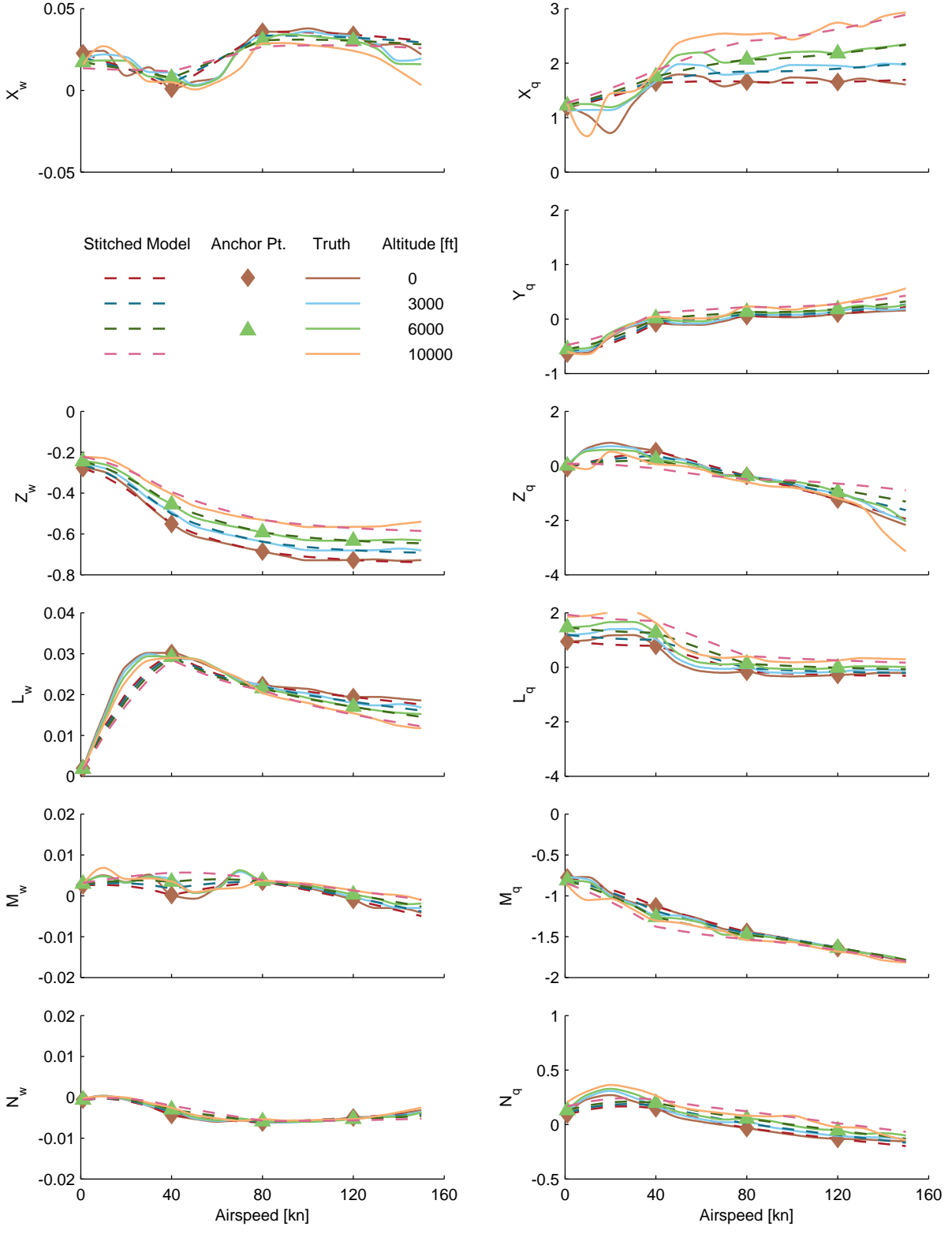
Figure C.18: Verification of altitude extrapolation, UH-60 stitched model, stability derivatives (cont.)
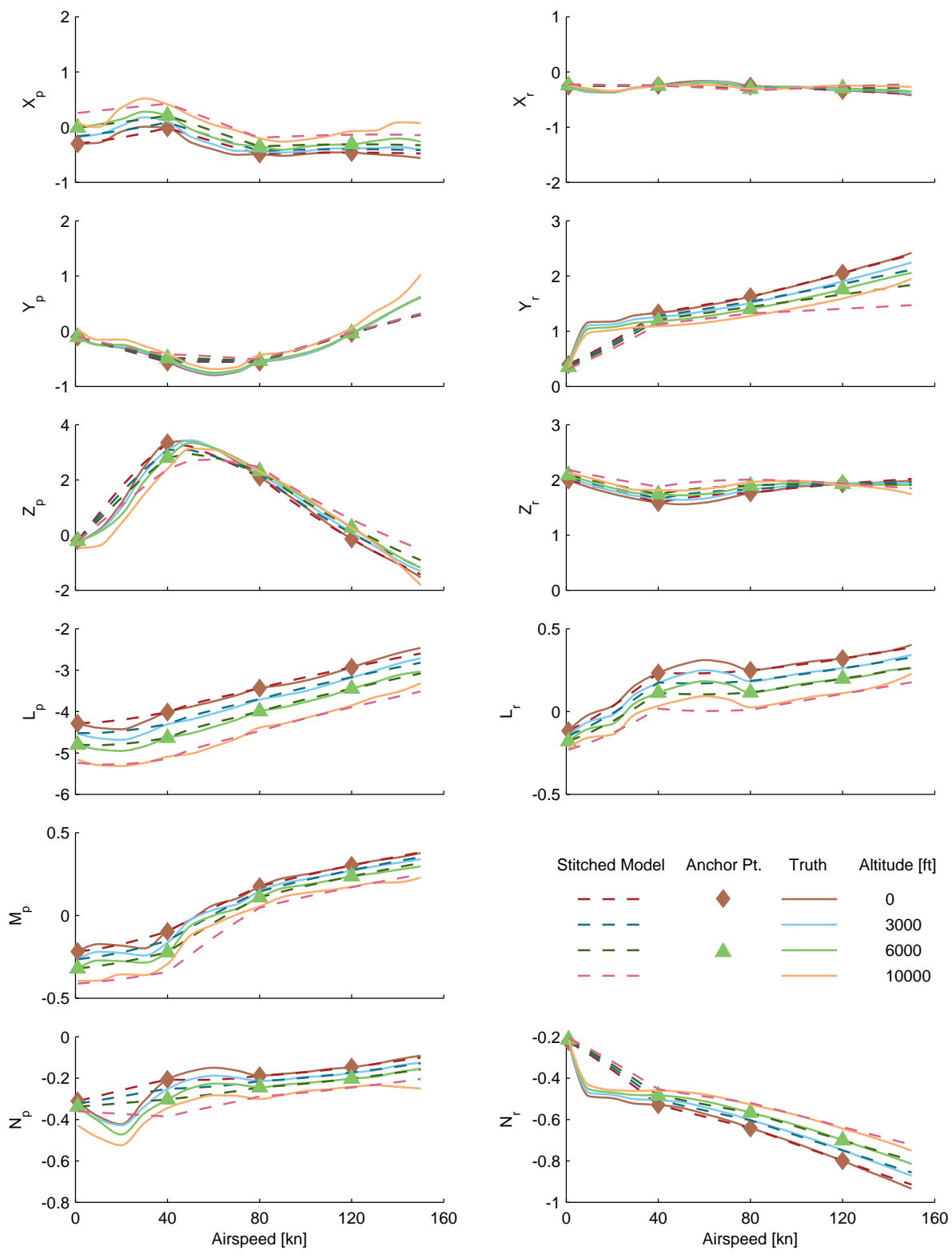
Figure C.18: Verification of altitude extrapolation, UH-60 stitched model, stability derivatives (cont.)
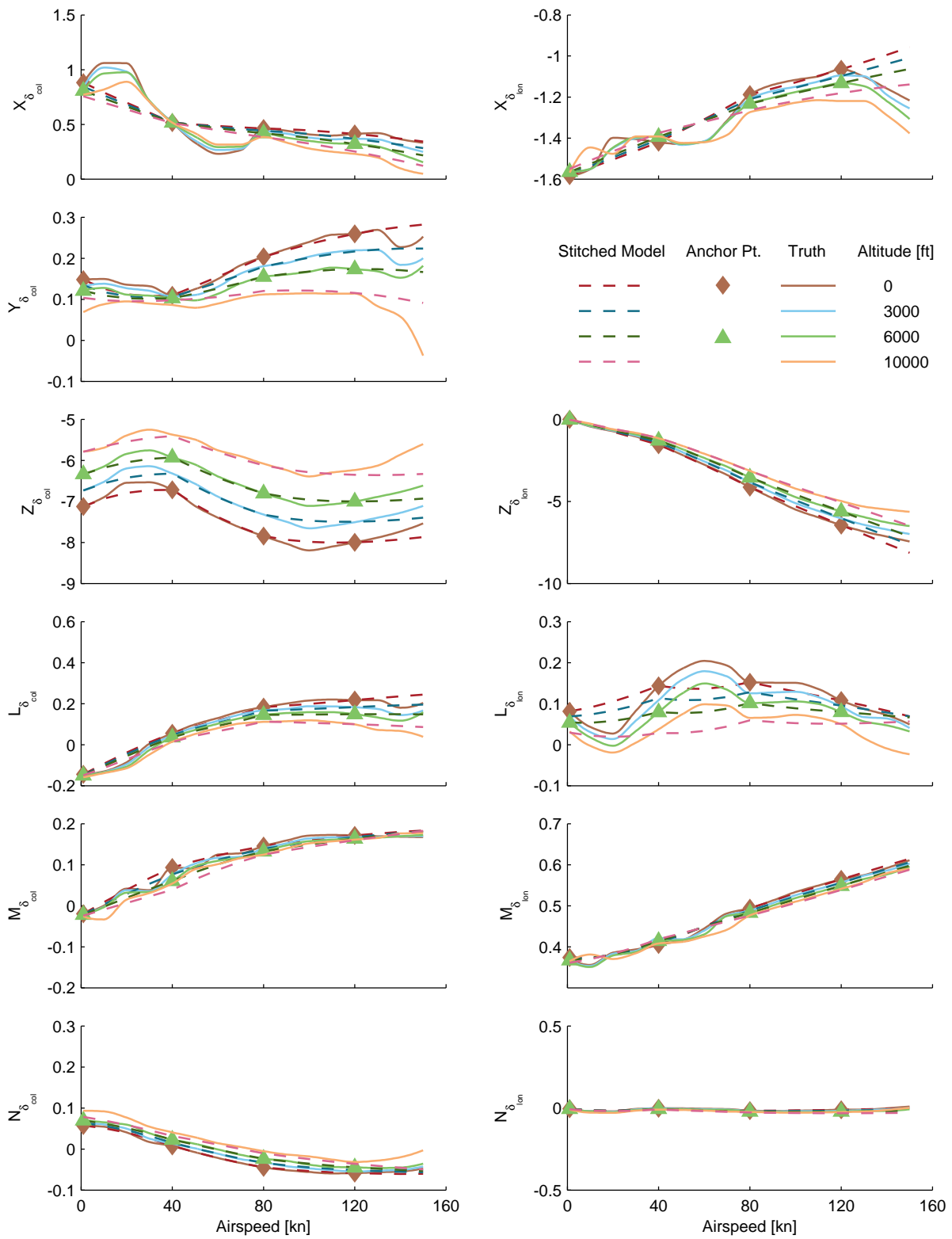
Figure C.19: Verification of altitude extrapolation, UH-60 stitched model, control derivatives.
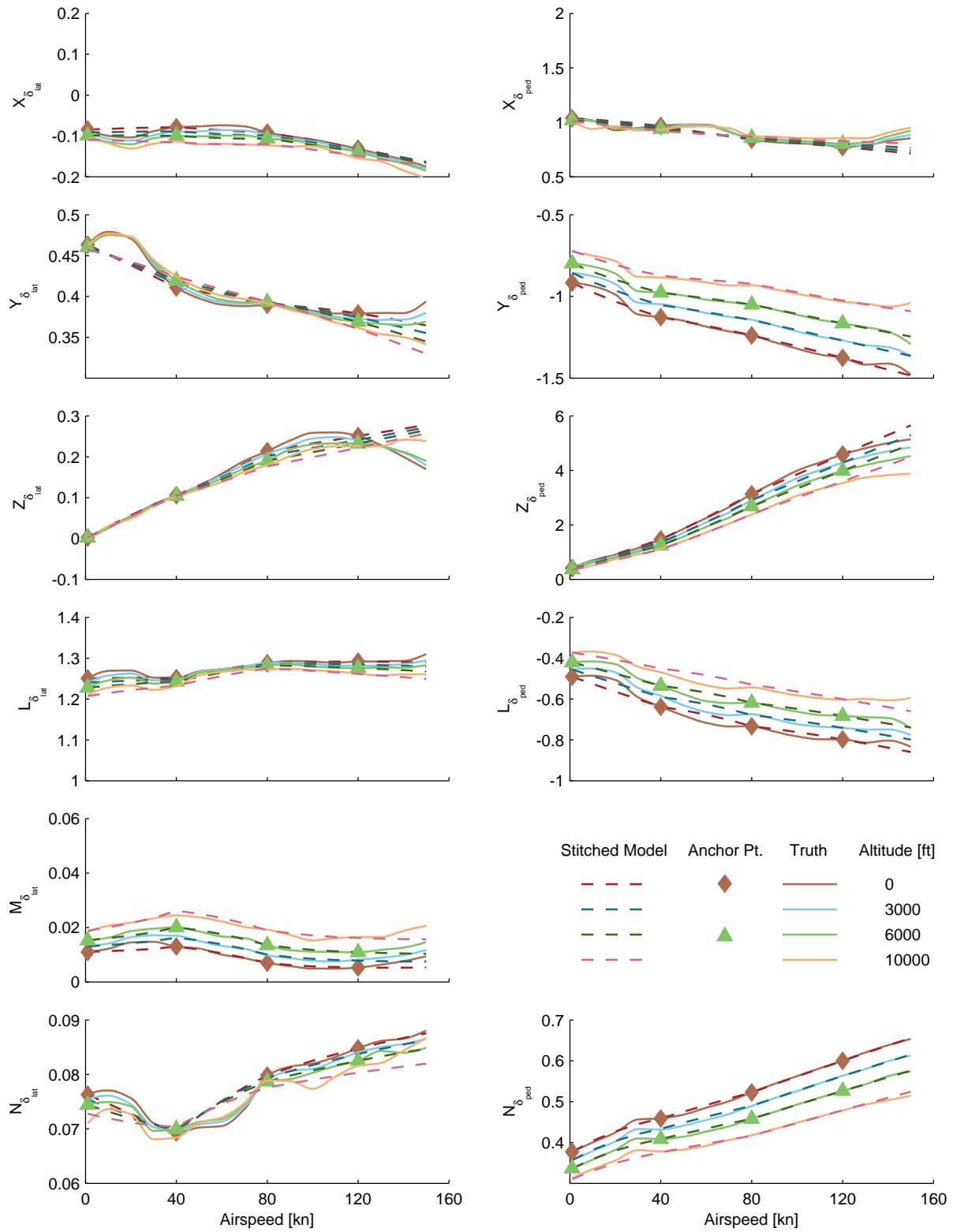
Figure C.19: Verification of altitude extrapolation, UH-60 stitched model, control derivatives (cont.)

C.5 Sling-Load Weight

Figures C.20–C.22 show the complete trim and quasi-steady stability and control derivative comparison results for the UH-60 with sling load verification, as presented in Section 4.8. Linear interpolation between (and extrapolation beyond) the trim data and dimensional stability and control derivatives of the two anchor configurations within the stitched model was performed to simulate the alternate sling-load weight configurations.
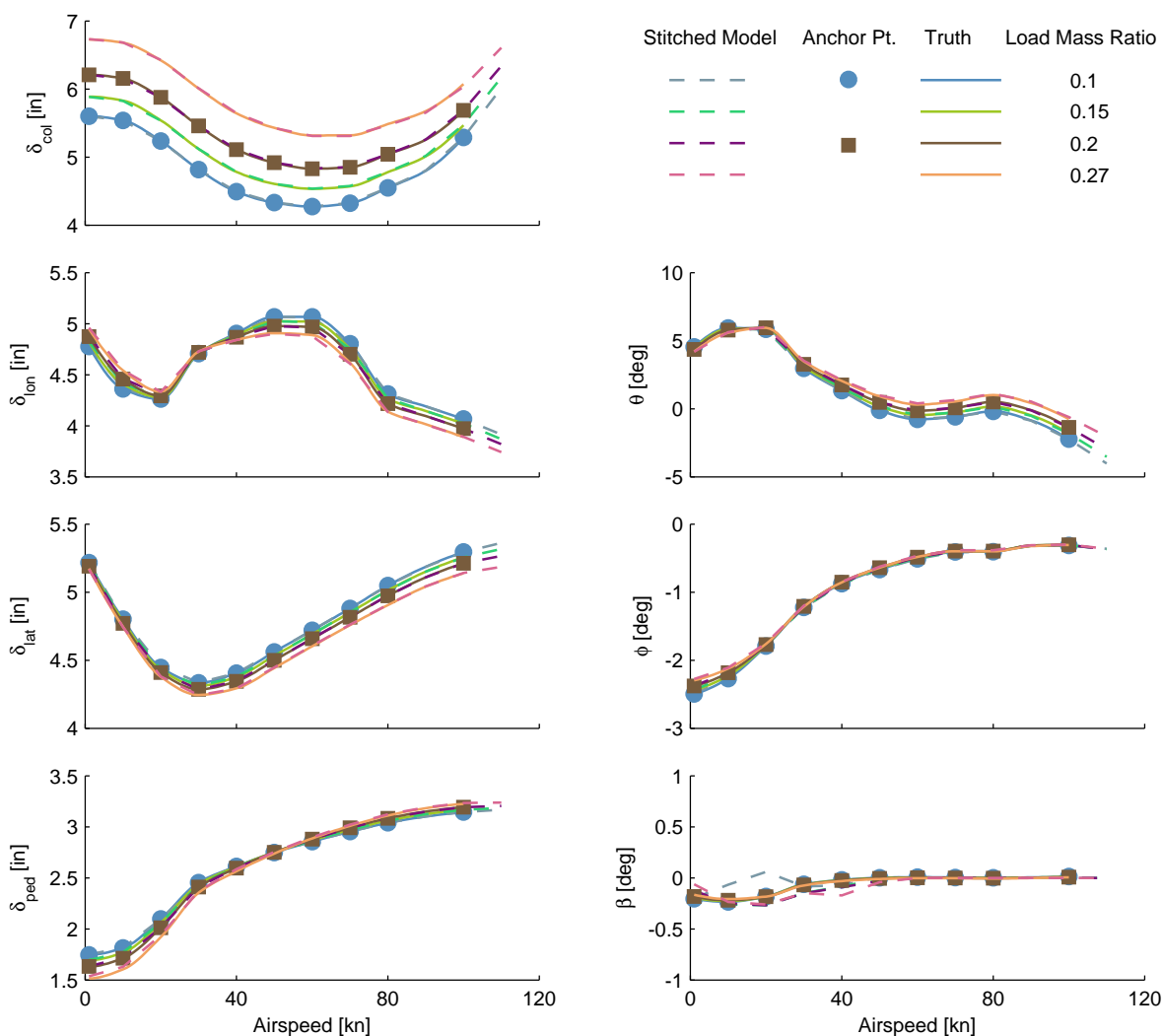

Figure C.20: Alternate configuration verification, sling-load weight, UH-60 stitched model, trim.
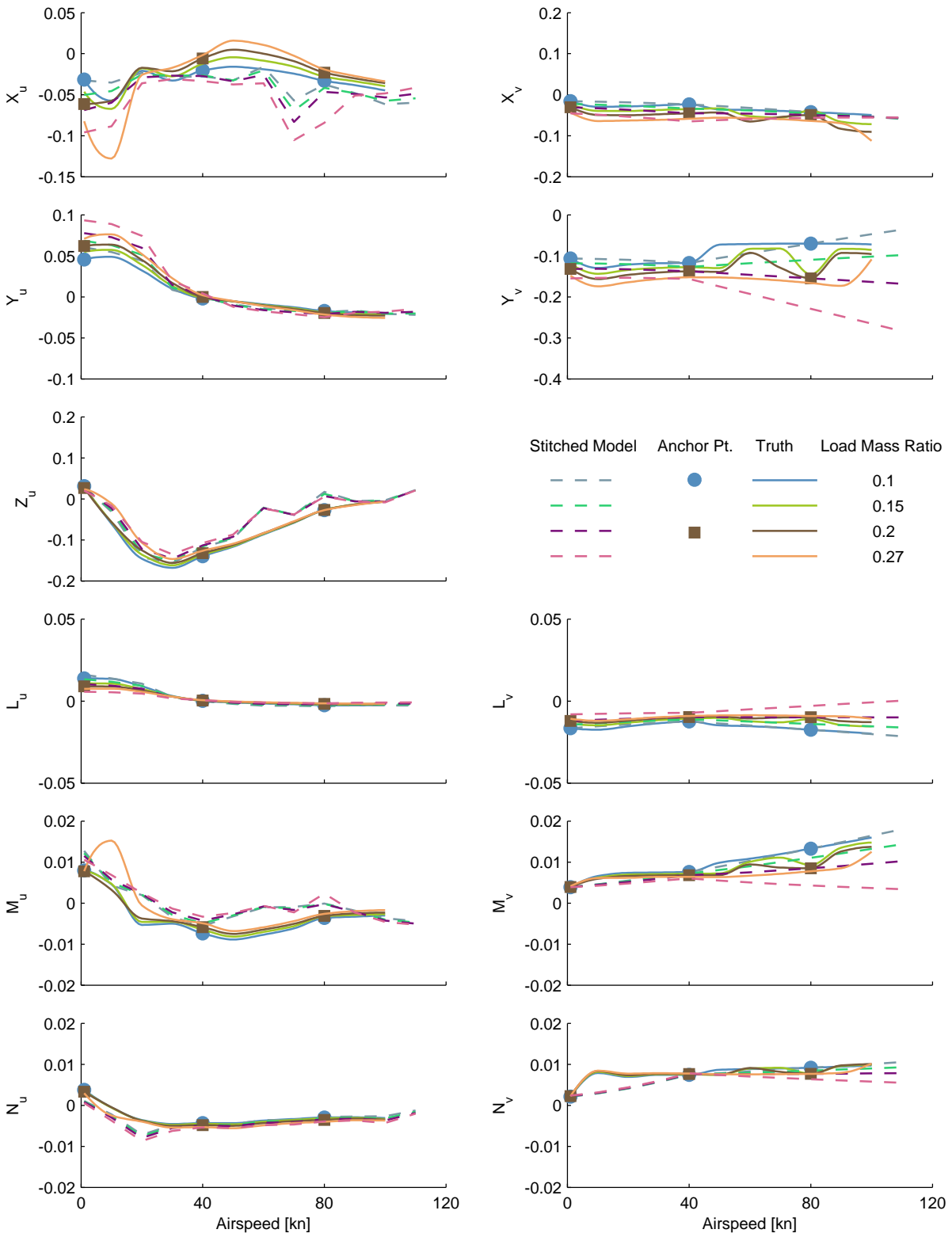
Figure C.21: Alternate configuration verification, sling-load weight, UH-60 stitched model, stability derivatives.
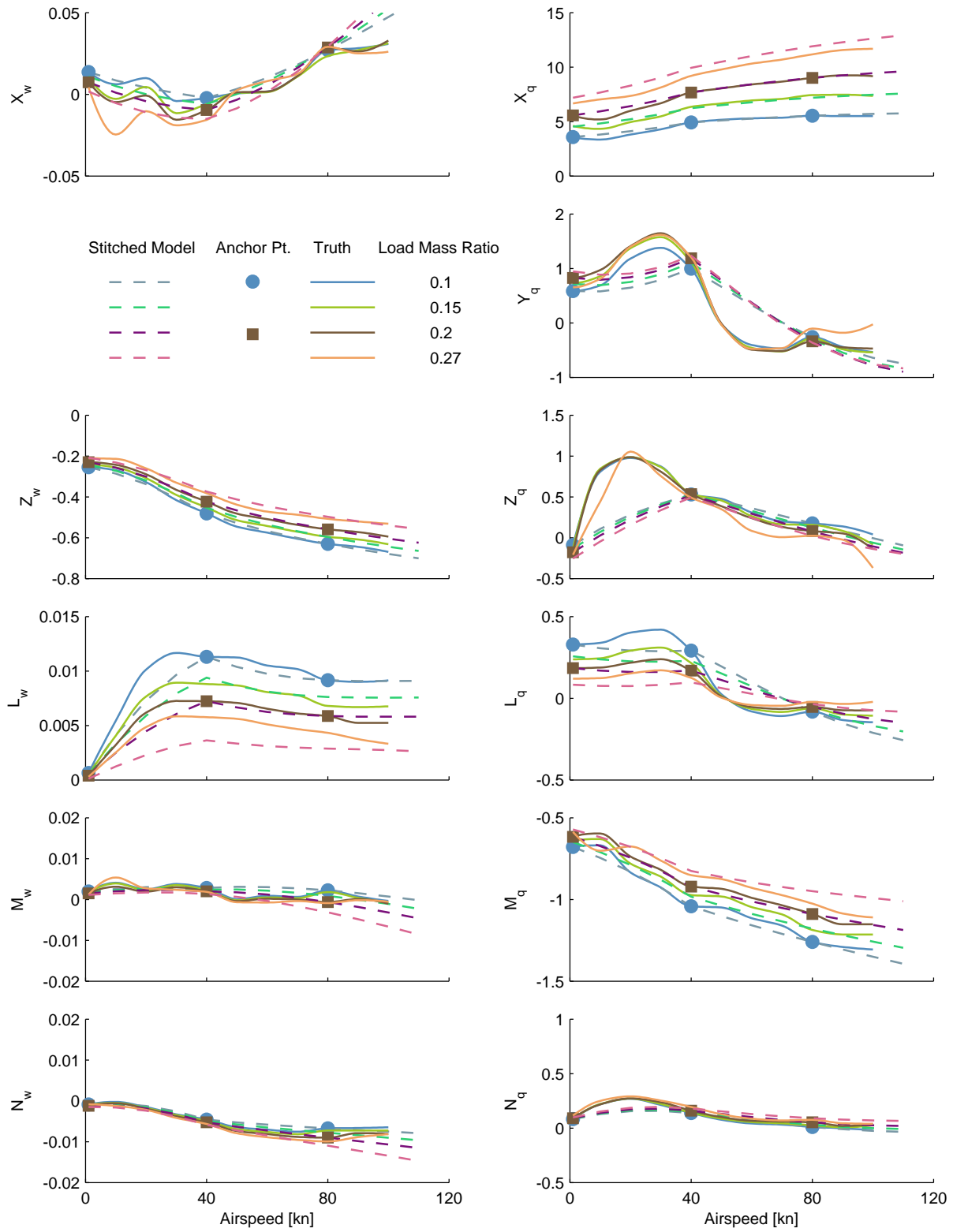
Figure C.21: Alternate configuration verification, sling-load weight, UH-60 stitched model, stability derivatives (cont.)
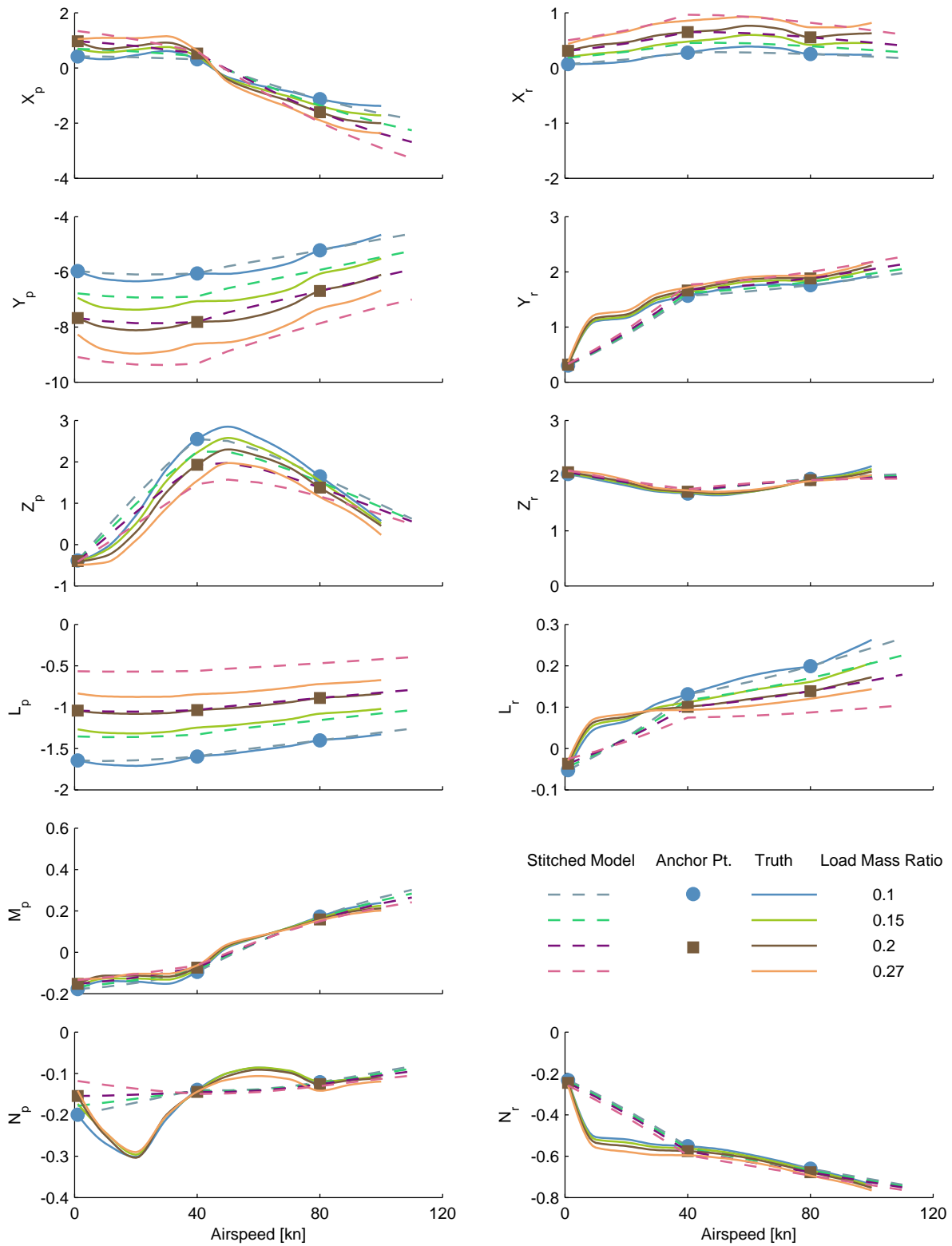
Figure C.21: Alternate configuration verification, sling-load weight, UH-60 stitched model, stability derivatives (cont.)
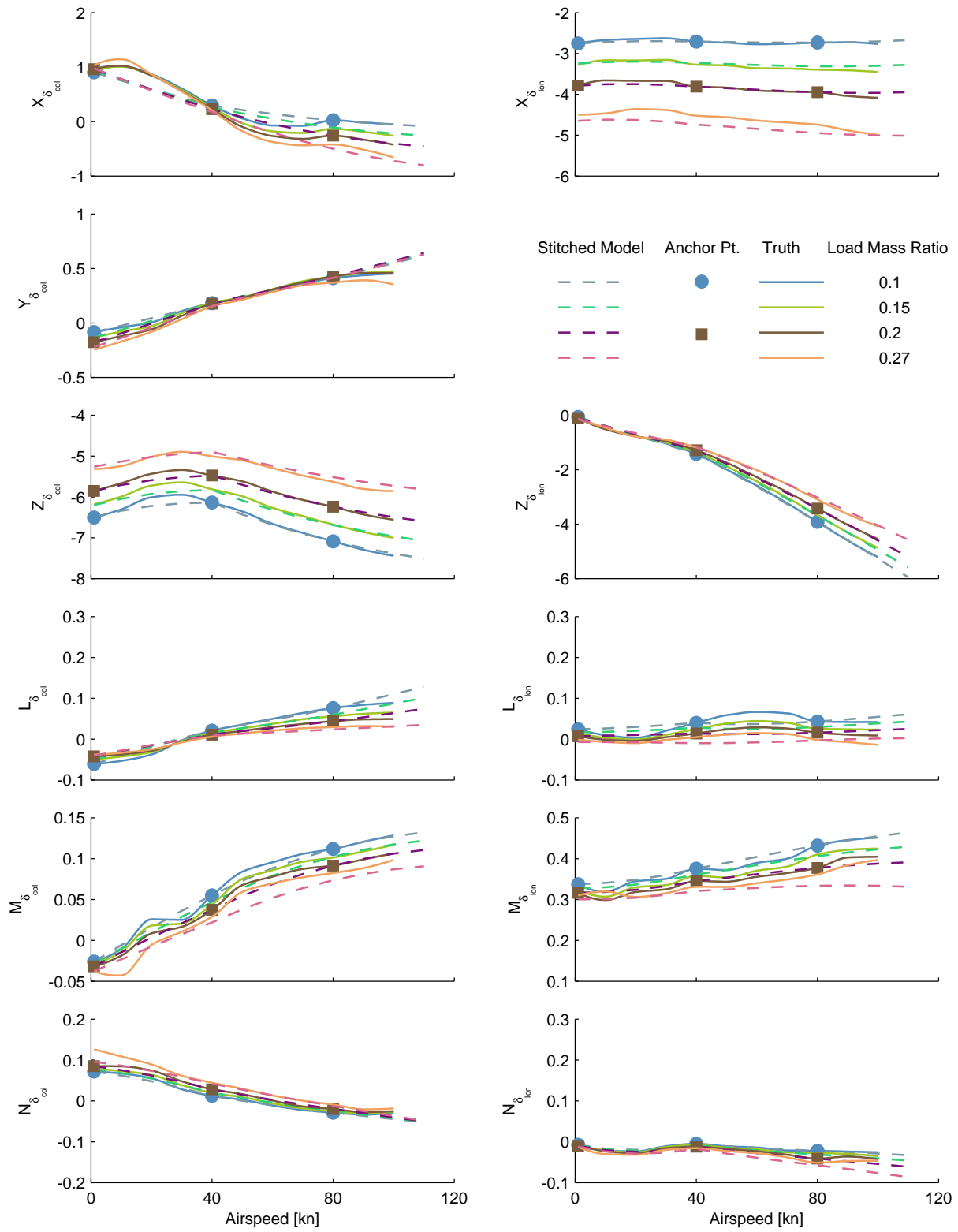
Figure C.22: Alternate configuration verification, sling-load weight, UH-60 stitched model, control derivatives.
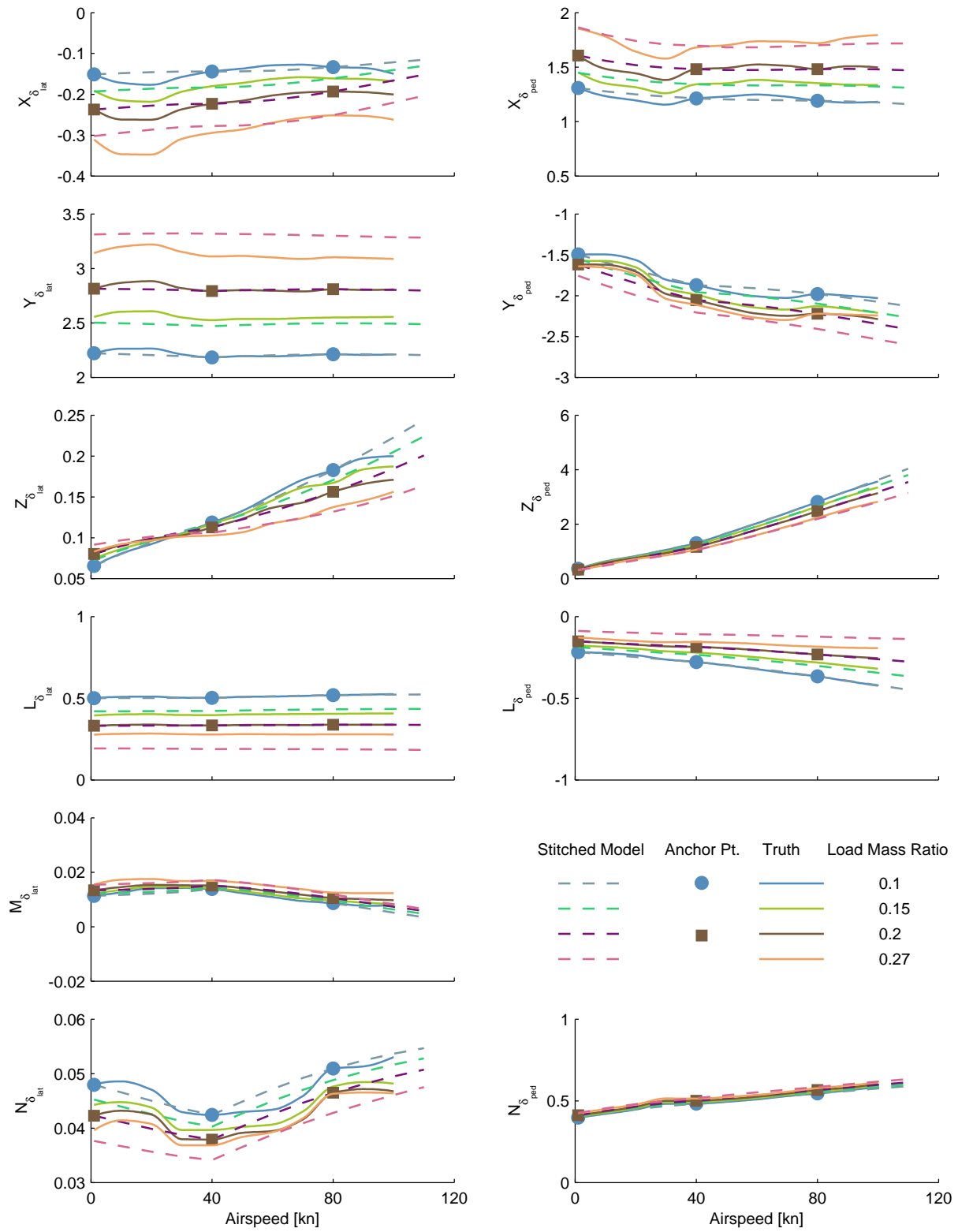
Figure C.22: Alternate configuration verification, sling-load weight, UH-60 stitched model, control derivatives (cont.)

References

[1] Tischler, M. B., *Aircraft and Rotorcraft System Identification: Engineering Methods with Flight Test Examples*, American Institute of Aeronautics and Astronautics, Inc., Reston, VA, 2nd ed., 2012.

[2] Marcos, A. and Balas, G. J., "Development of Linear-Parameter-Varying Models for Aircraft," *AIAA Journal of Guidance, Control, and Dynamics*, Vol. 27, No. 2, March–April 2004.

[3] Aiken, E. W., "A Mathematical Representation of an Advanced Helicopter for Piloted Simulator Investigations of Control-System and Display Variations," NASA TM 81203, AVRADCOM TM 80-A-2, July 1980.

[4] Tischler, M. B., "Aerodynamic Model for Piloted V/STOL Simulation," Systems Technology, Inc., WP 1171-2, Hawthorne, CA, May 1982.

[5] Zivan, L. and Tischler, M. B., "Development of a Full Flight Envelope Helicopter Simulation Using System Identification," *Journal of the American Helicopter Society*, Vol. 55, No. 022003, 2010, pp. 1–15.

[6] Lawrence, B., Malpica, C. A., and Theodore, C. R., "The Development of a Large Civil Tiltrotor Simulation for Hover and Low-Speed Handling Qualities Investigations," 36th European Rotorcraft Forum, Paris, France, September 2010.

[7] Mansur, M. H., Tischler, M. B., Bielefield, M. D., Bacon, J. W., Cheung, K. K., Berrios, M. G., and Rothman, K. E., "Full Flight Envelope Inner-Loop Control Law Development for the Unmanned K-MAX," American Helicopter Society 67th Annual Forum, Virginia Beach, VA, May 2011.

[8] Downs, J., Prentice, R., Dalzell, S., Besachio, A., Ivler, C. M., Tischler, M. B., and Mansur, M. H., "Control System Development and Flight Test Experience with the MQ-8B Fire Scout Vertical Take-Off Unmanned Aerial Vehicle (VTUAV)," American Helicopter Society 63rd Annual Forum, Virginia Beach, VA, May 2007.

[9] Greiser, S. and Seher-Weiss, S., "A contribution to the development of a full flight envelope quasi-nonlinear helicopter simulation," *CEAS Aeronautical Journal*, Vol. 5, No. 1, March 2014, pp. 53–66.

[10] Spires, J. M. and Horn, J. F., "Multi-Input Multi-Output Model-Following Control Design Methods for Rotorcraft," American Helicopter Society 71st Annual Forum, Virginia Beach, VA, May 2015.

[11] McRuer, D., Ashkenas, I., and Graham, D., *Aircraft Dynamics and Automatic Control*, Princeton University Press, Princeton, NJ, 1973.

[12] MATLAB version 7.14.0.739 (R2012a), The MathWorks, Inc., Natick, MA, 2012.

[13] Stevens, B. L. and Lewis, F. L., *Aircraft Control and Simulation*, John Wiley & Sons, Inc., Hoboken, NJ, 2nd ed., 2003.

[14] Anon., "Flying Qualities of Piloted Aircraft," MIL-STD-1797B, Department of Defense Interface Standard, February 2006.

[15] Lusardi, J. A., von Gruenhagen, W., and Seher-Weiss, S., "Parametric Turbulence Modeling for Rotorcraft Applications – Approach, Flight Tests and Verification," *Proceedings of the Rotorcraft Handling Qualities Conference*, November 2008.

[16] Roskam, J., Malaek, S., Anemaat, W., and Gerren, D., "Advanced Aircraft Analysis: A User Friendly Approach to Preliminary Design and Analysis," *Proceedings of the AIAA Techfest XVI*, November 1989.

[17] Tobias, E. L., Tischler, M. B., Berger, T., and Hagerott, S. G., "Full Flight-Envelope Simulation and Piloted Fidelity Assessment of a Business Jet Using a Model Stitching Architecture," AIAA Modeling and Simulation Technologies Conference, Kissimmee, FL, January 2015.

[18] Anon., "U.S. Naval Test Pilot School Flight Test Manual – Fixed Wing Stability and Control Theory and Flight Test Techniques," USNTPS-FTM-No. 103, Naval Air Warfare Center, Aircraft Division, Patuxent River, MD, January 1997.

[19] Roskam, J., *Airplane Design*, Roskam Aviation and Engineering Corporation, Ottawa, KS, 1985.

[20] Kim, F. D., Celi, R., and Tischler, M. B., "High-Order State Space Simulation Models of Helicopter Flight Mechanics," *Journal of the American Helicopter Society*, Vol. 38, No. 4, October 1993, pp. 16–27.

[21] Howlett, J. J., "UH-60A Black Hawk Engineering Simulation Program: Volume I – Mathematical Model," NASA CR-166309, December 1981.

[22] Lusardi, J. A., Blanken, C. L., Braddom, S. R., Cicolani, L. S., and Tobias, E. L., "Development of External Load Handling Qualities Criteria for Rotorcraft," American Helicopter Society 66th Annual Forum, Phoenix, AZ, May 2010.

[23] Cooke, A. K. and Fitzpatrick, E. W., *Helicopter Test and Evaluation*, American Institute of Aeronautics and Astronautics, Inc., Reston, VA, 2002.